

Crustal Structure
of the Mid-Atlantic Ridge at 5 ° South:
Two Contrasting Spreading Segments

Dissertation
zur Erlangung des Doktorgrades
der Mathematisch-Naturwissenschaftlichen Fakultät
der Christian-Albrechts-Universität zu Kiel

vorgelegt von
Lars Planert

Kiel, Mai 2006

Referent: Prof. Dr. E. R. Flüh
Koreferent: Prof. Dr. T. Reston
Tag der mündlichen Prüfung: 11.07.2006

Zum Druck genehmigt: Kiel, 11.07.2006

Der Dekan
gez.

Abstract

Faulting and magmatism are typical of many lithosphere plate boundaries, but perhaps nowhere more intimately linked than at slow spreading mid-ocean ridges. This study presents results of a seismic refraction experiment which determines the crustal and upper mantle structure at the Mid-Atlantic Ridge at 5° South. Seven intersecting seismic profiles were acquired at two morphologically contrasting spreading segments separated by a 70 km offset transform fault. This ridge-transform intersection is unusual in that a pronounced inside corner massif with a corrugated upper surface south of the fracture zone has been split by a change in location of active seafloor spreading, resulting in an outside corner massif and the absence of a volcanic ridge in the northernmost part of the median valley.

Two different tomographic approaches are used in order to obtain velocity models from the seismic data: first-arrival tomography and joint refraction and reflection tomography. Major variations in the velocity structure and crustal thickness are observed along-axis and perpendicular to the ridge. The Monte Carlo uncertainty analysis shows that most of the model parameters are well constrained, with 0.05-0.1 km/s standard deviation for velocity and 0.1-0.25 km standard deviation for reflector depth nodes.

In the northern segment, the along-axis average crustal thickness has increased from 5.6 ± 0.3 km to 6.8 ± 1.3 km within 4 Ma. The increase is accompanied by a more focussed melt supply to the segment center, where crustal thickness reaches up to 9 km. The median valley is characterised by a central hour-glass shaped rise of the seafloor and anomalously low velocities at depths of ~ 2.5 km bsf which indicates the presence of elevated temperatures and perhaps small portions of partial melt. This suggests that the northern segment is currently in a magmatically active period. Away from the segment center, the crust thins to 5-6 km at the segment ends. The reduction in crustal thickness is entirely accommodated by the thinning of the lower crust; lower velocities in the upper crustal portions may indicate fracturing and alteration of the thin crust and underlying mantle.

Most parts of the southern segment are underlain by anomalously thin crust. The thinnest portions (2.4-3 km) are associated with the flanks of the inside corner high (ICH) and a series of sub-basins, which may correspond to a fossil 2nd order non-transform discontinuity prior to the ridge jump. The inside corner high is characterised by strong lateral velocity heterogeneities. In places, anomalously high velocities up to 6 km/s are observed in the uppermost few hundred meters. Beneath the Moho, a pronounced mantle transition zone reveals velocities of 7.2-7.5 km/s. In contrast, outside corner crust is characterised by “typical” layer 2 velocities in the upper crust and a smaller mantle transition zone. The lower mantle velocities directly beneath the Moho at the ICH and its rifted portion may derive from post-emplacement modification (e.g. hydrothermal alteration) related to the subsequent rifting. The crust between the ICH and its rifted portion is relatively thin

(~ 4 km) and does not exhibit a well-developed axial volcanic ridge. These observations are typical for a “cold” segment end, which is in general agreement with seismological studies.

Zusammenfassung

Tektonik und Magmatismus prägen das Bild vieler Plattengrenzen; das gilt im Besonderen für langsam spreizende mittelozeanische Rücken, wo beide Prozesse unmittelbar aufeinander treffen. Diese Arbeit präsentiert die Ergebnisse refraktionsseismischer Messungen am Mittelatlantischen Rücken bei 5° Süd. Entlang sieben seismischer Profile wurde hier für zwei morphologisch sehr unterschiedliche und durch eine Transformstörung mit 70 km Versatz getrennte Segmente die Geschwindigkeitsstruktur der Kruste und des oberen Mantels bestimmt. Die 5° Süd Rückenversatzzone weist als besonderes Merkmal sowohl ein *Inside Corner High* als auch einen durch einen Versatz der Spreizungsachse davon abgetrennten Splitter an der *Outside Corner* auf. Beide Massive sind durch gut sichtbare Gleitstreifen an der Oberfläche gekennzeichnet.

Die in dieser Arbeit dargestellten seismischen Geschwindigkeitsmodelle, die auf Ergebnissen einer Tomographie der Ersteinsätze und einer gemeinsamen Tomographie von Ersteinsätzen und Reflexionen basieren, weisen ausgeprägte Variationen der Krustendicke und Geschwindigkeitsstruktur auf, sowohl senkrecht als auch parallel zur Spreizungsrichtung. Eine Monte Carlo Abschätzung der Modellfehler ergibt, dass grosse Modellbereiche mit Standardabweichungen von 0.05-0.1 km/s für Geschwindigkeiten und 0.1-0.25 km für Reflektortiefen sehr genau bestimmt sind.

Im nördlichen Segment ist ein Anstieg der mittleren Krustenmächtigkeit von 5.6 ± 0.3 km auf 6.8 ± 1.3 km innerhalb einer Zeitspanne von 4 Mio Jahre zu beobachten. Dieser Anstieg geht einher mit einer zunehmenden Fokussierung der Schmelzen auf Bereiche im Segmentzentrum, was dort zu maximalen Krustenmächtigkeiten von 9 km führt. Das *Median Valley* weist im Segmentzentrum eine Aufwölbung des Meeresbodens auf. In diesem Bereich deutet eine negative Geschwindigkeitsanomalie in ~ 2.5 km Tiefe auf stark erhöhte Temperaturen und evtl. geringe Anteile partieller Schmelzen hin, was den Schluss zulässt, dass sich das nördliche Segment zur Zeit in einer magmatisch aktiven Phase befindet. Die Krustenmächtigkeit nimmt mit zunehmender Entfernung vom Segmentzentrum bis auf 5-6 km an den Segmentenden ab. Die Ausdünnung findet dabei ausschließlich auf Kosten der Unterkruste statt. Niedrigere Geschwindigkeiten in den oberen Bereichen der Kruste deuten auf eine zunehmende Zerklüftung und Alteration der dünnen Kruste und des darunter liegenden Mantels hin.

Grosse Teile des südlichen Segments sind durch ungewöhnlich geringe Krustenmächtigkeiten gekennzeichnet. Die dünnste Kruste (2.4-3 km) wird dabei an den Flanken des *Inside Corner Highs* (ICH) gemessen sowie im Bereich einer Ansammlung von kleineren Becken, die mit einer fossilen Rückenversatzzone zweiter Ordnung räumlich korreliert. *Inside Corner* Kruste ist gekennzeichnet durch starke laterale Heterogenität in den seismischen Geschwindigkeiten, die in einigen Bereichen innerhalb weniger hundert Meter

Tiefe auf Werte >6 km/s ansteigen. Unterhalb der modellierten Kruste-Mantel-Grenze deuten Geschwindigkeiten von 7.2-7.5 km/s auf eine deutlich ausgeprägte Übergangszone hin. Im Gegensatz dazu ist die *Outside Corner* durch ‘typische’ *Layer 2* Geschwindigkeiten und Geschwindigkeitsgradienten in der Oberkruste und durch eine dünnere Übergangszone im oberen Mantel gekennzeichnet. Ursächlich für die ungewöhnlich niedrigen Mantelgeschwindigkeiten im Bereich des ICH und des davon abgetrennten Splitters könnten Hydratisierungsvorgänge sein, die mit der Zersplitterung und anschließenden Spreizung im Zusammenhang stehen. Die Kruste zwischen beiden Massiven ist mit ~ 4 km ungewöhnlich dünn und weist keinen vulkanischen Rücken auf. Das deutet darauf hin, dass dieses Segmentende zur Zeit magmatisch inaktiv ist, was im Einklang mit seismologischen Ergebnissen in dieser Region steht.

Contents

Abstract	v
Zusammenfassung	vii
1 Introduction	7
1.1 Mid-ocean ridges	7
1.2 Ridge segmentation	9
1.3 Processes at segment ends	11
1.4 Motivation and structural outline	15
2 Area of Investigation - MAR 5° South	19
2.1 Regional structural setting	19
2.2 Northern segment	20
2.2.1 Median valley	20
2.2.2 Crestal mountains	22
2.3 Southern segment	24
2.3.1 IC and OC massifs	24
2.3.2 Median valley	26
2.3.3 South and west of the IC massif	26
2.4 Related work	27
2.4.1 Segment evolution	27
2.4.2 Dredging	29
2.4.3 Microearthquake seismicity	30
2.5 Database for this study	32
3 Data processing	35
3.1 OBH/S data	35
3.2 Wave-equation datuming	39
4 First-arrival seismic tomography	41
4.1 Outline	41
4.2 Forward method	42
4.3 Inverse method	45
4.4 Results of the first-arrival tomography	48
4.4.1 Description of the procedure	48
4.4.2 Resolution and accuracy	52

4.4.3	Features of the models	57
5	Joint refraction and reflection tomography	73
5.1	Model parameterization	73
5.2	Forward method	74
5.2.1	Shortest path method (SPM)	74
5.2.2	Ray bending	77
5.2.3	Performance in a realistic model	78
5.3	Inverse method	82
5.4	Parameter adjustment	85
5.5	Results of the joint tomography - Profile 09	87
5.6	Resolution and Accuracy	92
5.6.1	Depth kernel weighting test	92
5.6.2	Synthetic anomaly test	94
5.6.3	Nonlinear Monte Carlo uncertainty analysis	97
6	Results	111
6.1	Results for Profile 10	111
6.2	Results for Profile 11	116
6.2.1	Evidence for elevated temperatures in the mid crust	121
6.3	Results for Profile 07/08	123
6.3.1	Density structure	128
6.4	Results for Profiles 02-05	131
7	Interpretation and Discussion	135
7.1	Northern segment	135
7.1.1	Across-axis variations in crustal thickness	135
7.1.2	Along-axis variations in crustal thickness	137
7.1.3	Ridge morphology and crustal thickness	138
7.2	Velocity structure of the transform valley	140
7.3	Southern segment	141
7.3.1	Nature of the crust in the IC and OC region	144
7.3.2	Implications for the mechanisms of rifting	146
7.3.3	Implications for rift propagation	149
8	Conclusions and Outlook	151
	Bibliography	154
A	Selected seismic record sections of Profile 07/08	167
B	Selected seismic record sections of Profile 09	177
C	Selected seismic record sections of Profile 10	187
D	Selected seismic record sections of Profile 11	195

List of Figures

1.1	Spreading rate dependent model of crustal accretion and mantle upwelling .	10
1.2	Three possible geological models for oceanic layer 3	12
1.3	Idealized along-axis section of two spreading segments	13
1.4	Schematic cross-section of a detachment fault and perspective view of Atlantis Massif	14
2.1	The Mid-Atlantic Ridge between Chain FZ and Ascension FZ	20
2.2	Bathymetric map of the work area	21
2.3	The median valley of the northern segment	23
2.3	Bathymetry of the southern segment	25
2.4	Reconstructed evolution of the segment end	28
2.5	Distribution of earthquakes recorded with the ocean bottom stations	31
2.6	Station distribution and shot geometry of the wide-angle seismic profiles . .	33
3.1	Seismic section of Profile 09 recorded by OBH46 (raw data)	36
3.1	Record section of OBH46 after processing	37
3.2	Seismic record section of Profile 07/08 recorded by OBH04	38
3.3	Record section of OBH71 (Profile 11) with different shot datums	40
4.1	2D and 1D finite-difference operators	43
4.2	Traveltime contours and ray paths calculated with the finite-difference algorithm for a realistic velocity model	44
4.3	Illustration of the “ringing effect”	49
4.4	An iterative top-to-bottom scheme	51
4.5	Traveltime residuals for the starting model and for the final model of Profile 10	52
4.6	Checkerboard test for Profile 07/08	53
4.7	Test with velocity anomalies positioned in key localities of Profile 07/08 . .	54
4.8	Influence of different starting models on the tomographic output of Profile 10	56
4.9	Final velocity models for the ridge-parallel Profiles 10 and 09	58
4.10	Seismic record section of Profile 10 recorded by OBH55 and OBH56	59
4.10	Seismic record sections of Profile 10 (continued)	60
4.11	Velocity-depth profiles at the profile intersections	61
4.12	Velocity-depth profiles extracted at specified key locations of Profile 09 . . .	62
4.13	Seismic record section of Profile 09 recorded by OBH44	63
4.14	Test with velocity anomalies positioned in key localities of Profile 09	64
4.15	Final velocity models for the ridge-perpendicular Profiles 11 and 07/08 . . .	66

4.16	Results for Profile 11 obtained using different tomographic approaches . . .	67
4.17	Seismic record section of Profile 11 recorded by OBH77	68
4.18	Seismic record section of Profile 07/08 recorded by OBH04	71
5.1	Irregular grid parameterized as a shared mesh beneath the seafloor	74
5.2	Hybrid forward algorithm	76
5.3	Traveltime error and ray dissimilarity due to different grid sizes	79
5.4	Performance of the hybrid forward algorithm	81
5.5	Assessment of smoothing weights for velocity nodes and depth nodes	86
5.6	Results of tomographic inversion using the FAST model as the starting model	88
5.7	Results of tomographic inversion using a minimum 1D starting model . . .	89
5.8	Traveltime residuals for the models	91
5.9	Test of velocity-depth ambiguity	93
5.10	Resolution test - shallower crust, lower crust/upper mantle	95
5.10	Resolution test - model periphery, reflector perturbation	96
5.11	Starting model randomization for Profile 09	97
5.12	Data randomization for Profile 09	99
5.13	Examples of randomized starting models and corresponding tomographic solutions and final RMS residuals	100
5.14	Final velocity model and Moho for Profile 09	102
5.15	Moho constrained by reflection coverage for Profile 09	103
5.16	Point correlation shown for individual model parameters	103
5.16	Point correlation shown for individual model parameters (continued) . . .	104
5.17	Model profile distributions and histograms for Moho depths	105
5.18	Histograms for uppermost mantle P-wave velocities	106
5.19	Seismic record section of Profile 09 recorded by OBH46	107
5.19	Seismic record sections of Profile 09 recorded by OBH37 and OBH39 . . .	108
5.20	Performance of the Monte Carlo uncertainty analysis in a synthetic test . .	109
6.1	Final velocity model and Moho for Profile 10	112
6.2	Velocity-depth profiles extracted from the final model for Profile 10	113
6.3	Seismic sections of Profile 10 recorded by OBH54 and OBH62	114
6.4	Histograms for uppermost mantle P-wave velocities for Profile 10	115
6.5	Point correlation for a velocity node and a reflector node for Profile 10 . . .	115
6.6	Final velocity model and Moho for Profile 11	117
6.7	Synthetic anomaly test and calculated point correlation for Profile 11 . . .	118
6.8	Seismic section of Profile 11 recorded by OBH64	119
6.9	Seismic section of Profile 11 recorded by OBH71	120
6.10	RMS data misfits assuming different mantle velocities for Profile 11	121
6.11	Velocity perturbation with depth in the median valley of Profile 11	122
6.12	Final velocity model and Moho for Profile 07/08	124
6.13	Selected model features of Profile 07/08	125
6.14	Seismic Record sections of Profile 07/08 recorded by OBH21 and OBH36 .	126
6.14	Seismic record sections of Profile 07/08 recorded by OBH19 and OBH29 . .	127
6.15	Gravity modeling for a variety of density models for Profile 07/08	129

6.16	Perspective view of the ICH area with Profiles 02, 04 and 05 and sections of Profiles 07/08 and 09 in the bathymetric framework of the ICH area . . .	132
6.17	Tomographic models and corresponding ray coverage for the shorter profiles	133
7.1	Velocity depth profiles - across-axis variations	136
7.1	Velocity depth profiles - along-axis variations	137
7.2	Comparison of ridge-parallel profiles at various mid-ocean ridges	139
7.3	Crustal thickness for the ICH area and its flanking regions	142
7.4	Velocity model for the development of the rifted ICH complex based on the tomographic model of Profile 07/08	143
7.5	Inside corner and outside corner crust on Profile 07/08	145
7.6	Models for the development of oceanic core complexes	147
8.1	Photographs of Sugar Head smoker and black smoker	153
A.1	<i>Profile geometry and station distribution of Profile 07/08.</i>	167
A.2	<i>Profile 07/08, OBH 22.</i>	168
A.3	<i>Profile 07/08, OBH 20.</i>	169
A.4	<i>Profile 07/08, OBH 06.</i>	170
A.5	<i>Profile 07/08, OBH 18.</i>	171
A.6	<i>Profile 07/08, OBH 30.</i>	172
A.7	<i>Profile 07/08, OBH 32.</i>	173
A.8	<i>Profile 07/08, OBH 34.</i>	174
A.9	<i>Profile 07/08, OBH 35.</i>	175
B.1	<i>Profile geometry and station distribution of Profile 09.</i>	177
B.2	<i>Profile 09, OBH 49.</i>	178
B.3	<i>Profile 09, OBH 48.</i>	179
B.4	<i>Profile 09, OBH 47.</i>	180
B.5	<i>Profile 09, OBH 45.</i>	181
B.6	<i>Profile 09, OBH 42.</i>	182
B.7	<i>Profile 09, OBH 41.</i>	183
B.8	<i>Profile 09, OBH 40.</i>	184
B.9	<i>Profile 09, OBH 38.</i>	185
C.1	<i>Profile geometry and station distribution of Profile 10.</i>	187
C.2	<i>Profile 10, OBH 63.</i>	188
C.3	<i>Profile 10, OBH 61.</i>	189
C.4	<i>Profile 10, OBH 60.</i>	190
C.5	<i>Profile 10, OBH 59.</i>	191
C.6	<i>Profile 10, OBH 58.</i>	192
C.7	<i>Profile 10, OBH 52.</i>	193
C.8	<i>Profile 10, OBH 51.</i>	194
D.1	<i>Profile geometry and station distribution of Profile 11.</i>	195
D.2	<i>Profile 11, OBH 65.</i>	196
D.3	<i>Profile 11, OBH 66.</i>	197

D.4	<i>Profile 11, OBH 67.</i>	198
D.5	<i>Profile 11, OBH 68.</i>	199
D.6	<i>Profile 11, OBH 70.</i>	200
D.7	<i>Profile 11, OBH 72.</i>	201
D.8	<i>Profile 11, OBH 73.</i>	202
D.9	<i>Profile 11, OBH 74.</i>	203
D.10	<i>Profile 11, OBH 76.</i>	204

Chapter 1

Introduction

“The birth of the oceans is a matter of conjecture, the subsequent history is obscure, and the present structure is just beginning to be understood.”

Harry Hammond Hess in *“A History of Ocean Basins”* (1962)

Seafloor spreading at mid-ocean ridges was identified more than 40 years ago as the key which unlocked the plate tectonic revolution (Hess, 1962; Dietz, 1961). Since the days of Hess and Dietz hypothesis a lot of effort has been spent on the understanding of the forces that shape the topography of the spreading center, the processes that create the mafic igneous crust, the deformation and metamorphism that modify it, and the relationships among these parameters. There is perhaps no better place to study the interactions of faulting and magmatism than at mid-ocean ridges. Unlike old continental terranes or ophiolite complexes, they are not end-members of a complex geologic history, but reveal views of ongoing tectonic and magmatic activity, which directly affect the structure of the new created oceanic crust. This study focusses on the seismic velocity structure of the oceanic crust and hence, on the relative importance of faulting and magmatism at a ridge-transform intersection at the slow spreading Mid-Atlantic Ridge.

1.1 Mid-ocean ridges

Mid-ocean ridges are the sites of the most voluminous magmatic activity on Earth and the largest and most active extensional tectonic regime on the planet. The relation between these processes varies substantially, and the end-members are commonly discussed in terms of fast and slow spreading ridges. Fast spreading ridges, which are characterised by full spreading rates >80 mm/a, form the largest volumes of oceanic crust (e.g. at the East Pacific Rise), but slow spreading ridges are considered to be the most common type of ridge when measured by the length of the axis. With increasing surveying of seafloor age and morphology, people have suggested new end-members and transitional types of this simple classification. Super-fast spreading, perhaps reaching up to 210 mm/a in the middle Miocene, has been reported for parts of the Cocos-Pacific plate boundary (Wilson, 1996), and an ultra-slow spreading class of ridge (<20 mm/a) can be found at the Southwest Indian Ridge (e.g. Muller *et al.*, 1999) and in the Arctic (Gakkel Ridge, Mohns Ridge;

e.g. *Tolstoy et al.*, 2001; *Klingelhöfer et al.*, 2000). To refer to the transitional character between slow- and fast spreading of the Juan de Fuca Ridge in the northern Pacific and the Southeast Indian Ridge with the Australian-Antarctic Discordance, an intermediate spreading class of ridge was introduced (full spreading rates of 40-80 mm/a). As a result of this diversification, the Mid-Atlantic Ridge (MAR) and parts of the Central Indian Ridge are the main remaining exponents of the slow spreading type of ridge.

One of the earliest observations of the seafloor structure was the dichotomy between the axial morphology of the Mid-Atlantic Ridge and the East Pacific Rise (*Heezen*, 1960; *Menard*, 1960). This observation has been developed to a systematic pattern of morphological and structural characteristics, which has been related to spreading rate. Fast spreading ridges are characterised by narrow axial highs, low-relief abyssal hills and magma lenses at shallow depths (e.g. *Detrick et al.*, 1987; *Toomey et al.*, 1994; *Macdonald*, 1998; *Small*, 1998). Slow spreading ridges are characterised by a major axial graben, mostly - but not always - an axial volcanic ridge and large abyssal hills (e.g. *Smith and Cann*, 1993). No magma chamber has so far been imaged on a ridge with a pronounced median valley (*Detrick et al.*, 1990; *Sinton and Detrick*, 1993), although lower velocities, probably associated with significant fractions of melt, have been detected at slightly greater depth than at fast spreading ridges (*Canales et al.*, 2000a). However, dramatic changes in these parameters can occur without significant changes in spreading rate over relatively short along-axis distances. Prominent examples are the Reykjanes Ridge in the North Atlantic, which spreads at ~ 20 mm/a, but has an axial high and a crustal magma body at 2.5 km depth (e.g. *Sinha et al.*, 1998), or the Australian-Antarctic Discordance, which is characterised by a pronounced axial valley and by rouged, chaotic seafloor morphology, though the full spreading rate of 72 mm/a is “high intermediate” (e.g. *Okino et al.*, 2004).

Most models for axial topographic relief indicate that stretching the strong brittle lithosphere of slow spreading ridges produces an axial valley (e.g. *Poliakov and Buck*, 1998; *Buck et al.*, 2005). This is consistent with the observation that the depth and magnitude range of earthquake activity at slow spreading ridges is greater than at fast spreading ridges, which lack axial valleys (e.g. *Huang and Solomon*, 1988). *Phipps Morgan and Chen* (1993) presented a model for crustal accretion in which the thermal structure at the ridge-axis is governed by the rate of heat supply to the crust by magma injections and the efficiency of heat removal through hydrothermal circulation. They showed that at a given spreading rate, the thermal state of the ridge is very sensitive to magma supply to the crust (i.e. crustal thickness). This suggests, that the ultimate control on axial morphology is the thermal structure of the ridge-axis, which is a function of both spreading rate and magma supply. Large-scale variations in magma supply are commonly attributed to differences in temperature, composition and the flow regime of the mantle, whereas the origin of local variations is still matter of considerable debate (*Kuo and Forsyth*, 1988; *Lin et al.*, 1990; *Magde and Sparks*, 1997).

The fundamental influence on the variables that change with spreading rate along the mid-ocean ridge system seems to be whether or not a steady-state magma reservoir can be sustained at a given location (*Sinton and Detrick*, 1993; *Phipps Morgan and Chen*, 1993; *Perfit and Chadwick*, 1998). Where magma supply is continuous and robust, volcanism can keep-pace with or dominate over tectonism; where magma supply is intermittent, faulting tends to dominate. For slow spreading ridges like the Mid-Atlantic Ridge the

variation in the degree of magma input also has profound influence on the resulting structure of the oceanic crust. Models of internal stratigraphy of the crust have become more complex with the introduction of ephemeral magma chambers, which intermittently feed an irregular mush zone beneath the axial valley (*Sinton and Detrick, 1993*), as well as tectonism and hydrothermal alteration in the accretion zone. Understanding this spatial and temporal pattern still poses a big challenge for present-day geoscientists.

1.2 Ridge segmentation

Mid-ocean ridges are partitioned into morphologically distinct segments on a variety of scales (e.g. *Sempere et al., 1990; Macdonald et al., 1991*). Discontinuities that define first-order segments are rigid transform faults. Higher order ridge segments terminate at non-transform discontinuities (NTD) that are nonrigid. Overlapping spreading centers and oblique shear zones are examples of second-order discontinuities found at fast- and slow spreading centers, respectively. NTDs as well as transform faults may migrate along axis and hence, individual ridge segments may lengthen and shorten with time (*Schouten et al., 1987*). Mid-ocean ridge segmentation is dependent on spreading rate; large offset transform faults are more frequently found at slower spreading rates (e.g. *Macdonald, 1998*). It is yet unresolved whether segmentation has a magmatic or lithospheric origin. It may arise from the three dimensional nature of flow and melt migration in the underlying mantle or may be a consequence of lithospheric dynamics and tectonics, perhaps related to the plate geometry during continental breakup (e.g. *Lawson et al., 1996; Kleinrock et al., 1997*).

Bathymetry and sea surface gravity are two properties which are easily measured and which show systematic along-axis variations. Commonly, the residual mantle bouguer anomaly (RMBA) is extracted from the free air gravity anomaly by removing the predicted effects of seafloor topography and mantle thermal structure (e.g. *Kuo and Forsyth, 1988*). Independent of spreading rate, obtained results show consistently lower RMBAs at the segment centers than at the segment ends. However, along-axis gradients in the RMBA are consistently higher at slow spreading centers than at fast spreading centers (*Lin and Phipps Morgan, 1992*). The regional peak-to-trough amplitude of the RMBA is also greater along the Mid-Atlantic Ridge (30-60 mgal) than at the East Pacific Rise (10-20 mgal). At the MAR, circular or “bull’s eyes” RMBA lows are sometimes found at the segment midpoints. Axial seafloor depth commonly deepens away from the segment center towards the end of the segment, i.e. seafloor depth profiles “mirror” the RMBA anomaly. This simple relationship is observed to be independent of spreading rate, but the wavelength of the undulations is shorter and the amplitude is larger at slow spreading ridges (e.g. *Macdonald, 1998*). Although RMBAs may arise from variations in crustal and upper mantle density, as well as variations in crustal thickness, these anomalies are typically used as a proxy for crustal thickness, or they are downward continued to the crust-mantle interface (thereby assuming a uniform thickness for the crust) to obtain a model of crustal thickness variations. If the residual anomalies are due solely to variations in crustal thickness, the obtained anomalies for the Mid-Atlantic Ridge imply crustal thinning of up to 3-4 km near transforms (*Kuo and Forsyth, 1988*).

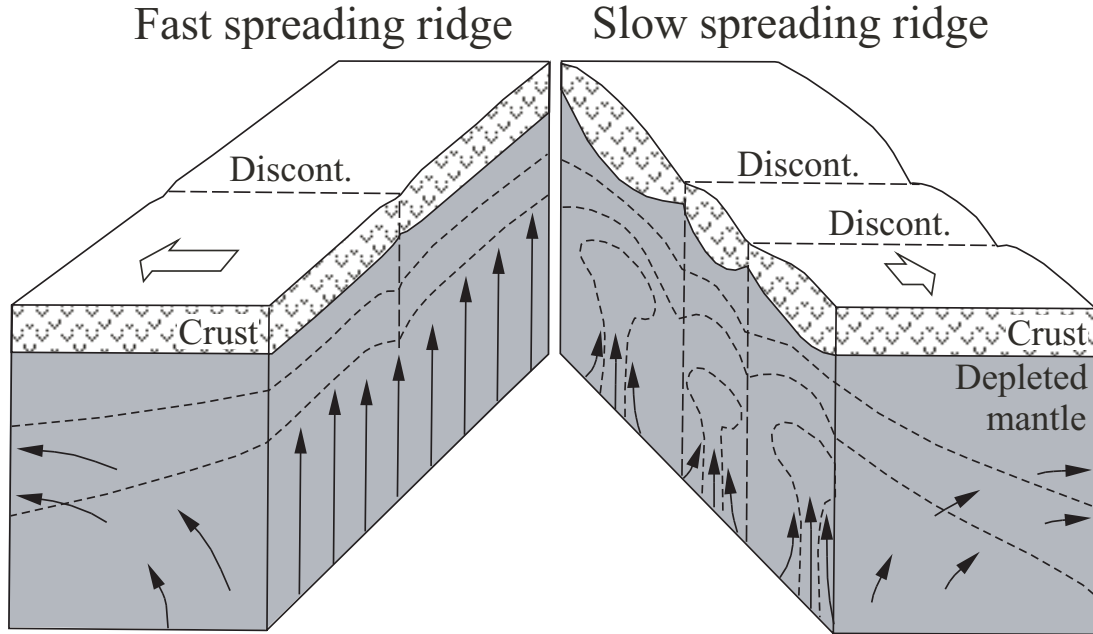


Figure 1.1: *Spreading rate dependent model of crustal accretion and mantle upwelling that is consistent with bathymetry and gravity observations (from Lin and Phipps Morgan, 1992). Solid arrows indicate mantle flow direction. Open arrows indicate plate motion. Dashed lines in the mantle show isotherms. Gravity data suggests that the crustal thickness is relatively uniform at fast spreading ridges (left). Slow spreading ridges reveal a higher degree of segmentation and crustal thickness variations (right). At fast spreading ridges smaller 3D upwelling components may still occur, but might have a smaller impact on crustal thickness variations due to along-axis melt migration in a persistent low-viscosity magma chamber (Lin and Phipps Morgan, 1992).*

The along-axis gravity data indicate that the amplitude of along-axis crustal thickness variations decreases with increasing spreading rate (Lin and Phipps Morgan, 1992). This spreading rate dependent crustal accretion style may originate in the mantle. At slow spreading ridges mantle upwelling might be plume-like (3D), whereas it is more sheet-like (2D) at fast spreading ridges (cf. figure 1.1). These differences are perhaps related to the increasing importance of plate driven flow relative to buoyant mantle flow with increasing spreading rate (Lin and Phipps Morgan, 1992). The effect of 3D buoyant flow components on crustal thickness variations at fast spreading centers might be smaller due to along-axis melt migration along a persistent low-viscosity crustal magma chamber.

In contrast to the along-axis uniformity of the East Pacific Rise, crustal accretion at the Mid-Atlantic Ridge seems to be a complex and heterogeneous process. This is related to both slower spreading rates and the much higher degree of segmentation. Morgan and Forsyth (1988) showed that the thermal effects of transform offsets due to conductive cooling by the juxtaposed older (i.e. colder) lithosphere do not strongly affect ridge-axis melting close to the transform. Instead, the major influence of a transform offset on melt-

ing beneath a ridge-transform intersection is due to the muting effect of mantle upwelling. However, the small along-axis dimensions (~ 50 km) of the observed RMBA variations at the Mid-Atlantic Ridge are difficult to explain by models of buoyant and plate driven partial melting, where convective instabilities typically grow at wavelengths > 150 km. Recent numerical studies, which include the effect of buoyancy-driven melt migration, are able to reproduce the observed pattern (*Magde and Sparks, 1997*). In these scenarios, melt is driven upslope both along-axis and across-axis at the base of the thinning lithosphere towards the segment center.

An important caveat of gravity derived crustal thickness is that lateral variations in crustal density are rarely considered (e.g. *Minshull, 1996*). However, seismic studies have observed a disproportional thinning of the higher density lower crust at the segment boundaries, which suggests that the along-axis crustal density is not uniform (*Tolstoy et al., 1993; Hooft et al., 2000; Canales et al., 2000b*). This implies that the thinner crust at ridge-offsets is consistently less dense and, in contrast, the thicker crust at segment centers is consistently denser than average. Together, this results in an underestimation of the crustal thickness variations interpreted from gravity data. Hence, along-axis crustal thickness variations based on gravity data, which do not take into account lateral density variations, should be treated with caution. This reveals clearly that seismic data are needed to better constrain the crustal thickness variations and possible changes in the crustal velocity structure, in particular in the vicinity of ridge-transform intersections, where these variations should especially become apparent.

1.3 Processes at segment ends

The correlation of seismic velocity data with ophiolitic stratigraphy suggests that the oceanic crust may be formed of an upper 1-2 km thick layer of basaltic lavas and dikes, underlain by a 3-5 km thick sequence of gabbros (papers from Penrose Conference on Ophiolites, *Geotimes*, volume 17, 1972; cf. figure 1.2). This model is consistent with recent seismic data acquired at fast spreading crust (e.g. *Harding et al., 1989; Vera et al., 1990; Grevenmeyer et al., 1998*). It does not, however, account for the exposures of lower crustal and mantle rocks on the seafloor at slow spreading ridges (e.g. *Karson and Dick, 1983; Mével et al., 1991; Tucholke and Lin, 1994; Cannat et al., 1995; Lagabrielle et al., 1998*).

Direct observations at major fault escarpments, which provide a “tectonic window” into the subsurface, cast significant doubts on the prevailing global application of an ophiolite model for oceanic crust and the interpretation of marine seismic data based on this model (*Karson, 1998*). The relatively simple, rather uniform and layered “seismic velocity structure” of the oceanic crust might in many places map alteration and porosity effects rather than the fundamental geological structure. The majority of tectonic windows are located at slow spreading settings and indicate a much more complex arrangement of rock units than suggested by geophysical and ophiolite models, although it is possible that a layered ophiolite-like crust prevails in regions of relatively high magma budget. In many places a discontinuous basaltic cover overlies a complex plutonic assemblage, which appears to have been constructed by multiple, syntectonic intrusive events resulting in extremely complex patterns of igneous, deformational and metamorphic features. Thin lava flows often lie di-

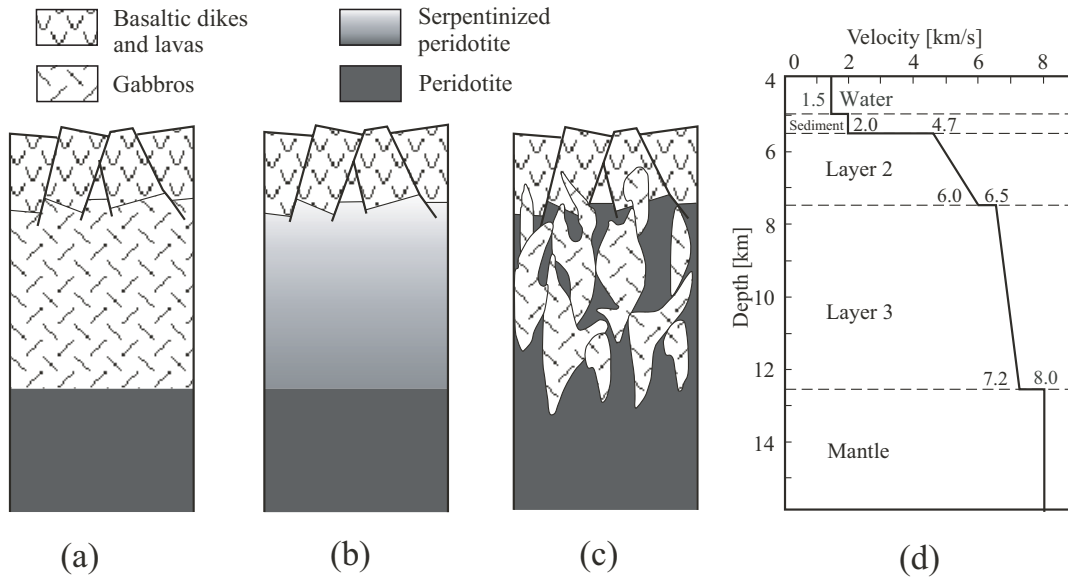


Figure 1.2: *Three possible geological models for oceanic layer 3 (modified from Cannat, 1993). (a) A continuous gabbro layer (Penrose Conference on Ophiolites, Geotimes, volume 17, 1972). This model may apply to oceanic lithosphere created at fast spreading ridges with a long-lasting axial magma chamber. (b) A layer of serpentized mantle peridotites (Hess, 1962). (c) A discontinuous layer 3, made of gabbroic intrusions into mantle peridotites, which may be partially serpentized. This model may apply to oceanic lithosphere created at magma-poor mid-ocean ridges, in regions where peridotites frequently crop out (Cannat, 1993). (d) Standard layered velocity section through oceanic lithosphere (White et al., 1992).*

rectly over mantle peridotite without intervening gabbroic lower crust, or peridotite crops out along the ridge flanks and at the ends of individual spreading segments (e.g. Cannat, 1993; Cannat et al., 1995; Karson, 1998; Lagabrielle et al., 1998).

Currently, there is an active debate whether the emplacement of mantle rocks at the seafloor is a purely tectonic phenomenon that would occur during cyclic periods of reduced magmatism or amagmatic extension (Karson and Dick, 1983; Mutter and Karson, 1992; Tucholke and Lin, 1994), or whether it is a consequence of a long-lasting reduced magma budget either due to local causes as expressed at segment discontinuities or more regional causes involving large domains of the ridge-axis and the underlying mantle (Cannat, 1993; Cannat et al., 1995; Lagabrielle et al., 1998). The first class of models assumes that a relatively normal layered crust is formed during stages of large magma supply and is subsequently sheared and thinned. The latter class of models implies a quasi-steady-state accretion process in which little if any mafic material is added to the mantle undergoing serpentinization, uplift and lateral spreading (cf. figure 1.3). Furthermore, the two models imply a different assessment of the temporal and spatial correlation of faulting and magmatism for the crustal evolution at slow spreading ridges. The fundamental question is: Are these two processes decoupled in time and space or do they occur coevally on the scale of tens to hundreds of thousands of years?

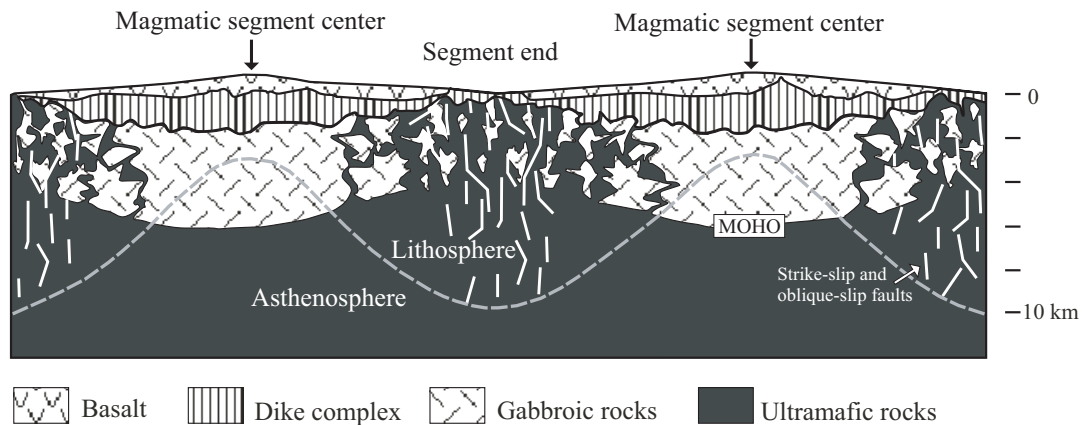


Figure 1.3: Sketch showing an along-axis section of two idealized spreading segments (from Cannat et al., 1995). $4\times$ vertical exaggeration. Magmatic segment centers reveal a thick, continuous and layered crustal section. Towards the segment ends the crust becomes progressively thinner and more discontinuous. Tectonic spreading dominates over magmatic accretion. Such a crust may be present in settings, where serpentinites and gabbros frequently crop out at the seafloor. Due to melt focussing effects, the lithosphere is thinnest at the segment center and thickest at magma-poor segment ends. MOHO=Mohorovičić discontinuity, i.e. the crust-mantle boundary.

Many authors have pointed out that tectonic extension at segment ends of slow spreading ridges is in fact an asymmetrical process in which structural features analogous to continental metamorphic core complexes are formed by low-angle normal (detachment) faulting at the inside corner (i.e. the region bounded by the ridge and the active transform or NTD). This hypothesis is based on bathymetric and geophysical observations of domal massifs (*inside corner highs*), and these features have been termed “oceanic core complexes” or “megamullions” (e.g. Tucholke and Lin, 1994; Tucholke et al., 1998; Cann et al., 1997; Blackman et al., 1998). In this scenario, the upper surface of an inside corner high is the exposed footwall of the detachment fault and the outside corner (i.e. the region bounded by the ridge and the inactive fracture zone or NTD, characterised by low-relief volcanic morphology) represents the hanging wall of this fault. Morphologically, inside corner highs are often characterised by flat or gently dipping surfaces and prominent spreading-parallel striations with wavelengths ranging from a kilometer down to a centimeter scale (Cann et al., 1997; Mitchell et al., 1998; Tucholke et al., 1998; Escartin and Cannat, 1999; Ranero and Reston, 1999; Reston et al., 2002; MacLeod et al., 2002; Searle et al., 2003; Okino et al., 2004). These striations most likely represent abrasion marks, in which the kilometer-scale corrugations may relate to the linkage of precursory structures as the detachment fault formed, although alternative interpretations as compressional structures (Tucholke et al., 1998) and ridge-perpendicular extensional faults (Karson, 1998) have also been suggested (cf. figure 1.4). The abundance of gabbros and peridotites at the fault surface demonstrates that detachment faulting is responsible for

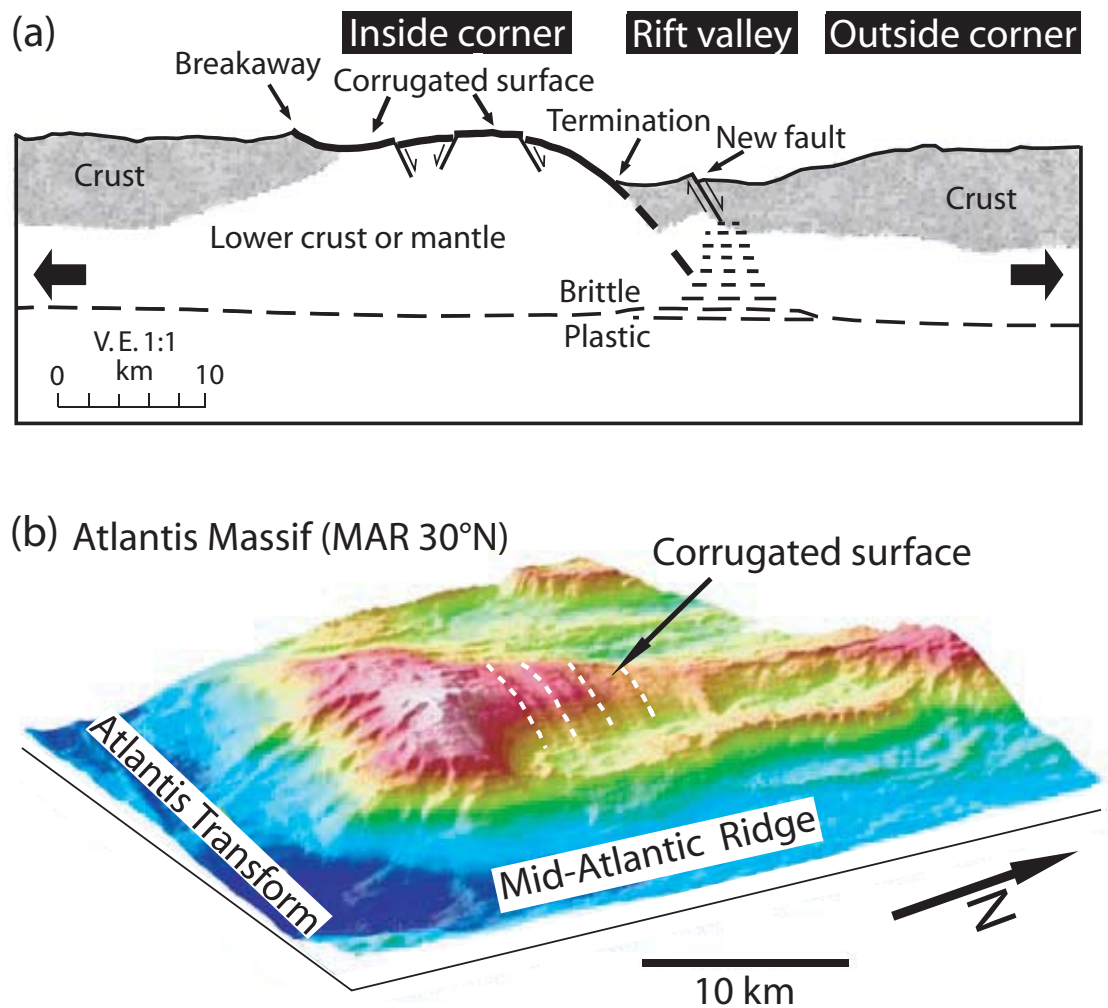


Figure 1.4: (a) Schematic cross section of detachment fault (bold line) forming an oceanic core complex at a slow spreading ridge (modified from Tucholke et al., 1998). A magmatic phase has stopped the exhumation process related to the large detachment fault, as indicated by the formation of a new fault in the weakened rift valley lithosphere. Dashes indicate the brittle-plastic transition zone. The domed surface of the core complex is cut by secondary, bending-related high-angle faults and is characterised by spreading-parallel corrugations (not shown). Thick black arrows indicate plate spreading direction. (b) Perspective view of the Atlantis Massif inside corner high, which is an oceanic core complex at the Mid-Atlantic Ridge at 30° N (modified from Schroeder and John, 2004). Corrugations (i.e. abrasion marks) are related to slip on the detachment fault.

the exhumation of lower crustal and upper mantle rocks (Cann et al., 1997; Escartin and Cannat, 1999; Tucholke et al., 2001; Reston et al., 2002; MacLeod et al., 2002; Escartin et al., 2003). Positive RMBA anomalies (e.g. Blackman et al., 1998) and high seismic P-wave velocities at shallow depths (Collins and Detrick, 1997) suggest that these structures are characterised by extremely thin mafic crust, which supports the idea of tectonic “unroofing” of the upper crustal portions in the detachment model.

There is not yet a consensus about how the formation of oceanic core complexes is related to the thermal regime of the ridge and why the formation of these features is restricted to the inside corner of ridge-axis discontinuities. Insights from numerical models of plate separation, dike intrusion and faulting suggest that at least three conditions have to be met (*Buck et al.*, 2005). First, the position of the hanging wall block, which is bounded by the fault and an axial dike, has to be stationary with respect to the thinnest lithospheric portions at the ridge-axis. This implies a certain ratio of magmatic accretion and plate separation rate. Moreover, it implies that nearly all magmatic accretion occurs at the outside corner. Second, the lithosphere cannot thicken very fast with distance from the axis. Otherwise it would eventually be easier to form a new fault cutting the axis, and the first fault would be abandoned. Finally, the amount of fault weakening must be large and has to occur moderately slowly with strain.

The first two conditions imply some critical constraints for the thermal state of the ridge, which might explain why the formation of oceanic core complexes is restricted to segment ends of ultra-slow, slow- and some intermediate spreading settings. Furthermore, the first condition would provide a simple explanation for the formation of these features at the inside corner: Assuming that the kinematics of a stationary hanging wall block bounded by the fault and an axial dike is correct, an outside corner core complex would require slip on the (otherwise inactive) extension of the transform fault; hence, having this block on the inside corner minimizes the total shear strain across the transform (*Buck et al.*, 2005).

However, although numerical models can provide some critical constraints for the formation of oceanic core complexes, many questions remain, in part owing to the lack of significant sub-bottom information. For example, major uncertainties include the bulk distribution of lithologies exhumed in the core complex, the dip angle of the detachment fault and its depth extent within the lithosphere, the level of magmatism during the period of active fault slip, the role of the fault in facilitating fluid penetration and serpentinization of the mantle, and the possible role of weak mineral phases such as serpentine in lubricating the detachment. Finally, one should mention that a single and universal model of asymmetric tectonic extension at segment ends cannot be applied for all portions of the Mid-Atlantic Ridge (*Cannat et al.*, 1995; *Lagabriele et al.*, 1998). Large-scale detachment faulting may be a reasonable explanation for the emplacement of serpentinites and mafic plutonic rocks at the seafloor during core complex formation, but it might not be a suitable explanation for the abundance of these lithologies (also at the outside corner) at other portions of the world's mid-ocean ridge regime.

1.4 Motivation and structural outline

As mentioned above, crustal accretion at slow spreading mid-ocean ridges is thought to reflect the three-dimensional geometry of mantle and magma-flow beneath the ridge (*Lin and Phipps Morgan*, 1992). The magma-supply is focused beneath the segment centers. At segment ends, spreading inevitably leads to faulting in the absence of robust magma input. As a consequence, large variations in the structure of the oceanic crust are predicted, as confirmed by several observations:

- Residual gravity anomalies

Along-axis studies of the Mid-Atlantic Ridge show a good correlation between shallower average topography and negative residual gravity anomalies at the segment centers and deeper average topography and positive residual gravity anomalies at the segment ends (e.g. *Kuo and Forsyth*, 1988). Modeling of these anomalies in terms of varying thickness of a continuous crustal layer suggests that the crust formed at segment ends is 3-4 km thinner than at segment midpoints. The specific geometry and internal structure of this crustal layer is, however, still insufficiently determined, largely because the scale of geological observations is much smaller than that of gravity studies. Seismic studies (e.g. *Tolstoy et al.*, 1993) have confirmed that crustal thickness variations can fully account for the observed gravity anomalies. But these studies also observed significant lateral variations in the crustal velocity structure. This suggests that lateral changes in crustal density are a significant error-source for gravity derived crustal thickness data, which results in a systematic underprediction of the “true” variations.

- Ultramafic exposures

Numerous dredging, diving, and drilling cruises have shown that mantle-derived ultramafic rocks locally crop out at the Mid-Atlantic Ridge. These places often correlate with areas of positive gravity anomalies, suggesting that they are characterised by a thin mafic crust and by a relatively starved magmatic activity (e.g. *Cannat et al.*, 1995). Horizontal extension is then accommodated mostly by tectonic stretching resulting in the formation of a discontinuous crust and the emplacement of lower crustal and mantle lithologies at the seafloor. In these areas the oceanic crust is expected to reveal significant deviations from the “layered model”.

- Oceanic core complexes

In response to reduced magmatism and the special lithospheric geometry at ridge-offsets, large-scale detachment faulting results in the asymmetric denudation of plutonic rocks suites at the inside corner of slow spreading segment tips (e.g. *Tucholke and Lin*, 1994). The mechanics of these processes as well as the internal structure of these features are not well understood. Positive residual gravity anomalies (*Blackman et al.*, 1998) and anomalously high seismic velocities (*Collins and Detrick*, 1997) suggest in places a very thin crust and/or significant deviations from the 1972 *Penrose Conference* layered oceanic crust model.

The aim of this study is to provide seismic constraints on the variation of the velocity structure of the oceanic crust and the upper mantle in a tectonically dominated spreading setting. The results of this study might be relevant for the general interpretation of residual gravity anomalies in terms of crustal thickness variations, as well as for existing models of melt-supply variations and oceanic core complex formation at slow spreading ridges. The study area at the Mid-Atlantic Ridge at 5° South was well chosen on the basis of satellite derived bathymetry data, which suggested the presence of a well-developed oceanic core complex at the inside corner of a 1st order ridge-axis discontinuity, and with the focus on the following three questions:

- How does the crustal velocity structure vary along-axis and across the transform fault?
- Is the velocity structure of the inside/outside corner pair consistent with existing “detachment” models previously suggested for oceanic core complex formation?
- Are there temporal variations in the crustal accretion process?

This thesis is divided into the following parts:

Chapter 2 introduces the geological setting of the work area and gives a summary of related geophysical studies at the MAR at 5° S. Following, the seismic experimental layout is described.

Chapter 3 provides a description of the processing applied to the seismic wide-angle data set.

Two different tomographic approaches are used in this study to obtain the seismic velocity structure from the given dataset. Chapter 4 introduces the first-arrival tomographic approach, presents the obtained velocity models and discusses the robustness of the derived solutions.

Chapter 5 describes the joint refraction and reflection tomography, and elaborates on questions such as resolution and uncertainty.

The final tomographic velocity models are described in Chapter 6. Differences to the first-arrival tomographic results are discussed, and results of gravity modelling are presented. Chapter 7 discusses the implications of the obtained results for the models of ridge segmentation and core complex formation.

Finally, Chapter 8 gives a summary and conclusion of this study, as well as providing an outlook for future investigations at the Mid-Atlantic Ridge at 5° South.

Chapter 2

Area of Investigation - MAR 5° South

2.1 Regional structural setting

The GERSHWIN experiment (Geophysical Experiments to investigate Ridge Segmentation - HoW INside and outside corners form) investigated the Mid-Atlantic Ridge at 5° S during cruise M47/2 of RV METEOR. During five weeks of ship time, a combination of geophysical and geological experiments were carried out, including bathymetric mapping (*Reston et al.*, 2002), microearthquake seismicity (*Tilman et al.*, 2004), dredging (*Flueh et al.*, 2000) and refraction seismology. The latter forms the database for this study.

Figure 2.2 shows the bathymetric map of the study area based on the *Hydrosweep*® recordings during cruise M47/2. The work area covers the Mid-Atlantic Ridge between 4°20' S and 5°40' S and extends to about 50-85 km distance from the ridge axis. A well pronounced dextral transform fault (hereinafter referred as 5° S FZ) offsets the ridge by ~70 km and divides the working area into two distinct spreading segments. Both segments are characterised by a well-developed rift valley with an observed trend of 345°.

The work area is located between two major ridge offsets (>200 km; cf. figure 2.1): The Chain Transform Fault at about 2° N, which is the southern branch of the East-West trending equatorial mega-shear zone, and the Ascension Transform Fault at about 8° S. In the NUVEL-I plate model the direction of spreading is perpendicular to the axial trend of 347° with a full spreading rate of 32 mm/a (*DeMets et al.*, 1990).

The ridge axis between 2° N and 8° S is frequently interrupted by smaller first order discontinuities (less than 100 km ridge offset). The pattern of these ridge jumps does not reveal a systematic trend. It changes several times between left-stepping and right-stepping. It is not possible to predict the finer segmentation of the ridge axis from the satellite derived bathymetry data (*Smith and Sandwell*, 1997) in the proximity of the work area. However, a sinistral transform fault near 4° S and the Ascension FZ in the south suggest that, on a 1st order scale, both segments are characterised by alternating ridge offsets. Although the hydrosweep coverage of the work area is not complete (cf. figure 2.2), the ridge-axis of the northern segment seems to be offset by a sinistral 2nd order ridge-axis discontinuity close to 4°32' S, which would imply an along-axis segment length of 60-65 km. Despite the relatively short distance to the Ascension (Circe) hot spot, isotope studies indicate no mixing trend within the MORB population, which presumably reflects no influence of the nearby plume (*Hanan et al.*, 1986; *Fontignie and Schilling*, 1996).

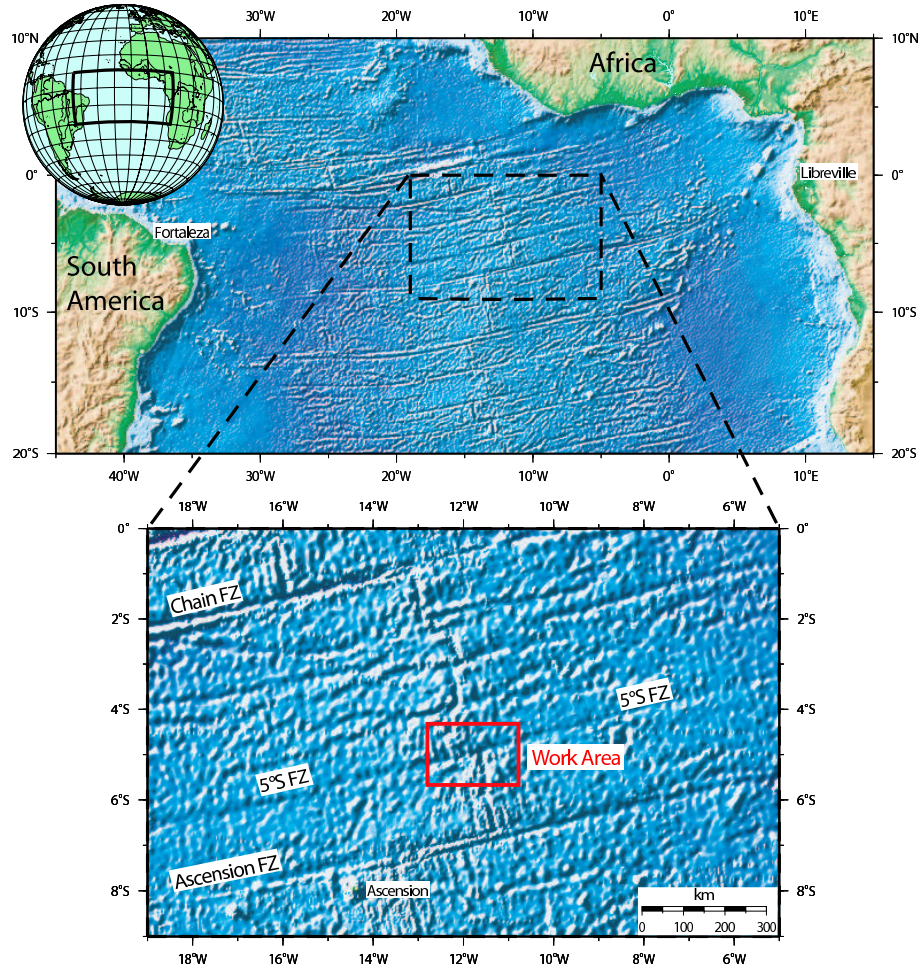


Figure 2.1: *The Mid-Atlantic Ridge at 5° South. Between the Chain FZ and Ascension FZ, the pattern of axial discontinuities does not reveal a systematic trend. Satellite derived bathymetry data (Smith and Sandwell, 1997) suggest alternating offsets for both segments of the work area on a 1st order scale.*

2.2 Northern segment

2.2.1 Median valley

In the northern segment, the median valley floor varies along axis in width and cross-sectional relief (cf. figure 2.3). In the east, a large, relatively continuous fault displaces the crust vertically often with throws of more than 1 km; by contrast, several smaller faults cause significantly smaller displacements to form the western bounding walls. The resulting asymmetry in cross-sectional relief may vary but is significant throughout the entire segment.

The median valley floor widens and narrows along its length, but at its base within its central part is typically 5-10 km wide. Towards the southern segment end, where its

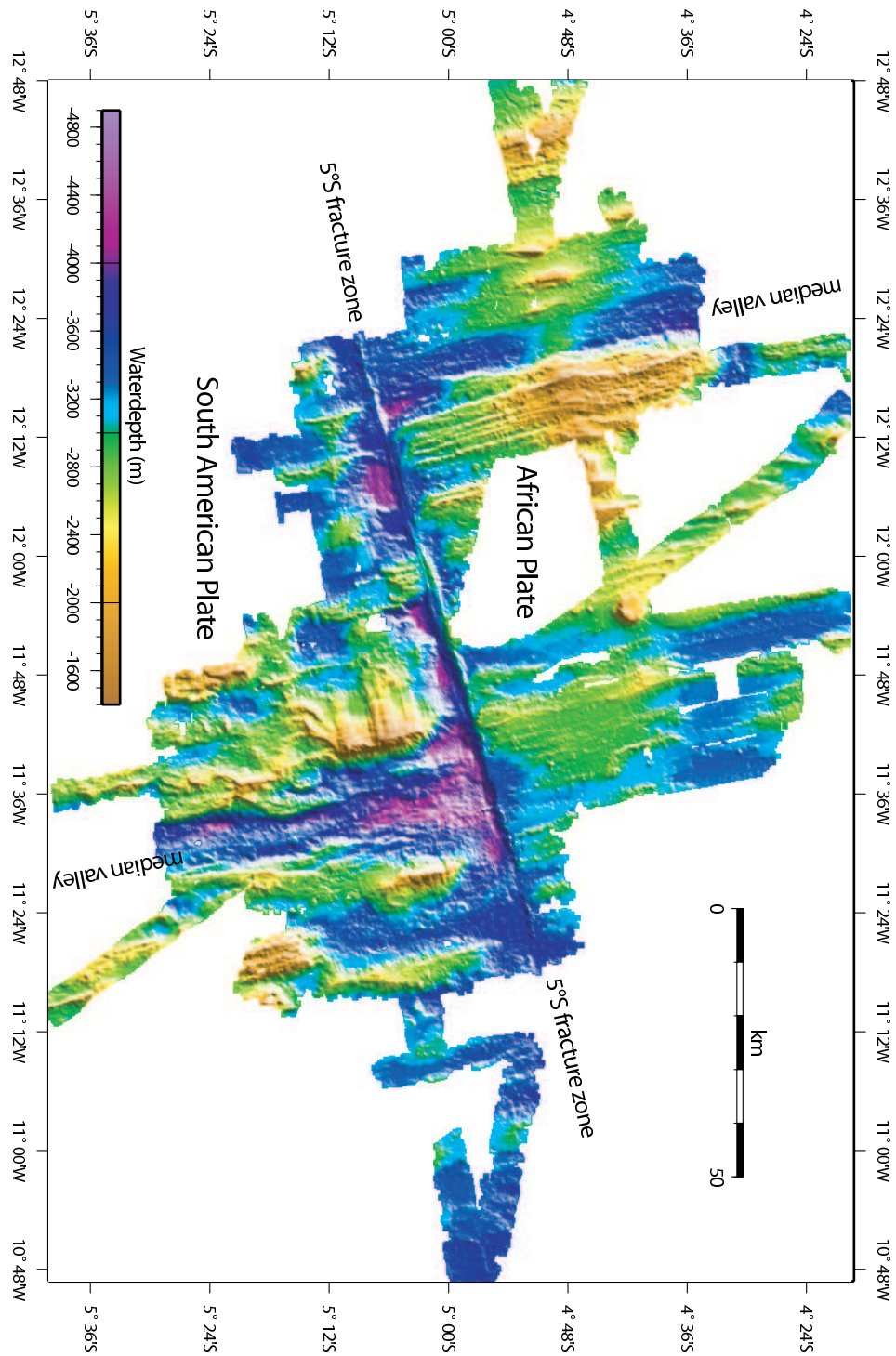


Figure 2.2: Bathymetric map of the work area based on Hydrosweep data collected during cruise M47-2. The 5° S transform fault divides the study area into two distinct spreading segments. Both segments are characterised by a well-developed rift valley with an observed trend of 345°

eastern bounding fault overlaps with a more easterly located fault scarp, the median valley widens to perhaps more than 15 km. Here, it is difficult to follow its western bounding fault which seems to run out when approaching the 5° S FZ.

Seafloor depths shallow from more than 4 km close to the transform to less than 3 km in the central part of the northern segment. Close to 4°48' S, the median valley floor forms a broad ~10 km wide hour-glass shape plateau with water depths of around 3 km. The seafloor morphology on top of this bulge seems to be smoother (at least on a Hydrosweep scale) and to lack larger individual volcanic edifices compared to the adjacent portions of the median valley.

Interestingly, within a 2 km long portion situated on top of this bulge three hydrothermal fields were discovered by (*Haase et al.*, subm.): the high temperature Red Lion and Turtle Pits sites and the diffuse low-temperature Wideawake site. RV METEOR cruise M64/1 studied the vent fluids, fauna and precipitates at these hydrothermal fields (*Haase and Lackschewitz*, in press). Turtle Pits black smokers gave fluid temperatures of ~400 °C, which is close to the critical point of seawater at this depth. These are the highest temperatures measured so far in vents at the entire MAR, indicating that the fluids rise without significant interaction with seawater or conductive cooling from their origin in the crust. *Haase et al.* (subm.) suggested that the high heat flux and the relatively high iron and hydrogen contents of the fluids are caused by a very recent intrusion and/or eruption event at Turtle Pits. The abundance of fresh glassy sheet flows in the area indicates a strong volcanic activity. The youngest observed lava covers parts of the Wideawake mussel field and is probably less than 10 years old. On 25/26th of June 2002, the segment was seismically active, and one may speculate whether this was related to an emplacement of lava flows.

North of the bulge, seafloor depths increase to maximum values of 3.8 km for the resolved portions of the median valley. The western scarps are much more subdued, building up only 0.5 km relief, compared to almost 2 km at the adjacent eastern bounding walls. The major bounding faults can be reliably traced up to 4°36' S, suggesting a relatively constant median valley width of ~8 km.

A well-developed axial volcanic ridge (e.g. *Smith and Cann*, 1993) is absent in the northern segment. In contrast, individual volcanic edifices are scattered over the whole width of the inner floor. In some cases they are partly incorporated into the rifted bounding walls. Seamounts seem to cluster directly north and south of the elevated bulge, where they form coalesced volcanoes and larger volcanic ridges that almost extend over the whole width of the median valley floor. The lack of individual seamounts on top of the bulge could indicate that eruptions have piled up a single large volcano here. Although magmatism is clearly focused on the central part of the segment, it is not restricted to it, as it is indicated by the abundance of seamounts in close proximity to the 5° S FZ.

2.2.2 Crestal mountains

Perpendicular to the median valley bulge and hence in flow-line of the current segment center, a couple of large seamounts can be identified both east and west of the ridge-axis (cf. figure 2.2). These edifices usually stand out more than 0.5 km above the surrounding seafloor, and in one case (at 12°06' W) exhibit a single flank of more than 1 km height.

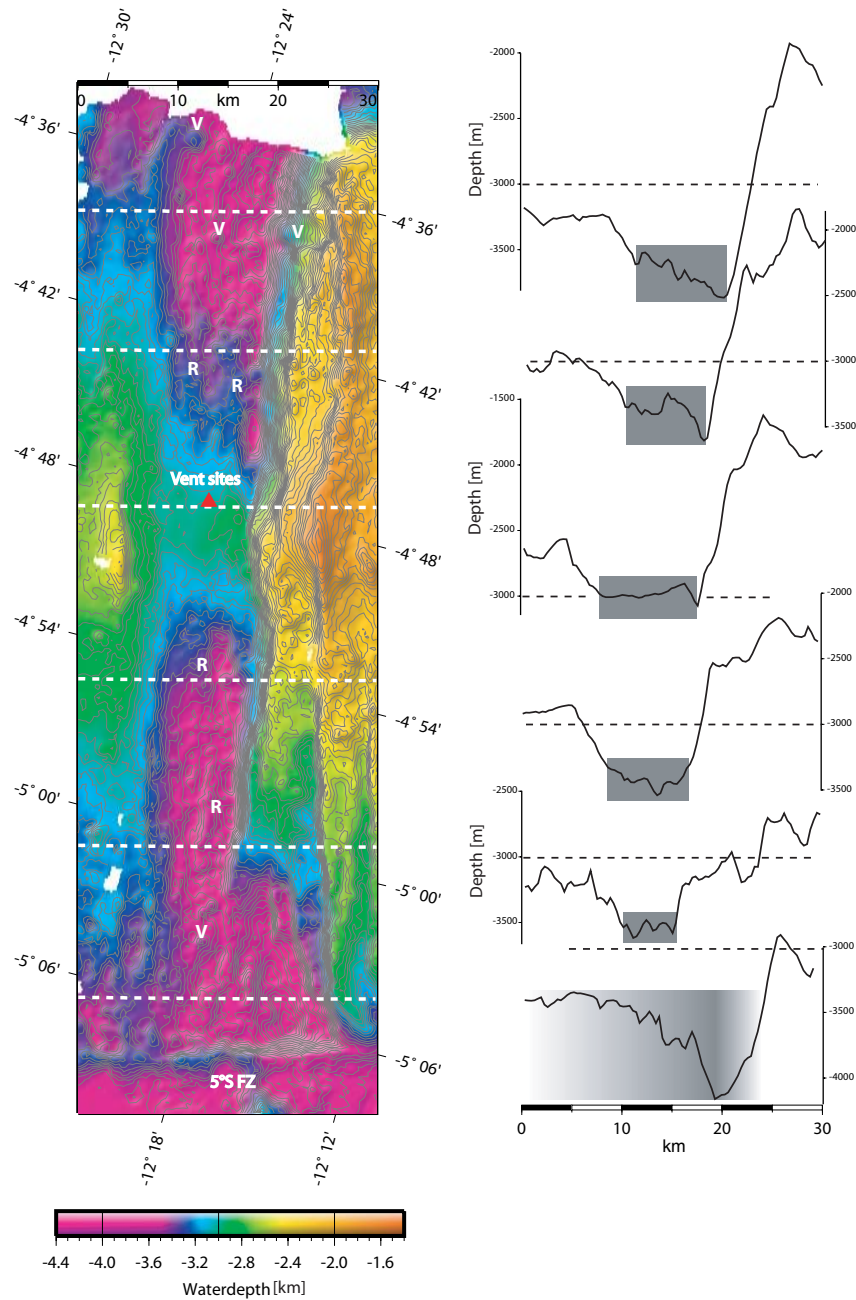


Figure 2.3: (Left): Bathymetry of the median valley floor and its bounding flanks contoured every 50m. The depth of the inner floor shallows towards the segment center where it forms a hour-glass shape rise. The high temperature Turtle Pits hydrothermal field is located on top of this bulge (red triangle). Near-circular volcanic edifices (labelled V) and elongated ridges (labelled R) are found throughout the whole inner valley floor. The white dashed lines mark the locations of the axial-relief profiles shown right. (Right): Across-axis relief sampled at different locations along axis (10 fold exaggeration). The black dashed line at 3000m water depth is shown for comparison. Black-shaded areas indicate the width of the inner valley floor.

Their shapes vary; some of them are cut by faults and form half-moon like structures, others are almost circular (e.g. at 11°55' W) with a crater-like depression on top. Although Hydrosweep coverage is sparse, their presence seems to be restricted to a relatively narrow band, running in flow-line of the current segment center.

Off-axis, the northern segment is characterised by a quite regular ridge-parallel tectonic fabric. The major faults of the rift mountains (i.e. the former median valley bounding faults) can sometimes be continuously traced over more than 60 km distance. On their crests, these faults often exhibit aligned seamount chains which can extend directly until they reach the 5° S FZ. There is no indication for an inside corner high on the resolved seafloor portions of the northern segment.

2.3 Southern segment

2.3.1 IC and OC massifs

The geological setting of the segment south of the 5° S FZ was first described by *Reston et al.* (2002), based on Hydrosweep bathymetry data collected on RV METEOR cruise M47/2. The most striking geological features are two massifs on either side of the median valley (cf. figure 2.3). At the inside corner (south of the active transform and ~10 km west of the median valley), a pronounced inside corner high (ICH) stands out more than 3000 m above the adjacent transform valley floor. It rises up to a height of 1450 m below sea level and thus represents the highest elevation within the working area. Towards the transform, the massif is bounded by steep flanks (more than 3000 m difference in elevation over less than 10 km distance), but towards the median valley, the drop of 2000 m over less than 5 km is even higher. The steep scarps towards the median valley and towards NE are gullied, probably indicating some mass wasting off an originally steeper flank. In contrast, the western slope of the ICH is gentle, losing less than 2 km elevation over 20 km, and exhibits well defined transform-parallel corrugations. With amplitudes of tens of meters and wavelengths of up to 2 km, these corrugations can sometimes be traced over more than 10 km. A large corrugation at about 5°09' S is related to a change in elevation of 300-400 m and divides the massif into a higher northern part, which perhaps extends further to the west, and a less elevated southern part. The southern limit of the massif is initiated at 5°11' S by a ~45° turn of the eastern flank and a resulting SW-trending fault scarp in the south. The observed oceanic core complex is similar to other lineated domal massifs (or megamullions) in slow- and ultraslow spreading regimes (*Blackman et al.*, 1998; *Tucholke et al.*, 1998).

On the opposite outside corner an elongated massif rises to an elevation of 1650 m, which is only 200 m less than the ICH. Its eastern flank is convex to the east and shows a drop of 1600 m over a distance of 5 km. On its surface, it also exhibits transform-parallel lineations, which resemble those of the ICH. The flank towards the ridge axis is markedly steeper (2100 m change in elevation within 5 km) and its shape is straight. For all its size, the massif was not predicted by free-air satellite gravity (*Sandwell and Smith*, 1997), so its emergence was not expected.

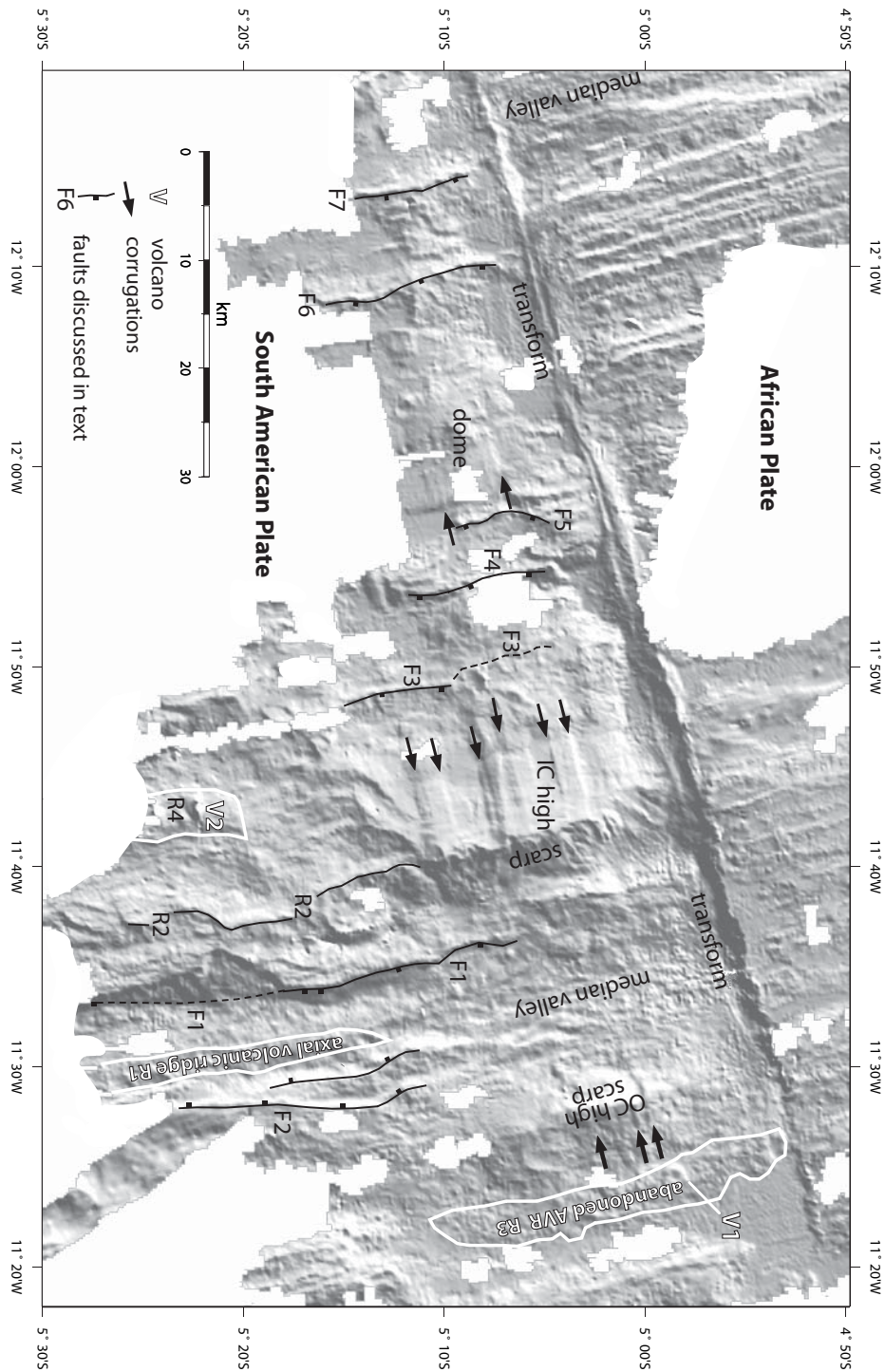


Figure 2.3: Bathymetry of the southern segment (modified from Reston et al., 2002). Main features are marked and discussed in text: arrows= transform parallel corrugations; F= faults; R= ridges; V= possible volcanic edifices. Two pronounced massifs of similar ridge-parallel extent and comparable height occur directly south of the 5° S FZ at the inside and at the outside corner of the present spreading axis.

Further to the east, bathymetry data reveals a rough area of bumpy terrain, suggesting a volcanic origin, with a relief of up to ~ 400 m. It contains several circular edifices (in one case - at $11^{\circ}24.5' \text{ W}$, $4^{\circ}58.5' \text{ S}$ - with a crater-like depression on top) and thus resembles in shape and structure an axial volcanic ridge (*Smith and Cann*, 1990, 1992). The ridge extends northwards directly until it reaches the fracture zone. To the south, axial relief decreases and finally runs out at about $5^{\circ}10'$ as the ridge and the surrounding axial valley turn slightly to the SW, perhaps due to a prior 2nd order discontinuity. Further south at about $11^{\circ}20' \text{ W}$, $5^{\circ}18' \text{ S}$, a pronounced elevated massif, unfortunately only partly covered by Hydrosweep bathymetry, marks the inside corner of this putative ridge offset. Unlike the other two massifs, this one shows no corrugations on its surface.

2.3.2 Median valley

South of $5^{\circ}10' \text{ S}$, the active spreading axis of the southern segment is marked by a well developed median valley with major bounding faults on either sides and a well developed axial volcanic ridge. On its western border, an inward facing fault, marked as F1 in figure 2.3 runs with a strike of $\sim 355^{\circ} \text{ N}$. At about $5^{\circ}17' \text{ S}$, it slightly turns to $\sim 350^{\circ} \text{ N}$ and continues until $5^{\circ}06' \text{ S}$, where it runs out, or perhaps turns west, as the median valley widens approaching the 5° S FZ . On the eastern side, a major fault zone, marked as F2 in figure 2.3, runs northwards until $5^{\circ}18' \text{ S}$, where it splits into two branches, which run sub-parallel and can both be traced until $\sim 5^{\circ}10' \text{ S}$. The western branch is situated closer to the ridge axis and thus probably represents a more recent phase of faulting. The axial volcanic ridge seems to die out north of $5^{\circ}10' \text{ S}$, where the median valley begins to widen and to lose its clear defined bounding faults.

2.3.3 South and west of the IC massif

Starting from the south-eastern corner of the inside corner high, a ridge named R2 in Figure 2.3 runs southwards with a trend of $\sim 170^{\circ}$ and may represent a fault scarp. Its strike-parallel course and the fact that its eastern flank runs directly into the eastern scarp of the massif suggest that the ridge represents the structural continuation of the core complex to the south, and thus both may have formed at the same time.

West of the inside corner high flank and the area characterised by the corrugated surface, the ridge named F3 may represent the breakaway (the top of the footwall prior to exhumation) of the oceanic core complex. The ridge starts at $5^{\circ}14' \text{ S}$ and can be traced to the north until at least $5^{\circ}08' \text{ S}$. The ridge F4 trends roughly 170° southwards up to at least $5^{\circ}10' \text{ S}$. Its southern continuation is less clear due to complicated morphology and sparse data at the edges of the survey area. However, F4 may represent the breakaway of the northern part of the core complex. This would imply that F3 would have formed at a later stage after the initiation of the detachment process, possibly related to the observed downthrowing of the southern portion of the inside corner high. As an alternative, *Reston et al.* (2002) suggested the existence of two breakaways, related to two overlapping IC massifs. However, the observed ridge-perpendicular slope on the corrugated surface is indicative of relative vertical motions of the two parts of the oceanic core complex.

Where the northern continuation of the “breakaway” ridge F4 intersects the transform, the width of the transform is markedly decreased associated with the elevation of the seafloor west of F4. *Reston et al.* (2002) pointed out that footwall uplift of F4 could account for the observed local uplift of the seafloor. In this area, the plate boundary seems to consist of two sharp valleys with a narrow ridge in between, resulting in a cross-width of less than 2 km for the transform.

Centered at 12°02'W/5°11'S, a small domal massif stands out ~600 m above the surrounding seafloor. It shows weak corrugations on its surface, probably related to a former period of detachment faulting, and thus it appears to be a fossil inside corner high. Further west, two 170° trending ridges spaced ~20 km apart show a central uplift. This might be interpreted as footwall uplift, resulting in a displacement that was insufficient for an oceanic core complex to develop.

2.4 Related work

2.4.1 Segment evolution

The eastern scarp of the IC massif and the western scarp of the OC massif have a parallel strike, are placed exactly opposite to each other and are unusually steep as well as similar in shape and size with a difference in elevation of less than ~200 m. Based on these observations *Reston et al.* (2002) suggested that both massifs may have been conjoined originally and that their splitting was initiated by a change of the active spreading axis. Hence, the OC massif represents a smaller fragment of a formerly intact single core complex. Following their interpretation, the axial volcanic ridge east of the OC massif corresponds to a now abandoned spreading axis, whereas the northern continuation of the well developed axial volcanic ridge in the southern part of the median valley (R1 in figure 2.3) represents the currently active axis of seafloor spreading.

Reston et al. (2002) reconstructed the evolution of the spreading process on the basis of bathymetric data by merging single fault scarps on either sides of the median valley consecutively together. Their aim was to match the fabric of the seafloor in allowing only for movements in a transform-parallel direction. Assuming a constant full spreading rate of 32 mm/a, they estimated a time span of 0.3 Ma of spreading to restore ~9 km of median valley seafloor (cf. figure 2.4). As a result, faults F1 and F2 reveal a very close match, which indicates that the initiation of both faults was coeval and probably related to the locus of former spreading. In a second phase, the inside-facing scarps of the two massifs are conjoined, revealing an almost perfect fit for a time span of 0.75 Ma of spreading. On top of the massifs, single corrugations can be traced from one side to the other, which supports the idea of a formerly intact single core complex.

Assuming ridge R2 as the spreading axis at the onset of rifting of the core complex, its formation could be associated with footwall uplift of the western block. Other prominent ridges on either sides of the axis are the well-developed volcanic ridge R3 in the east and the morphologically similar ridge R4 in the west. R4 is situated in ~10 km distance from the central axis at the edge of available swath data. Its morphology is indicative of volcanic origin (e.g. the isolated volcano at 11°43'W, 5°22.5'S) and resembles in cross axial relief and width the ridge R3 east of the massif. As an alternative, the southern branch

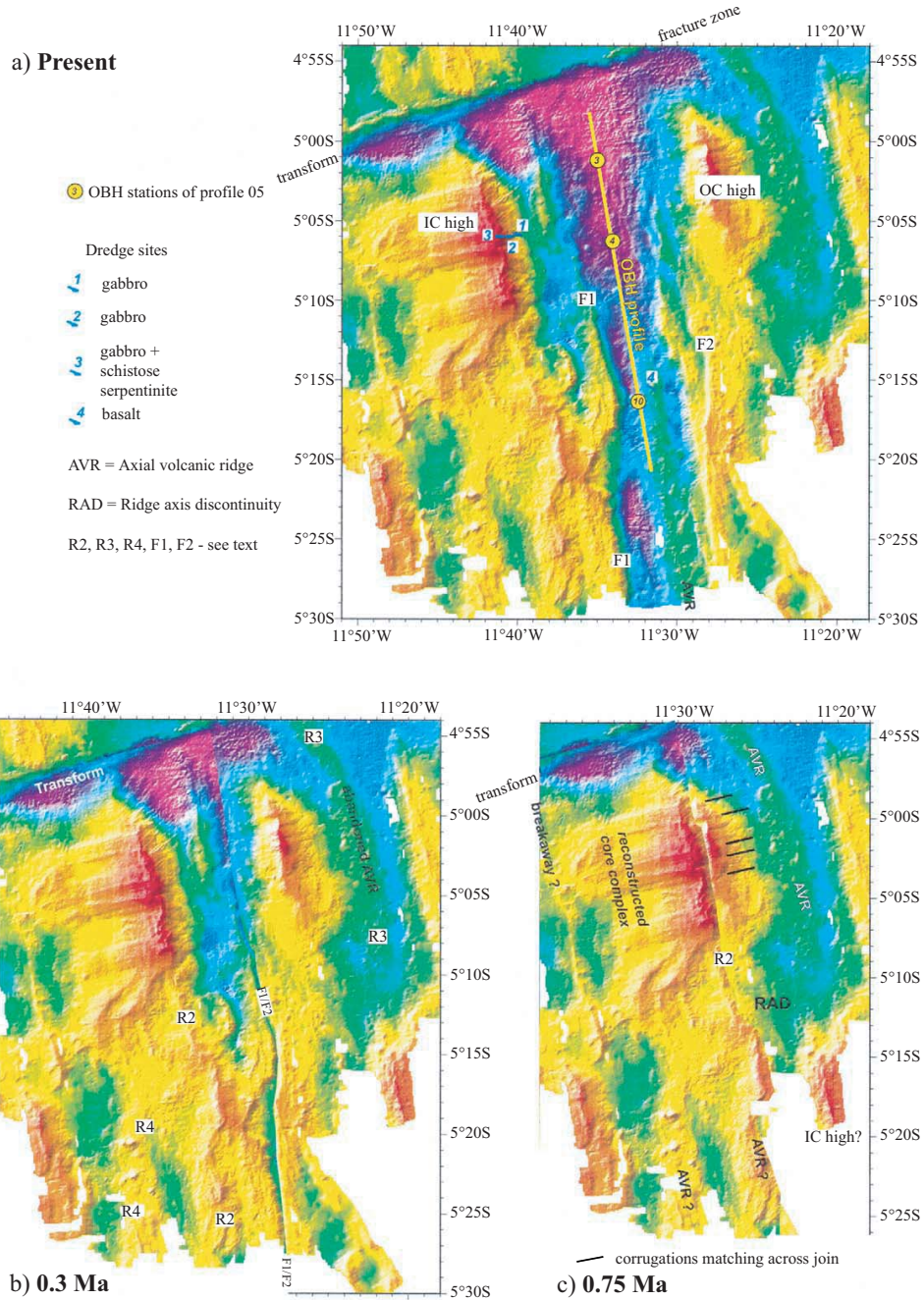


Figure 2.4: *Reconstructed evolution of the segment end (from Reston et al., 2002). (a): Present day situation. (b): 0.3 Ma reconstruction, where faults F1 and F2 are merged together. (c): Assuming a time span of 0.75 Ma of spreading, the transform facing scarps of the two massifs are conjoined. Single corrugations can be traced from one side to the other which supports the idea of a formerly intact single core complex. Note that the continuation of the median valley and the location of the axial volcanic ridge further south is unknown.*

of R2 could have acted as an axial volcanic ridge prior to the initiation of rifting.

In either scenario, the median valley stepped to the west at the southern tip of the reconstructed core complex. This was probably related to a second order ridge axis discontinuity (RAD). The southern portion of the axial volcanic ridge R3 curves slightly to the west and finally diminishes. The elevated massif south of the abandoned axial volcanic ridge would in this scenario be situated at the southern inside corner of the RAD and thus, could present a fossil inside corner high. As pointed out above, the continuation of the median valley south of the RAD is less clear. A slight curvature to the east is noticeable for both possible candidates of axial volcanic ridges when they approach the RAD from the south. At the southern border of the reconstructed core complex, the SW-trending fault scarps could represent traces of the NW boundary faults of the RAD.

Reston et al. (2002) proposed two possible scenarios for the initiation of the rifting event: If ridge R4 is representing the southern continuation of the spreading axis, the RAD would form a Z-shaped structure with IC massifs at its northern and at its southern margin. In this case, the initiation of rifting would be related to an extremely decreased melt supply. This could have resulted in the formation of a new spreading axis which is located in the center of the RAD and which propagates both to the north and to the south rather by tectonic processes. Alternatively, R2 could have been the axial volcanic ridge for the southern part, and it simply propagated northwards through the IC massif, possibly due to a magmatic event, e.g. a major dike intrusion. In this case, segmentation would be rather controlled by spatial variations in melt supply.

2.4.2 Dredging

Crustal thickness and composition at segment ends of slow spreading ridges is commonly believed to be highly variable (e.g. *Detrick et al.*, 1993). Observed lithologies at inside corner highs suggest that in these areas lower crustal or upper mantle rocks have been exhumed and emplaced at the seafloor during a process of detachment faulting (*Tucholke and Lin*, 1994; *MacLeod et al.*, 2002; *Cannat*, 1993; *Cannat et al.*, 1995). In this context, the rifted IC massif offers the rare opportunity to assess the lithologic composition beneath the surface of such a footwall structure and to sample directly the interior of an oceanic core complex. During RV METEOR cruise M47/2, three sites were dredged at different portions of the eastern scarp of the ICH, and a final dredge was made at the northern tip of the axial volcanic ridge (for the locations of the dredge hauls see figure 2.4).

Assuming that potential samples exposed at different depths of the scarp could indicate the internal sequence of the massif, a variety of lithologies were recovered (cf. table 2.1): Moderately fresh gabbros with a variety of textures were dredged at the middle and upper portion of the scarp (Dredge 1 and Dredge 2). At the very top of the scarp, adjacent to the corrugated surface, serpentinized peridotites as well as weathered gabbros were recovered (Dredge 3). The gabbros are altered, but largely undeformed, whereas the serpentinites are all strongly sheared and mylonitized in anastomosing networks, compatible with the proximity of the slip surface (*Reston et al.*, 2002). The lack of serpentinites within the deeper dredge hauls may indicate that they are restricted to the surface of the detachment fault. One possible explanation could be that they were originally sheared out along the fault where they later acted as a thin lubricating film during the exhumation process.

Dredge 1: base of scarp E of IC high 11°39.7 W-11°40.1 W, 5°06.0 S-5°07.0 S; water depth: 3044-2772 m	4 pieces of gabbro, largest 25x14x13 cm coarse to fine grained, mesocratic to melanocratic texture
Dredge 2: midway up scarp E of IC high 11°40.4 W-11°40.2 W, 5°05.9 S-5°06.1 S; water depth: 2520-2000 m	20 pieces of gabbro and plagioclase gabbro, largest 58x40x30 cm, mainly coarse-grained, some medium, variety of textures
Dredge 3: near top of scarp E of IC high 11°40.7 W-11°41.3 W, 5°06.0 S; water depth: 1958-1633 m	blocks of undeformed, altered gabbro, 1 less altered gabbro (73x63x27 cm), blocks of sheared serpentinite (largest 84x42x27 cm), very fine-grained, dark green, anastomosing schistosity, slickensides
Dredge 4: high on axial volcanic ridge 11°31.9 W-11°31.4 W, 5°15.3 S-5°15.6 S; water depth: 3454-3215 m	1 block (36x36x36 cm) of vesiculated pillow basalt with glassy surface, various small pieces of basalt and glass

Table 2.1: *Summary of dredge locations and lithologies recovered (from Reston et al., 2002).*

2.4.3 Microearthquake seismicity

For the passive part of the GERSHWIN experiment, a seismological network consisting of 13 ocean bottom stations was deployed on the inside corner high and in the adjacent median valley for a total recording period of 10 days (*Tilmann et al.*, 2004). A total of 148 locatable earthquakes were detected during this experiment (cf. figure 2.5). The majority of events seem to cluster within a 5-8 km wide section of the median valley, bounded to the north by the transform fault and to the south by the northern tip of the axial volcanic ridge. North of $\sim 5^{\circ}10'$ S, earthquakes are concentrated towards the western flank, marked by fault F1 in figure 2.5, whereas they occur across the whole width of the median valley south of this area. Event depths lie between 1-8 km below seafloor. Calculated focal mechanisms for a northern group of closely spaced events reveal a pattern of normal faulting with a strike perpendicular to the spreading direction.

A small number of earthquakes occurred beneath the ICH in depths of 4-8 km below seafloor. *Tilmann et al.* (2004) proposed that these few events accommodate tensile stresses underneath the ICH. Since they could not calculate focal solutions, their argumentation follows *Wolfe et al.* (1995), who interpreted events beneath a seismically much more active ICH in the North-Atlantic to occur within a diffuse zone of extension. However, assuming that the observed seismicity pattern is representative, it argues that extension is minor within the inside corner high compared to the median valley.

A cluster of earthquakes also occurred at OBH16 near the southern end of the survey (cf. figure 2.5). The four earthquakes with well-constrained depths lie between 6-10 km below sea level. Other events are likely to have originated at the transform fault, although their considerable distance from the network makes their localization a bit speculative (*Tilmann et al.*, 2004).

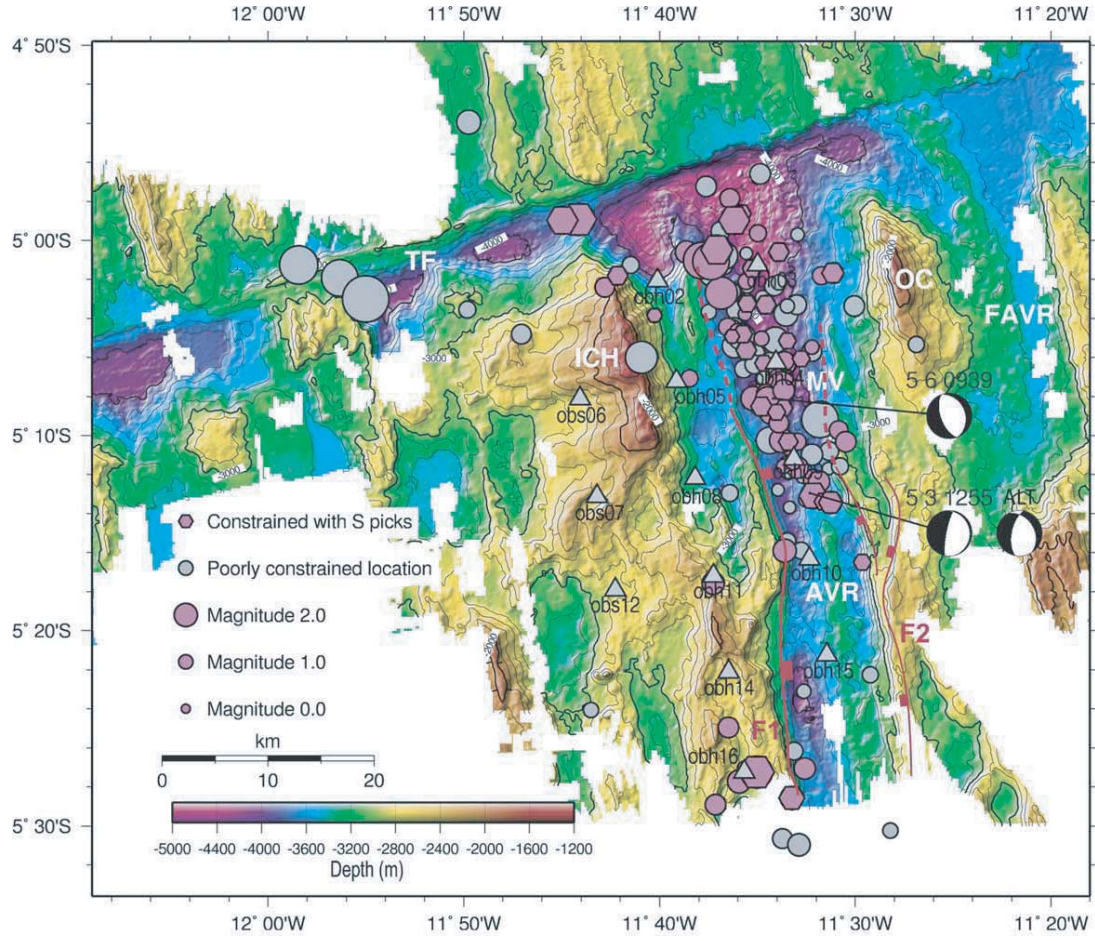


Figure 2.5: *Distribution of earthquakes recorded with the ocean bottom stations (modified from Tilmann et al., 2004). Red circles and hexagons are events located with at least five stations and azimuthal gap $< 300^\circ$; hexagons indicates at least one S arrival was used. Grey circles are marginally located events not fulfilling above criteria. Grey triangles are station locations. Composite focal mechanisms for two groups of events are shown as lower hemisphere projections (with an alternative solution -ALT- for the southern group, resulting from the use of a different velocity model) For a detailed description, refer to Tilmann et al. (2004). Marked morphological features have the same nomenclature as in the previous figures. The dashed lines show the possible continuation of the faults where their morphological expression is less clear.*

Interestingly, the presence of the well-defined volcanic ridge further south correlates well with the absence of locatable events. Surprisingly, the transition from the seismically active portion to the aseismic part of the median valley occurs very abrupt, with no or only little decrease in earthquake depths near the southern margin. The lack of seismicity could indicate that the ridge might be hot and active, whereas for the seismically active portion, the maximum earthquake depth (8 km below the median valley seafloor), the large cross-axial relief as well as the distribution of event magnitudes (with a moment b value of 0.8) support the idea of a “cold” segment end (Tilmann et al., 2004).

2.5 Database for this study

Four intersecting wide-angle seismic profiles with a length of 110-170 km were acquired for the active part of the GERSHWIN experiment. These lines run both parallel and perpendicular to the ridge axis and extend well into the northern and southern segment in order to resolve the large-scale structure of the 5° S ridge-transform intersection (cf. figure 2.6). On these profiles, between 12 and 17 *IFM-GEOMAR* ocean bottom hydrophones (OBH) and ocean bottom seismometers (OBS) (*Flueh and Bialas, 1996; Flueh et al., 2002*) were deployed with an average instrument spacing of 3 nm. Additionally, seismic data for three shorter profiles of up to 60 km length and six deployed OBH/S stations each were acquired in the area of the inside corner high and the adjacent median valley. The instrument spacing was 6 nm for these shorter profiles.

Profile 07/08 consists of two overlapping smaller profiles and some stations of the seismicity network and runs south of the 5° S FZ. With a total length of 170 km and its spreading-parallel direction, the profile provides the dataset to assess the temporal variations in crustal accretion at this segment end. However, it is primarily intended to resolve the internal structure of the inside/outside corner pair in order to verify existing models of oceanic core complex formation. On this profile, 17 instruments recorded a total of 2600 shots.

Profile 09 crosses Profile 07/08 in the area of the ICH. These two longer lines together with the three shorter lines form a dense seismic dataset for the inside corner area of the southern segment, which allows to resolve possible variations in the internal structure of an oceanic core complex. Profile 09 is 150 km long and extends well into both segments. The line is intended to map the variations in crustal structure across an ICH and across a transform fault. On Profile 09, a total of 1400 shots were recorded by 13 seismic stations.

Profile 10 runs parallel to Profile 09 roughly 25 nm further to the west. It crosses the 5° S transform fault but with its 110 km length focuses more on the northern segment, where 10 out of 12 stations are deployed. In its northern portion, the profile runs ~15 km east of the ridge-axis through the crestral mountains. A total of 1370 shots form the seismic dataset to map along-axis variations in crustal thickness within the northern segment and across the transform fault.

A last East-West trending profile completes the grid of the four longer seismic wide-angle lines. Profile 11 crosses the median valley of the northern segment at its shallowest portion directly at the pronounced seafloor bulge. With 130 km length and a total of 1400 shots, the line was designed to resolve temporal variations in crustal accretion as well as the evolution of oceanic crustal structure with age. A few kilometers west of OBH64, the profile crosses a circular elevation of the seafloor, which is likely to present an exposed volcano.

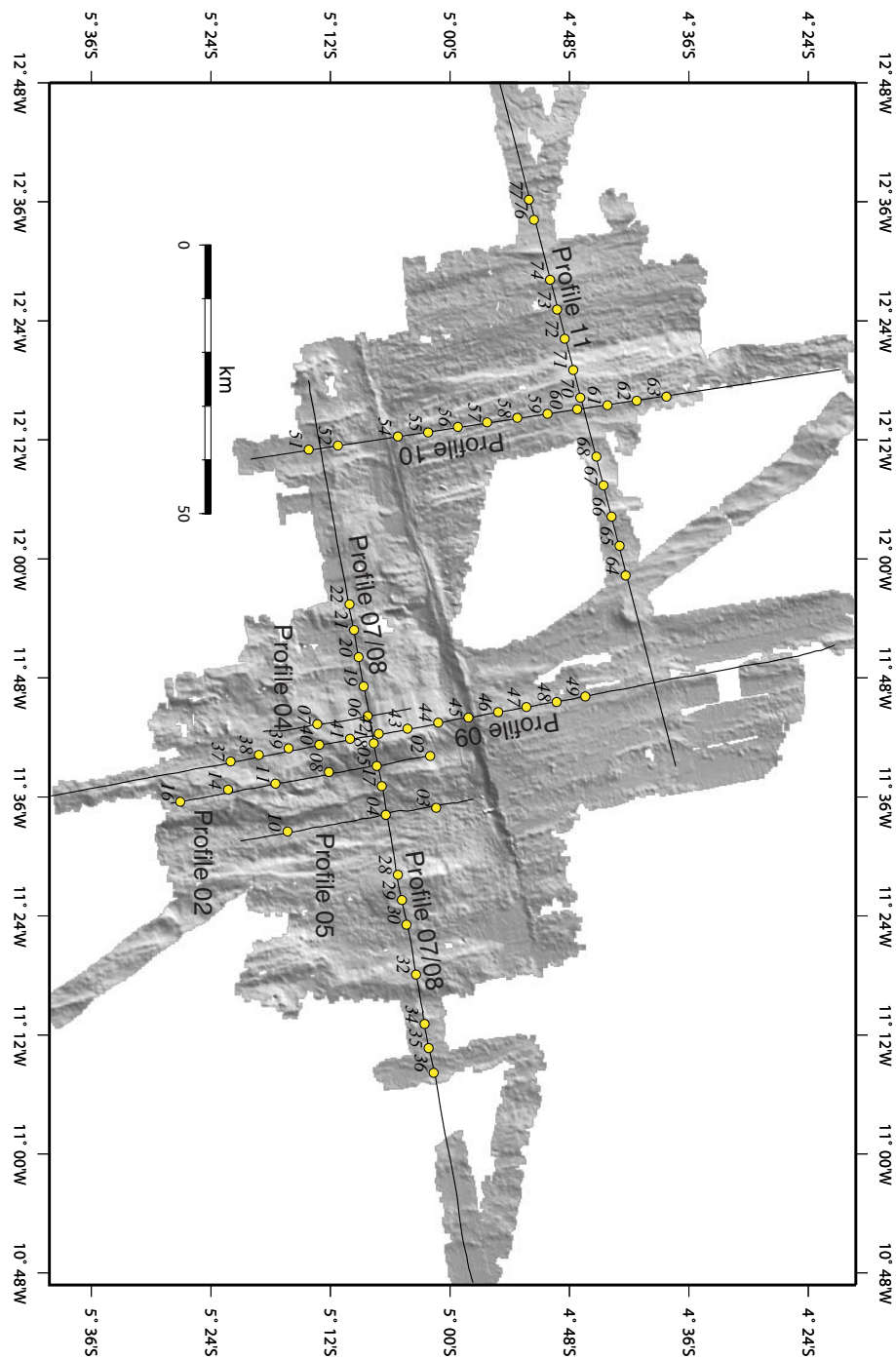


Figure 2.6: *Station distribution and shot geometry of the wide-angle seismic profiles.*

Chapter 3

Data processing

3.1 OBH/S data

During the crustal refraction survey, altogether 8500 shots were successfully recorded by a total of 65 OBH/S stations along 7 intersecting profiles. The seismic source was a cluster of three 32 l *Bolt* air guns towed at 10 m depth. The shots were recorded continuously at 10 ms sampling rate. A shot interval of 60 s resulted in a nominal shot spacing of 120 m. The ocean bottom units were either equipped with differential pressure gauges (DPG) or with piezoelectric hydrophones. Additionally, the OBS were fitted with seismometers. However, due to the rough topography these instruments did not couple well to the seafloor, such that few usable data were acquired. In contrast, the pressure sensors usually provided clear signal onsets for P-waves, sometimes up to offsets of 80 km and only limited by the range of the profile. Some OBH stations also recorded converted S-waves, which converted back from S to P at the seafloor beneath the instruments. As a result, the subsequent analysis is based on the DPG and hydrophone recordings, providing a total of just over 110,000 seismic traces.

Pre-processing involves as a first step the relocation of the ocean bottom units by using the arrival time of the P-wave, which propagates through the water column, and the exact shot point geometry. The station position is determined in profile direction by solving a least-squares minimization problem. The algorithm does not change the water depth of the stations, which is later adjusted to fit the high-resolution Hydrosweep bathymetry data. In a second step, a time correction is applied to the data assuming linear clock drift of the data logger between synchronization with GPS-time at the beginning and at the end of the experiment. OBS06 and OBH04 stayed at the sea bottom for the recording of three different seismic profiles. An examination of direct P-wave arrival times at profile intersection points allows precise clock drift rates to be determined, and suggests an overall timing accuracy of ~ 10 ms and a final positioning accuracy of ~ 50 m for these stations. This is within the limits of arrival time sampling, accuracy of the P-wave velocity in the water (1.495 km/s) and GPS derived accuracy of the shot locations.

An example of seismic raw data sorted into a common receiver gather is presented in figure 3.1 a. Several kinds of high-amplitude noise mask most of the seismic phases, especially low-frequency noise below 2 Hz (marked A in figure 3.1), but also constant signal noise (marked C) and coherent noise at ~ 2.5 Hz, which is possibly due to air gun problems

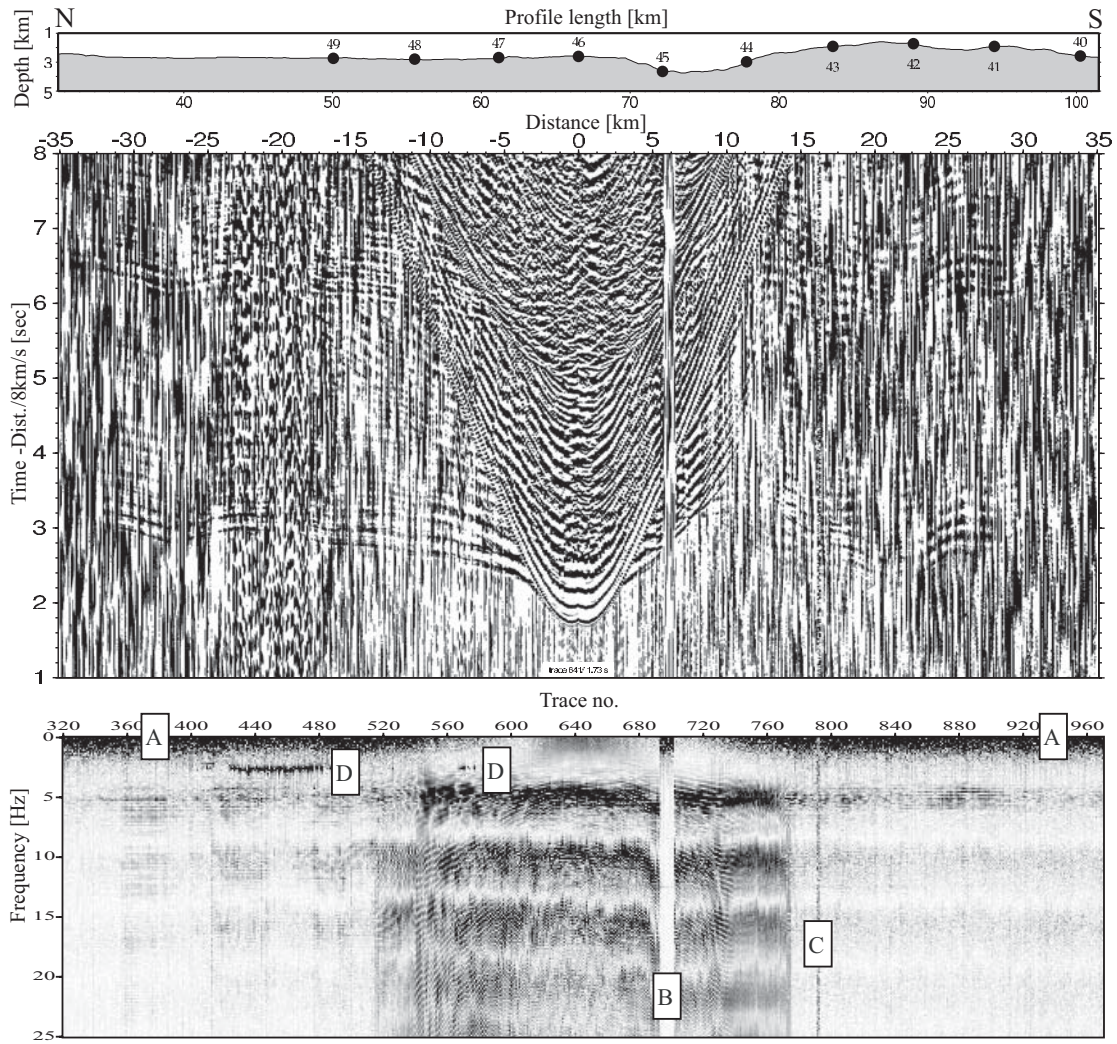


Figure 3.1: (a): Seismic section of Profile 09 recorded by OBH46 (raw data) together with the corresponding frequency spectrogram (bottom). Several types of high-amplitude noise mask the seismic phases and are also visible in the spectrogram. A: low-frequency noise, B: dead traces, C: constant signal noise, D: unknown noise. For a discussion, see text.

(marked D), as well as dead traces due to air gun failure (marked B) and different levels of ambient noise are visible.

The signal's main frequencies lie between 4 and 7 Hz, which corresponds to a wavelength of 200-1750 m for P-wave velocities of 1.5-7.0 km/s. In order to remove low-frequency noise and possible zero level shifts of each trace, the seismic data are filtered with a Kaiser minimum phase high-pass filter with the 3 db point at 2 Hz.

In a second step, a time-dependent predictive deconvolution is applied to effectively shorten the length of the wave-shape and thereby increase the resolution in the time domain (Wiener, 1949). In marine surveys, the use of air gun sources involves the presence of oscillating bubble pulses. A deconvolution assumption is that these bubble signals are

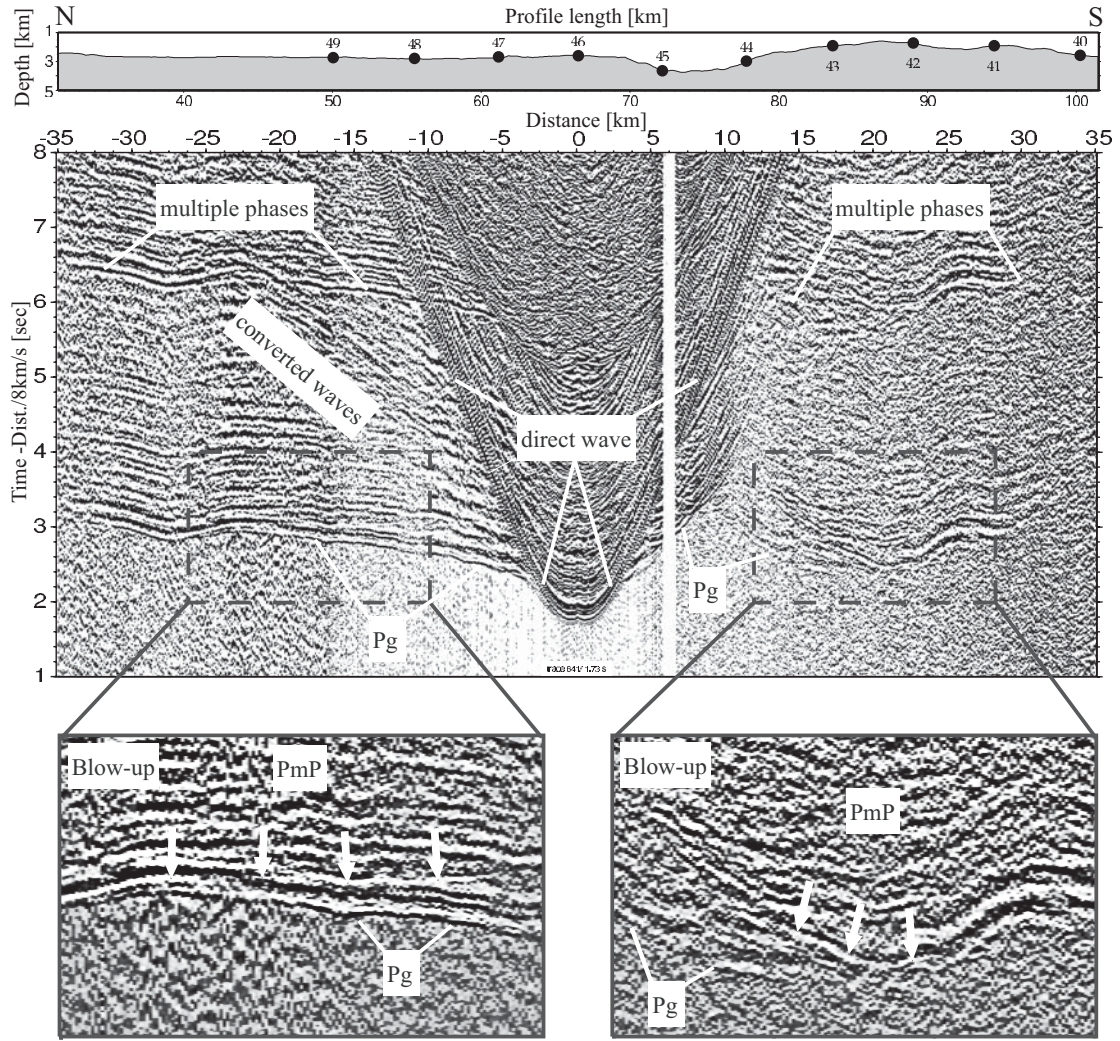


Figure 3.1: **(continued)** (b): Record section of OBH46 after processing (see text). Note that the noise is markedly suppressed and temporal resolution increased, which allows for the identification of secondary arrivals like reflection phases (see blow-ups). Pg: arrivals of crustal turning rays, PmP: reflection at the crust-mantle boundary.

predictable, whereas the Earth's reflectivity constitutes a series of random spikes. The effect of the adopted Wiener filter operator is to remove the predictable effects of the bubble reverberations to produce a signal which is free of the disturbant interference of multiple and primary phases. A measure of the predictability involved is the auto-correlation function of the signal. In this study, the auto-correlation of seismic traces shows that the first bubble pulse of the *Bolt* gun arrives 0.2s after the primary phase. Thus the effect of the predictive deconvolution is to zero the auto-correlation for times $t > \alpha$, where α is the prediction lag, at each trace within the particular time window. The algorithm involved to calculate the deconvolution operator is the *Wiener-Levinson* least-squares approximation. The Wiener filter is constructed by zeroing the autocorrelation for times between 0.05s and 0.25s. An artificial level of white noise (0.1% pre-whitening) is introduced before

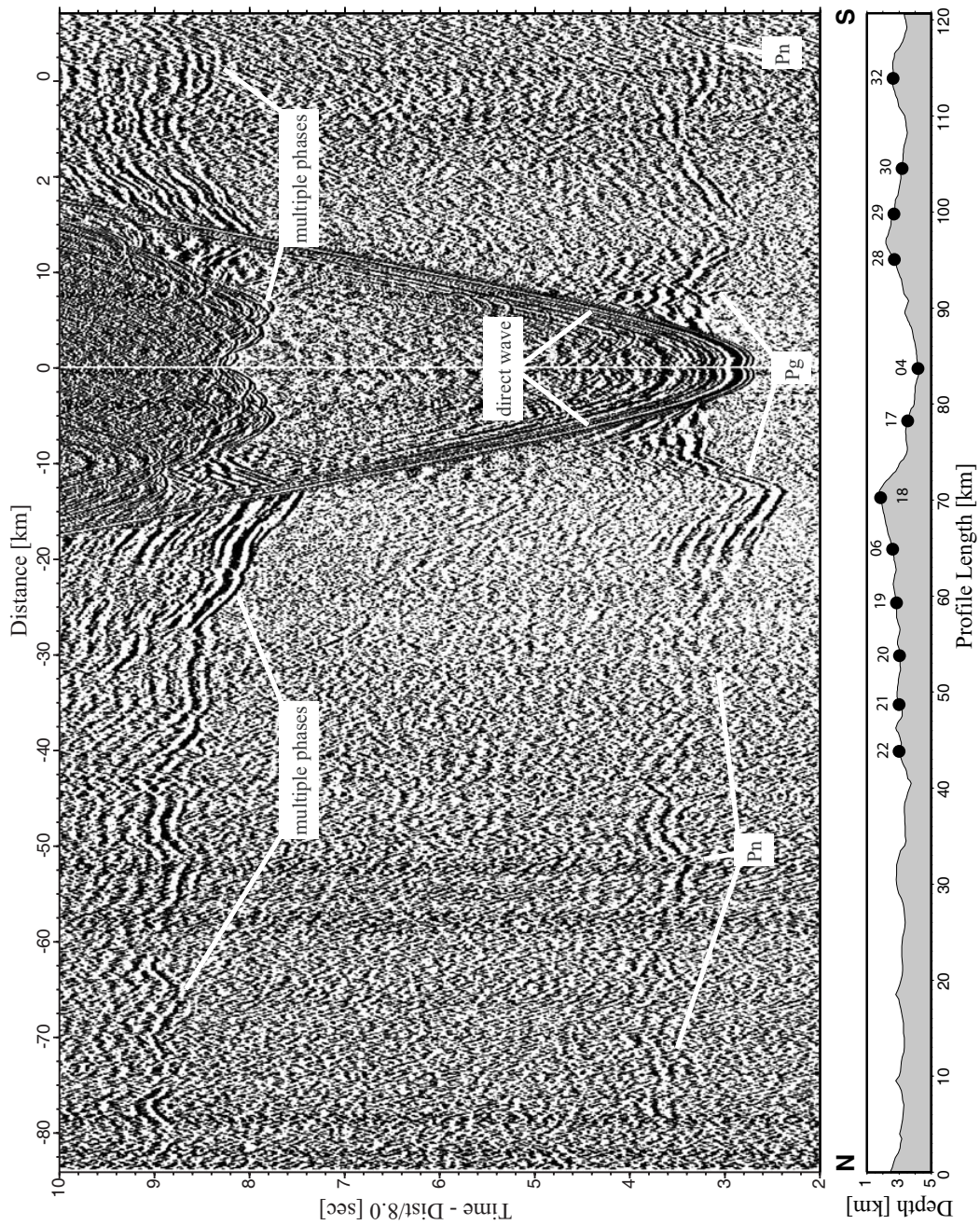


Figure 3.2: *Seismic record section of OBH04 (Profile 07/08) after processing. Available seismic phases reach up to offsets of 80km, but are often dominated by the extreme topography of the seafloor, suggesting the use of further correction methods (cf. section 3.2). Pg: arrivals of crustal turning rays, Pn: arrivals of mantle turning rays.*

deconvolution to ensure numerical stability. The filter operator is restricted to specified time-gates of 3s to account for source signal absorption and filtering effects with depth due to greater attenuation of higher frequencies. All parameters are carefully chosen to minimize the tradeoff between temporal resolution and high-frequency artificial noise suppression resulting in the preservation of the overall spectral shape of the input data.

In a final processing step, time and offset-variant *Ormsby* filtering is applied in which the passband moves towards lower frequencies as record time and offset increases to compensate dispersion due to attenuation.

Figure 3.1 b shows the same seismic section as figure 3.1 a after the processing is applied. All types of noise, including the bubble phases, which are responsible for the “ringy” character of the raw seismic section, are suppressed. Temporal resolution increased, providing the opportunity to identify secondary arrivals like *PmP* phases (reflections at the crust-mantle boundary). However, the seismic phases are dominated by the extreme topography of the seafloor, which suggests the use of further correction methods.

3.2 Wave-equation datuming

Wave-equation datuming is the name given to upward or downward continuation of seismic time data when the purpose is to redefine the reference surface on which the sources and receivers are located (e.g. *Berryhill, 1979*). The most interesting applications of the technique are those in which the redefined reference surface is an actual geologic interface having a known irregular topography and a large velocity contrast. Wave-equation datuming serves to remove the spurious effect such an interface has on the arrival times of reflected and refracted phases travelling through it.

In marine data where the seafloor has considerable topography and the layers below the water column have a significantly higher velocity, variations in the thickness and velocity of the water layer cause fluctuations in the arrival times of reflected and refracted phases (cf. figure 3.2). Usually, such fluctuations are regarded to be spurious because they make it difficult to distinguish between different seismic phases. Hence, removing these fluctuations often leads to an effective separation of first breaks from secondary arrivals like *PmP* reflections.

Seismic sections can be datum corrected by static shifting, i.e. by time-shifting every seismic trace by an amount defined by the difference in elevation between the two reference surfaces and a known or estimated velocity model. However, several previous studies (e.g. *Berryhill, 1979*; *Shtivelman and Canning, 1988*) have shown that this method fails in its objective wherever ray paths deviate significantly from the purely vertical, that is e.g. in areas of significant lateral changes in elevation between the input and output datum or with the presence of dipping reflectors. A more accurate solution for the datum problem can be obtained using wave-equation datuming. This method was previously employed and successfully tested for MCS data (e.g. *Berryhill, 1979*; *Shtivelman and Canning, 1988*) and wide-angle OBS data (e.g. *Chen and Chang, 1999*).

In this study, the shots are redatumed from the sea level to the seafloor, using a constant P-wave velocity of 1.5 km/s for the water layer (cf. figure 3.3). The wave-field extrapolation procedure used is a Kirchhoff summation method following the approach of *Berryhill (1979)* with the asymptotic far-field approximation of *Shtivelman and Canning (1988)*. It is implemented in the Seismos processing package.

Figure 3.3 presents the seismic record section of OBH71 of Profile 11 before and after datum correction by wave-equation extrapolation with the two corresponding shot datums (sea level and seafloor). Downward continuation produced a good focusing and good

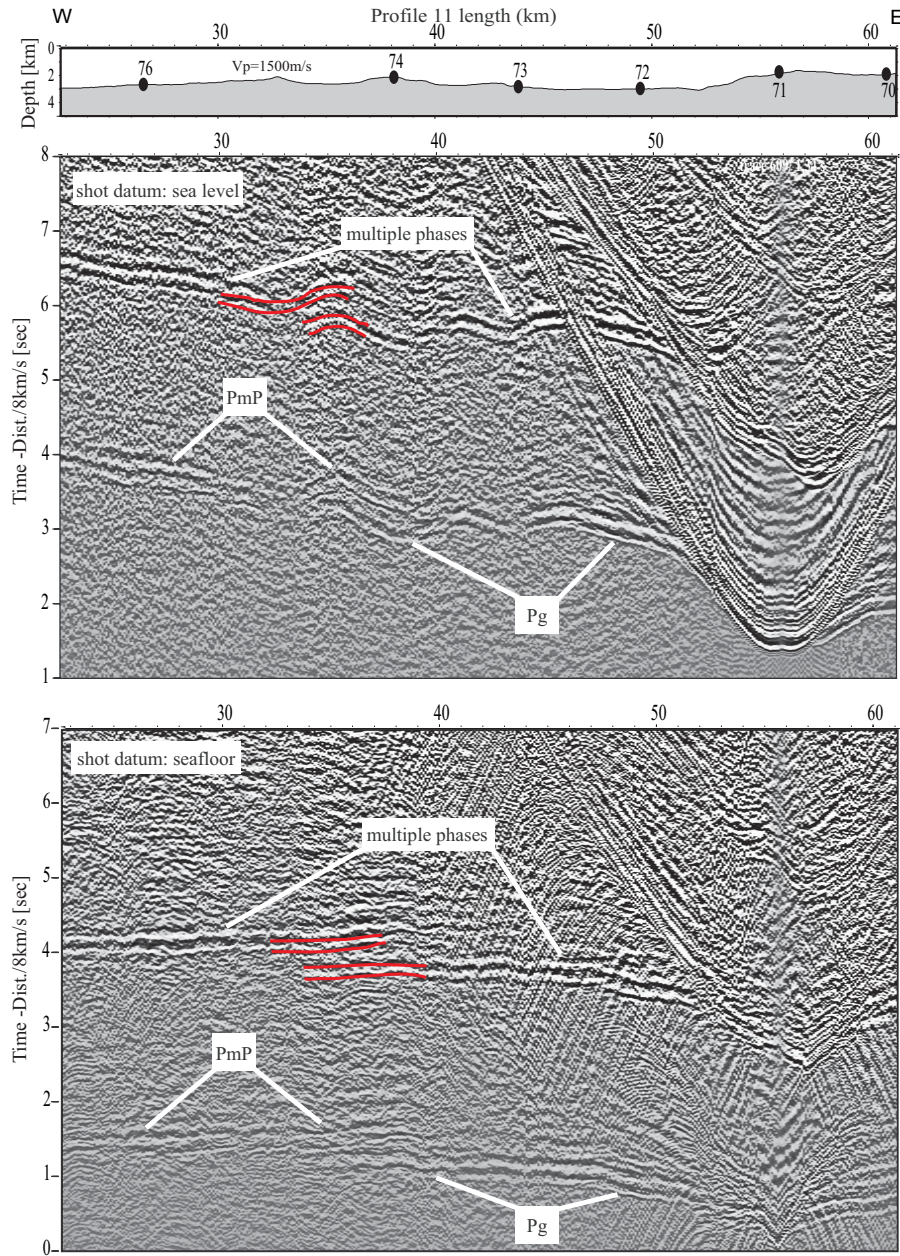


Figure 3.3: Record section of OBH71 (Profile 11) with shot datums at sea level (top) and seafloor (bottom), respectively. Downward continuation produced a good focusing and good restoration of the different seismic phases. A strong *PmP* phase is visible after removing the distortions caused by the overlying water layer.

restoration of the different seismic phases. Unlike in the upper seismic section, where the presence of a reflection at larger offsets can only be guessed, a *PmP* is clearly visible after removing the distortions caused by the seafloor topography. Hence, the applied method improves the ability of phase identification which in turn is crucial for subsequent arrival picking that is done manually on the un-corrected seismic record sections.

Chapter 4

First-arrival seismic tomography

4.1 Outline

Two different tomographic methods are used in this study with the goal to determine the 2D velocity structure from the given seismic dataset. The first method is refraction tomography, which is restricted to first-arrival traveltimes, and the second is a joint refraction and reflection tomography, which additionally uses secondary arrivals to simultaneously invert for velocity structure and Moho depths. The refraction tomography package used is FAST (First Arrival Seismic Tomography) (*Zelt, 1998*), which applies the forward algorithm and a similar regularized inversion method as described by *Zelt and Barton (1998)*. The joint refraction and reflection tomography package is TOMO2D (*Korenaga, 2000*).

Both methods are iterative, and new ray paths are calculated during each iteration by using Fermat's principle to linearize the inversion. A combination of smoothing and damping constraints is applied in both methods in order to regularize the system of equations and to restrict the maximum amount of model updates not to violate the linearization assumptions.

The methods differ in the implementation of the forward algorithm: The refraction tomography applies a finite-difference solution of the Eikonal equation on a regular grid to calculate the first-arrival traveltimes field (*Zelt and Barton, 1998*). The joint traveltimes inversion uses a hybrid scheme based on the shortest path and the ray bending method (*Korenaga et al., 2000*). The hybrid scheme is implemented on an irregular grid and achieves the desired accuracy by adjusting the graph template size, which makes it a very flexible and efficient tool for the calculation of ray paths and traveltimes (*Zhang and Toksöz, 1998*).

Both methods also differ in their implementation of the regularization constraints. In the first-arrival tomography, a “jumping strategy”, as defined by *Shaw and Orcutt (1985)*, is used so that the model constraints operate on the total model perturbation with respect to a starting model (*Zelt, 1998*). For the joint tomography, a “creeping strategy” (*Shaw and Orcutt, 1985*) is applied, which regularizes the perturbation with respect to the solution of the previous iteration (*Korenaga et al., 2000*). Hence, in an iterative approach, both strategies differ in their assessment of the initial model. The first strategy always favours a solution close to the starting model, whereas the latter should provide a solution which contains less bias towards this initial model.

In the absence of a *priori* information of the expected model structure and in the light of the different implementations of the regularization constraints, special attention is turned to a possible bias of the solution due to the choice of the starting model. For the refraction tomography, a more conservative strategy is pursued in deriving a constrained 2D starting model on the basis of preliminary tomographic solutions and forward modelling (Luetgert, 1992). Since the implementation of damping constraints penalizes perturbations with respect to the starting model, the starting model is supposed to be already close to the final solution in order not to violate the linearization assumptions. In contrast, for the joint tomography, a wide range of randomly generated 1D starting models is used in a nonlinear Monte Carlo approach to calculate the uncertainty in the final model parameters due to variations in the initial model and realistic data errors.

4.2 Forward method

The most computationally “expense” and important step in traveltime inversion is the forward modelling step associated with the ray tracing technique used. Rather than tracing single rays from point to point through a medium to determine the source-receiver traveltime, an alternative is to track the propagation path of the whole wavefront (e.g. Vidale, 1988). This approach involves the calculation of traveltimes from the source to all possible receiver nodes in the grid. For marine surveys, where the number of receivers is usually much smaller than the number of shots, wavefront methods are attractive, because in simply reversing the ray’s propagation path they simultaneously calculate the traveltime from a single receiver to all shot locations thereby having no problems in tracing diffracted rays, head waves or ray paths through shadow zones (Zhang and Toksöz, 1998).

Vidale’s method is formulated for a structure defined by a square grid of velocity nodes (cf. figure 4.1). If the traveltime of a ray at the node 0 is t_0 , then the traveltime at node 1 is given by

$$t_1 = t_0 + h \frac{u_0 + u_1}{2}, \quad (4.1)$$

where h is the node spacing and u_0 and u_1 are the slowness values at node 0 and node 1 respectively. The traveltime at node 3 is determined using the eikonal equation which describes the traveltime $t(x, z)$ of a propagating wave through a slowness field $u(x, z)$ by:

$$\left(\frac{\delta t}{\delta x}\right)^2 + \left(\frac{\delta t}{\delta z}\right)^2 = u^2(x, z). \quad (4.2)$$

The two differential terms can be approximated with finite differences:

$$\frac{\delta t}{\delta x} = \frac{1}{2} \left(\frac{t_1 - t_0}{h} + \frac{t_3 - t_2}{h} \right) = \frac{1}{2h} (t_1 + t_3 - t_0 - t_2) \quad (4.3)$$

$$\frac{\delta t}{\delta z} = \frac{1}{2} \left(\frac{t_2 - t_0}{h} + \frac{t_3 - t_1}{h} \right) = \frac{1}{2h} (t_2 + t_3 - t_0 - t_1).$$

Substituting equation 4.3 in 4.2 gives the traveltime at node 3:

$$t_3 = t_0 + \sqrt{2(h\bar{u})^2 - (t_2 - t_1)^2}, \quad (4.4)$$

where $u = \bar{u}$ is the average slowness of all nodes under consideration. The traveltimes to the next set of grid nodes are then calculated progressively away from the source along

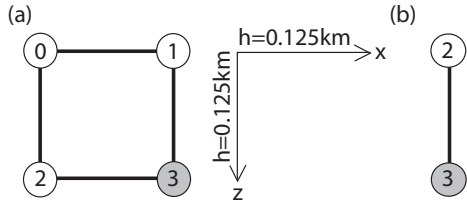


Figure 4.1: (a) 2D and (b) 1D finite-difference operators (scaled with respect to the applied node spacing). The traveltimes at the grey node is calculated from the times at the other nodes.

squares of increasing size, like the sides of an “expanding cube”. The arrival times at each node need to be sorted and the path with the minimum time represents the seismic traveltimes. Ray paths can then be obtained by following the steepest gradient of the time field from a receiver back to the source (Vidale, 1988).

A severe drawback of this “expanding cube” is that the times do not necessarily have to represent first-arrival traveltimes, especially in the presence of large velocity contrasts. Another problem with the original scheme is that, due to its geometry, the traveltimes on the faces of the cube are computed only with the times at grid nodes within the volume. Therefore, the method was modified by *Hole and Zelt* (1995) to be valid also for large velocity gradients using (1) the inclusion of head wave operators and (2) a reverse propagation step, which is initialized if head wave operators are used (*Hole and Zelt*, 1995). To illustrate this modifications, imagine a steep velocity gradient or a velocity discontinuity at the bottom edge of figure 4.1 a, with the velocities beneath nodes 2 and 3 significantly higher than in the overlying volume. The correct ray path to node 3 (it is thereby assumed that the 4 nodes are placed beyond the point where critical refraction occurs) would then run parallel to this discontinuity directly from node 2 to node 3 with the velocity of the underlying volume. For equation 4.4 this could result either in a negative number beneath the square root or in a violation of causality by producing a time at node 3 which is less than the times at one of the nodes (node 1) used to calculate it (*Hole and Zelt*, 1995). Therefore, a better solution is to introduce the 1D head wave operator:

$$t_3 = t_2 + hu \quad (4.5)$$

that represents a straight ray between the two considered nodes (*Hole and Zelt*, 1995).

Hence, possible first-arrivals at node 3 include (1) body waves that travel through the volume of grid nodes (calculated using equation 4.4), (2) diffracted or head waves that cross one of the faces of the “expanding cube” (calculated using equation 4.1) and (3) diffracted or head waves that travel along the edges of the grid cells (calculated using equation 4.5) (*Hole and Zelt*, 1995). All possible arrivals are computed for each node and the arrival with the minimum time is kept as the first-arrival.

In the above example of a down-going wave, the occurrence of a head wave parallel to one face of the “expanding cube” means that the calculated times within the volume are possibly not the “true” first-arrival traveltimes and therefore, the times within the cube need to be updated in applying a reverse propagation step (*Hole and Zelt*, 1995). In practice, after traveltimes have been computed throughout the entire model, the reverse step is initiated at the face farthest away from the source that contains a node timed with a head wave operator. The traveltimes field is computed upward and initial times are replaced if the calculated times are smaller (*Hole and Zelt*, 1995).

Sources and receivers can be placed anywhere in the model, and the bathymetry is

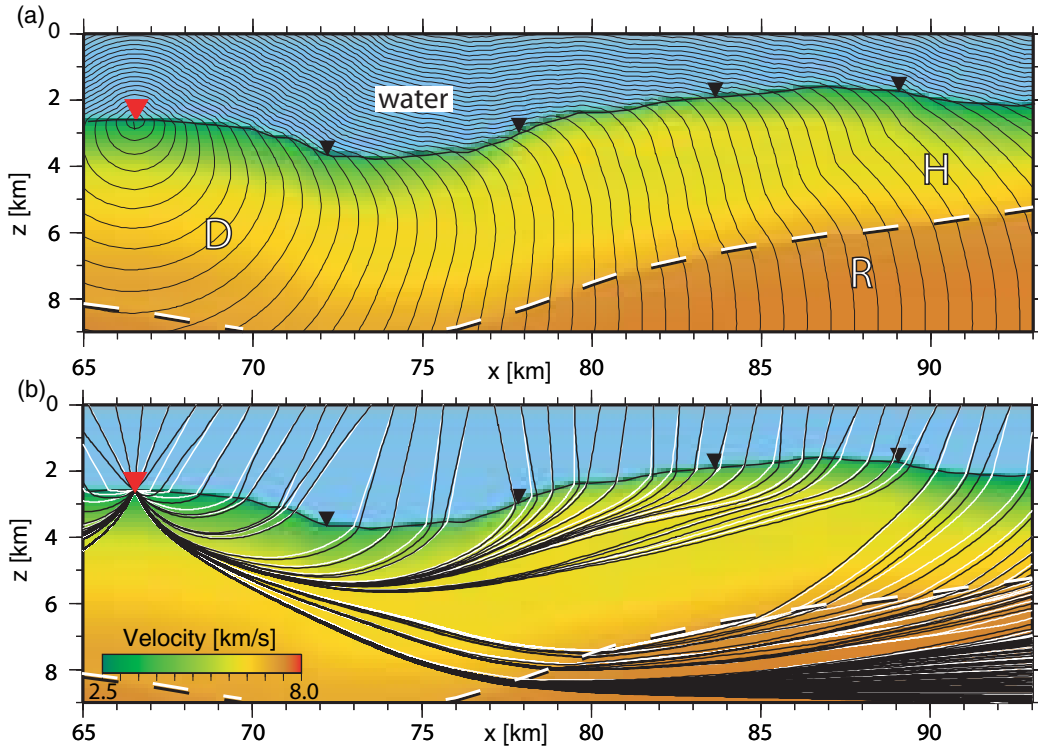


Figure 4.2: Traveltime contours and ray paths calculated with the finite-difference algorithm for a realistic velocity model (head wave operators and reverse propagation steps incorporated). The black/white dashed line marks a sharp velocity contrast of ~ 0.3 km/s. (a): First-arrival traveltimes, computed on a 125×125 m grid, shown at 0.2 s intervals after 2 reverse computational steps. D=direct waves; R=refracted waves; H=head waves. (b): Finite-difference ray paths (black) for sources placed every 750 m at sea level, together with a highly accurate solution of the hybrid ray-tracing scheme (white). Calculated finite-difference traveltimes for the rays shown in (b) are on average 4.3 ms smaller, which can rather be due to the difference in model parameterization than indicative of a systematic misfit.

treated in two ways. First, the velocity at a depth closest to the corresponding bathymetry depth equals the average of the true velocity over half the node spacing above and below the node. Second, the traveltimes for nodes near a source (OBH) are calculated applying a straight ray approximation within a small cube around the source, thereby using the water velocity if the node lies above the source, and the sediment velocity if the node lies below the source (Zelt and Barton, 1998).

Figure 4.2 illustrates the traveltimes contours and corresponding ray paths in a realistic velocity model on a 125×125 m grid, calculated with the modified finite-difference algorithm of Hole and Zelt (1995), including the use of head wave operators and reverse propagation steps. The background velocity model used for the calculations here is also taken as a reference model for the forward calculations with the hybrid ray-tracing scheme of the joint tomographic approach, and corresponding results and model features are described in more detail in section 5.2.3. The model comprises a sharp velocity contrast of ~ 0.3 km/s at the

black/white dashed line where emanating wavefronts refract (R) and head waves (H) are generated which form the first-arrival times above the velocity contrast at greater offsets (cf. figure 4.2 a). In figure 4.2 b, first-arrival ray paths that follow the steepest traveltimes gradient are computed for sources placed at sea level every 750 m. As a reference, a highly accurate solution produced by the hybrid ray tracing routine (cf. section 5.2.3) used in the joint tomographic approach is shown (white rays). The mean traveltimes difference between the two ray sets is -4.3 ms, i.e. traveltimes computed using the finite-difference scheme are on average slightly smaller than the corresponding traveltimes of the hybrid ray tracing algorithm. However, these small discrepancies could be due to the difference in model parameterization, especially due to the way the two approaches incorporate the seafloor as a sharp velocity boundary, rather than being indicative of a systematic difference. Interestingly, rays traced with finite-differences do not necessarily run straight through the water layer, although a constant water velocity is used for computations. Instead, they “follow” awkward kinks in the traveltimes field, originally introduced by the coarse sampling of the rough seafloor topography. It is shown in section 5.2.3 that the use of the hybrid ray tracing scheme for the forward solution efficiently incorporates a complex seafloor topography into the model parameterization (due to the use of an irregular grid) and that it can decrease the introduced traveltimes errors to a negligible level.

4.3 Inverse method

The forward and inverse problems are parameterized separately for reasons of flexibility and computational efficiency. In the following, the forward and inverse parameterization is referred to as the slowness and perturbational model, respectively. The number of perturbational nodes is typically much less than the number of nodes used to define the slowness. This allows for a computationally tractable inversion which is able to evaluate the forward problem on a complex model, and to improve the data fit (if desired) using a coarser perturbational scale (e.g. *Toomey et al.*, 1994). In this study, a perturbational model is used that is parameterized on a 1x0.25 km grid. Away from the grid nodes, each point within the model is defined by bilinear interpolation between the four surrounding model values.

The traveltimes along a ray path P is

$$t_{obs} = \int_P u(r) dr, \quad (4.6)$$

where r is the position vector, dr is the infinitesimal ray path length and $u(r)$ is the slowness at point r . If $u(r)$ changes, the ray path changes, thus the ray path depends on the solution of this nonlinear problem. The perturbational model $\delta u(r)$ is related to an initial model $u_0(r)$ by

$$\delta u(r) = u(r) - u_0(r). \quad (4.7)$$

According to Fermat’s variational principle the traveltimes along the ray path P with the minimum traveltimes is stationary for an infinitesimal perturbation δu , resulting in a small change in traveltimes:

$$\delta t = t(u + \delta u) - t(u) \approx \int_P \delta u dr. \quad (4.8)$$

In linearizing the problem it is assumed that small changes in traveltimes are solely related to velocity heterogeneities. Therefore, the deviation of the ray path is ignored. The residual equation 4.8 can be discretized with respect to the individual perturbational model parameters and written collectively as a matrix equation

$$d = G \delta m, \quad (4.9)$$

where d is a $n \times 1$ vector which contains the traveltimes residuals, δm is the unknown $m \times 1$ model perturbation vector, and G is the $m \times n$ Fréchet derivative matrix (e.g. *Menke, 1989; Toomey et al., 1994*). The partial derivatives with respect to slowness in matrix G are simply the path lengths distributed to relevant model perturbational nodes. Since the number of observed data n can be smaller than the number of model parameters m , and rays might be unevenly distributed within the model space, many entries in a row of G are zero, and consequently the matrix is sparse. The unconstrained model parameters, from an inverse point of view, make the problem ill-posed.

The solution to equation 4.9 is to find a δm that minimizes the misfit between observed and predicted traveltimes. If it is assumed that the error in the relationship $d_{obs} \approx d_{pred} = G \delta m_{est}$ is Gaussian, then a least-squares measure of this difference is suitable (e.g. *Menke, 1989*):

$$\min \|d_{obs} - G \delta m_{est}\|^2. \quad (4.10)$$

Uncertainties based on the assigned picking errors σ_i , $i = 1, \dots, n$ are used to weight the data according to their quality by writing the *objective function* $\Psi(m)$ that has to be minimized as:

$$\Psi(\delta m_{est}) = (d_{obs} - G \delta m_{est})^T C_d^{-1} (d_{obs} - G \delta m_{est}), \quad (4.11)$$

where C_d is the diagonal data covariance matrix with diagonal elements σ_i^2 (e.g. *Menke, 1989*).

If equation 4.11 is under-determined, the unconstrained parameters can take *any* value without affecting a least-squares solution, and hence many δm will fit the data. To address this *non-uniqueness*, model regularization adds additional constraints to the inverse problem. In practice, one often uses *a priori* information to regularize the *a posteriori* solution (cf. *Scales and Snieder, 1997*). Within the FAST algorithm, a user-specified combination of smallest, flattest and smoothest perturbation constraints, each being allowed to vary with depth, is used to tune the iterative inversion in such a way that the retrieved model has agreeable features. The regularization method is “jumping” (*Shaw and Orcutt, 1985*), i.e. all constraints are applied on the total model perturbation with respect to the original starting model. For the smallest perturbation constraint, this means that a higher weighting encourages solution models to be close to the starting model. In contrast, a higher weighting of flatness and smoothness constraints penalizes enhanced model structure, precisely enhanced structure within the perturbational model with respect to the starting model. In the first case, the gradient of the perturbational model parameters is regularized, using two 1D finite-difference approximations of the first derivatives, resulting in two model covariance matrices C_H and C_V for the horizontal and vertical directions. In case of the smoothness regularization, the curvature of the perturbational model parameters is regularized, using two 1D finite-difference approximations for the second derivatives, resulting again in two model covariance matrices (*Zelt, 1998*).

Because of the large variation of slowness with depth, an even distribution of slowness perturbation along the ray will bias the final velocity model towards increased levels of heterogeneity at greater crustal depths (e.g. *Toomey et al.*, 1994). Therefore, the model covariance matrices C_H and C_V are scaled with the prior slowness, leading to two non-zero elements $-1/u_i, 1/u_i$ in each row for flatness and to three non-zero elements $1/u_i, -2/u_i, 1/u_i$ for smoothness regularization (*Zelt*, 1998).

The solution is a tradeoff between the norm of the traveltime residuals and the norm of the model, where the latter is subject to user-adjustable constraints. It can be determined by minimizing an objective function such as:

$$\mathcal{F} = (d_{obs} - G \delta m_{est_n})^T C_d^{-1} (d_{obs} - G \delta m_{est_n}) + (m_{est_n} - m_0)^T C_m^{-1} (m_{est_n} - m_0), \quad (4.12)$$

where $m_{est_n} = m_n + \delta m_{est_n}$, m_n is the slowness model after n iterations, m_0 is the slowness of the starting model, and C_m is an *a priori* model covariance matrix. Here, C_m is separated into C_H , C_V and C_P . C_H and C_V are the above described model covariance matrices, either invoking flatness or smoothness constraints. The matrix C_P , which is a penalty matrix on the model perturbation, is simply the identity matrix, scaled with the prior slowness (*Zelt*, 1998).

There are three free weighting parameters that control the relative importance of the regularization constraints and the data fit: The tradeoff parameter λ controls the relative weighting of minimizing the data misfit versus minimizing the additional model constraints, and the scalar α controls the relative importance of weighting smoothness/flatness versus smallest perturbation within the regularization part. s_z operates the relation between vertical versus horizontal smoothness/flatness.

In practice, data residuals and the Fréchet derivative matrix G are computed in the forward ray tracing step. In the inverse step, the under-determined solution is complemented with weighted measures of regularization terms, applied as additional equations in the inverse problem. Since all regularization terms in equation 4.12 are allowed to vary with depth, the rows of the regularization matrices are finally scaled with additional depth-weighting factors. The resulting system of linear equations is solved, using the sparse matrix solver LSQR (*Nolet*, 1987). After each nonlinear iteration, the updated perturbational model is regridded on the finite-difference grid and ray paths and traveltime residuals are computed again until finally the predicted data fit the observed data within the limits of preassigned uncertainty. A good estimate of the quality of fit can be obtained by calculating the normalized χ^2 parameter:

$$\chi^2 = \frac{1}{N_{res}} \sum_{j=1}^{N_{res}} \left(\frac{\delta t_j}{\sigma_j} \right)^2, \quad (4.13)$$

where δt_j is the element of d corresponding to the j th traveltime datum, σ_j is the pick-uncertainty in that datum, and N_{res} is the absolute number of traveltime residuals. If the uncertainties are well-estimated, uncorrelated and follow a Gaussian distribution, then a satisfactory fit is obtained on average across the model if $\chi^2 = 1$.

4.4 Results of the first-arrival tomography

The results of the first-arrival tomography are presented in three parts: first, a summary of the procedural details is given, then a description of the applied resolution analysis, and finally a characterisation of the derived solution models. The description of the individual model features is supplemented in the next chapter on the basis of the results of the joint refraction and reflection tomography.

4.4.1 Description of the procedure

According to equation 4.12, there are three free tradeoff parameters plus the depth depending weighting factors of the regularization matrices. However, α , s_z and the depth factors are held fixed during all iterations, whereas several values for λ can be tested within each iteration by applying sweeps on the inverse step (*Zelt and Barton, 1998*). In order to produce a minimum-structure model, inversion is initially started at a high λ value. The value is then decreased in (usually 5) steps per nonlinear iteration, and that value is selected to be the starting value for the next iteration which obtains the smallest data residuals. In order to avoid that the inversion algorithm gets trapped into a local minimum, a slightly smoother solution than that obtained with the optimum λ parameter is taken as a starting model for the next iteration (*Zelt, 1998*). For the last iteration, a value of λ is determined which produces a $\chi^2 = 1$.

Rather than applying “flatness” constraints, a regularization in terms of “smoothness” is preferred here because a better data fit could usually be obtained with virtually no difference noticeable in model structure. On the basis of several runs and comparison with supplementary forward-modelling (*Luetgert, 1992*), a value of $s_z = 0.15$ is finally chosen for all profiles to operate the relation between vertical and horizontal smoothness. This value is similar to the $s_z = 0.125$ derived by *Zelt and Barton (1998)*. However, the slightly lower weighting of horizontal smoothness here allows for higher structural variation in this dimension, which should be considered as reasonable in a mid-ocean ridge regime. The depth dependency of the regularization constraints is adopted as a linear increase of smoothness-weighting with depths in order to avoid the emergence of small-scale model structure in greater depths, which would not be resolvable with the available dataset anyway. The relative importance of fitting smallest perturbation equations versus smoothness equations can be adjusted invoking a single weighting parameter α . In the vast absence of *a priori* information regarding the expected model structure, maintaining the smoothness is weighted 9 times higher ($\alpha = 0.9$) than maintaining small perturbations from the starting model.

The selection of the starting model is important within the applied tomographic approach because in linearizing the problem, it is assumed that only small model perturbations with respect to a starting model are reliably determined (*Zelt and Barton, 1998*). In applying a “jumping strategy” as described above (cf. section 4.3), the regularization equations operate on the total perturbation with respect to the starting model. As a consequence, even in an iterative approach the tomography will always favour a solution that is close to the starting model. This is especially the case in model areas which are not adequately sampled by available ray coverage, and thus are almost entirely governed by the applied smoothness or smallest perturbation constraints.

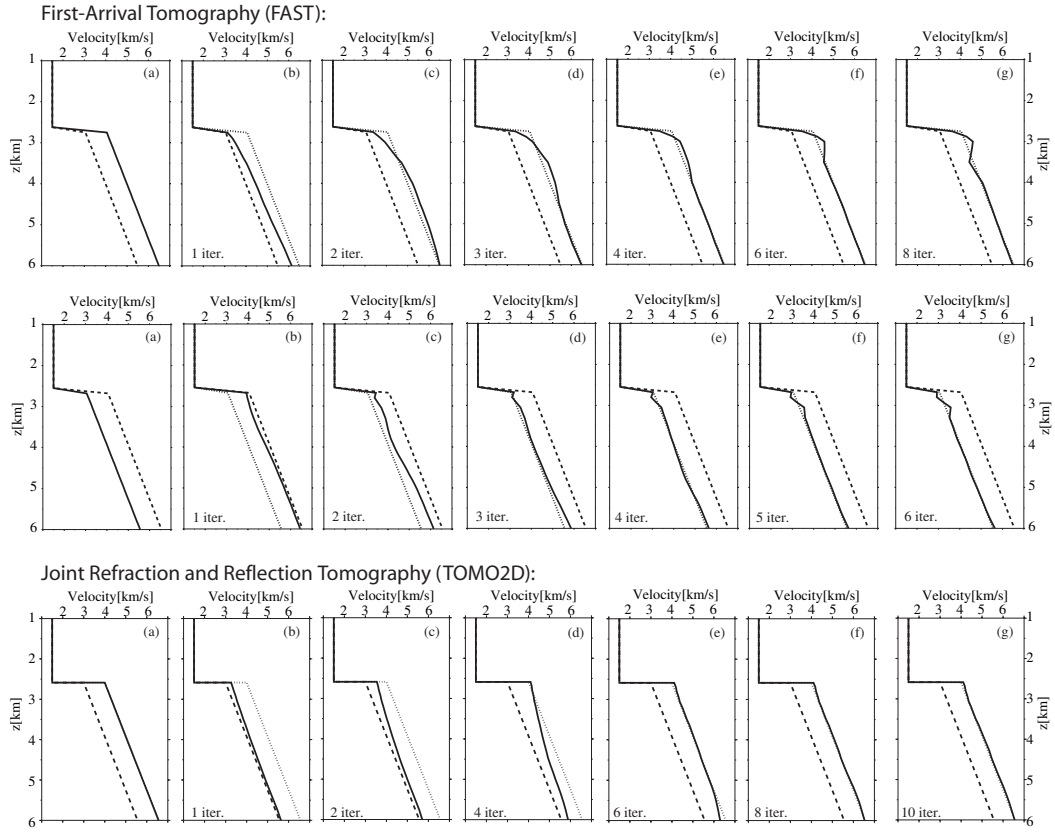


Figure 4.3: Illustration of the “ringing effect” produced by the regularized least-squares inversion of the first-arrival tomography when modelling a steep velocity gradient at the seafloor. Synthetic traveltimes are computed with the solid-line model in (a) using the original shot/receiver geometry of Profile 09. The velocity-depths profiles are all extracted directly beneath an instrument location (OBH46). Starting from the dashed-line model in (a), inversion results are shown after different iterations (b-g). On the contrary, the results obtained with the joint refraction and reflection tomography (bottom) show virtually no “ringing” beneath the seafloor.

Figure 4.3 illustrates the effect produced by a sharp velocity gradient in a regularized least-squares inversion, and furthermore it shows a substantial drawback of the regular-grid parameterization of the first-arrival tomography applied here. Taking the model geometry and station distribution of Profile 09, synthetic traveltimes are obtained from a simple 1D model defined by a fixed seafloor velocity and an underlying velocity gradient of 0.75 s^{-1} (solid line in figure 4.3a). Gaussian noise is added to the data, which are inverted with a 1D starting model (lower or higher velocity, the same velocity gradient - dashed line in figure 4.3a). To reveal a closer look at the velocity fluctuations, the same velocity-depth section is shown for different iterations. The section is extracted beneath OBH46, i.e. in an area characterised by enhanced ray coverage. For comparison, the same test is done with the joint refraction and reflection tomography method described in more detail in the next chapter.

In case of the first-arrival tomography, the sum of model updates closely resembles the predicted solution after 6-8 iterations (cf. figure 4.3 g). But directly beneath the seafloor, the velocity sequence contains small fluctuations which are reminiscent of the “ringing effect” that may be produced if high-frequency components are removed from a waveform (also known as *Gibbs’ phenomenon*). The analogous effect could occur here, because smoothing suppresses the high-frequency model structure (*Hobro et al.*, 2003). In this case, the effect is restricted to the region directly beneath the seafloor where velocity gradients are highest. But a similar effect can be expected if a very high velocity gradient or a velocity jump is introduced somewhere else in the model.

From the considerations above it is clear that if a starting model is far from the true model, model updates will suffer from the described effects, and hence near seafloor velocities obtained with the first-arrival tomography have to be considered as unreliable. Therefore, a good starting model is needed for the uppermost part of the model, even in areas of available stations coverage and sufficient ray coverage. A successful way to avoid this problem is shown by the joint tomography. It uses an irregular grid (parameterized as a “hanging mesh”), which simply excludes the high-gradient zone from the velocity parameterization. As a result, near seafloor velocities virtually do not suffer from the “ringing effect” (cf. figure 4.3 bottom).

In order to obtain a solution that is as free as possible from artefacts introduced during large model updates, a good 2D starting model is constructed on the basis of preliminary tomographic solutions and forward modelling (*Luetgert*, 1992). A top-to-bottom scheme is applied by starting initially with a simple 2D input model and rays recorded within offsets smaller than 15 km (cf. figure 4.4). In an iterative approach, the initial input model is updated, taking the tomographic solution of the previous step as a reference. In this context, updating means that the velocity trend is adopted in adjusting the seafloor velocities as well as those iso-velocity lines, which are reliably covered by the available ray coverage. In order to avoid “local minima” within the model-space and to assure a relatively undisturbed ray propagation in greater depths, the deeper layers of the model remain initially flat. Finally, in invoking additional picks with greater offsets, the deeper velocities up to 6.5 km/s are adjusted as well, resulting in a “constrained starting model” for the final inversion where all available picks are included (cf. figure 4.4).

For all profiles, the constrained starting models are obtained following the above described scheme. In all cases discussed below, the seismic velocity model is defined on a 1.0 km × 0.25 km grid using a 125 m parameterization in both dimensions for the forward calculations. The seafloor is incorporated in both the forward and the inverse computational steps gridded at 125 m intervals depicted from the *Hydrosweep*® bathymetry. Uncertainties of the traveltimes are evaluated individually for each pick on the basis of visually assigned accuracy for the first-breaks (ranging between ±30 ms and ±110 ms). Uncertainties usually increase with offset, and average values vary slightly for the different profiles due to overall changes in data quality. Before the final tomographic inversion, RMS traveltime residuals for the different profiles lie within the range of 60-110 ms which results typically in a normalized $\chi^2 \sim 3$. Taking up 8 iterations, the misfit is reduced to final values of 45-57 ms. Figure 4.5 shows the traveltime residuals with respect to the observed data for Profile 10 after different stages of the tomographic approach. For the constrained starting model, where velocity trends in the upper layers are already adopted,

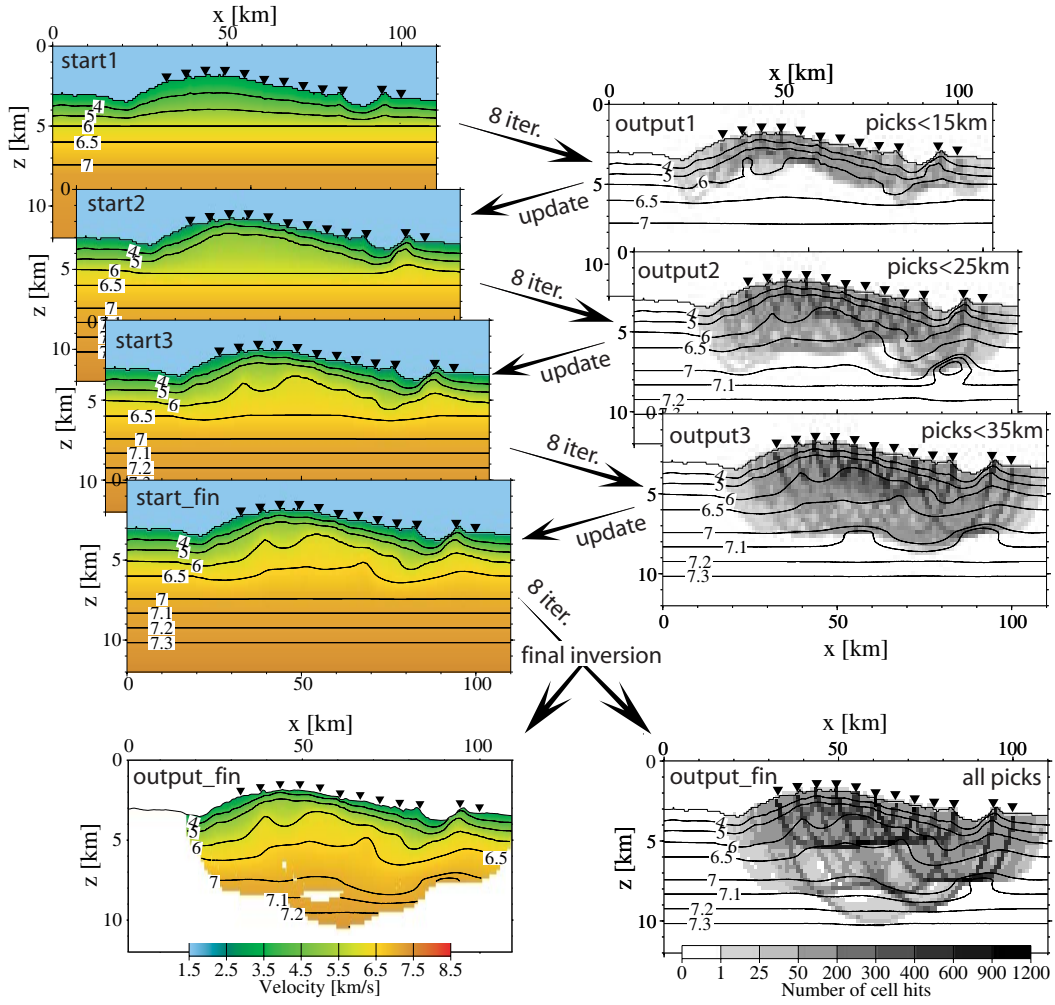


Figure 4.4: An iterative top-to-bottom scheme is applied to obtain a constrained 2D starting model (here shown for Profile 10). Starting with a simple input model and rays within 15km offset, the resulting tomographic output is used to adopt velocity trends within a new model (start2). Deeper layers of the model remain flat. Invoking later additional picks from greater offsets, the model is progressively updated, which finally results in a constrained “starting model” (start_fin). In a final step, the last model is used together with all available picks to invert for a solution.

this leads to $\text{RMS} = 62 \text{ ms}$ and a corresponding $\chi^2 = 4.0$. Due to the good data quality on this line (probably related to its ridge-parallel strike and quite subdued topography), assigned pick-uncertainties are comparatively low, which results in a higher-than-average χ^2 even though the initial RMS value is the lowest for all profiles. However, especially at greater profile distance, calculated traveltimes clearly reveal significant misfits. After 8 iterations a much better overall fit is achieved, resulting in a final $\text{RMS} = 46 \text{ ms}$ and a $\chi^2 = 0.9$. Still, some residuals exceed their predefined uncertainty limits. This is especially valid for rays that penetrate the deeper areas beneath the transform fault (cf. figure 4.9). This could indicate that the data have sampled small-scale heterogeneities that it cannot resolve.

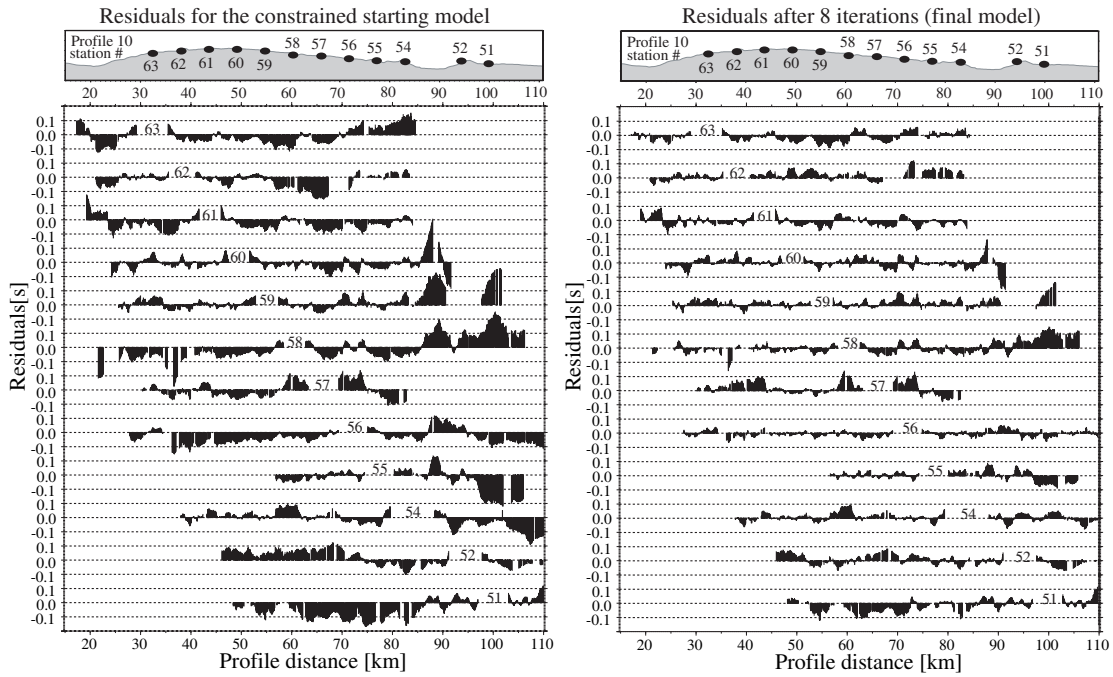


Figure 4.5: *Traveltime residuals for the constrained starting model (left) and for the final model (right) of Profile 10. Residuals are shown for each seismic station and the station number marks the corresponding position within the profile geometry.*

4.4.2 Resolution and accuracy

Synthetic anomaly tests

A common practice for evaluating the resolution of a tomographic solution is to reconstruct a pattern of known anomalies using the same source-receiver geometry as in the real experiment (e.g. *Toomey et al.*, 1994). The rationale behind this approach is that if a known model structure with similar length scales to the final solution model can be recovered using similar ray paths, then the solution should be reliable. In the so-called “checkerboard test”, an alternating pattern of low and high velocity anomalies is superimposed on a reference model (usually the starting model) and the anomaly pattern has to be retrieved starting from the model without anomalies. The lengths scales of the anomalies should be similar to the smallest wavelength structures recovered in the solution model of the real experiment. However, one may ask whether a checkerboard structure can be representative of the true perturbations. Furthermore, in applying an iterative approach in a nonlinear regime, the ray paths will depend on the velocities, hence a checkerboard test will, strictly speaking, only account for the nonlinearity in the anomaly model, not for the nonlinearity in the true model. Therefore, a better approach would be to use the identical ray set of the original solution and apply only a single iteration (e.g. *Toomey et al.*, 1994).

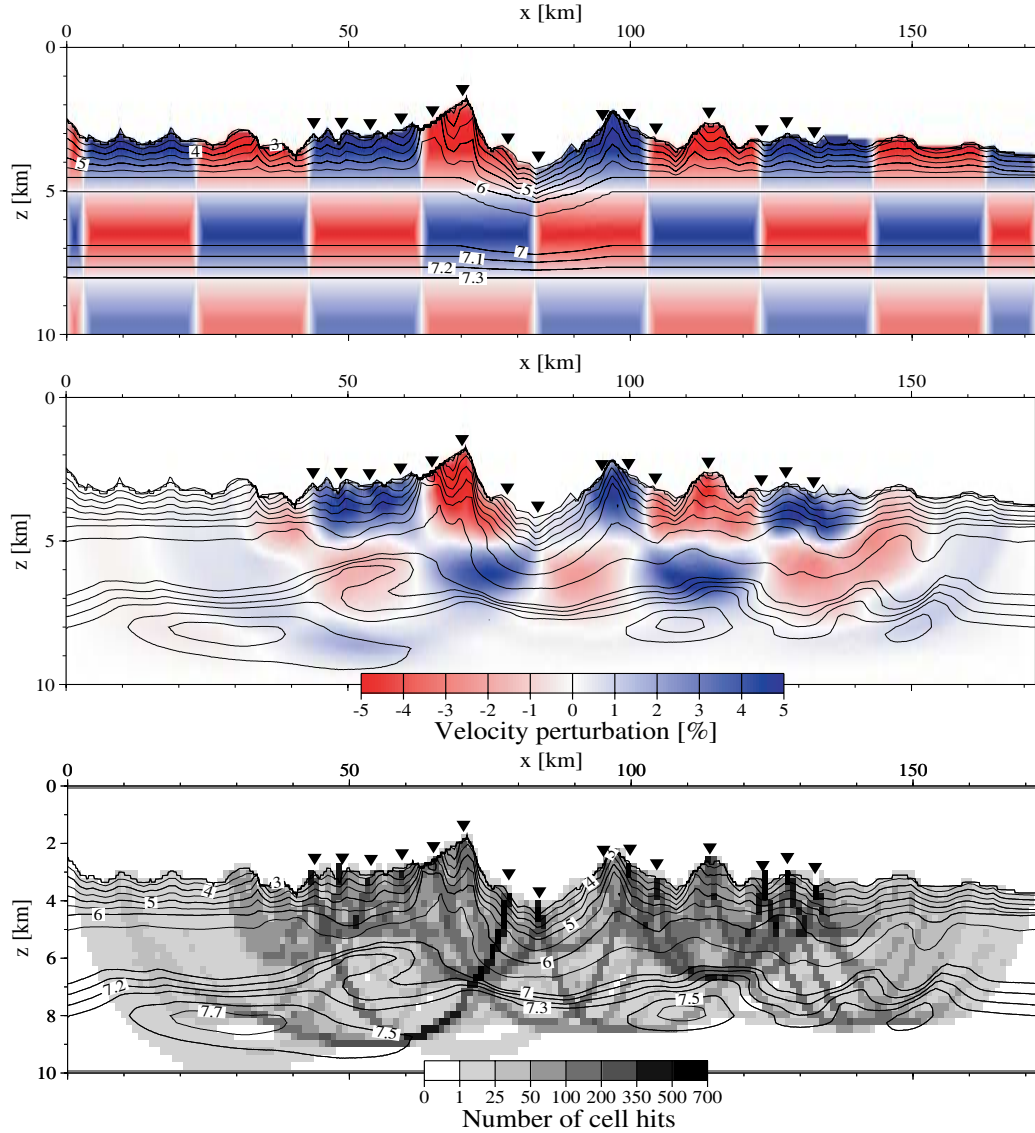


Figure 4.6: *Checkerboard test for Profile 07/08. (Top): Velocity reference model, indicated by velocity isolines and a pattern of alternating positive and negative velocity perturbations. The perturbations cover rectangles of 20km \times 3km size and take values of 5% for the two upper rows and 3% for the lower row. (Center): Recovered anomaly pattern after 8 iterations and iso-velocity lines of the final solution of Profile 07/08 (see text for discussion). (Bottom): Ray coverage for the retrieved anomaly model and iso-velocity lines of the final solution of Profile 07/08. 5 \times vertical exaggeration.*

Since the applied top-to-bottom scheme here already involves a series of previous tomographic steps, the definition of the “starting model” in its original sense is not possible. The same argument is valid for the velocity perturbations between the initial model and the final solution, because some of them are already adopted in the previous model updates. Hence, for the following tests, the reference model is defined as indicated by the iso-velocity lines in figures 4.6 top and 4.7 top. The seafloor velocities are already incorporated from the constrained starting model in order to avoid the emergence of small-scale

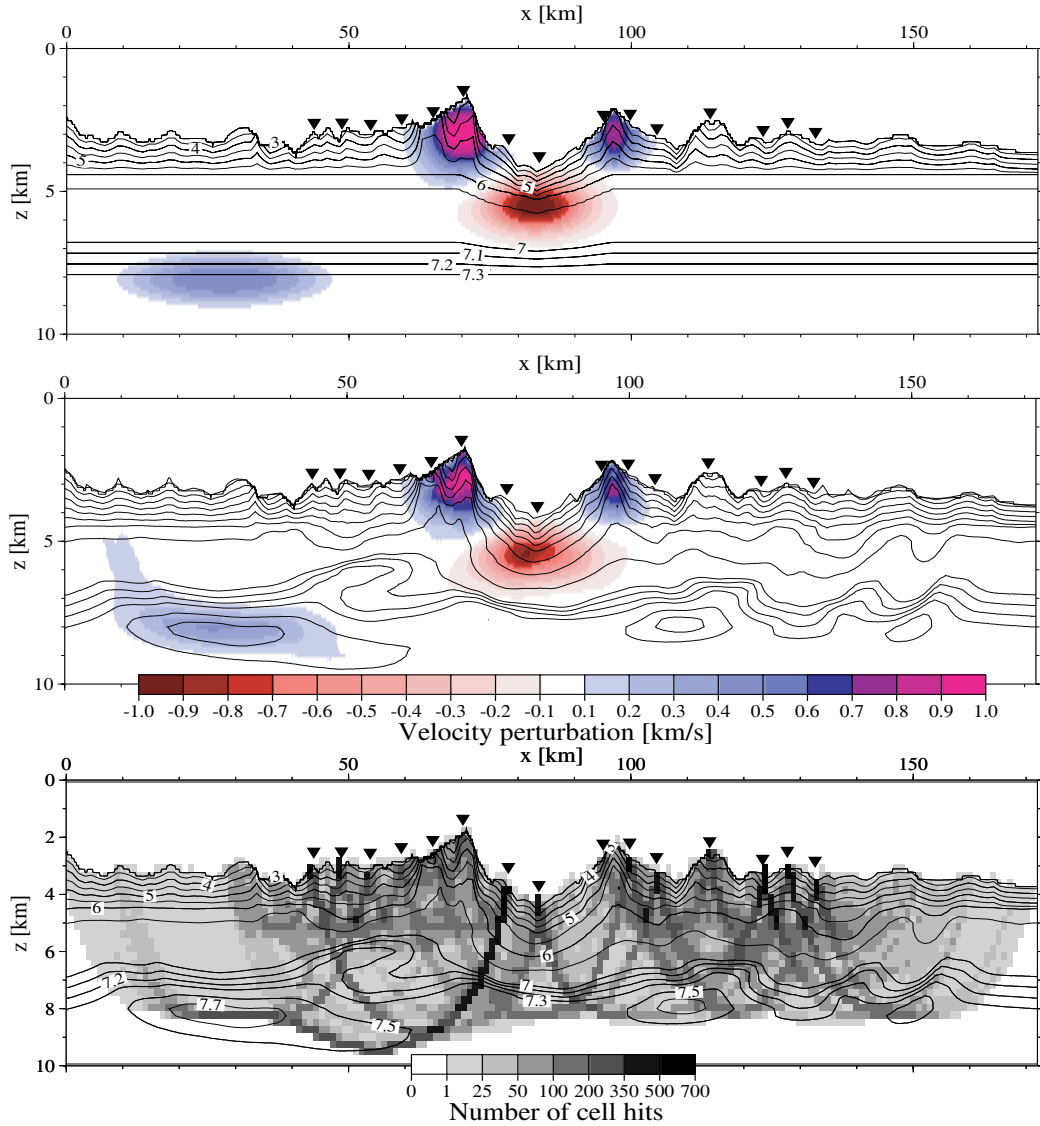


Figure 4.7: *Test with velocity anomalies positioned in key localities of Profile 07/08. (Top): Anomaly pattern with iso-velocity lines of the reference model. (Center): Recovered anomaly pattern after 8 iterations together with iso-velocity lines of the final solution of Profile 07/08. (Bottom): Ray coverage for the retrieved anomaly model together with iso-velocity lines of the final solution of Profile 07/08. 5 \times vertical exaggeration.*

velocity fluctuations in the shallowmost model portions (cf. section 4.4.1). Below, the velocities are linearly interpolated, first between the seafloor and the 6.0 km/s iso-velocity line, and further down between those iso-velocity lines shown in the two figures.

An alternating velocity pattern of 20 km \times 3.0 km rectangular velocity perturbations with an amplitude of 5% (3% in case of the lowermost row, respectively) is superimposed on the above described reference model (cf. figure 4.6 top). Synthetic traveltimes are computed for this model using the same source/receiver geometry as in the real experiment. Gaussian noise with a standard deviation equal to the pick-uncertainty is added to the data, and the resulting traveltimes are then inverted starting from the reference model, in

an attempt to recover the checkerboard pattern.

The retrieved anomaly pattern after 8 iterations is shown for Profile 07/08 in the center part of figure 4.6. The iso-velocity lines of the final tomographic solution (cf. figure 4.15) are plotted for orientation purposes. Within the area of available stations coverage and in the uppermost parts of the model, the recovered velocity pattern resembles the original shape fairly well, and retrieved (maximum) amplitudes reach up to more than 96% for individual checkers. A moderate recovery is regained in the central row with recovered perturbations between 36% and 55% for negative anomalies and up to 90% for the positive anomalies. However, enhanced leakage has blurred the original shapes, especially for the negative anomalies at the edges of available stations coverage. Due to the lack of ray coverage, the test fails to resolve the original pattern in the lowermost parts of the model, but still retrieves some perturbation which in case of the positive anomaly near kilometer 50 results in respectable 62% amplitude recovery. Beyond the instrument locations the limits of resolution do not reach up to the dimensions of the checkerboard pattern. In fact, this is even true for regions with significant ray coverage (cf. figure 4.6 bottom), but this does not necessarily have to apply for a different setting of anomalies, as it is shown in the next synthetic test.

This test is used to reconstruct distinct synthetic anomalies that are positioned in key locations of Profile 07/08. Regions of high geological interest are e.g. the crustal structure at shallower levels beneath the inside corner high compared to corresponding areas beneath the outside corner or the median valley. For the determination of mantle velocities, a reliable velocity model is also needed for certain deeper levels at greater offsets. Using the same reference model as in the previous test, a pattern of four distinct synthetic anomalies is used to simulate those perturbations observed in the real experiment. The original perturbations reveal different shapes and sizes, and amplitudes reach up to ± 1.0 km/s beneath the inside corner high and the median valley, 0.8 km/s beneath the outside corner and 0.5 km/s for those areas, which presumably sample the upper mantle (cf. figure 4.7 top). Following the same procedure as in the previous test, an anomaly pattern is retrieved after 8 iterations which pretty much resembles the original perturbation. For the shallower anomalies, almost 100% recovery of the maximum amplitude is achieved for the positive perturbations, and still 92% can be retrieved in case of the negative one beneath the median valley (cf. figure 4.7 center). Respectable 83% recovery for the deep anomaly with only minor leakage indicates that a positive perturbation in this area gathers sufficient ray coverage to become at least partially resolvable.

The success in retrieving a synthetic anomaly pattern suggests that a similar structure can be resolved in the real experiment. Hence, it can be inferred from the foregoing tests that within the area of available stations coverage, the tomographic solution is sensitive to even small velocity perturbations of less than 5% at least in the upper layers of the model. In case of significant velocity perturbations, the resolvable length scales are in the order of ~ 10 km at certain key locations. Beyond the stations and at greater depths, the small-scale structure, especially if of alternating type, is barely resolvable and moreover suffers from significant blurring. But the respectable recovery of the deep-lying positive velocity anomaly in both tests suggests that large-scale features are fairly well constrained here.

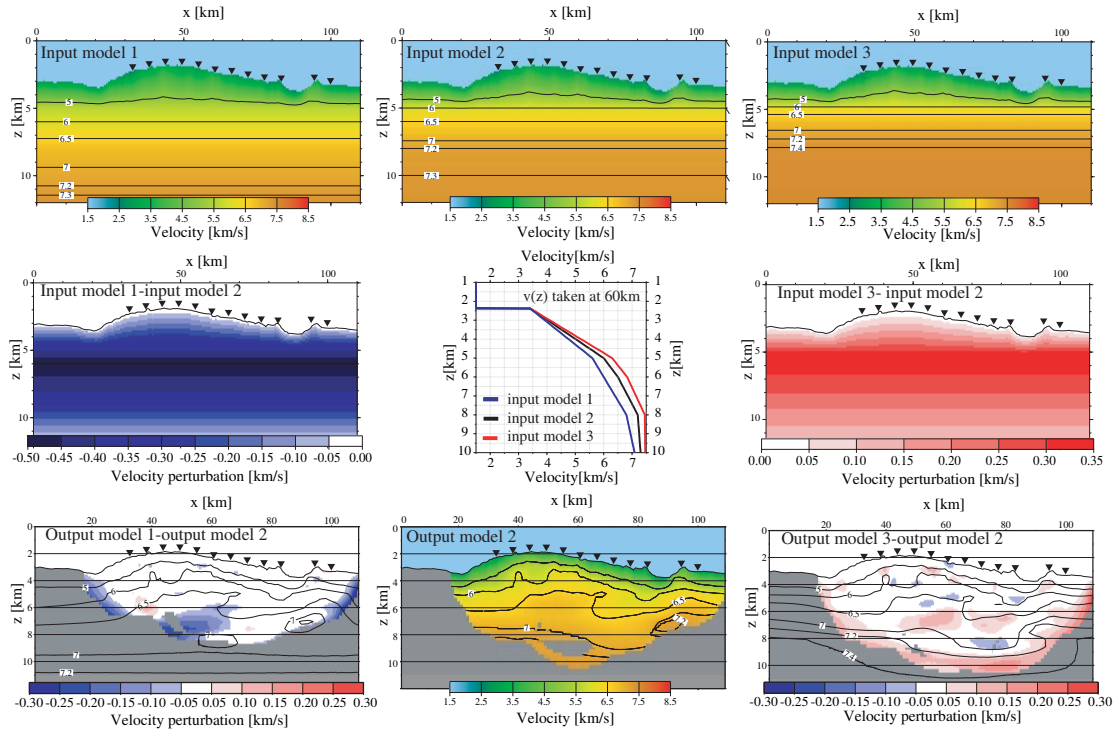


Figure 4.8: *Influence of three different starting models (top) on the tomographic solution of Profile 10. The starting models consist of identical seafloor velocities, but different underlying velocity gradients (center). After 8 iterations, almost identical output models are derived for the central part of Profile 10 (bottom). The contour lines in the final perturbational models are taken from the corresponding output models.*

Impact of different starting models

The top-to-bottom scheme of starting model obtainment described in section 4.4.1 avoids the problem of model non-uniqueness usually associated with the use of different starting models. However, an elaborate examination regarding the impact of different starting models upon the tomographic solution is done for all profiles using the joint refraction and reflection tomography, and corresponding results are presented in section 5.6. In case of the first-arrival tomography, a compromise is made in evaluating the effect of three different starting models, which exhibit identical seafloor velocities, but different underlying velocity gradients (cf. figure 4.8).

Taking up 8 iterations, the different output models reveal almost identical features in the central part of Profile 10. Furthermore, all results closely resemble the final tomographic solution presented in figure 4.9 in the following section, although revealing slightly more structure in case of the three models shown here. This close similarity indicates that the tomographic algorithm is robust and produces stable results in the way it is applied here. However, at the edges of available ray coverage, the impact of the starting model is still visible. Due to the small amount of available rays, and in order to produce a smooth solution, these areas experienced smaller model updates resulting in a significant bias towards the initial model. Besides, the same phenomenon can explain the different depth

penetrations of the final models as being biased by the initially different velocity gradients (a higher velocity gradient results in a deeper ray penetration, and vice versa).

4.4.3 Features of the models

The final results of the first-arrival tomography are presented in figure 4.9 for the ridge-parallel profiles and in figure 4.15 for the ridge-perpendicular profiles. The models are plotted at the same scale ($5\times$ vertical exaggeration) and centered with respect to the transform fault (TF) or the median valley (MV), respectively. Velocity contours are drawn every 0.5 km/s and additionally, between 7.0 km/s and 7.3 km/s, every 0.1 km/s. The same contour spacing and colour table are used for all final tomography models in the following chapters.

A first step in evaluating the quality of a tomographic image is to examine the distribution of seismic ray paths. In this case, a summation over all rays that hit an individual cell of the inverse grid results in a “ray hit count” for the entire model. As expected, the number of ray hits is greater directly beneath the seismic stations because rays usually travel almost vertical the uppermost few hundred meters to the stations. Other factors that can lead to a focusing of ray paths are changes in the vertical velocity gradient, often related to distinct structural boundaries like the intra-crustal boundary (layer 2/layer 3) or the crust/mantle boundary (Moho). In these cases, a greater ray hit count is the result of rays that turn at these depths and travel horizontally for a significant distance (cf. Profile 10 in figure 4.9). A locally higher value of ray coverage does not necessarily imply an increase in spatial resolution. For example, a nonuniform (only vertical incidence, virtually no turning rays) and unevenly (rather sparse coverage between individual stations) distributed coverage will hamper the spatial partitioning of a model perturbation into neighboring grid cells along the rays in the uppermost hundreds of meters. However, it can be inferred from figures 4.4 and 4.6 that the resolved regions reach up to depths of 4-8 km below seafloor, with the best resolved areas usually lying at depths of 2-3 km where most of the crustal rays turn.

Profile 10

Profile 10 runs in a ridge-parallel direction and crosses the active transform near kilometer 87 (cf. figure 4.9). On the northern segment, it covers ~ 0.8 Ma crust (calculated assuming symmetric spreading of 16 mm/a half spreading-rate) which now forms a part of the rift mountains. At its southern tip, it penetrates into ~ 4.3 Ma crust of the southern segment. The P-wave velocity structure of Profile 10 is obtained from the tomographic inversion of 8000 first arrivals. For the final model, the residual traveltimes between the observed and the predicted arrivals yield a RMS of 46 ms. An inspection of the contour map of Profile 10 reveals a relatively undisturbed velocity field for the whole resolvable profile and depth range. The pronounced short-wavelength ridge-parallel morphology of the rift mountains (cf. figure 2.2) as well as the significant seafloor relief do not seem to percolate into depth and result in major lateral velocity heterogeneities here, probably due to the ridge-parallel strike of the profile. The northern segment is characterised by seafloor velocities of 3.0-3.4 km/s, which decrease slightly to values of ~ 2.7 km/s at the

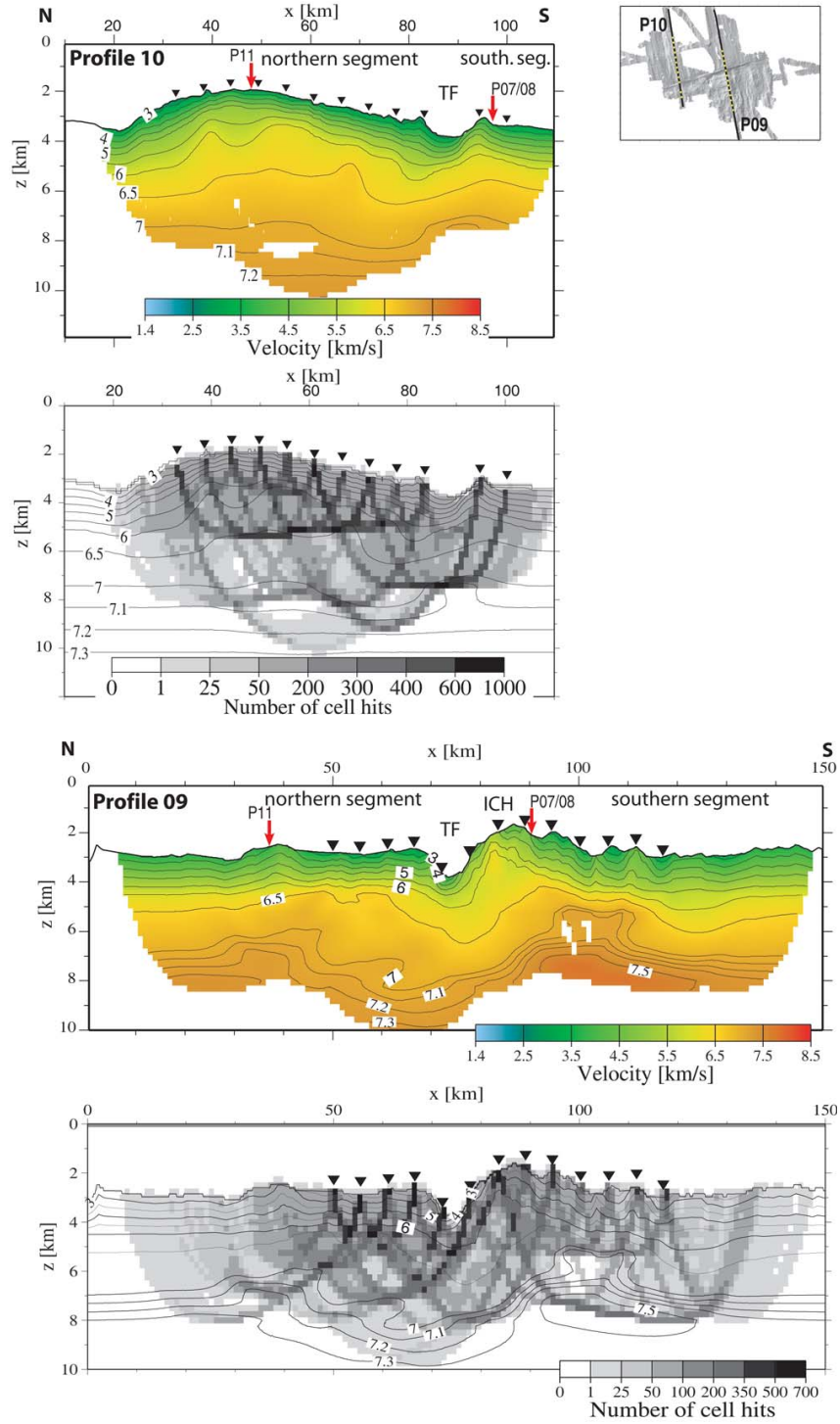


Figure 4.9: Final velocity models for the ridge-parallel Profiles 10 and 09 together with corresponding ray hit count. Models are plotted centered with respect to the transform fault (TF) at the same scale ($5\times$ vertical exaggeration). Final RMS values are 46 ms for Profile 10 and 56 ms for Profile 09. ICH=inside corner high.

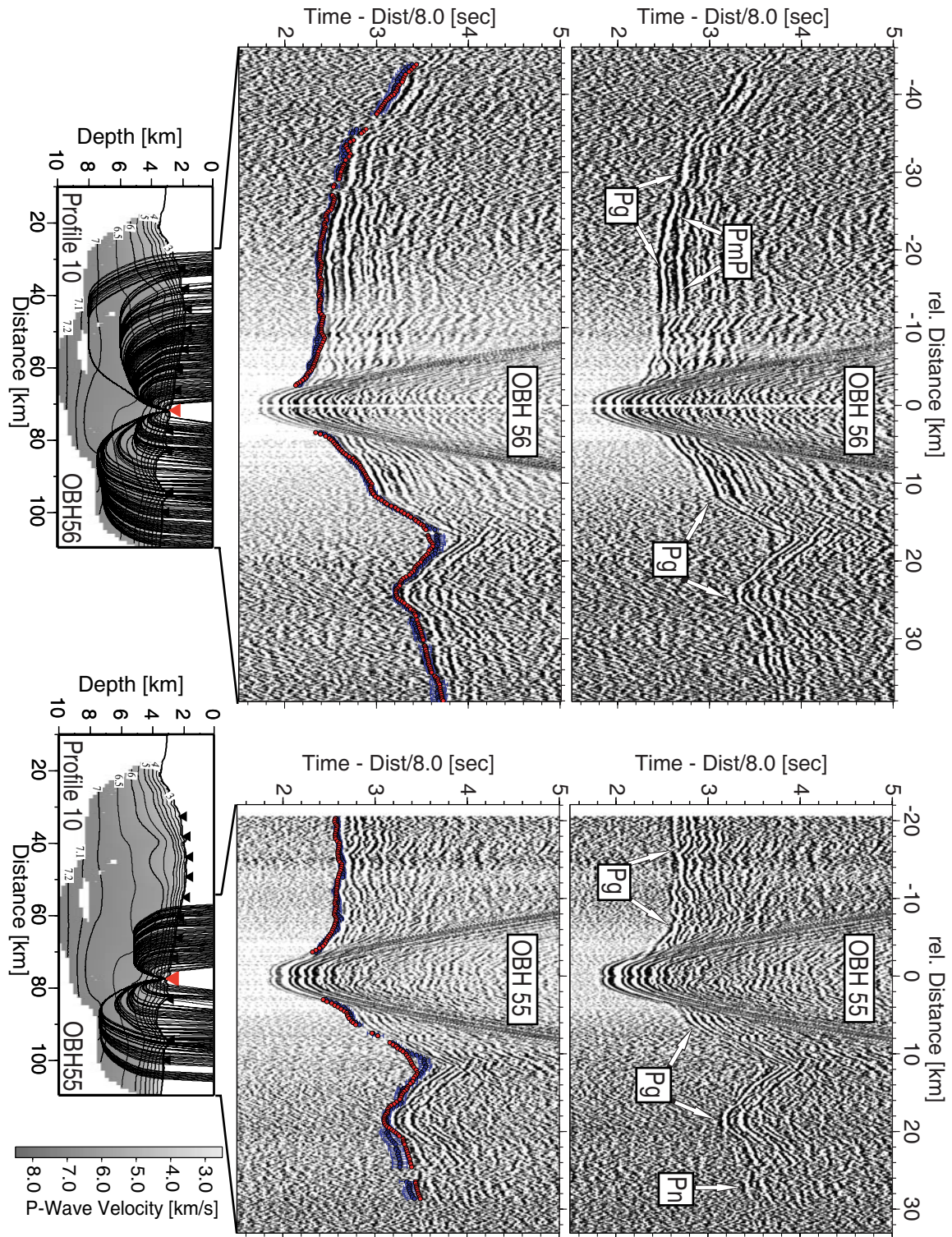


Figure 4.10: *Seismic record sections of Profile 10. See caption on next page for details.*

northern wall of the transform. In the uppermost 1.5-2.0 km, velocities increase to values of 5.7-6.0 km/s. Below, velocities rise more gently towards maximum values of ~ 7.2 km/s. The high-gradient upper portion of the crust does not show much variations along the profile. Only the southern wall of the transform is characterised by elevated upper crustal velocities starting with seafloor velocities >4.0 km/s. Since this positive anomaly is consistently present in all output models (cf. figures 4.4 and 4.8), it seems to be a stable feature of the tomographic solution.

The dominant portion of the resolved velocity structure (up to 85% near kilometer 60) is characterised by seismic velocities >6.0 km/s and vertical gradients of $\sim 0.2 \text{ s}^{-1}$, which is typical of an oceanic layer 3 in young (i.e. immature) oceanic crust (e.g. *White et al.*, 1992). Towards the transform, this portion is reduced to $<60\%$ within the resolvable depth range. A closer look at the profile intersection with line 11, which lies in a region that is well sampled by seismic rays, reveals a very good agreement of both tomographic solutions with no sign of anisotropy (cf. figure 4.11 a).

In the central part of the northern segment, lower crustal velocities reach up to maximum values >7.2 km/s in depths of ~ 7.5 km bsf although the previous synthetic test reveals some influence of the starting model in this region (cf. figure 4.8). Beneath the transform fault, perhaps slightly shifted towards the southern segment, maximum velocities reach up to comparable magnitude within depths of only ~ 3.5 km. Here, velocities >7.2 km/s are also postulated by the three solutions derived with the different starting models in figure 4.8. Figure 4.10 shows the seismic record sections of OBH55 and OBH56, which both constrain the high-velocity region beneath the transform. In the following chapters, all seismic record sections are reduced with 8 km/s and plotted at the same scale. Interpreted seismic phases are labeled *Pg* for rays turning within the crust, *Pn* for rays turning in the uppermost mantle or the mantle transition zone, and *PmP* for secondary arrivals (that are actually not included in the tomographic inversion here but used later for the joint inversion), marking reflections in the crust-mantle boundary or the top of the mantle transition zone, respectively. The term mantle transition zone is used in this study to allow for the fact that observed seismic velocities of 7.3-7.7 km/s are too low to represent normal peridotitic mantle and too high to be consistent with a gabbro sequence. The top of this layer is treated as a first-order discontinuity and referred to as Moho, and corresponding reflections from this discontinuity are referred to as *PmP*.

In the center part of the figure, the calculated traveltimes are shown together with the associated pick-uncertainties. The corresponding ray paths are presented in the lower part. For clarity, every third ray and traveltime is shown. Both stations reveal an excellent fit to the observed data over most offsets. The seismic record of OBH55 exhibits a phase, which

Figure 4.10: **(Previous page)** *Seismic record section (reduced to 8 km/s) of OBH55 and OBH56. (Top): Interpreted seismic phases. (Center): Computed traveltimes and associated pick-uncertainties. Interpreted seismic arrivals are labeled: Pg (turning rays within the crust), PmP (reflected rays at the Moho), and Pn (turning rays in the upper mantle). (Bottom): Corresponding ray paths through the final tomographic solution of Profile 10. Velocity contours are annotated in km/s. Only every third ray and traveltime is shown.*

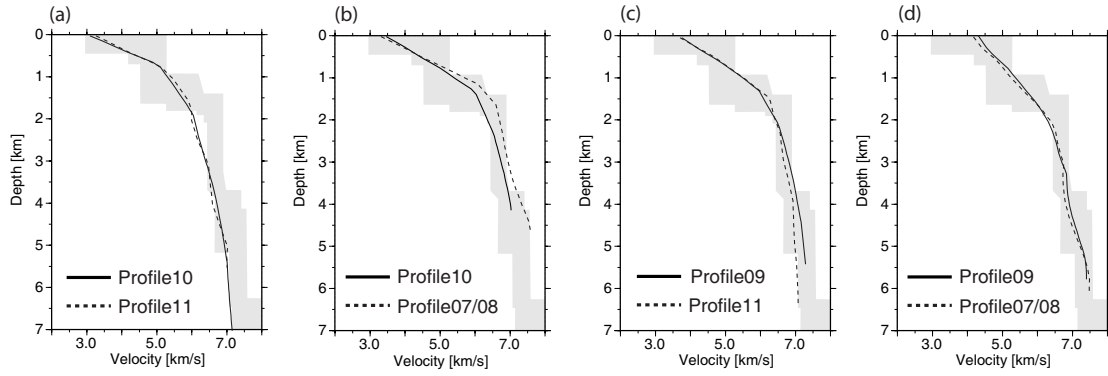


Figure 4.11: *Velocity-depth profiles at the profile intersections. Shaded backgrounds show, for reference purposes, the compilation of profiles in 1-7 Ma Atlantic crust of White et al. (1992). Depth is labeled below seafloor. (a): Intersection of Profiles 10 and 11 (~ 0.8 Ma crust). (b): Intersection of Profiles 10 and 07/08 (~ 4.3 Ma crust). (c): Intersection of Profiles 09 and 11 (~ 4.1 Ma crust). (d): Intersection of Profiles 09 and 07/08 (~ 0.9 Ma crust). Note that (b) and (c) are located beyond the area of available station distribution.*

is interpreted as P_n based on the observation that it runs slightly faster than the P_g , which becomes the secondary arrival. Negative traveltime residuals of ~ 80 ms here indicate that the obtained velocities (7.1 - 7.2 km/s) likely represent a lower limit. Interestingly, seismic phases of OBH56 that sample the same region show no clear phase-change and reveal a good fit to the observed data. Recapitulating, this suggests perhaps slightly higher velocities, but for sure a greater structural complexity of the transition zone between the northern and the southern segment, just as it is illustrated by the tomographic solution of figure 4.9. In the profile intersection immediately south of the transform, corresponding velocities of Profile 07/08 also predict higher values (cf. figure 4.11 b). Even though in case of Profile 07/08 the crossing point is far outside the region of available stations coverage, the resolution test in figure 4.7 comprises a good recovery for a deep-lying high-velocity anomaly with some leakage into the overlying structure. A possible leakage could also contribute to the higher velocities observed at mid-crustal depths in case of Profile 07/08 in figure 4.11 b.

Profile 09

Approximately 50 km to the east, Profile 09 runs almost parallel to Profile 10. Divided by the active transform fault, it covers roughly 75 km of both the northern and the southern segment. The crust of its northern part is ~ 4.1 Ma old and, unlike the younger crust of Profile 10, shows no rise of seafloor depths towards the segment center and furthermore exhibits slightly less ridge-parallel morphology. Its ~ 0.9 Ma old southern part is mainly occupied by the inside corner high core complex, which rises from the bottom of the transform fault more than 2100 m within less than 13 km and extends roughly up to kilometer 100. Further south, the regional morphology is somewhat more subdued but still shows considerable relief.

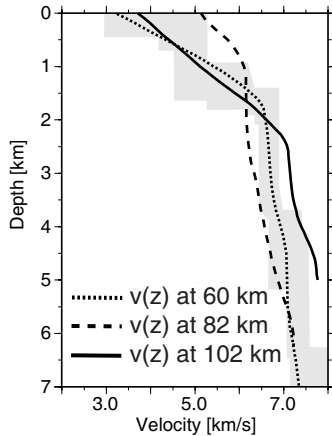


Figure 4.12: Velocity-depth profiles extracted at specified key locations of Profile 09: “typical” northern segment crust (60km), northern inside corner flank (82km), southern inside corner flank (102km). The velocity profiles are horizontally averaged over 5km and extracted from the model of figure 4.9. Shaded backgrounds show, for reference purposes, the compilation of profiles in 1-7 Ma Atlantic crust of White et al. (1992). Depth is labeled below seafloor. For a discussion, see text.

The final velocity model for Profile 09, which is based on the inversion of 6000 first-arrivals, yields a RMS of 56 ms. The two most prominent features revealed by the contour map of figure 4.9 are the anomalously high velocities in depth <1 km beneath the transform facing flank and in depths of ~ 2.5 -5 km beneath the southern termination of the core complex. A comparison of the velocity-depth profiles extracted in these areas shows that the near-seafloor anomaly beneath the transform facing flank exceeds 1 km/s compared to typical northern segment crust of significant older age (cf. $v(z)$ extracted at 82 km in figure 4.12). The anomaly reaches its greatest extent near kilometer 82 in approximately 5 km distance of the highest point of the core complex. Here, sub-seafloor velocities of ~ 5.5 km/s increase to 6 km/s within depths of 0.8 km. However, the area of elevated near-surface velocities extends far down the flank and approximates the deepest portion of the transform fault. Its extent in depth is mainly restricted to the uppermost 1-1.5 km. Below, profiles yield a ~ 3 km thick volume of velocities of 6-6.5 km/s, characterised by very low velocity gradients of $\sim 0.1 \text{ s}^{-1}$.

Beneath the southern termination of the inside corner high, at depths of 2.5-5 km, the tomographic image in figure 4.9 reveals anomalously high velocities, which stand out 0.5-0.8 km/s from velocities sampled at similar depths immediately north and south of this bulge. From the contour map and the extracted velocity profile in figure 4.12 (the solid line extracted at 102 km) it might be argued that the high-velocity anomaly is subdivided into an upper portion with velocities of 7-7.2 km/s and a lower portion where velocities exhibit significant vertical gradients and reach up to maximum values of 7.7-7.8 km/s. The lateral extent of the upper portion is roughly 15 km, whereas it approximately doubles that value in case of the latter. Although the available Pn phases are of somewhat moderate quality, velocities >7.5 km/s are sampled by a total of 5 stations (OBH39, OBH41-44). Figure 4.13 shows as an example a seismic record section of OBH44, which is situated at the transform facing flank of the core complex and which is used in particular to constrain the emergence of the velocity bulge at greater depths. At offsets >22 km, rays enter the described upper portion of the high-velocity anomaly. Due to the decrease in the vertical velocity gradient, the seismic energy which turns at these depths is less, and hence the signal-to-noise ratio of the recorded data becomes progressively poorer. At offsets >34 km, rays that finally run through the deeper portion of the anomaly and have turned there due to the increased vertical velocity gradient reveal a slightly better overall data quality.

Results of a synthetic reconstruction of comparable velocity perturbations imposed on

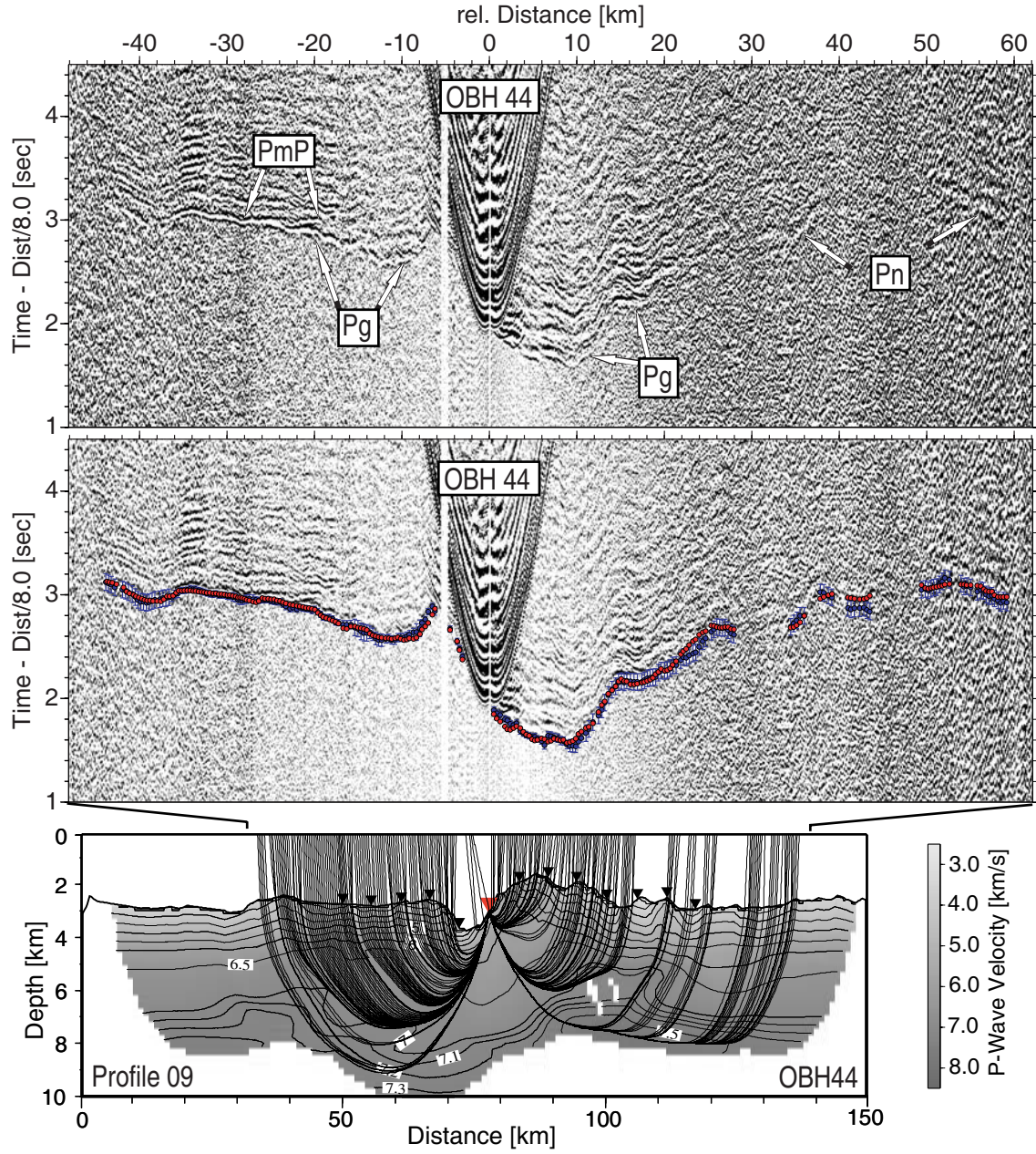


Figure 4.13: *Seismic record section of OBH44, located at the transform facing flank of the core complex on Profile 09. Available seismic phases constrain the velocity structure of the inside corner high and in particular the emergence of the velocity bulge at greater depths. To the north, no Pn is visible, but a clear PmP (not modeled) marks the lower boundary of the crust.*

a simple starting model (cf. section 4.4.2) reveal a good recovery for the different anomalies. In case of the positive near-surface anomaly, more than 90% of the maximum amplitude is regained with a very good match of the original shape (cf. figure 4.14). For the deeper high-velocity perturbation, the amplitude recovery is slightly less, but the reconstruction

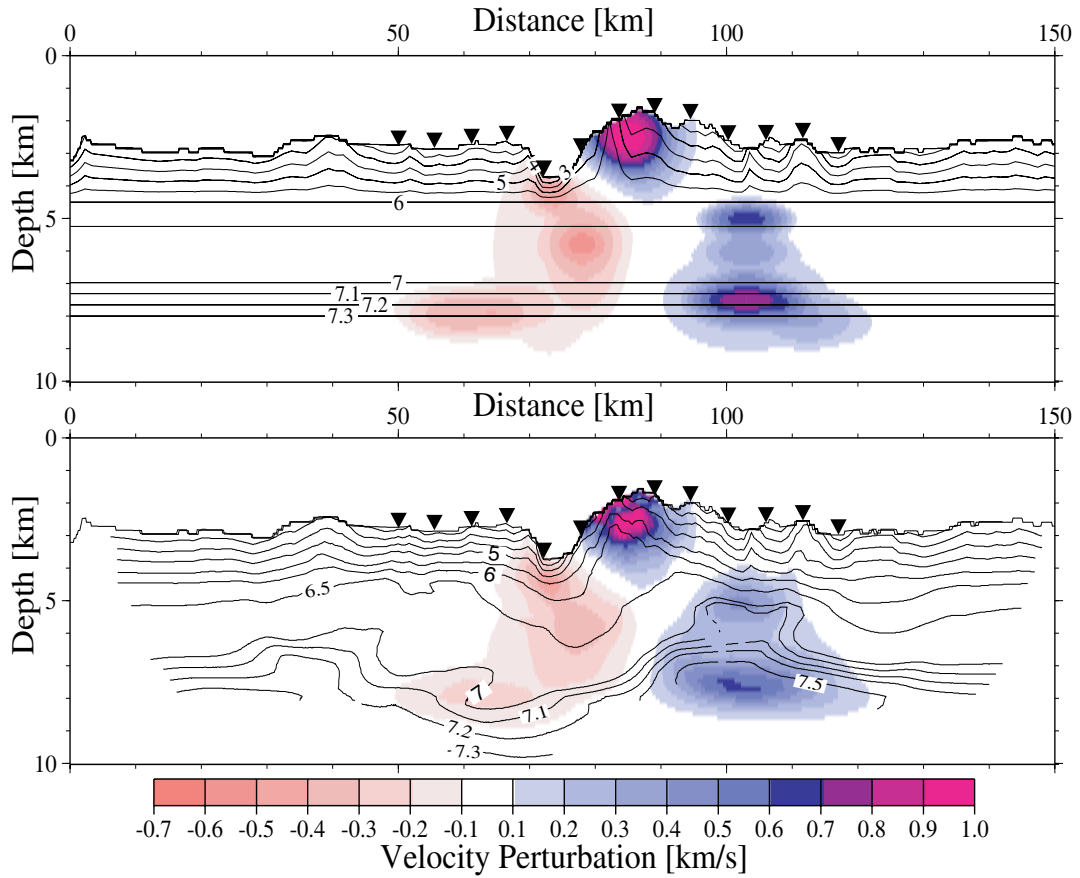


Figure 4.14: *Test with velocity anomalies positioned in key localities of Profile 09. (Top): Anomaly pattern with iso-velocity lines of the reference model. (Center): Recovered anomaly pattern after 8 iterations together with iso-velocity lines of the final solution of Profile 09. (Bottom): Ray coverage for the retrieved anomaly model together with iso-velocity lines of the final solution of Profile 09. 5 \times vertical exaggeration.*

still reveals no significant blurring. There is virtually no interference with the near-surface anomaly and no overlap between the upper and lower portion of the deeper anomaly in particular. The latter is consistent with the predominantly horizontal ray path distribution in this region. However, the test fails to regain the small positive anomaly placed at 6 km depth, which is probably due to fact that candidate rays have been “absorbed” into the adjacent high-velocity anomalies. Hence, the transition from the upper to the lower portion could possibly be obscured by the lack of ray coverage, although the overall structure of the high-velocity anomaly is reliably constrained.

The northern segment is characterised by a relatively uniform upper crust with sub-seafloor velocities of 3-3.6 km/s. Away from the transform and within the area of available stations coverage, velocities reach up to ~ 6.5 km/s within the uppermost 1.5 km. This increase corresponds to average vertical velocity gradients of 0.4 - 0.5 s $^{-1}$. But the major portion of the crust is formed by a pronounced layer3 with velocities of 6.5-7.2 km/s and corresponding vertical gradients of 0.1 - 0.2 s $^{-1}$ (cf. $v(z)$ at 60 km in figure 4.12). Compared

to the younger crust of Profile 10, this suggests an average increase of 0.5 km/s for velocities at the layer2/layer3 boundary, which for both profiles is well constrained due to the accumulation of turning rays (cf. the ray hit count in figure 4.9).

The contrasting pattern of northern segment crust and inside corner crust becomes very apparent in the seismic data. Although OBH44 in figure 4.13 is located on the southern segment, data quality improves significantly for rays that travel through the lower crust of the northern segment. This usually results in greater available offsets and clearer signal onsets, including some high-energy *PmP* reflections at offsets of ~ 20 -30 km. The transform fault marks the locus of transition from the regular crust of the northern segment to the anomalous crust of the inside corner high. From North to South, this is reflected by a change towards higher velocities at shallower depths and towards slightly lower velocities at intermediate depths of the crust. However, in the lowermost crust, velocities again indicate a slight increase. The resolution test in figure 4.14 evaluates the sensibility of the derived tomographic solution in the transition zone. Results demonstrate that the ability to reconstruct the pattern of negative anomalies which are placed at different crustal levels is good. In case of the uppermost perturbation, both the shape and the maximum amplitude is regained. For the deeper anomalies, 65-67% of the original amplitude is recovered with only minor blurring, resulting once again in no overlap of the individual shapes. Thus the anomalous velocities beneath the flank probably do not bias the adjacent velocities of the northern segment, and vice versa.

Profile 11

Profile 11 is located on the northern segment. It runs in spreading direction and crosses the ridge-axis near kilometer 48. Towards the west, it covers seafloor up to an age of ~ 3 Ma and to the east up to an age of ~ 5.25 Ma, respectively. The tomographic solution is based on the inversion of 7800 first-arrivals and has a *RMS* of 57 ms.

The final velocity model is shown in figure 4.15 and reveals, as the most striking feature, a portion of relatively low velocities centered on the spreading axis. Compared to the off-axis crust beneath the rifted flanks, the velocity contrast can exceed 0.8 km/s in depths of 2-2.5 km bsf where most of the crustal rays turn. However, the vertical extent of this negative anomaly reaches throughout the whole sampled depth range. In the median valley, sub-seafloor velocities of 2.6-2.8 km/s reach up to ~ 5 km/s in the uppermost kilometer. Below, the velocity increase becomes progressively slower, resulting in very low velocities in the lower crust ($V_p=6.5$ km/s are not reached until 4.4 km below the seafloor). A region of velocities >6.5 km/s, placed at mid-crustal depths near kilometer 40, is constrained by at least 5 overlying stations and suggests that the anomalously low velocities are restricted to 7-10 km off-axis. Below, the width of the low-velocity portion disperses to the west and exceeds that of the overlying part, resulting in a localized region of negative vertical velocity gradients. Low-velocity zones (LVZ) are known to occur beneath axial magma chambers and have been imaged with tomographic methods beneath the spreading axis on fast-spreading crust (e.g. *Toomey et al.*, 1994). But in this case the LVZ is placed at some distance from the spreading-axis. Because the available ray coverage is poor in the relevant depth (there are virtually no turning rays), this feature could perhaps

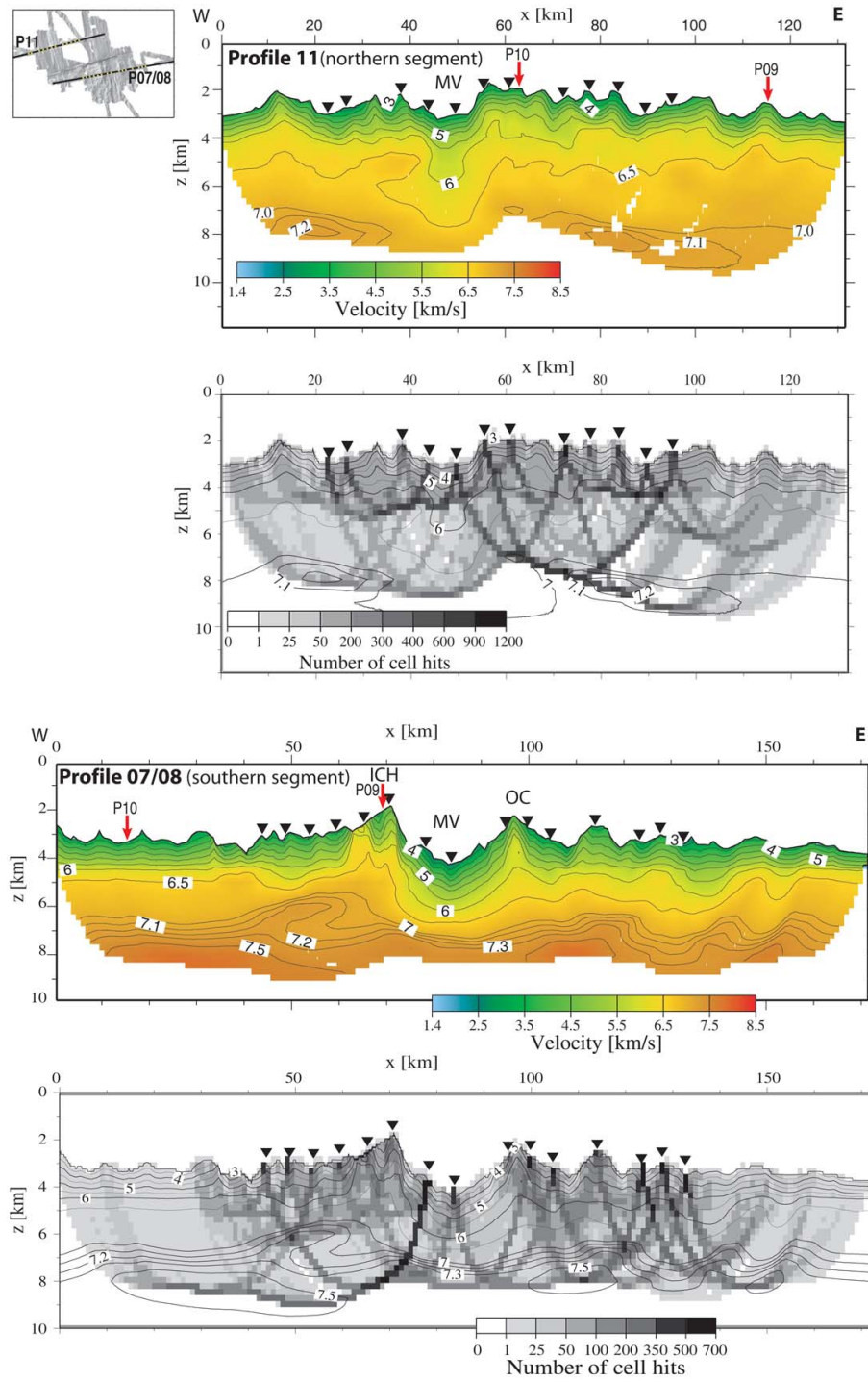


Figure 4.15: *Final velocity models for the ridge-perpendicular Profiles 11 and 07/08 together with corresponding ray hit count. Models are plotted centered with respect to the median valley (MV) at the same scale ($5\times$ vertical exaggeration.). Final RMS values are 57 ms for Profile 11 and 45 ms for Profile 07/08. ICH=inside corner high; OC=outside corner; MV=median valley.*

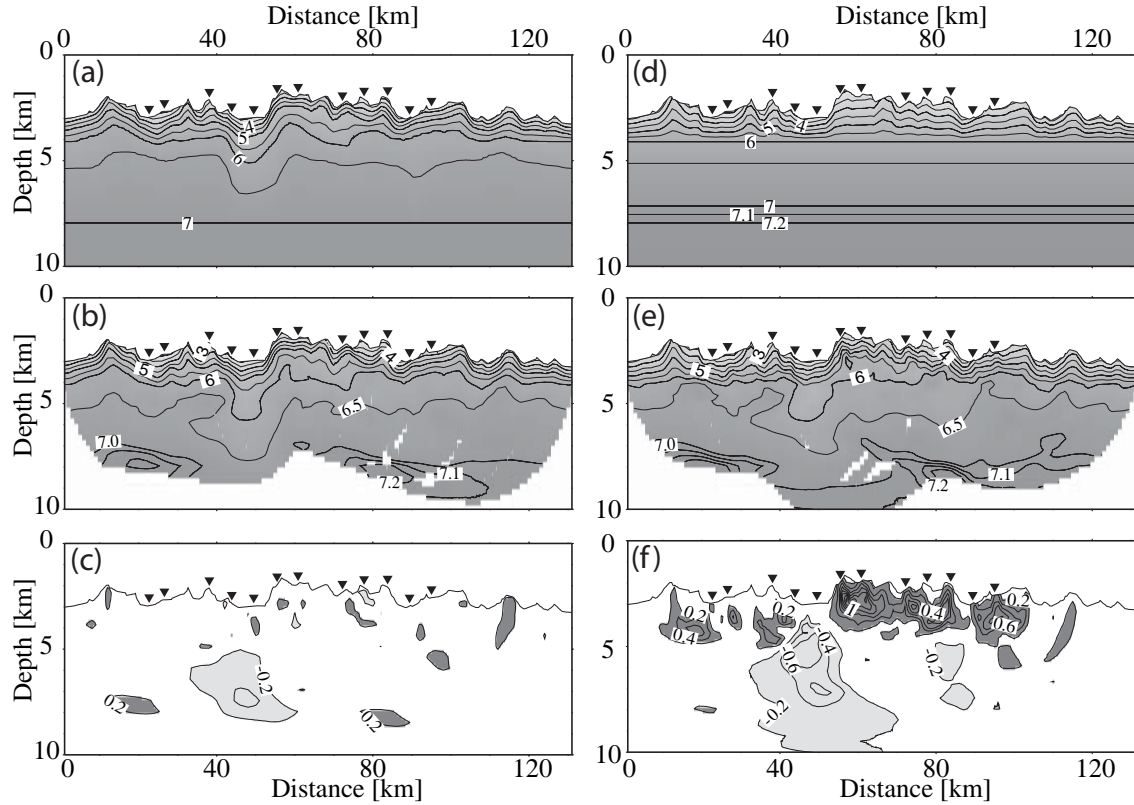


Figure 4.16: *Results (final model and corresponding model perturbation) obtained using different tomographic approaches. (a)-(c): Top-to-bottom approach with (a) the final starting model, (b) the result after 8 iterations (RMS=57 ms), and (c) the corresponding model perturbation resulting from the tomographic inversion. (d)-(f): Simple 2D approach with (d) the starting model (defined in the upper part by linear interpolation between the seafloor velocities from (a) and the flat 6 km/s iso-velocity line, and in the lower part by linear interpolation on the shown contour interval), (e) the result after 8 iterations (RMS=60 ms), and (c) the corresponding model perturbation. Areas with no ray coverage in (b) and (e) are masked. Contour interval and shading for the models are as in figure 4.17 and contour interval for the perturbations is 0.2 km/s. Negative perturbations < -0.2 km/s are lightly shaded and positive perturbations > 0.2 km/s are darkly shaded. Note the similarities of the results in (b) and (e). Perturbations are greater in (f) than in (c) because of the different starting models.*

represent an artefact. However, it is not likely to be affected by a bias in the starting model since several tomographic approaches with different starting models (top-to-bottom as well as simple 2D initial models) produce similar phenomena. The emergence of the LVZ is thus insensitive to uncertainties in the initial model (cf. figure 4.16).

The velocities in the upper crust show consistent variations along the profile, especially within ranges of ~ 25 km from the ridge-axis. At greater distances, an inspection of the contours in figure 4.15 reveals a more subdued pattern, also characterised by on average faster upper crustal velocities. For example, the 6 km/s iso-velocity contour rises from 2.9 km depth below seafloor in the median valley to average values of less than 2 km

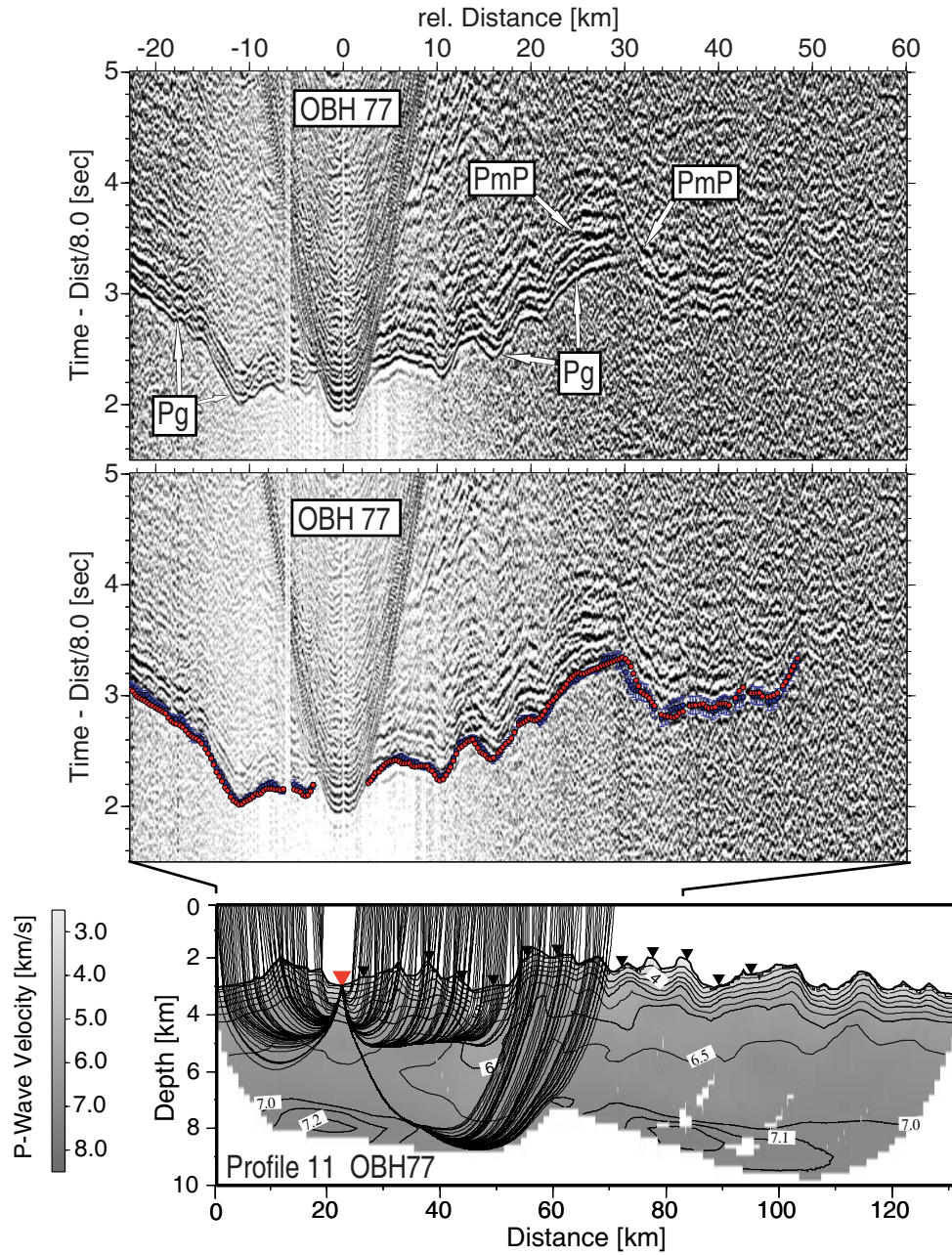


Figure 4.17: *Seismic record section of OBH77, the westernmost station of Profile 11. Available seismic phases constrain the velocity structure of the low-velocity anomaly beneath the spreading-axis. A PmP phase (not modeled) indicates the lower boundary of the crust.*

in the adjacent rift mountains and finally undulates around values of 1-1.5 km, which compares well with the velocities of Profile 09 sampled in the corresponding depths at the line intersection (cf. figure 4.11 c). For the deeper layers, a similar increase of average velocities with distance (i.e. age) from the spreading axis is discernible. But the exact geometry, or rather if the rise occurs gradually or rather abruptly, as it is indicated by the

6.5 km/s iso-velocity contour, has to be considered as less certain here due the reduced ray coverage which results in a significant dispersion of the recovered velocity perturbations along the (few) available ray paths. However, velocities of 7.2 km/s in depths of 5-6 km suggest close-to-normal crustal values (e.g. *White et al.*, 1992) at distances of 25-35 km from the axis.

Figure 4.17 shows the seismic record section of OBH77, which among others is used to constrain the extent of the low-velocity anomaly centered at mid-crustal depths beneath the median valley. Furthermore, it illustrates the impact of this anomalous structure on the available seismic phases. The very good data quality at closer offsets abruptly worsens near 30 km because corresponding rays have followed a very different path around this feature. But even for stations that are located in closer proximity to the ridge-axis, the locus of the anomaly is associated with enhanced absorption of the seismic energy and often represents the limit of available seismic offsets. On the other hand, a number of rather strong *PmP* phases comprises additional constraints for the joint refraction and reflection tomography.

Profile 07/08

Profile 07/08 is located on oceanic crust which is created at the inside and outside corner of the southern segment. The line runs ridge-perpendicular, i.e. $\sim 6^\circ$ oblique to the transform fault, and crosses the current rift-axis near 83 km. Assuming symmetric spreading at a half-rate of 16 mm/a, it covers the region from ~ 5.2 Ma old crust in the west to ~ 5.6 Ma old crust in the east. The tomographic solution, which is presented in figure 4.15, is based on the inversion of 6550 first-arrivals and reveals a *RMS* of 45 ms.

The resolved velocity structure of Profile 07/08 differs significantly from the results obtained for the almost parallel profile, which covers segment-center crust of the northern segment. The inside corner and its adjacent flanks are characterised by strongly varying lateral seafloor velocities of 3.7-5.7 km/s, which in case of the western flank rise up to 6 km/s in the uppermost few hundred meters. The opposite outside corner reveals slightly lower seafloor velocities of 3-4 km/s which rise up to 6 km/s in 2-2.5 km depth. The suspect pattern of strong heterogeneities sampled at the inside corner deserves a closer examination. Its principal emergence is proven to be independent of the starting model and it is furthermore constrained by the forward modelling. In case of the tomography, a possible influence of a too coarse grid-spacing in the region of extreme topography can be ruled out since calculations on higher-resolution grids result in even more pronounced heterogeneities. Furthermore it is shown in the next chapter that comparable results are achieved with a completely different velocity parameterization (i.e. with a “hanging mesh”). A closer look at the bathymetry in that particular area reveals (cf. figures 2.2 and 2.6) that the relevant sector is placed exactly on a profile-parallel flank of a pronounced scarp which seems to separate the entire core complex into a northern and southern portion. In particular, some ship tracks exhibit locally greater water depths in the region between the high-velocity extremes which suggests a possible artefact in case of the decreased velocities due to the assumptions of two-dimensionality. In this context, the response of the adjacent velocities would be an increase in order to compensate for this loss.

The synthetic resolution test in figures 4.7 reveals another possible impact on the tomographic solution of Profile 07/08. For the inversion, the strongly heterogeneous seafloor velocities are already incorporated in the starting model in order to avoid velocity fluctuations (“ringing” - see above) in the shallowmost portion of the crust. However, the recovered anomaly pattern allows for the strongly varying ray distribution, in that the positive perturbations are recovered best directly beneath the stations but perhaps also due to bending of candidate ray paths around the (in total) lower velocities in between. Summing up, there might be some interference in the uppermost hundreds of meters, which are barely resolvable due to near vertical ray paths, and the lower velocities in between could perhaps be an artefact of the strictly two-dimensional model structure. The latter is also documented by a tendency towards higher velocities in the shallowmost crust for Profile 09 at the line intersection (cf. figure 4.11 d).

In the median valley, seafloor velocities of 2.5-2.7 km/s that rise up to 5 km/s in the uppermost 1-1.5 km closely resemble the corresponding values of the northern segment. But below, the resolved velocity structure differs fundamentally from its northern counterpart. The underlying portion of the crust is characterised by virtually no major decrease in the velocity gradient, resulting in the presence of velocities >7.4 km/s in depths of 4 km beneath the ridge-axis and the adjacent flank of the inside corner and in depths of 4.5 km beneath the opposite flank of the outside corner, respectively. P-wave velocities typical of layer 3 (6.5-7.2 km/s) are restricted to a small portion of ~ 1 km thickness. Corresponding velocity gradients are totally absent. Further east, at ~ 25 km distance from the spreading-axis, velocities reach up to 7.7-7.8 km/s at comparable depths. However, at the profile intersection with line 09 (cf. figure 4.11 d) and beneath the western flank of the core complex, 0.3-0.5 km/s reduced velocities indicate an asymmetric model.

Figure 4.18 shows the seismic record section of OBH04 which is placed on the median valley floor and governs almost the complete range of shots generated on Profile 07 (Profile 07/08 was constructed by merging together two overlapping individual seismic lines - Profile 07 and Profile 08). Available seismic phases reach up to maximum offsets of 80 km and are used in particular to constrain the velocity structure of the uppermost mantle. At closer offsets the phases are dominated by the extreme topography of the inside-outside corner pair. For offsets >44 km to the west, corresponding rays sample a pronounced portion of velocities >7.5 km/s located at depths of ~ 4.5 km and beyond the area of available stations coverage. Except for OBH04, this anomaly is constrained by 4 more stations (OBH17, 18, 20, 21) over a considerable distance and reveals maximum velocities of 7.7-7.8 km/s. This type of anomaly is the subject of a synthetic resolution test (cf. figure 4.7) and corresponding results suggest that its occurrence is reliable although perhaps not fully developed in the model.

In summary, the results of the first-arrival tomographic inversion demonstrate that the covered oceanic crust of the northern segment is characterised by a regular upper crust and a clear transition towards a pronounced layer 3. In places, the results exhibit anomalous velocities, for example in the median valley where very low velocities are observed throughout the whole depth range, or close to the transform fault where velocities >7.2 km/s are placed in depths of ~ 3.5 km. The relatively frequent occurrence of rather strong *PmP* phases promises additional information from the following joint refraction and reflection tomography.

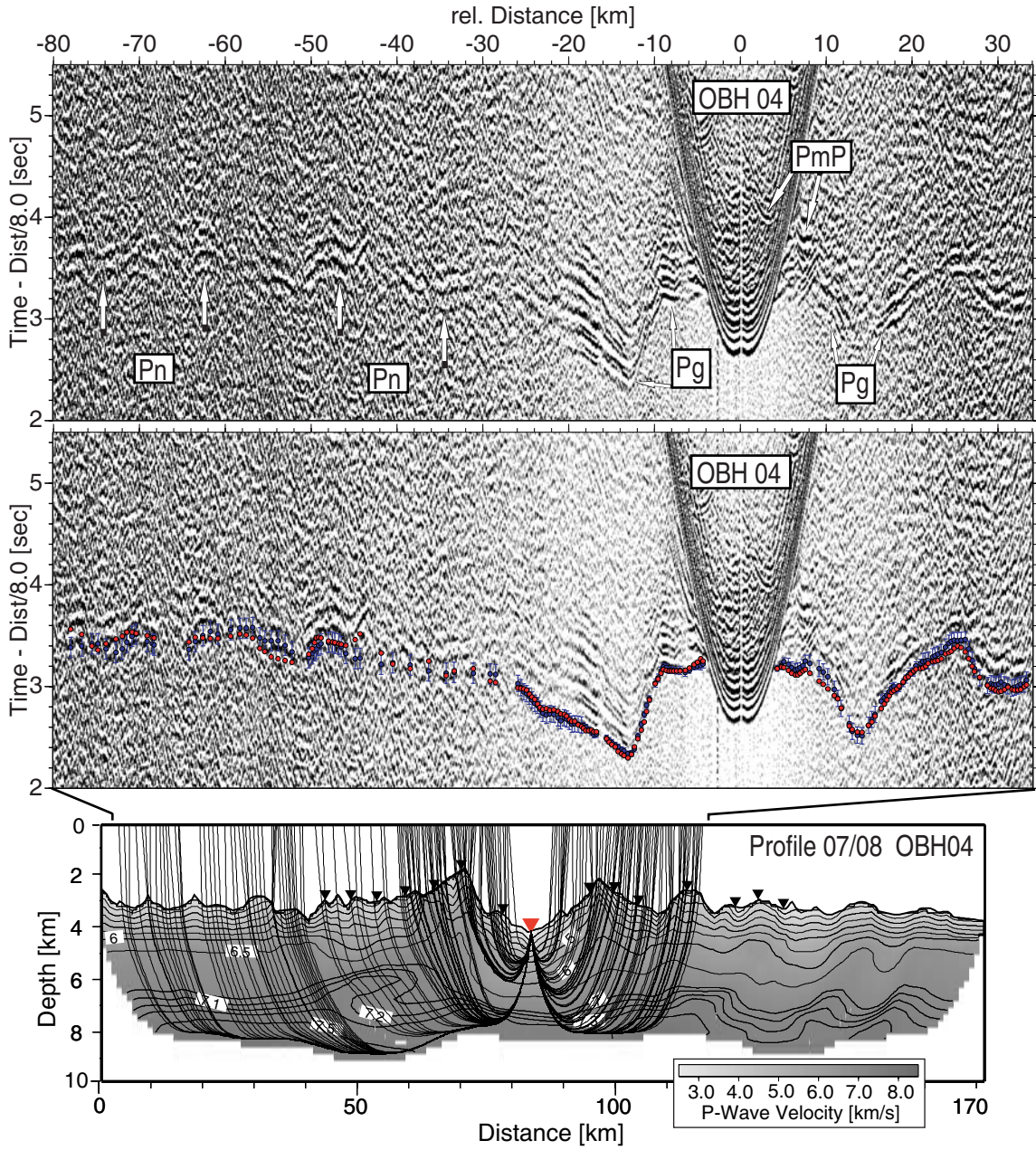


Figure 4.18: *Seismic record section of OBH04, which is located in the median valley of Profile 07/08. Available seismic phases reach up to maximum offsets of 80km and are used in particular to constrain the velocity structure of the uppermost mantle.*

For the southern segment, derived models suggest a completely different geological setting. Upper crustal velocities reveal strong lateral heterogeneities accompanied with anomalously high seafloor velocities, in particular beneath the flanks of the inside corner high. Almost uniform velocity gradients in the median valley suggest a thin or virtually absent layer 3. A well constrained pattern of velocities 7.3-7.8 km/s is indicative of a mantle transition zone at depths of 3.5-5 km. The character of this feature will be the subject of particular interest in the next chapter, because the inclusion of *PmP* phases,

although rather of moderate quality in these regions, will pose additional constraints on its geometry.

Chapter 5

Joint refraction and reflection tomography

5.1 Model parameterization

The two dimensional velocity model is parameterized as a shared mesh beneath the seafloor (*Korenaga et al.*, 2000). Seafloor topography is explicitly included in the method by vertically sharing the columns of nodes to follow local seafloor relief (cf. figure 5.1). Unlike in the finite-difference parameterization, grid node spacing can vary both in the horizontal and vertical dimensions. Bilinear interpolation is used in each parallel shaped grid cell, resulting in a smooth velocity field between different cells. Grid node spacing is the same for forward calculations and for the inverse step. Thus, the mesh must be fine enough to account for an accurate forward theoretical result (cf. section 5.2.3). It should be finer than the expected velocity variations caused by the spatial limits of structural features not to introduce any bias to the tomographic velocity solution. For the steep vertical and lateral velocity gradients that typify mid-ocean ridge structure a nodal spacing in the order of hundreds of meters or less is necessary (e.g. *Toomey et al.*, 1994; *Van Avendonk*, 1998). The use of an irregular grid provides the ability to arrange a dense sampling in areas of large topographic relief or in regions where a dense ray coverage comprises a higher spatial resolution. On the other hand, it is possible to increase the grid size with depth or in areas of sparse ray coverage at the edges of the model to effectively use available computational resources (cf. figure 5.4).

A reflector is represented as an array of linear segments whose nodal spacing is completely variable and independent of that used in the velocity grid (*Korenaga et al.*, 2000). The horizontal coordinate of each segment is held constant, whereas its vertical value is updated in the inverse solution. Although a velocity discontinuity at the reflector is fundamental for the generation of reflected phases, this is not explicitly treated in the modelling. Instead, a “floating reflector” approach is used to update reflector depths freely without changing adjacent velocity nodes (*Korenaga et al.*, 2000). Disregarding smoothing constraints, this means that e.g. Pn rays are needed to update sub-Moho velocity nodes.

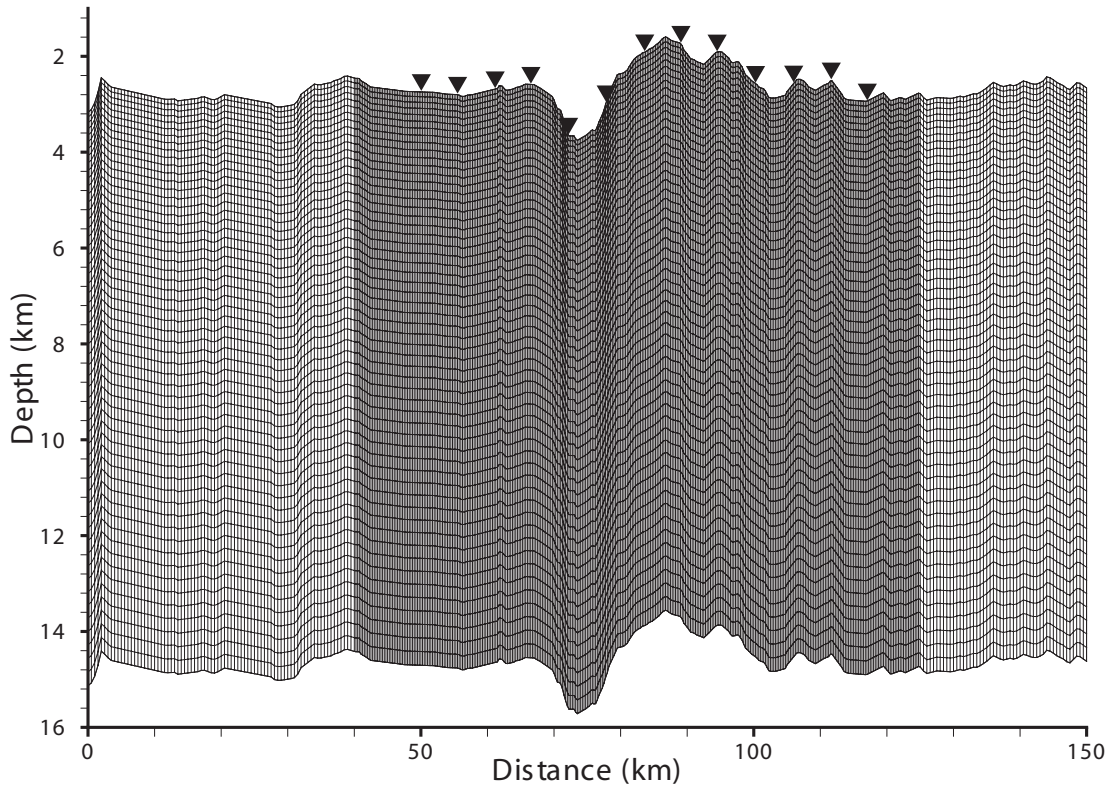


Figure 5.1: *Irregular grid parameterized as a shared mesh beneath the seafloor (here shown for Profile 09). It consists of 471×57 parallelogram-shaped grid cells of variable size.*

5.2 Forward method

The TOMO2D code (Korenaga, 2000) utilizes a hybrid ray tracing scheme based on the shortest path method (or graph method) (Moser, 1991) and the ray bending method, similar to the one developed by Papazachos and Nolet (1997) and Van Avendonk (1998). The method is efficient both in terms of computational resources and memory requirements.

5.2.1 Shortest path method (SPM)

The SPM is a technique that originated in network theory and was first applied to seismic ray tracing calculations by Nakanishi and Yamaguchi (1986). Like the finite-difference scheme described in the previous chapter, the SPM tracks the propagation path of the whole wavefront. It is based on Fermat's minimum traveltime principle for seismic ray paths and on algorithms which have been developed for the calculation of shortest paths between nodes in a network. Ray paths of minimum traveltime emanating from a point source are found by straight line connections to all the nodes surrounding the source. From Huygens' principle, it is clear that the neighboring nodes can be treated as scattering sources. The velocity model is sampled at the node location, and is bilinearly interpolated between them. Each connection is given a weight equal to the traveltime of a seismic wave along it. The weight is computed as the numerically integrated slowness along this straight line. The shortest path between two points follows those connections

for which the sum of the weights is smallest and, according to Fermat's principle, is an approximation of the seismic ray between the two points. In the more general case where the source point or the receiver point are not coincident with a node location, a simple extrapolation procedure is used to find the correct traveltime.

By forcing seismic ray paths to follow the connections of a network, one introduces errors in the ray geometry and in the traveltime along the ray. Ray paths usually travel zig-zag in homogeneous or smooth velocity zones, resulting in longer ray paths and higher traveltimes (*Moser, 1991; Fischer and Lees, 1993*). This often leads to a systematic over-prediction of seismic velocities. Hence, the error in traveltime and ray geometry depends upon the number of nodes and the number of connections per node (*Moser, 1991*). Errors are worst in propagation directions which are poorly covered by available connections (e.g. *Van Avendonk et al., 2001*). Therefore, *Korenaga et al. (2000)* utilized a forward star, originally introduced by *Moser et al. (1992b)*, to obtain a good coverage of search directions for available ray paths. Figure 5.2a shows the lower right quadrant of a mixed fifth/tenth order forward star that is used for the shortest path method within this study. The use of a higher order forward star as well as a denser sampling of grid nodes provides a better solution but requires extra computation time. For crustal velocity models, where the vertical velocity gradient usually dominates the horizontal gradient, a star that preferentially searches the downward direction has shown favorable characteristics with respect to an isotropic star with the same number of nodes (*Van Avendonk et al., 2001*). Furthermore, *Zhang and Toksöz (1998)* and *Fischer and Lees (1993)* showed that an elaborate choice of nodes and search directions can improve efficiency and reduces the error for refraction traveltimes by nearly 50%. In this study, the results of the SPM within the hybrid algorithm only serve as an initial guess for subsequent ray bending refinements. Therefore, ray paths and traveltimes should be close enough to the true ones to ensure that the ray bending technique will not fail to converge to a global minimum traveltime path. Moreover, iterating the ray bending method from a poor SPM solution proves to be slower and makes the hybrid ray tracer less efficient (*Van Avendonk et al., 2001*). In our case, we use a mixed fifth/tenth order forward star, identical to the one used by *Korenaga et al. (2000)* and similar to the 3×7 forward star used by *Van Avendonk et al. (2001)* who both worked on refraction datasets with somewhat comparable geometries.

One drawback of the shortest path algorithm in its simplest form is that only global minima are found. Later arrivals, such as multiples and reflections which do not travel along the shortest path, are not detected. It is therefore necessary to formulate constraints on the shortest paths so that a specific set of nodes which lie on an interface has to be visited. In the applied method of *Korenaga et al. (2000)*, a constrained shortest path algorithm of *Moser (1991)* is used to handle interfaces. In a first step, all shortest paths from a source node to all other nodes are calculated. The traveltimes of the nodes on the interface are then selected, and the SPM is reinitialized from these nodes that act now as secondary sources. The resulting traveltimes are the traveltimes of shortest paths that are constrained to visit the interface node set (*Moser, 1991*).

Because the water column is outside the sheared mesh, the graph algorithm would be incomplete without the connection of the shot location within the water layer and the seafloor node or receiver. Given the traveltime field from a shot to all nodal points on the seafloor, the minimum time path is found by searching over all possible paths connecting

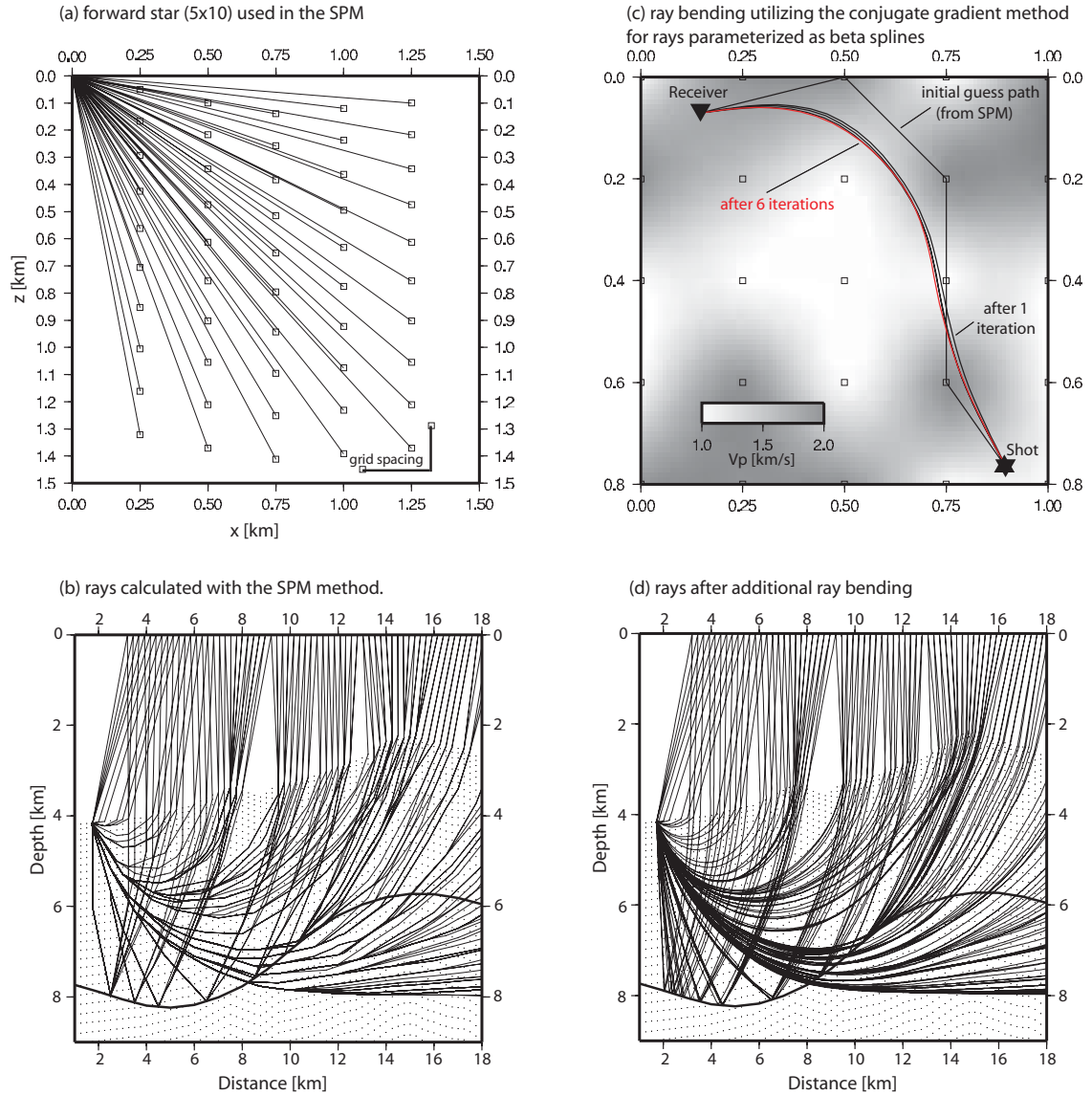


Figure 5.2: *Hybrid forward algorithm. (a): Forward star used in the shortest path method with no vertical exaggaration. (b): Rays calculated with the SPM. The background model is a part of the tomographic output for Profile 07/08. (c): Bending with conjugate gradients from an initial guess path in a complicated medium, with velocities smoothly varying from 1.0-2.0 km/s. Traveltimes: initial guess path 0.825996s, after 6 iterations 0.786604s (no analytic solution known). (d): Rays of figure (c) after additional ray bending.*

the two endpoints. By Fermat's principle, the path with the minimum traveltime approximates the seismic ray path and yields the approximate traveltime.

Figure 5.2 b shows a computation geometry of Profile 07/08. An ocean bottom station recorded refracted and reflected phases generated by equally spaced sources close to the sea surface. The corresponding ray paths are calculated with the shortest path method and therefore, must connect between grid nodes. As a result, these paths often show awkward kinks. Clearly, ray bending is required for further refinement.

5.2.2 Ray bending

After computation of the shortest path solution, the ray paths to all shot points are refined with the conjugate gradient ray bending technique of *Moser et al.* (1992a). According to Fermat's principle, the gradient ∇T of the traveltime T vanishes for a true seismic ray path with a stationary traveltime. The variation of the traveltime along an initial guess path due to small perturbations in its geometry, for which ∇T is a measure, gives an indication about how to change the path in order to search for a minimum of T . The conjugate gradient method iteratively optimizes the calculated traveltimes of the preliminary path to find the nearest path with a stationary traveltime. A priori, it is by no means clear whether the resulting path is a global or only a local minimum. Therefore, an initial path close to the global minimum has to be provided by the preceding SPM in order to allow ray bending to focus on the right minimum in traveltimes. However, the bending algorithm can not diverge, because each non-zero gradient results in a lesser amount of traveltime. In practice, small round-off errors in the differentiation process can prevent the algorithm to find a stationary path. To account for this, the iteration process is stopped, if the traveltime reduction over an iteration falls below a specified threshold value.

The bending method used in the TOMO2D code uses a conjugate gradient search where rays are parameterized as beta-splines. This approach avoids inaccuracies in concave slowness regions (low velocity zones) and results in a considerably higher accuracy and efficiency. After the SPM, the ray is defined by a number of points (grid nodes) connected with straight line segments ("polygonal paths"). Considering the behaviour of two nodes with a concave slowness region in between, the integral over the linear interpolated slowness, as a measure of traveltime predicted by the bending algorithm, would systematically underestimate the exact traveltime which is an integral over the real slowness. This means that a minimization algorithm which is simply based on "polygonal paths" would always exclude points from this low velocity region, as a consequence resulting in a completely wrong ray path and traveltime (*Moser et al.*, 1992a). A possible solution to this problem is the use of a different discretization method, e.g. to use a parameterization, where the spacing of points is adapted to variations in the velocity gradient (e.g. *Van Avendonk et al.*, 2001). However, this often requires extra computation time, whereas interpolation results in a considerably saving of time, as it is shown by *Moser et al.* (1992a). The above mentioned interpolation with beta-splines is especially efficient for ray bending, because a huge variety of curves can be expressed by a relatively small number of control points. The number of points to be perturbed within the conjugate gradient search can be much smaller than the number of points to be integrated over, i.e. compared to the "polygonal paths", the minimization can be done much more efficiently with the same accuracy, or much more accurate with the same computational effort. In the presence of discontinuities, the beta-spline curve representation is modified in that a constrained conjugate gradient search is used. Similar to the constrained SPM described above, the location parameters of a point of the ray are forced to lie on the interface.

Figure 5.2 c demonstrates bending with conjugate gradients from an initial guess path of six points in a complicated medium, with velocities smoothly varying between 1.0 km/s and 2.0 km/s. Ray bending resulted in a smooth ray path and reduced the traveltime from 0.825996 s to 0.786604 s within six iterations, using a tolerance level of 10^{-6} s. Therefore,

ray bending has markedly improved the ray path and traveltime calculation, as it is also shown in figure 5.2 d for a realistic model of Profile 07/08.

5.2.3 Performance in a realistic model

To assess the accuracy for a realistic model geometry where no analytical solution is available, a solution produced by the hybrid ray tracing routine is taken as a reference using a very fine grid of $\sim 2.64 \cdot 10^7$ nodes and a 10×25 order forward star. Compared to the velocity mesh of figure 5.1, this means that grid node spacing is reduced by a factor of 10, both for the horizontal and vertical direction. The forward calculation on the reference model takes approximately 55 hours on a computer with an AMD Opteron Processor 848 (2200 MHz CPU, 8Gb RAM) and has to be regarded as very accurate, so that the difference from calculations on a rougher grid (respectively lower order forward star) can be fully ascribed to the inaccuracies introduced by the coarser parameterization.

In figure 5.3, the reference solution is compared to a forward calculation that is performed on the grid shown in figure 5.1 using a fifth/tenth order forward star. For a detailed description of the different grids and search directions, see figure 5.4. Each ray is compared by two error measures with respect to the reference solution: deviation in traveltime and ray path misfit (dissimilarity). Ray dissimilarity is calculated similar to *Korenaga et al.* (2000) by:

$$\sqrt{\sum_{n=1}^{100} \frac{|p_n - q_n|^2}{100}},$$

where p_n and q_n are points along the two rays with ray path lengths equal to $\frac{n}{100}$ of the full ray path length.

As a background model for computations, a tomographic solution of Profile 09 is used. This model is slightly modified within the mantle to account for a wide range of possible variations of the crust-mantle transition and mantle structure, respectively. In the North, a velocity jump of 0.3-0.6 km/s (depending on the velocities of the lower crust) to 7.6 km/s is introduced at the Moho, whereas in the South, beneath the Moho-bulge, a more gradual change in mantle velocities from 7.4-7.6 km/s over 1.6 km depth is adopted. The resulting model has to be regarded as representative for the study area at 5° S; it combines variations in crustal and mantle velocity structure, crustal thickness and topographic seafloor relief. Sources are distributed every 750 m over the whole range of the profile. Refracted rays are constructed for a receiver gather where the instrument is positioned at the seafloor near kilometer 66 on the profile. Within profile coordinates 25 km and 95 km, additional rays are forced to reflect at the Moho. As for the velocity structure, the synthetic shot-receiver geometry resembles the true conditions fairly close, with maximum available offsets of ~ 80 km in the real seismic data.

Because the seafloor topography is explicitly included in the velocity mesh, a coarse model parameterization results in a poor sampling of seafloor relief. Taking into account the large seismic velocity contrast between water and sub-seafloor, which can reach values of more than 4.0 km/s, under-sampling of seafloor topography will be a distinct error source for the calculated traveltimes and ray paths. This factor is especially concerning because, within this study, the highest seismic surface velocities often go along with pronounced relief, i.e. unusual high topography, for example at the inside corner high.

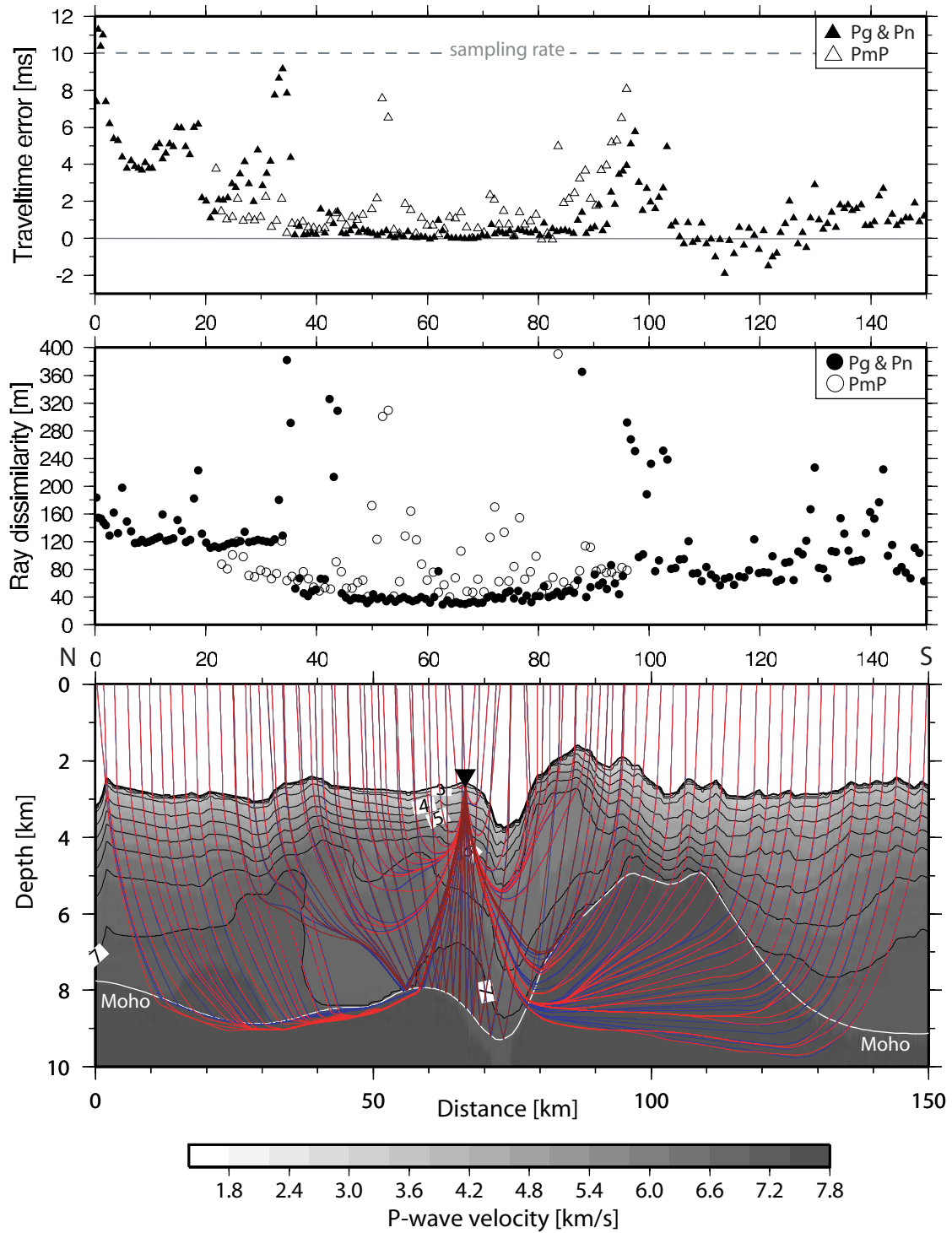


Figure 5.3: Traveltime error and ray dissimilarity due to different grid sizes. (Top): Traveltime error of PmP rays (open triangles) and refracted rays (black triangles). The error averages 1.71ms for PmPs and 1.90ms for refracted rays. (middle): Ray dissimilarity of PmP rays (open circles) and refracted rays (black circles) for each individual ray with respect to its source distance. Average values are 102m for PmPs and 98m for refracted rays. (Bottom): Ray paths for the reference solution (blue; PmP: dark blue) and the calculation on the coarser grid (red; PmP: dark red) together with seismic velocities and the reflector boundary. Only every third ray is shown.

The Moho reflector represents a similar, but due to its smaller velocity contrast probably less distinct error source owing to a coarse model parameterization. However, grid node spacing increases with depth, as do the differences between the coarse and the fine grid. Since the Moho reflector shows considerable relief, introduced traveltimes errors can probably reach up to comparable magnitude.

Results of the comparison of the reference solution and the calculation on the much coarser parameterization show that the hybrid forward algorithm, utilizing a search directions defined as a fifth/tenth order forward star, performs well in terms of accuracy and efficiency for horizontal node spacings of 0.25-0.5 km and vertical node spacings of 0.1-0.25 km (see figure 5.3). Calculation on the coarse grid took only 30 s compared to the 55 h of the reference solution. The traveltimes error averages 1.71 ms for PmP phases and 1.90 ms for refracted rays, which is in the range of $\sim \frac{1}{5}$ of the sampling rate. Maximum errors reach up to values slightly higher than 10 ms for some rays, but still, due to their large offsets, the error is roughly in the order of 0.1 % with respect to their absolute traveltimes. Traveltimes errors seem to accumulate slightly with offset. However, in some areas the above described influence of both the seafloor and the Moho markedly decrease the accuracy, e.g. between 0-34 km and 85-120 km profile distance for Pn rays, which results also in a more scattered distribution of traveltimes errors. Between 50-60 km, larger errors in both traveltimes and ray paths are perhaps related to the sparser coverage of downward-propagation directions, provided by the lower order forward star.

Ray paths are never far from the reference ray paths (102 m average for PmPs and 98 m for refracted rays, respectively). Some correlation of ray path misfit to traveltimes error is visible in terms of that large misfits result in distinct time differences for individual rays. However, in certain areas (e.g. between 0-34 km), a larger spread in traveltimes errors coincides with an apparently more focused and constant distribution of ray dissimilarities. Near kilometer 35, a pronounced change in ray dissimilarity of ~ 50 m is visible between rays that turn within shallower layers of the crust and rays that turn within the mantle. This small jump allows for the fact that mantle-turning rays pass through much deeper areas of the model and hence areas of coarser vertical node spacing. A closer look at the sub-Moho region here reveals that Pn rays do not always refract at the discontinuity but at the next lower grid-cell boundary. This is due to the fact that reflector nodes do not necessarily have to coincide with velocity nodes.

The opposite effect, namely that a larger spread in ray path misfit apparently coincides with small errors in traveltimes, is visible near kilometer 42. In this case, probably due to the very small vertical velocity gradient in combination with the sparser forward star, the affected rays followed a very different path, but had a similar traveltimes.

Figure 5.4 sums up the effects of different grid spacings and search directions with respect to the same reference solution. Gray shaded grid sizes mark the accordant solutions of the detailed comparison described above and in figure 5.3. For each computation, the resulting mean traveltimes error, the resulting mean ray dissimilarity and the corresponding total CPU time as well as the SPM-to-bending time ratio is shown. Results demonstrate that the total computation time increases rapidly with the number of grid nodes (note the logarithmic scale at the lower axis of figure 5.4). For the more densely sampled models the relative merit of ray bending is little, whereas for the coarser grids, the hybrid method spends more time on ray bending than on the initial graph method. As shown by *Van*

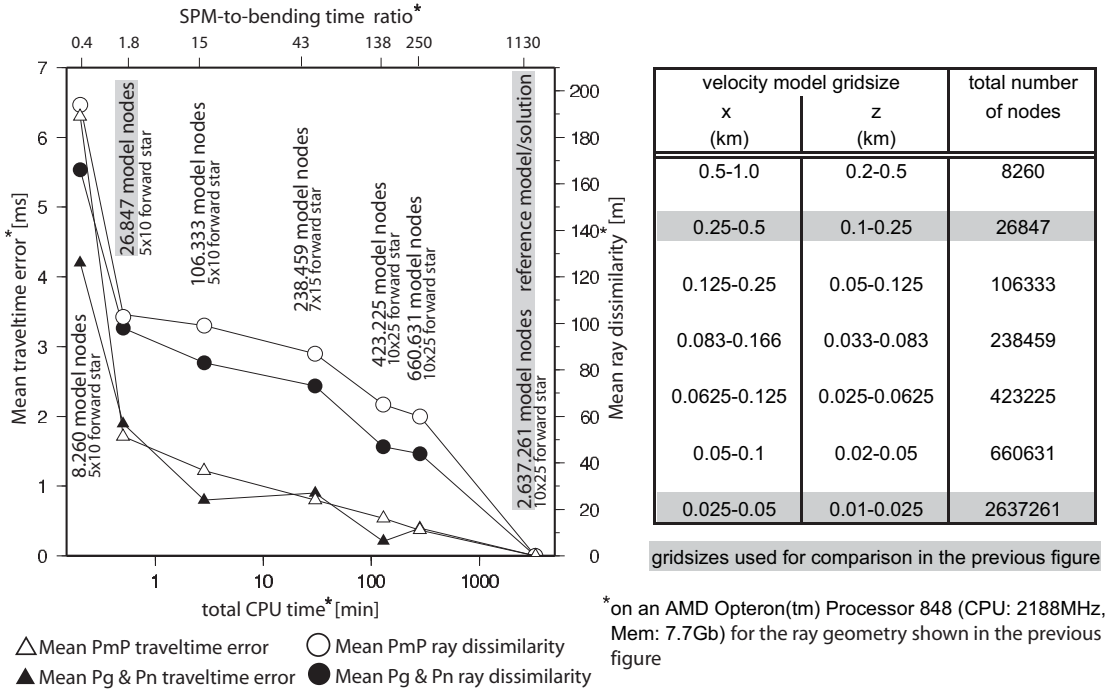


Figure 5.4: Performance of the hybrid forward algorithm for different grid sizes and search directions (Left): Error measures (mean travelttime error, mean ray dissimilarity) and corresponding SPM-to-bending time ratio and total CPU time (note the logarithmic scale) for different grid sizes and search directions. Results are shown for refracted rays (filled symbols) and reflected rays (open symbols), using the same reference solution and model/shot geometry as in figure 5.3. (Right): Corresponding grid parameters for the different solutions.

Avendonk et al. (2001), an efficient mix of SPM and ray bending accounts for roughly equal amounts of computation time. Time spent on the shortest path computation increases rapidly with model volume (number of model nodes), while the time spent on the bending refinement primarily rises with the number of ray paths, and to some degree also depends on the quality of the SPM solution.

For the first two solutions shown in figure 5.4, a relatively large decrease in both travelttime error and ray dissimilarity is obtained with a reasonable increase of computational effort. Using finer grids, the relative improvement becomes poor compared to the disproportional huge increase of CPU time. Interestingly, a more densely sampled grid does not always decrease the mean travelttime error, and additionally sometimes barely changes the mean ray dissimilarity. One possible reason for this could be that rays are traced from slightly different endpoints at the seafloor due to an uneven (horizontal) interpolation of the initial node spacing (second solution), causing slightly longer or shorter rays than their odd counterparts. Some rays might be very well approximated with a certain node spacing, and using a slightly smaller grid size changes the node position in such a way that the ray cannot be approximated as well. This effect may be especially relevant for small (vertical) changes in node placement at the Moho discontinuity and the resulting paths of Pn rays.

As it was shown in the previous chapter, a comparison between rays traced with the finite-difference scheme and the reference solution reveals a mean traveltime misfit of -4.3 ms and a mean ray dissimilarity of 356 m. But rather than being indicative of a systematic over-prediction of the hybrid traveltimes (if so then due to the influence of the SPM method - cf. section 5.2.1), this can be fully due to the difference in model parameterization.

From the foregoing error graphs it is clear that using a limited number of velocity nodes and a lower order forward star introduces inaccuracies in terms of traveltime errors and ray path misfits to the forward solution. Increasing the number of nodes and the amount of available search directions improves the solution somewhat, but finally at the expense of a significant loss of efficiency. However, for all grids of figure 5.4, mean traveltime errors are noticeably smaller than the sampling rate, and except for the coarsest grid individual traveltime errors hardly exceed 10 ms. Ray paths usually approximate the true ray paths fairly well, again with the exception of the coarsest grid of figure 5.4. For the somewhat similar profile geometries (model volume, topographic relief, available picks) of this study, and also to ensure comparability of the different models, a uniform model parameterization is used for the final tomographic approach described in the next section. For all profiles, a horizontal node spacing of 0.25 km is chosen in the central part. At the edges of the models, spacing increases to 0.5 km. Anticipating a loss of seismic resolution with depth, the vertical node spacing linearly increases from 0.1 km at the seafloor to 0.28 km at a depth of 12 km below seafloor (cf. figure 5.1). For possible individual node connections, a fifth/tenth order forward star is used within the shortest path algorithm, and a maximum number of twelve reference points per ray for the beta-spline interpolation, in combination with a tolerance level of 10^{-5} s as stopping criterion, is adopted for the bending refinements.

5.3 Inverse method

For the inverse step, a tomography algorithm of *Korenaga* (2000) is applied to the traveltime data. Similar to the first-arrival tomography described in section 4.3, the method utilizes Fermat's principle to linearize the inversion and applies smoothing and damping constraints to regularize the system of normalized equations. Finally, the linear system of equations is solved using the sparse matrix solver LSQR (*Paige and Saunders*, 1982).

An infinitesimal perturbational model $\delta u(r)$ is linearly related to a traveltime residual δt_j by (cf. section 4.2):

$$\delta t_j = \int_{P_j} \delta u \, dr. \quad (5.1)$$

Similarly, reflection traveltime residuals can be linearly related to slowness perturbations and vertical changes in reflector depths by:

$$\delta t_j = \int_{P_j} \delta u \, dr + \left. \frac{\delta T}{\delta z} \right|_{x=x_j} \delta z(x_j), \quad (5.2)$$

where x_j is the reflecting point of the j th ray.

The residual equations 5.1-5.2 can be discretized and written collectively as a matrix equation

$$d = G \delta m, \quad (5.3)$$

using the same nomenclature as in section 4.3. The partial derivatives with respect to slowness in matrix G are simply the path lengths distributed to relevant velocity nodes. The depth sensitivity part, i.e. the partial derivatives with respect to depth, is given by the incident angle of the ray, the inclination of the reflector and the slowness in the point of reflection as derived by (*Bishop et al.*, 1985). Following the argumentation of section 4.3, the model update vector δm is scaled with the model parameters in the original starting model $\delta m' = C_m^{-1/2} \delta m$, d is scaled with the data covariance matrix $d' = C_d^{-1/2} d$, and the Fréchet derivative matrix is normalized through the relation $G' = C_d^{-1/2} G C_m^{-1/2}$ to avoid a possible solution bias towards a model that is characterised by increased levels of heterogeneity at greater crustal depths (*Toomey et al.*, 1994). The diagonal data covariance matrix C_d contains the *a priori* pick-uncertainties of the rays. To define the pick-uncertainties actually requires knowledge of the statistical distribution of the data errors, including both measurement and theory errors, which is usually not available (e.g. *Tarantola*, 1987). Furthermore, within the linear inversion approach, this knowledge is fundamental for estimating the velocity uncertainties of the tomographic output, precisely the *a posteriori* model variance. Invoking the simplifying assumption of independent, identically distributed Gaussian data errors leads to a practical inversion algorithm, but is somehow unrealistic in the case of hand-picked traveltime data (e.g. *Zhang and Toksöz*, 1998). However, a realistic assessment of model uncertainties is given later (Monte Carlo uncertainty analysis - cf. section 5.6 in this chapter), by inverting a number of random initial models with a number of random datasets, assigning more realistic data errors, and hence the applied Gaussian approach is merely used as an efficient solution finder (*Korenaga et al.*, 2000).

Equation 5.3 is under-determined, hence smoothness constraints need to be applied as additional equations in order to obtain a unique solution. Gaussian smoothing within one decay length is used for each perturbational model parameter in all smoothing matrices (e.g. *Toomey et al.*, 1994). The decay lengths (correlation lengths) are allowed to vary both in the horizontal and vertical direction. Since lateral variations in the Earth's structure are usually much weaker than vertical ones, horizontal smoothing constraints are commonly chosen an order of magnitude bigger than corresponding vertical smoothing constraints, and thus the vertical and horizontal smoothing matrices (labeled C_{Vv} and C_{Hv} in the following) are applied separately (e.g. *Toomey et al.*, 1994; *Van Avendonk et al.*, 1998b; *Korenaga et al.*, 2000). To be consistent with the normalization in the Fréchet matrix, each smoothing equation for an individual model perturbation δm_i is normalized by the slowness of the starting model ${}_o u_i$ (*Toomey et al.*, 1994):

$$\delta m_i {}_o u_i^{-1} = \frac{\sum_{j=1}^m \beta_j \delta m_j {}_o u_i^{-1}}{\sum_{j=1}^m \beta_j}. \quad (5.4)$$

The weights β_j decrease with distance from the i th model parameter in a Gaussian distribution:

$$\beta_j = \exp\left\{-\frac{(x_j - x_i)^2}{\tau_x^2} - \frac{(z_j - z_i)^2}{\tau_z^2}\right\}, \quad (5.5)$$

where τ_x and τ_z act as horizontal and vertical decay lengths (correlation lengths) for the weights β_j to assure that only nodal positions lying within one decay length of the particular model parameter are affected by the spatial smoothing constraints, i.e. are given non-zero weights. However, the horizontal and vertical correlation lengths of velocity variations within the Earth are *a priori* to a large extent unknown, which makes them a somewhat arbitrary, but nonetheless quite effective choice to restrict the possible model space (e.g. *Scales and Snieder, 1997; Toomey et al., 1994; Van Avendonk et al., 1998b; Korenaga et al., 2000*).

Within an iterative approach, the regularization method applied here is “creeping” (*Shaw and Orcutt, 1985*), i.e. all constraints are operative on an individual model perturbation δm_i which is defined with respect to the solution of the previous iteration. So far, the above formulations contain no information about the original starting model, except for the normalization terms. For comparison, the regularization method used in the first-arrival tomography is “jumping” (i.e. with respect to the starting model) and normalization is done using the prior model (cf. section 4.3).

The corresponding forward problem to equation 5.3 in block matrix form can then be written as (*Korenaga et al., 2000*):

$$\begin{pmatrix} d \\ 0 \\ 0 \\ 0 \end{pmatrix} = \begin{pmatrix} G_v & wG_d \\ \lambda_v C_{Hv} & 0 \\ \lambda_v C_{Vv} & 0 \\ 0 & w\lambda_d L_d \end{pmatrix} \begin{pmatrix} \delta m_v \\ \frac{1}{w}\delta m_d \end{pmatrix}, \quad (5.6)$$

where subscripts v and d for the Fréchet matrix and the model vector describe their velocity and depth sensitive components, respectively. λ_v and λ_d are the weights for the slowness and reflector depth perturbations which control the relative importance of the smoothing constraints with respect to the data misfit. C_{Hv} and C_{Vv} are the corresponding normalized smoothing matrices for velocity perturbations and C_d is the analogous smoothing matrix for reflector depth perturbations.

The depth kernel weighting parameter w controls the relative depth sensitivity in the Fréchet matrix. Because of the trade-off between media velocity and reflector depth (the velocity-depth ambiguity; e.g. *Bickel, 1990*) seismic traveltime data possibly exhibit ambiguities that prevent the resolution of a time anomaly into reflector structure and media velocity. Although major effort has been spent to assess the factors that control this unclarity especially for reflection seismic datasets (e.g. *Bickel, 1990; Ross, 1994; Rathor, 1997*), results are still limited to some simplified situations; a unifying theory for realistic model geometries (changes in ray coverage, lateral and vertical velocity perturbations, reflector relief, different shot-receiver geometries) is still missing. However, the existence of this ambiguity is a feature of the geometry of the subsurface and is not caused by the particular inversion algorithm (*Tieman, 1994*); nevertheless, the inversion algorithm can be used to assess its extent in effectively exploring the possible solution space invoking a wide range of values for w as the single controlling parameter (*Korenaga et al., 2000*).

The solution for δ_m in equation 5.6 is computed with the sparse matrix solver LSQR (Paige and Saunders, 1982). If a starting model is far from the final model, calculated ray paths can be far from the true ray paths through the Earth. Model updates become quite large, taking the model update vector outside the region of linearity, i.e. traveltimes are predicted badly and the succeeding iterations could eventually become unstable. In order to remain within the region of linearity, equation 5.6 is augmented with additional damping constraints

$$\begin{pmatrix} d \\ 0 \\ 0 \\ 0 \\ 0 \\ 0 \end{pmatrix} = \begin{pmatrix} G_v & wG_d \\ \lambda_v C_{Hv} & 0 \\ \lambda_v C_{Vv} & 0 \\ 0 & w\lambda_d C_d \\ \alpha_v D_v & 0 \\ 0 & w\alpha_d D_d \end{pmatrix} \begin{pmatrix} \delta m_v \\ \frac{1}{w}\delta m_d \end{pmatrix}, \quad (5.7)$$

where D_v and D_d are the velocity and depth damping matrices which can be derived from a penalty function for the magnitude of model perturbation (cf. Van Avendonk et al., 1998b), and α_v and α_d are the individual weighting parameters which control their particular strength. Additionally, data outliers, i.e. synthetic traveltimes with misfits exceeding a predefined value, can be excluded from each linear inversion step.

Therefore, each inversion step must be small and is controlled by a total of four weighting parameters (two for damping and two for smoothing). After each inversion step, a solution is obtained that is closer to the minimum, but still lies within the limits of linearity. Subsequently, new ray paths and traveltimes are computed with the new model and the inversion is initialized again. A series of these iterative steps can change an initial model dramatically if such a fit is required by the data.

5.4 Parameter adjustment

For all profiles, a laterally varying horizontal node spacing of 250 m in the central part and 500 m at the edges of the models is employed. Vertical node spacing linearly increases from 100 m at the seafloor to 280 m at a depth of 12 km below seafloor. Thus, a higher spatial resolution due to better ray coverage is anticipated for the upper and central parts of the models. Furthermore, increasing velocity node smoothing with depths for both horizontal and vertical correlation lengths is used in order to reduce small-scale model structure at greater depths, which would not be resolvable with the available dataset anyway. To minimize the influence of the *a priori* chosen smoothing length scales on the structural interpretation of geologic features like the transform fault or the ridge axis in the velocity models, vertical and horizontal correlation lengths are not allowed to vary laterally. Additionally, in order to ensure comparability of the derived model structure, the parameterization of smoothing length scales is the same for all profiles. Throughout the modelling, a horizontal correlation length of 1 km at the seafloor increasing linearly to 5 km at the bottom and a vertical correlation length increasing linearly from 0.1 km at the seafloor to 1.0 km at the bottom of each model is used. The above values are chosen on the basis of expected model resolution and a number of previous synthetic resolution tests. Since there is a tradeoff between the chosen correlation lengths and the corresponding

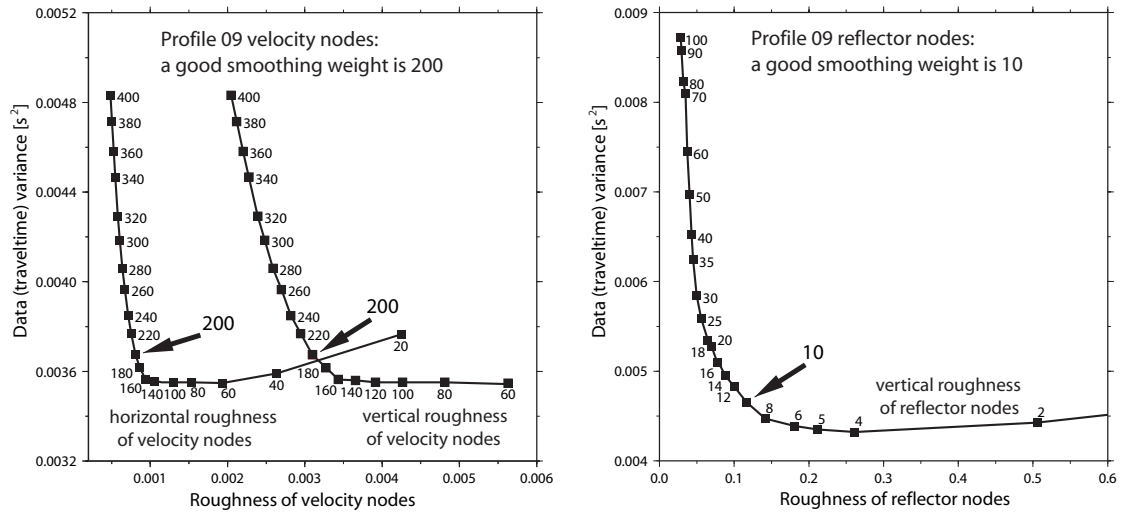


Figure 5.5: *Assessment of smoothing weights for velocity nodes (left) and depth nodes (right), testing different values in a single-step iteration. Here shown for Profile 09.*

smoothing weights in terms that a higher smoothing weight compensates a lower correlation length, but at the same time requires clearly less computational memory during the inverse calculations, the smoothing length scales are chosen rather less conservatively. For reflector nodes, the corresponding smoothing length scales are sampled from the horizontal 2D velocity correlation lengths at the appropriate depths.

Individual smoothing weights for each model are tested using a single-step inversion (cf. figure 5.5) and are later held fixed during all iterations. Appropriate smoothing weights should minimize the roughness of the tomographic output models but at the same time decrease significantly the data variance. Because the roughness is measured without reference to a background model (cf. *Phillips and Fehler, 1991*), this optimum value is not explicitly dependent upon the particular choice of the starting model. If during the later iterations either the refracted traveltimes or the reflected traveltimes converge much faster than the other, the chosen weights for the corresponding nodes are increased to allow for a uniform convergence of the data variances.

To prevent outliers from dominating the data, synthetic traveltimes with a normalized $\chi^2 > 4$ are consequently excluded from each iteration. Throughout all calculations, the number of outliers never exceed 3% for both refracted and reflected traveltimes and usually is less than 1% after the first iteration, indicating a minor role of outliers in this study.

Sweeps on velocity and depth damping weights are done at each iteration to restrict the average perturbation of velocity nodes to maximal 2% and the average perturbation of reflector nodes to maximal 6%. With increasing number of iterations, model updates become smaller, and hence damping is not required anymore. Depending on the chosen starting model, damping is stopped after 1-3 iterations.

5.5 Results of the joint tomography - Profile 09

In the following two sections, a detailed description of the applied modelling strategy is presented. It is shown how the final tomographic results are derived and how the stability of the solution is assessed under different sets of starting models and noise. For clarity and consistency, the corresponding calculations and figures are all taken from Profile 09, which can be regarded as a representative example because it covers both kinds of segments. The results for the other profiles are presented in chapter 6.

A starting model is constructed for Profile 09 from the final velocity solution of the first-arrival tomography. For this purpose, Gauss filtering is used with spatially varying window size taken from the 2D velocity correlation lengths (cf. figure 5.6 a). An initial reflector is defined by extracting and filtering the 7.25 km/s velocity isoline with a Gaussian window of 50 km. Traveltime residuals of this initial model have a standard deviation of 58 ms for refracted traveltimes and 145 ms for reflections. The velocity filter introduces a small bias resulting in a mean shift of -16 ms with respect to zero for refraction traveltimes. Reflected traveltimes are scattered around 72 ms mean, indicating that the initial reflector probably lies too deep. For all iterations, velocity model updates are less than 1.5%, hence no velocity damping is applied. After two iterations, reflector node updates become smaller than 6% and damping is completely ceased. From this stage on, the number of data outliers remain at a constant number of 13 ($< 0.2\%$), probably due to bad traveltime picks and remaining structure. After 5 iterations, model updates become $< 0.1\%$ for velocity nodes and $< 0.5\%$ for depth nodes. The data variance is reduced by 24% for refracted traveltimes and by 91% for reflected traveltimes. Including the outliers, this results in a standard deviation of 51 ms (with 1.3 ms mean) for refracted and 42 ms (with -4.6 ms mean) for reflected traveltimes (cf. figure 5.6 b).

Because the initial velocity model is already very close to the tomographic solution, and since preceeding synthetic tests showed that the emergence of high velocity gradients near the seafloor does not pose a major problem in the applied inversion, a second more general approach is pursued in re-initializing the tomography with a minimum 1D starting model.

A minimum 1D velocity model is derived from laterally averaging the final velocity solution of the first-arrival traveltime tomography. The obtained 1D velocity-depth profile is expanded laterally along the whole model range, starting for all velocity nodes at their individual seafloor depth. A flat-lying Moho at 8 km depth below sea level completes the obtained 2D starting model, which can be regarded as pretty far away from the real subsurface structure (cf. figure 5.7 a). This is also documented by higher initial traveltime misfits with a standard deviation of 105 ms for refracted rays and 237 ms for reflections. Initial model updates exceed our predefined bounds, hence damping is applied during one iteration for velocity nodes and during two iterations for reflector nodes. After 6 iterations, changes between two succeeding solutions become $< 0.16\%$ for velocities and $< 0.56\%$ for reflectors and the initial standard deviation of traveltime misfits is reduced to 53 ms for refractions and to 42 ms for reflections, which is equivalent of 74% variance reduction for refracted traveltime misfits and 97% variance reduction for reflected traveltime misfits, respectively (cf. figure 5.7 b).

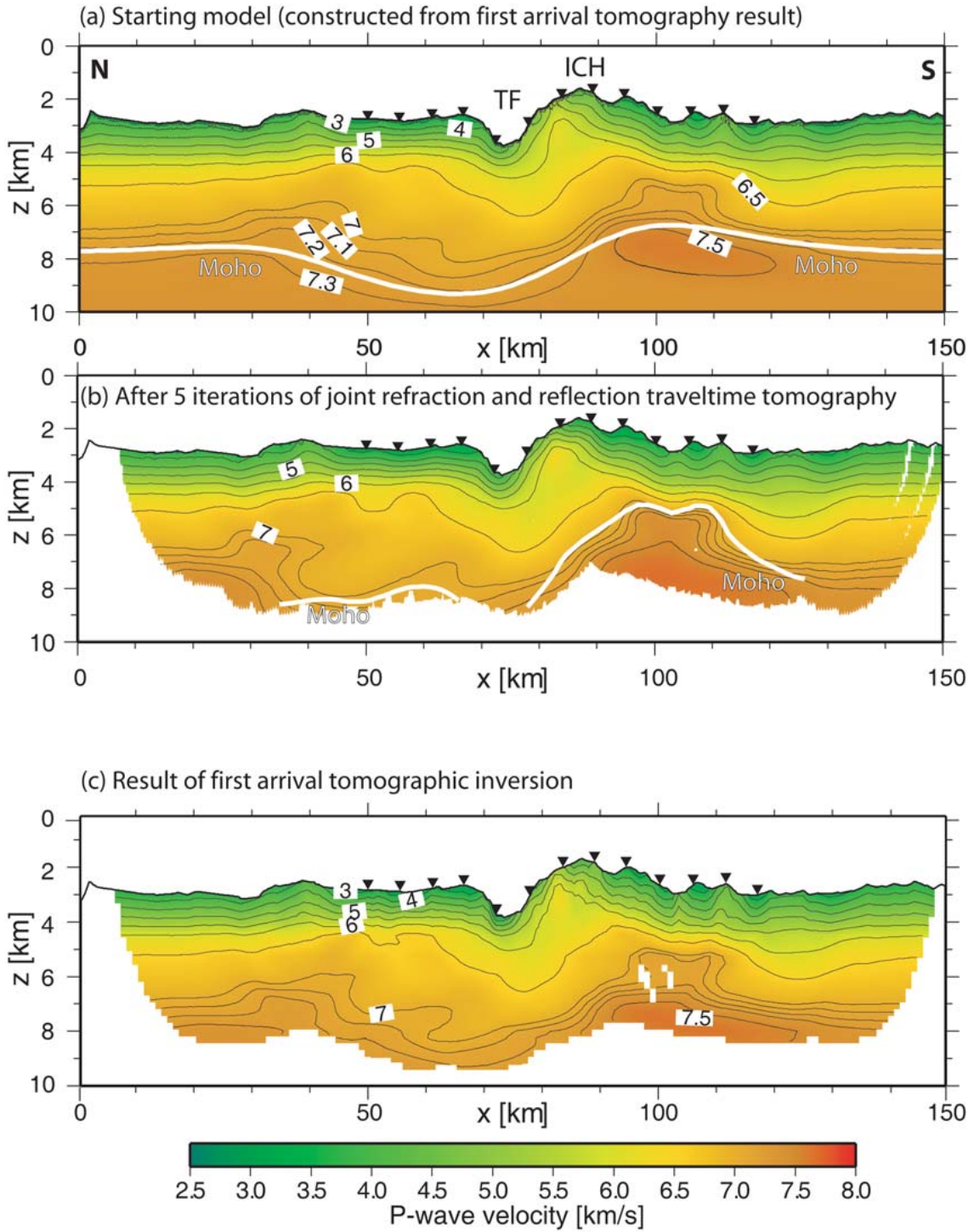


Figure 5.6: Results of tomographic inversion. (a): Starting model constructed by filtering the first-arrival tomographic solution. Initial moho is taken from the filtered 7.25 km/s velocity isoline. TF=transform fault; ICH=inside corner high. (b): After 5 iterations the standard deviation of the traveltime misfits is reduced to 50 ms around zero-mean. Model portions not constrained by ray coverage are blanked. (c): Velocity model derived from the first-arrival tomography, taken as a basis for the starting model in (a) and presented for comparison with the result in (b).

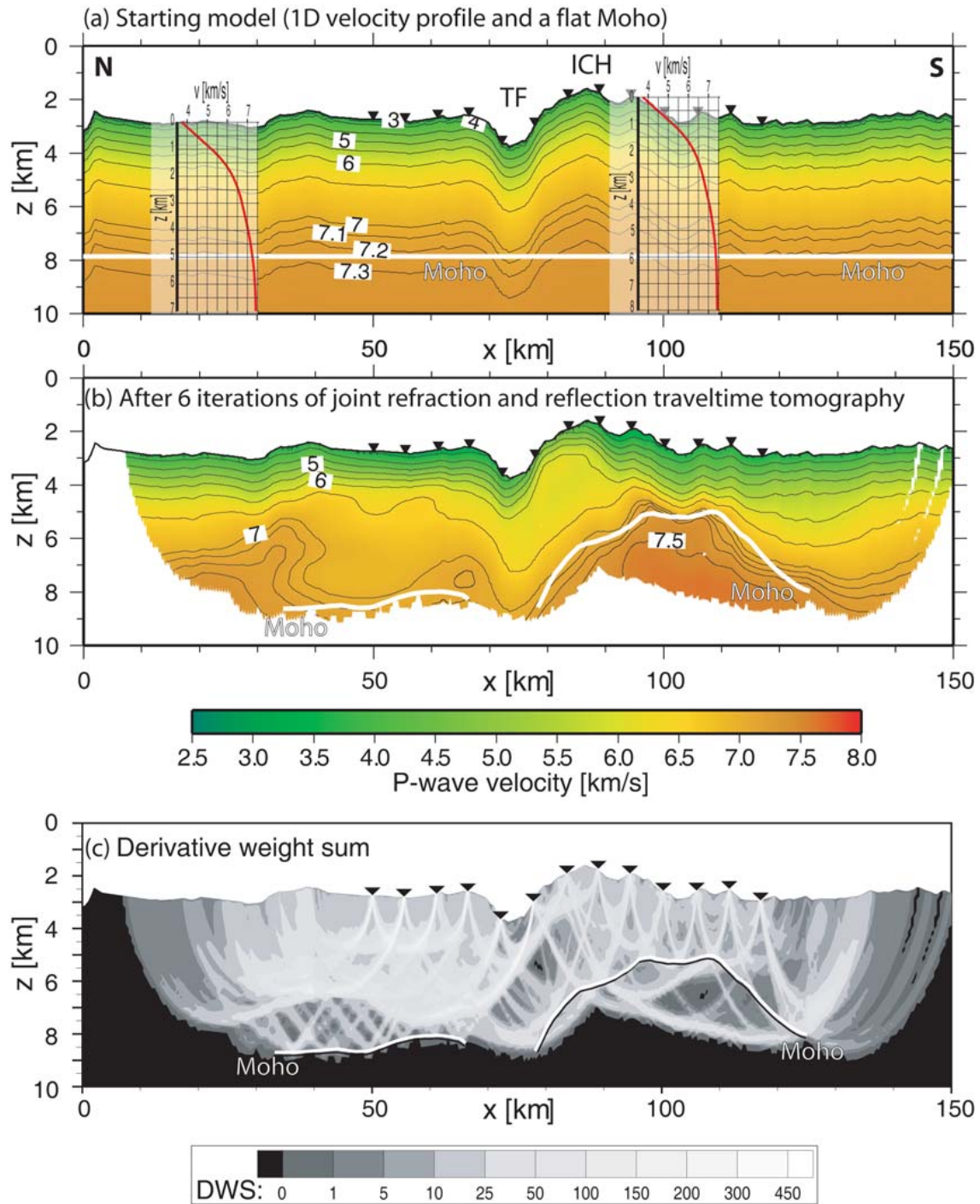


Figure 5.7: Results of tomographic inversion. (a): Starting model constructed by laterally averaging the first-arrival tomographic solution. Initial Moho lies flat at 8.0km depth below sea level. TF=transform fault; ICH=inside corner high.(b): Recovery obtained after 6 iterations. Model portions not constrained by ray coverage are blanked. The standard deviation of the traveltime misfits is reduced to 52ms around -1.2ms mean. (c): Derivative weight sum of the solution shown in (b).

The derivative weight sum (DWS), shown in figure 5.7c represents a perhaps more meaningful measure of ray distribution than the pure “ray hit count” introduced in the previous chapter (e.g. *Toomey et al.*, 1994). It is the column-sum vector of the normalized Fréchet derivative matrix, and hence a weighted sum of the path lengths influenced by a certain model parameter. Therefore, it is not solely the number of ray hits that affect the corresponding DWS value for a grid cell, but the proper length of each ray path within that cell and, due to the previous normalization of G , also the related pick-uncertainty of each ray, resulting altogether in a rough assessment of solution sensibility on the basis of data quantity and quality. In this context, higher DWS values can be ascribed either to a denser sampling of rays or to an accumulation of higher quality rays with smaller pick-uncertainties.

The tomographic output models in figure 5.6b and figure 5.7b both reveal very similar solutions, perhaps with slightly less structure in the first result which is derived from the Gauss-filtered starting model. In both approaches, the originally positive traveltime residuals for reflected rays constrain a pronounced Moho-bulge near kilometer 100, where the thickness of the oceanic crust is reduced to minimum values of ~ 2.5 km. Towards the southern end of the profile, Moho-depths rapidly increase to values > 4.5 km but due to a limited station coverage available reflection data ceases for kilometers > 123 (cf. figure 5.7c). Further south the derived reflector depths are entirely governed by the smoothing constraints.

North of the transform fault, crustal thickness increases to average values of 5.6 km within the area controlled by reflection coverage. Only a small crustal thickening is observed towards the segment center. There are no PmP arrivals from rays reflecting at any boundary directly beneath the transform fault, so the Moho cannot be defined as a seismic reflector along this region.

The velocity structure in figures 5.6b and 5.7b compares favourable to the results of the first-arrival tomography in figure 5.6c in particular, there are no major structural differences between the three models. The anomalous velocities and vertical velocity gradients in the area of the inside corner high (ICH), which are predicted by the first-arrival tomography, are also visible in the results of the joint tomography. Even in case of the more general 1D-approach, the strong lateral variability across the transform fault, but especially beneath the ICH and above the Moho-bulge, where derived values differ remarkably from the corresponding values in the starting model, is recovered well. Above the Moho-bulge, the output model in figure 5.7b reveals seismic velocities that almost increase linearly from 3.5 km/s near the seafloor to values > 7.0 km/s in 2.5 km depth. Upper mantle velocities can be resolved from available Pn rays. Although the exact depths of these turning rays possibly exhibit some uncertainties (cf. figure 5.7c), derived maximum velocities can be constrained to lie within the range of 7.5-7.8 km/s. Within the region of the inside corner high the seismic velocities in the uppermost crust are 1 km/s higher. This anomaly is not centered beneath the portion of highest elevation, but is shifted towards the transform facing flank of the core complex. Here, seismic velocities reach up to values > 6 km/s within the uppermost kilometer, followed by a sharp decrease in the velocity gradient and a more gradually increase of velocities in the lower parts of the crust. Although observed velocity gradients of ~ 0.1 - 0.2 s $^{-1}$ in the lower parts resemble values typically observed in oceanic layer 3, dominating velocities of < 6.5 km/s are slightly lower

than normal (~ 6.9 km/s; e.g. *White et al.*, 1992). Since almost identical velocities are predicted by the first-arrival solution, the recovered velocity structure should be considered as highly reliable.

North of the transform fault, a high-velocity gradient upper crust is in contrast to a low-velocity gradient lower crust which, in its bottom part, exhibits significant lateral heterogeneity. Near kilometer 35, a prominent high-velocity anomaly is placed throughout all output models, with velocities reaching up to ~ 7.3 km/s near the Moho, which in turn has to be considered as less certain due to the dearth of ray coverage. The high-velocity structure seems to be more elongated in case of the first-arrival result. This is probably due to a higher emphasis of maintaining vertical (instead of horizontal) smoothness in the joint tomography and indicates a small systematic difference in the corresponding results. The first-arrival tomography assumes a fixed weighting parameter which controls horizontal vs. vertical smoothness (here: $s_z = 0.15$) whereas the joint tomography allows for a more complex weighting via the variable chosen correlation lengths.

The distribution of traveltime residuals of both output models shows comparable fit. Even the more general approach with the minimum 1D starting model leads to an almost zero-mean, nearly Gaussian distribution of residuals after inversion (cf. figure 5.8). The few outliers that are still present are probably due to non-Gaussian noise, bad picks or remaining structure. However, the applied technique has to be regarded as successful in producing an unbiased model.

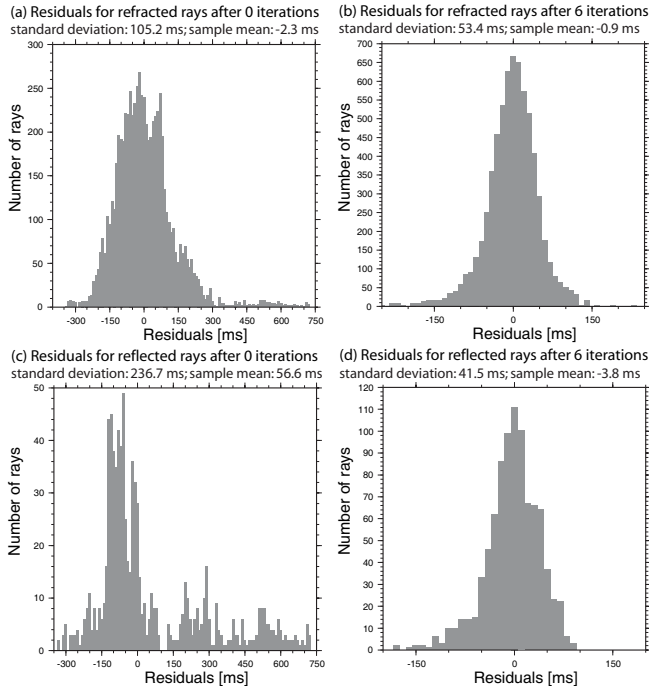


Figure 5.8: *Traveltime residuals for the models presented in figure 5.7. (a): For the minimum 1D starting model, initial residuals for refracted rays are already centered around zero-mean, but exhibit a significant standard deviation. (b): After 6 iterations the standard deviation is reduced and residuals show a nearly Gaussian distribution. (c): Before the inversion, some residuals for reflected rays reach up to 730 ms. (d): After 6 iterations the standard deviation is reduced to 42 ms. Outliers that are still present are probably due to non-Gaussian noise, bad picks or remaining structure.*

5.6 Resolution and Accuracy

The estimation of resolution and uncertainty of the model parameters is crucial for the later interpretation of the models. Therefore the inversion algorithm is tested on the real data set and on synthetic data sets for several reasons:

- (i) to evaluate the possible extent of the velocity-depth ambiguity on the real data set,
- (ii) to assess its ability to recover a known realistic model structure from a set of noisy traveltimes data,
- (iii) to evaluate any artefacts introduced during inversion,
- (iv) to systematically assess the influence of the starting model and realistic traveltimes-noise on the inverse solution,
- (v) to study the extent of parameter correlation within the model space for the applied tomographic approach.

5.6.1 Depth kernel weighting test

Redundant information about the subsurface is usually needed to separate traveltimes information of a geologic layer into depth to the layer and the interval velocity above it (e.g. *Bickel*, 1990). To assess the degree of this velocity-depth ambiguity in the applied inversion, a practical approach is pursued in repeating the inversion with the initial model of figure 5.7 a (minimum 1D velocity model/flat Moho at 8.0 km depth), using an otherwise identical parameterization but two end-member values ($w = 0.05$ and $w = 20$) for depth kernel weighting. For weights $w < 0.05$ and $w > 20$, either reflected traveltimes residuals or refracted traveltimes residuals do not decrease to acceptable values (cf. figure 5.8) within a reasonable number of iterations. As a stopping criterium for the inversion, a drop below 0.5% model update for both reflector and velocity nodes between two succeeding iterations is used. Figure 5.9 shows the derived output models and the perturbations in model velocity and reflector depth. Corresponding standard deviations for traveltimes misfits are 54 ms for $w = 0.05$ and 53 ms for $w = 20$ after the 4th and 8th iteration, respectively. A lower degree of depth weighting leads to smaller reflector updates but larger velocity updates and hence to a faster reduction of refraction traveltimes misfits (cf. figure 5.9 a), whereas a higher degree of depth weighting leads to smaller velocity updates but larger reflector updates, resulting in a faster reduction of reflection traveltimes misfits (cf. figure 5.9 b). Since for this profile the amount of available refraction data exceeds the amount of reflection data by a factor of ~ 6.5 , the individual rates of convergence and thus the number of required iterations differ for different values of w .

Whether traveltimes anomalies correlate or anti-correlate and cause ambiguities depends on several factors, mainly on the ray coverage and the angular distribution of rays as well as on their corresponding pick-uncertainties for a certain area, but also on the structural complexity of the subsurface itself (e.g. *Bickel*, 1990; *Ross*, 1994; *Tieman*, 1994; *Rathor*, 1997). For the tested configuration, the velocity perturbations between the two different output models are almost negligible over a wide model range (cf. figure 5.9 c). However, in certain areas, like at the top of the Moho-bulge, they reach up to ~ 0.3 km/s, perhaps

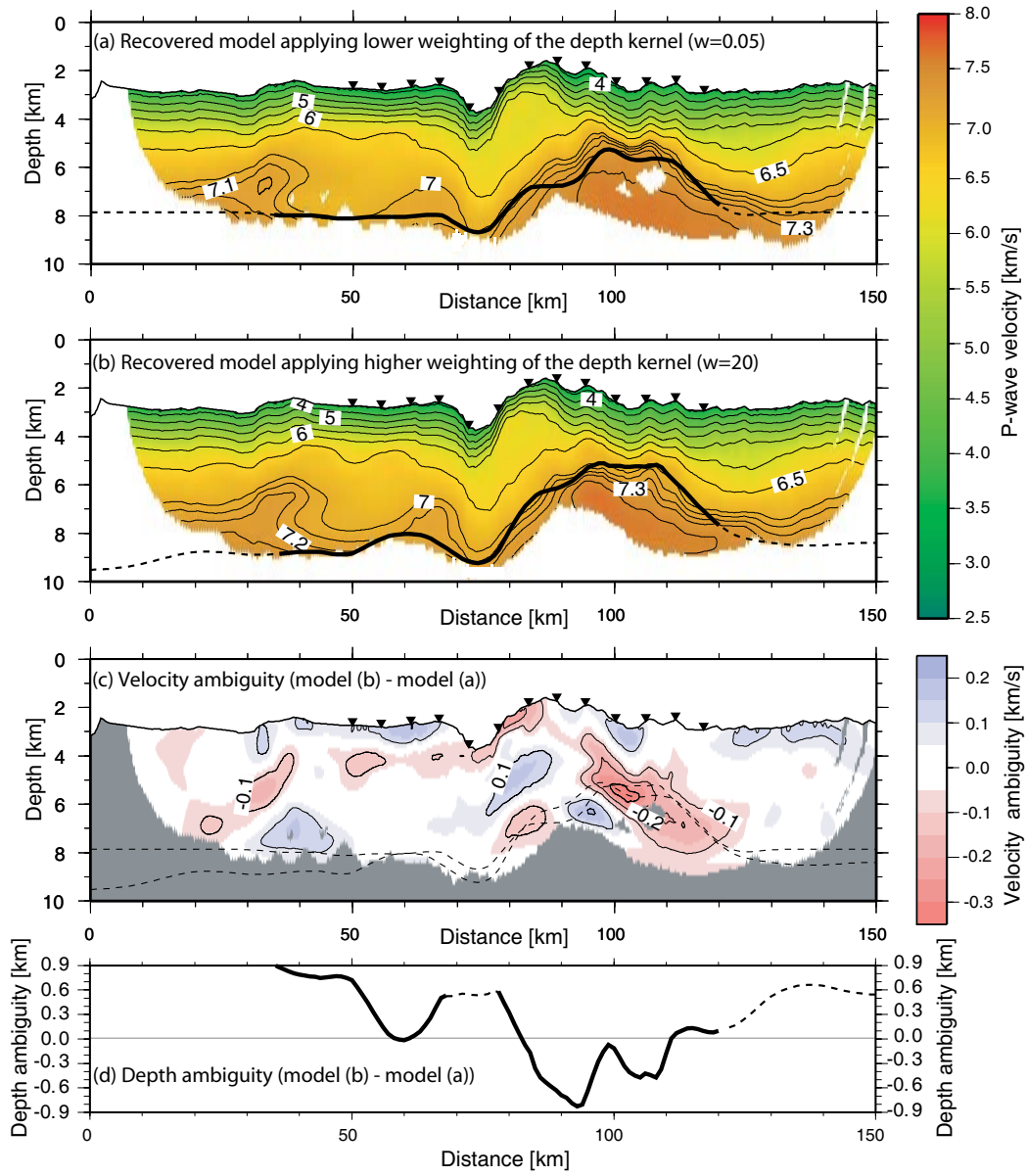


Figure 5.9: *Test of velocity-depth ambiguity applying different values for depth kernel weighting. Initial model is the same as in figure 5.7a and iterations are stopped when model updates fall below 0.5%. (a): $w = 0.05$ (after 4 iterations). (b): $w = 20$ (after 8 iterations). The standard deviation for traveltimes misfits is 54 ms and 53 ms, respectively. (c): Velocity perturbation between the models in (a) and (b). (d): Corresponding reflector perturbation. Dashed lines in (a), (b) and (d) indicate dearth of reflection coverage.*

due to greater structural complexity of the subsurface here. Reflector perturbations reach up to ± 900 m within the model range which is controlled by reflection coverage (cf. figure 5.9d). The increase towards the edges can be attributed to the initially nonuniform and finally almost complete loss of ray coverage due to the limited station distribution. The pronounced anomalies near kilometer 90 and directly beneath the transform are perhaps also consequences of local gaps in reflection coverage (cf. figure 5.15). The above men-

tioned smaller amount of available reflection data in combination with the equally chosen horizontal correlation lengths for velocity and depth nodes possibly leads to the obviously greater impact of different depth kernel weighting on reflector nodes in this dataset. For instance at the model edges where reflector uncertainties are large, the actual discrepancy in velocities is often small because the real model is smooth in these areas, and an almost identical velocity model has been constructed as a result of the applied smoothness regularizations. Therefore, for a final evaluation of structural model features it is necessary to carefully assess the corresponding ray coverage in order not to misinterpret certain areas which are almost entirely governed by the smoothing constraints.

The tomographic output models in figures 5.7 and 5.9 show in fact comparable travel-time fit but due to the above-mentioned different behaviour during convergence the three solutions can hardly be regarded as equally valid. Therefore, equal weighting of depth and velocity nodes is applied for all succeeding computations. However, velocity-depth ambiguity has to be rated as a significant factor of final model uncertainty.

5.6.2 Synthetic anomaly test

In order to demonstrate the resolving power of the data in different parts of the model, a set of synthetic tests is performed where a known model has to be resolved using the same profile geometry and data coverage as in the real experiment. The background model for the synthetic anomalies is a smooth version of the tomographic output model in figure 5.7 b. A set of Gaussian velocity anomalies with different amplitudes, shapes and polarities is imposed on this reference model and synthetic traveltimes are computed. Gauss-noise with a standard deviation equal to the half of the individual pick-uncertainty is added to the synthetic traveltimes, and the inversion is initialized using the minimum 1D velocity model with the flat Moho from figure 5.7 a as a starting model. The ultimate aim of this approach is to test the algorithm's capability of resolving small perturbations within the original tomographic output and whether during this process structure gets mapped into different areas.

In the first test (cf. figure 5.10 a) a pattern of three small velocity anomalies is placed within the uppermost crust of the central part of the model. Here, in the real data, the sum of velocity model updates with respect to the starting model is largest, reaching up to +25% and -15%, respectively. In the synthetic test, between 84-97% of the original maximum perturbation is recovered with only small velocity smearing and almost no visual effect on the recovered reflector depths. Ray coverage in the shallow and central parts of the model is usually good, but the limited angular distribution of rays near the seafloor and the possibility of under-sampling the somewhat small anomalies (due to bending of rays around these feature; *Van Avendonk et al.*, 1998b) poses a challenge for the inversion within this configuration. Furthermore, the inversion tends to suppress small scale perturbations in order to produce an otherwise smooth model due to the applied smoothing constraints. Some difference is noticeable between the *normally* polarized (*correlating* with the perturbations between starting model and original tomographic output) and the *inverse* polarized anomaly pattern (*anti-correlating* with the perturbations between starting model and original tomographic output). However, even in the first case, a good recovery

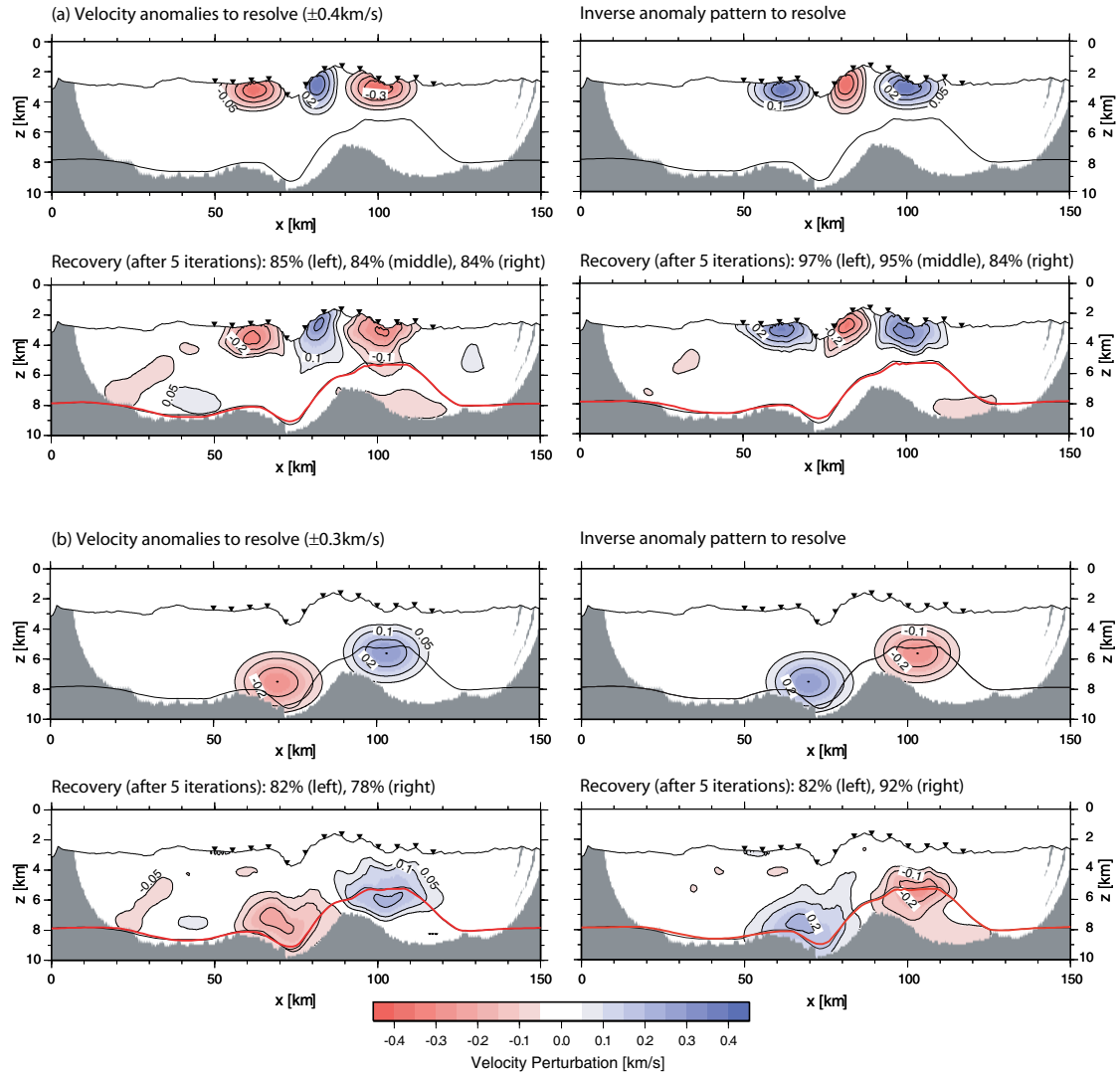


Figure 5.10: Resolution test using different sets of synthetic velocity anomalies within the shallower crust (a) and within the lower crust/upper mantle (b). The background model is the smoothed tomographic output (velocities and reflector) of figure 5.7b. As a starting model the minimum 1D velocity model with the flat lying initial Moho is used (cf. figure 5.7a). Recovery after 5 iterations is shown together with original output Moho (black line). For a discussion of the synthetic inversions see text.

of the individual anomaly shapes is achieved.

In part (b) of figure 5.10, a set of two larger synthetic velocity anomalies with slightly smaller maximum amplitudes is placed within the lower crust and, in case of the Moho-bulge, within the crust-mantle transition zone. This test is mainly to demonstrate that the emergence of higher velocities inside the Moho-bulge (+15% with respect to the starting model) is a stable and resolvable feature of the inversion. Although the anomalies are placed at greater depths, ray coverage is still sufficient to regain the original perturbations (78-92% recovery) with only small leakage into different structure.

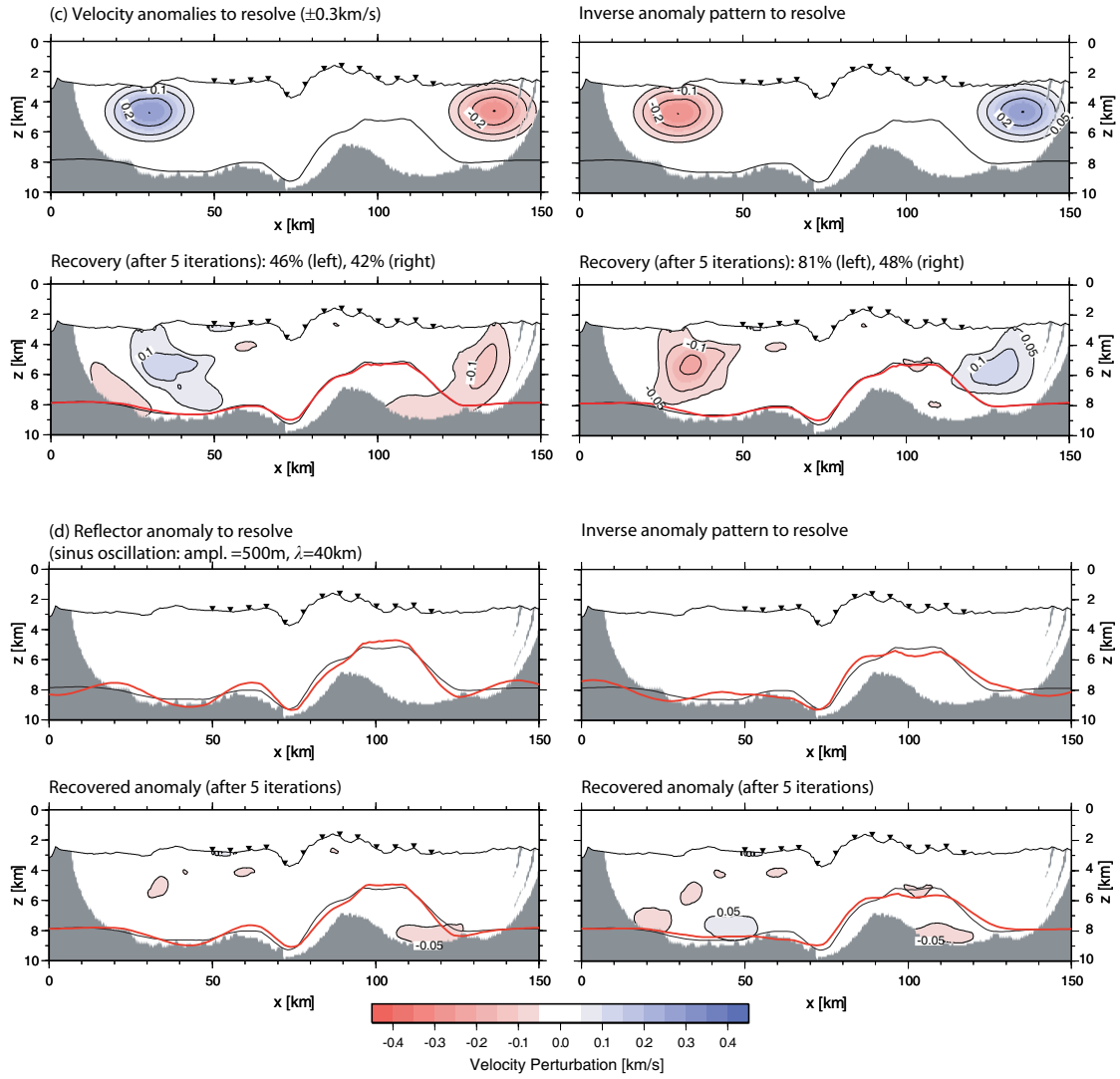


Figure 5.10: **(continued)** (c): Synthetic velocity anomalies are placed beyond the instrument locations at mid-crustal depths. (d): Synthetic reflector (red line) constructed by adding a $\pm 500 \text{ m}$ perturbation with 40 km wavelength to the original reflector (black line). For a discussion of the synthetic inversions see text.

Beyond the instrument locations, ray coverage significantly decreases but the tomographic output still shows considerable lateral structure ($+7\%$ near kilometer 30 with respect to the starting model). To verify that this is not just an artefact of the applied inversion, a third test with synthetic velocity anomalies placed near the model-edges within the mid-crust is conducted (cf. figure 5.10). In this case, the amount of recovery (42-81%) as well as the corresponding leakage strongly depends on the total amount of velocity perturbation, i.e. on the polarity of the synthetic velocity anomaly. This occurs because an anti-correlating anomaly pattern results in significantly less total structure within the desired output model, and hence, due to the sparser ray coverage, the increasing influence of the smoothness constraints leads to a better recovery of the model with less roughness. For the higher seismic velocities in the real data near kilometer 30 (cf. figure 5.7) this

would mean that resolution is sufficient to verify their existence but that their maximum extent and their exact location could possibly be obscured by the limited ray coverage.

In a last test, a synthetic reflector anomaly is constructed by adding a sinus-oscillation with an amplitude of 500 m and a wavelength of 40 km to the original output reflector. After 5 iterations a good recovery in most parts of the model is regained with only small leakage into adjacent velocity structure. As to be expected, a loss of resolution and slightly higher leakage is visible towards the model edges.

From the applied synthetic tests, crustal thickness is probably constrained to better than 200 m for the central part of the model. It is also shown that the horizontal and vertical resolution is good enough to regain even small changes from the original velocity perturbation near the seafloor. At greater depth within the central part of the model velocity perturbations are still constrained, particularly with regard on the complex structure of the Moho-bulge. There is no evidence for exceeding leakage of velocity into reflector structure or the reverse, in fact this is even true for perturbations beyond the instrument locations.

5.6.3 Nonlinear Monte Carlo uncertainty analysis

For a complete solution of a nonlinear inverse problem, it is essential to address the issue of uncertainty. Monte Carlo methods allow to quantify uncertainty in the response of several variables after a complex transfer function by estimating the *posterior covariance matrix* (Tarantola, 1987). In a practical approach, one can construct many realizations by inverting data with random errors with a number of random initial models. In assuming that all solutions are equally valid, the desired result is taken as an average over the num-

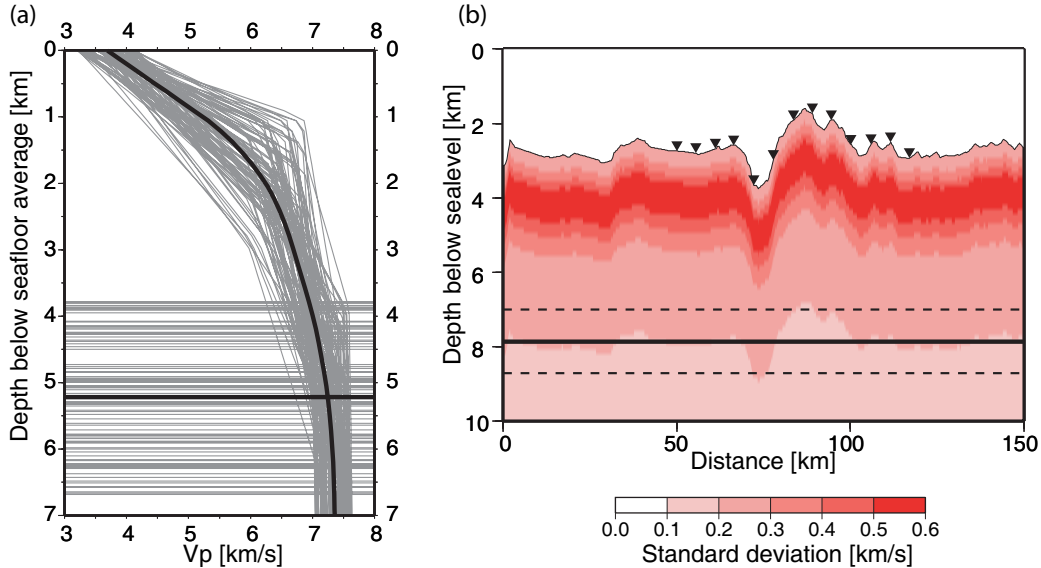


Figure 5.11: Starting model randomization for Profile 09 (a): 100 Monte Carlo ensembles (grey) for initial velocities and reflectors together with ensemble mean (black line). (b): Corresponding standard deviations for velocities (colour coded) and Moho-depths (0.855 km; indicated as dashed lines) together with mean starting reflector (black line).

ber of observations. Finally, one can predict the output uncertainty in terms of simple statistical quantities like the statistical error (*variance*) in this *mean* result (e.g. *Korenaga et al.*, 2000). Moreover, *model correlation* provides an effective measure how well each model parameter is resolved (e.g. *Zhang and Toksöz*, 1998). Since raypaths are allowed to be perturbed during each iteration, the applied approach is fully nonlinear.

For the construction of random initial models a sequence of pseudo random numbers, uniformly distributed in (0,1), is used to prepare a representative distribution of 1D velocity-depth profiles and initial reflector depths. The 1D profiles are build similar to *Korenaga et al.* (2000) by defining 5 controlling parameters such as top, mid, and lower crustal velocities and upper and lower crustal thicknesses. Initial reflector depths are derived from the corresponding crustal thickness quantities. The underlying mantle is characterised by a uniform velocity increase of 0.1 km/s between its top and the model bottom resulting for each 1D profile in slightly different velocity gradients.

The five controlling parameters are allowed to vary for each seismic line within certain predefined limits around the minimum 1D velocity-depth function (cf. figure 5.7a). A typical Monte Carlo ensemble consists of 100 realizations with an average standard deviation (the square root of the variance) of $\sim 5\%$ for initial velocities within the model region which is controlled by available ray coverage. From each ensemble a 2D starting model is constructed by hanging the 1D velocity profile beneath the seafloor and by placing a flat Moho in the corresponding reflector depth below sea level (cf. figure 5.11). This typically results in a standard deviation for initial reflector depths of $\sim 10\%$ (depth with respect to sea level) for each seismic line.

Unlike in the previous synthetic anomaly tests, where random Gauss noise is added to the synthetic traveltimes to *stabilize* the inversion (i.e. to reduce the possible solution space), random noise is used to simulate *true traveltimes errors* in the applied Monte Carlo approach. Errors in refraction traveltimes data are not arbitrarily *random* and generally do not have a zero-mean from a statistical point of view (*Zhang and Toksöz*, 1998). Instead, systematic errors can be introduced during the recording of the data (e.g. time-shifts) and especially during the picking of the traveltimes. Although extensive effort was spend on this dataset to remove the known introduced errors (e.g. instrument drift, time-shift during A/D-conversion, etc.), a possible small remainder cannot be completely ruled out. For instance, a comparison between seismically derived “zero-offset” water depths and corresponding echo-soundings leads to small discrepancies for some instrument locations. Therefore, similar to *Zhang and Toksöz* (1998), two types of errors are defined (cf. figure 5.12): (1) common-receiver errors, a random shift of ± 30 ms at all the shots from the same receiver, and (2) a correlated phase depending error which is caused by the travel-time picking uncertainty.

Zhang and Toksöz (1998) noted that assuming Gaussian errors for the absolute traveltimes is probably not realistic in the view of “manual” traveltime picking, because in most cases one would tend to pick rather the move-out of the first-break wave than the time solely based on a single trace. This is especially significant for seismic phases which cannot be completely reduced to horizontal flatness within a seismic section for picking. Therefore, a long-period phase depending error, comparable with the traveltime gradient error of *Zhang and Toksöz* (1998), is constructed by weighting randomly generated long-period noise with the pick-uncertainty of each phase. The maximum amplitude of this

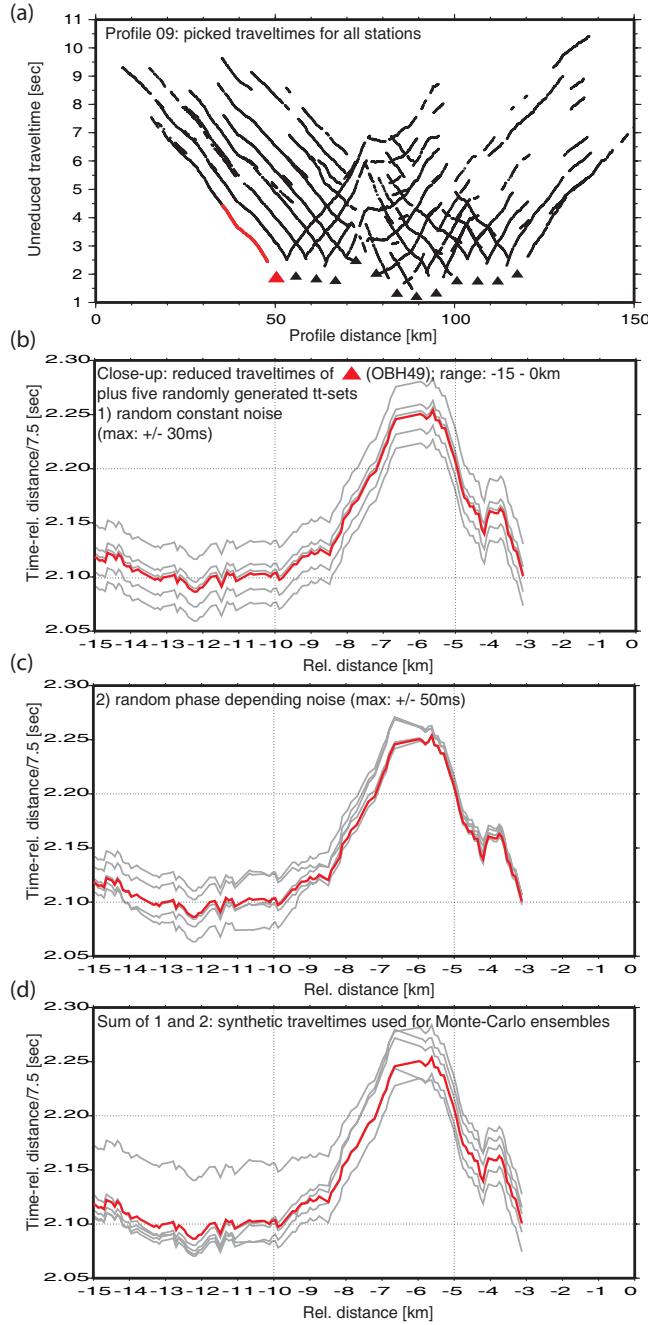


Figure 5.12: *Data randomization for Profile 09 (a): Picked traveltimes for all stations. The red picks are contemplated in the following close-ups with more detail. (b): Red picks from (a), plotted at a time-reduced scale, plus 5 synthetic traveltime sets (grey lines). Synthetic traveltimes are obtained by adding random noise of type (1), i.e. common-receiver errors (see text), to the original picks. (c): Like in (b), but noise of type (2), i.e. correlated phase depending errors (see text), is added to the original picks. (d): Synthetic traveltimes derived from summing up both types of noise from (b) and (c). The resulting traveltimes are used for the Monte Carlo uncertainty analysis.*

error depends on the assigned pick-uncertainty and can reach up to ± 50 ms for individual traces. Analogue to the previous model randomization, 100 data ensembles are built by adding the two types of random errors to the picked traveltime data (cf. figure 5.12).

In the applied Monte Carlo uncertainty analysis more than 100 realizations (thereof each input model is inverted with a different dataset) are calculated for each seismic profile using the same node spacing and inversion parameters as in the previous computation. As a convergence criterium, only those solutions are accepted which reduce the normalized $\chi^2 < 1$ within 20 iterations, resulting in at least 100 valid ensembles for each profile. Although the individual errors previously assigned to the different ensembles could be large, the approach is based on the assumptions that randomly generated errors are not

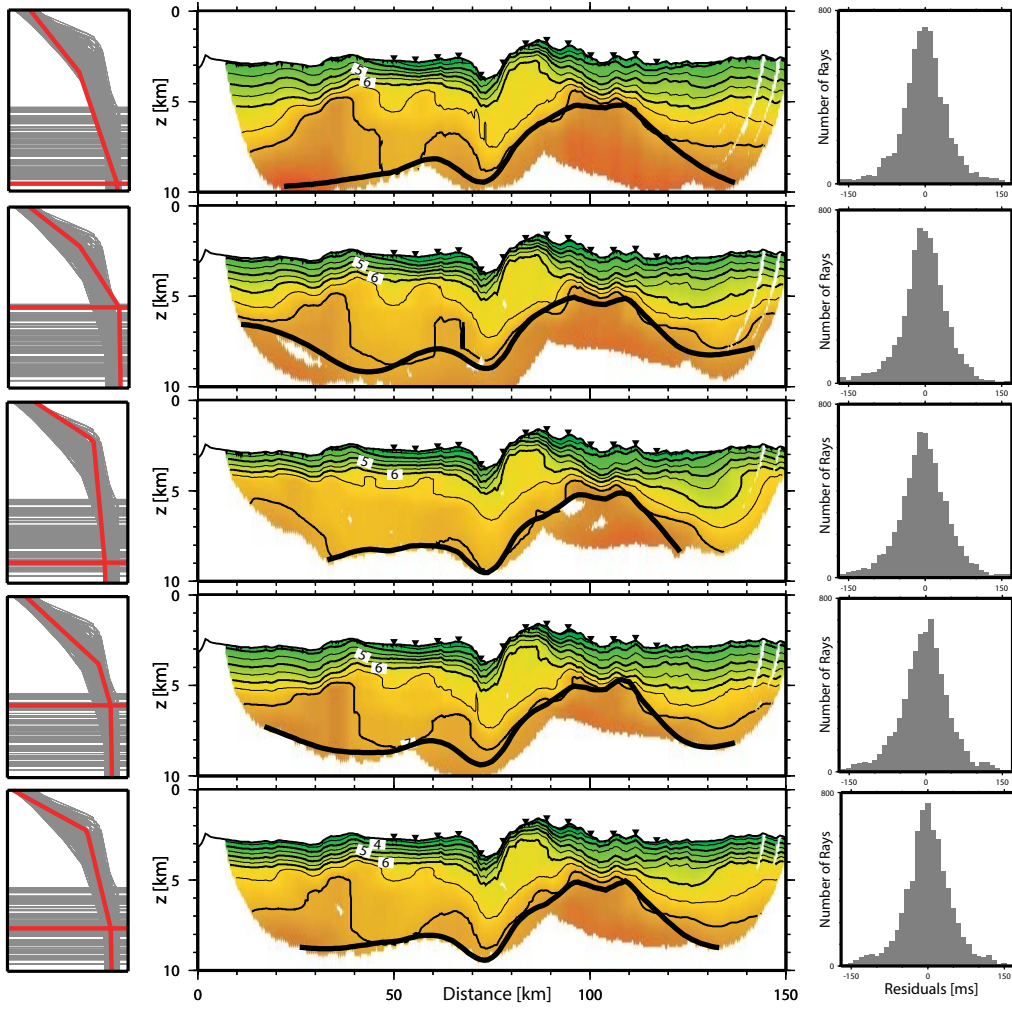


Figure 5.13: *Examples of randomized starting models (left) and corresponding tomographic solutions (middle) and final RMS residuals (right) used for the Monte Carlo uncertainty analysis for Profile 09. (Left): Each starting model consists of a 1D velocity-depth profile and a flat Moho, indicated by the red lines. The utilized 100 initial models cover a wide range of possible 1D velocity profiles and Moho-depths (grey lines). (middle): Although the initial models differ extremely, the output models look very similar in the central part. But beyond the instrument locations, they reveal marked differences. (Right): Histograms of RMS traveltimes residuals (for the models shown in the middle) can serve as an approximate gauge for the quality of fit.*

correlated, and in using a large number of realizations these errors on average will cancel each other out.

After randomization of Profile 09, initial RMS traveltimes residuals for individual Monte Carlo ensembles reach up to maximum values of 450 ms for refracted traveltimes and 610 ms for reflections. On average 7 iterations are applied until the normalized χ^2 is reduced to <1 and RMS residuals approach average values of 55 ms and 48 ms (including outliers), respectively. Figure 5.13 shows examples of randomized starting models and correspond-

ing Monte Carlo solutions used in the uncertainty analysis. Histograms of the final RMS residuals all reveal comparable shapes and follow a nearly Gaussian distribution, which is a gauge for a satisfactory fit to the real data.

Using the 100 Monte Carlo realizations, the *posterior model covariance matrix* is calculated by (e.g. *Zhang and Toksöz, 1998*):

$$C_m = \frac{1}{K} \sum_{k=1}^K (m_k - m_{aver})(m_k - m_{aver})^T, \quad (5.8)$$

where m_k is the solution of the k th realization and m_{aver} is the average velocity model taken over all valid solutions. C_m is symmetric but not sparse and consists of $\sim 25000 \times \sim 25000$ entries (depending on the model dimensions). The square roots of the diagonal elements are the *standard deviations* of the model parameters (including both velocity and reflector nodes), representing a kind of “error bar” for the average solution. The off-diagonal elements contain some information on how independent each model parameter is resolved. The point correlation for an individual model parameter i can be derived from (e.g. *Zhang and Toksöz, 1998; Hobro et al., 2003*):

$$\rho_i = \frac{C_m(i, n)}{(C_m(i, i))^{\frac{1}{2}} (C_m(n, n))^{\frac{1}{2}}} \quad n = 1, \dots, N, \quad (5.9)$$

where N is the number of model parameters. The correlation is valid for small perturbations around the average model structure and takes values between -1 and $+1$. A large positive value indicates a high correlation and a large negative value a high anti-correlation, hence both cases mean that the model parameter is not independently constrained.

Figure 5.14 shows the final velocity and reflector solution for Profile 09 which is taken as an average over all valid Monte Carlo realizations. The black-shaded area marks the limit in which 90% of the Moho-solutions fall (90% confidence interval for Moho-depths based on the Monte Carlo solutions). In the center part of the figure, the corresponding standard deviations for velocity and reflector nodes are shown.

The Monte Carlo derived velocity model is virtually congruent to the solution model derived from the minimum 1D starting model. It reveals a *RMS* of 54 ms (55 ms for refracted rays and 48 ms for reflected rays), which is slightly smaller than the corresponding misfit of the first-arrival tomographic solution (56 ms). The results further indicate that most of the model areas beneath the instrument locations are well constrained with standard deviations < 0.1 km/s for velocities and < 0.24 km for Moho depths. Interestingly, a very good resolution (standard deviation < 0.05 km/s) is shown even for some deeper areas, for instance in the lower crustal portions beneath the transform and the ICH slope, where available ray coverage is actually quite sparse. In this particular case, this occurs because nonlinear tomography would not allow the velocities in the lower crust to be higher, otherwise sub-Moho rays would move up and reduce the velocities. If velocities would be lower, rays which finally pass through the mid-crust would remove these low velocities. In the upper crust and directly beneath the instruments the ray coverage is highest, but derived standard deviations for velocities rarely drop below 0.05 km/s. A comparison with results from a similar approach, where 100 random models are inverted without adding random noise to the original traveltime data, reveals that this is mainly because the introduced common-receiver errors prevent even smaller uncertainties here. At the transform facing

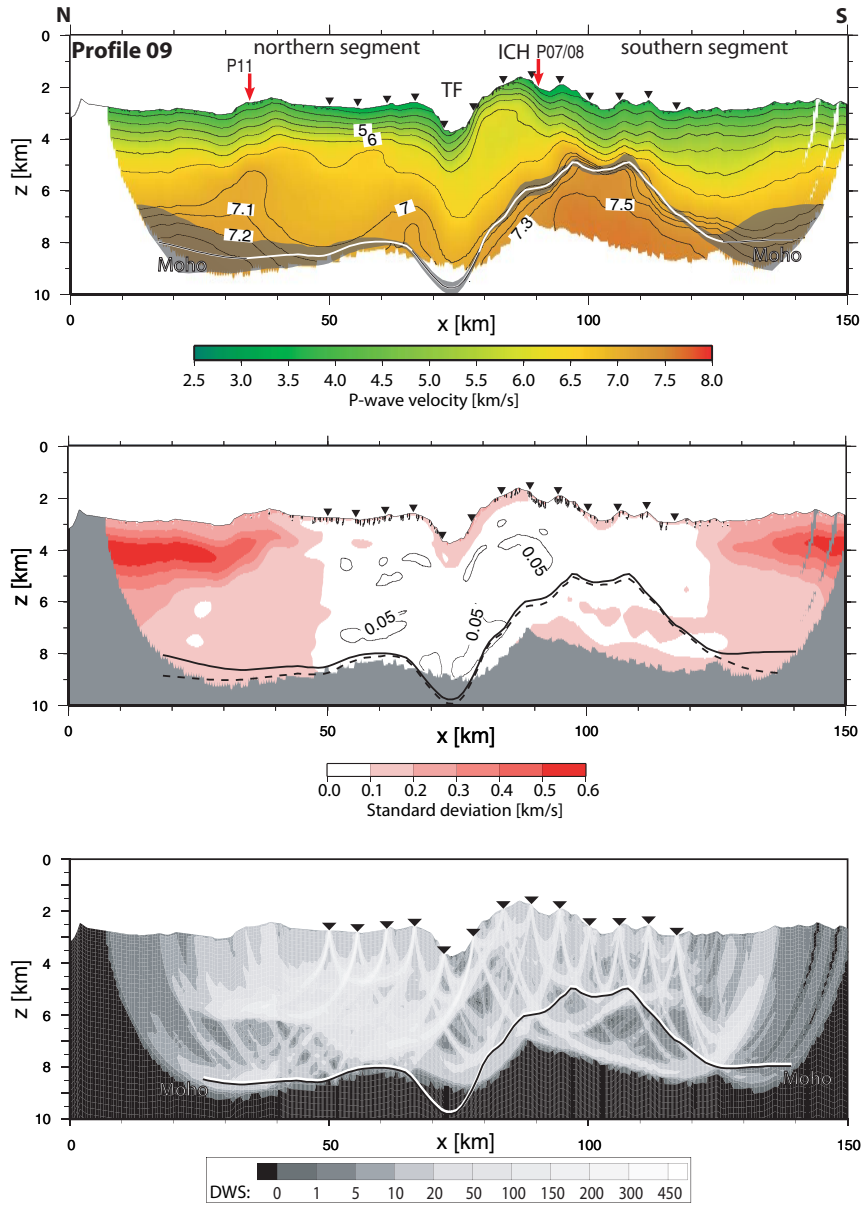


Figure 5.14: (Top): Final velocity model and Moho for Profile 09 derived from averaging all Monte Carlo solutions ($RMS=54$ ms). Black shaded areas are 90% confidence intervals for Moho-depths within the applied uncertainty analysis. White Moho is directly controlled by reflection coverage. (Center): Corresponding standard deviation for velocity and reflector nodes (dashed line, standard deviation is added to the corresponding reflector depth). Velocity contours are drawn at 0.05 km/s. (Bottom): Derivative weight sum for the final velocity model. Models are plotted with $5\times$ vertical exaggeration.

slope of the inside corner high and beneath the transform, near surface uncertainties are higher due to large model structure and partially sparse ray coverage (cf. figure 5.7 c). In general, velocity uncertainties do not necessarily have to increase with depth due to the fact that (1) the increase of the correlation lengths with depth results in tighter constraints on the possible velocity perturbations and (2) the applied starting model variations are

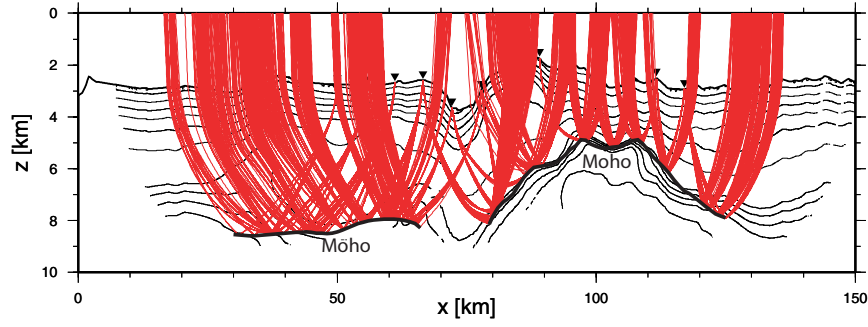


Figure 5.15: *Moho (thick black line) constrained by reflection coverage for Profile 09.*

smaller at greater depths.

As expected, the edges of the model, i.e. the areas beyond the seismic stations, are only poorly constrained. Here, the influence of the phase depending error is greatest, because these areas are mainly sampled through deep-turning rays with an assigned large

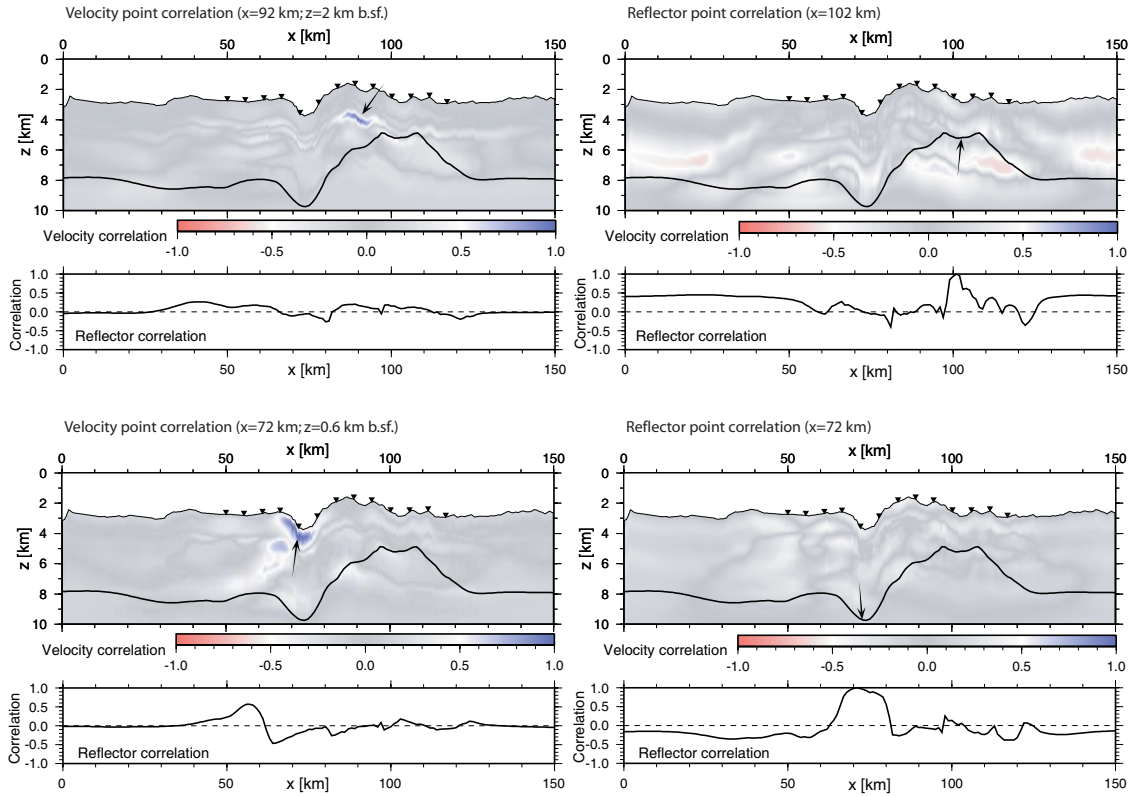


Figure 5.16: (a) *Point correlation shown for individual model parameters for Profile 09 (velocity nodes on the left and reflector nodes on the right). The black arrows indicate the position of the corresponding model parameter within the model space. A value close to (+1) or (−1) indicates correlation or anti-correlation with the corresponding model parameter.*

pick-uncertainty. But the main reason for the produced uncertainties is probably the sparse and predominantly nonuniform angular ray distribution resulting in small model updates and higher blurring of velocity structure and thus to a final model which is almost entirely governed by the applied smoothness regularizations, as it is also shown in the above synthetic tests.

Figure 5.15 shows the ray paths of all available PmP arrivals for Profile 09. There is a gap in reflection coverage directly beneath the transform fault. As a result, the obtained Moho depths in these area (cf. figure 5.14) are entirely governed by the smoothing constraints. In the northern segment, the crustal thickness decreases from ~ 6 km near 35 km profile distance to 5.2-5.5 km close to 65 km profile distance. The shallowing of Moho depth in the southern segment correlates well with a bulge of the 7.0-7.3 km/s velocity isolines. The crust is thinnest (2.3-2.5 km) close to 105 km profile distance, which corresponds to the southern margin of the inside corner high.

Calculated point correlations provide a direct measure how independent a certain model

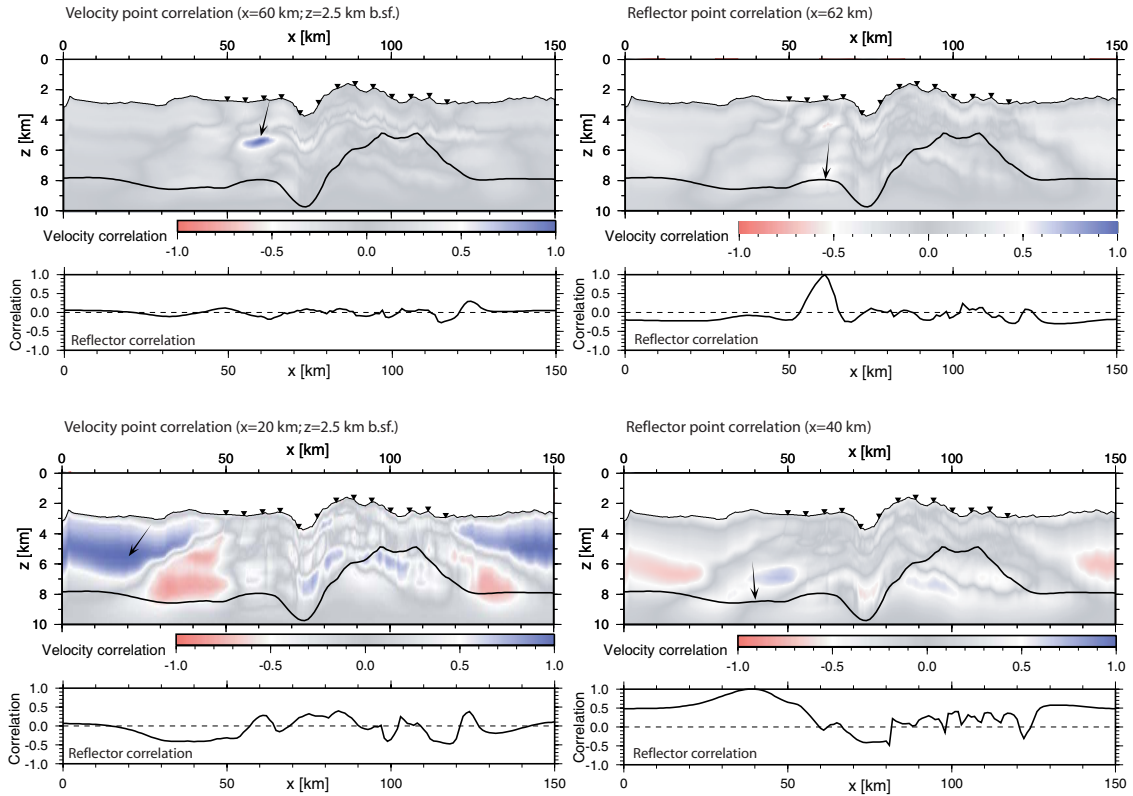


Figure 5.16: **(continued)**(b) *The correlation size and shape strongly depends on the location of the individual model parameter within the model space. The size can be almost as small as the corresponding correlation lengths applied in the regularization constraints (top). Outside the region of available stations coverage, model parameters are not independently resolved. The increased influence of the regularization constraints leads to a greater impact of the starting model, which results in a significant correlation over a wide model range (bottom).*

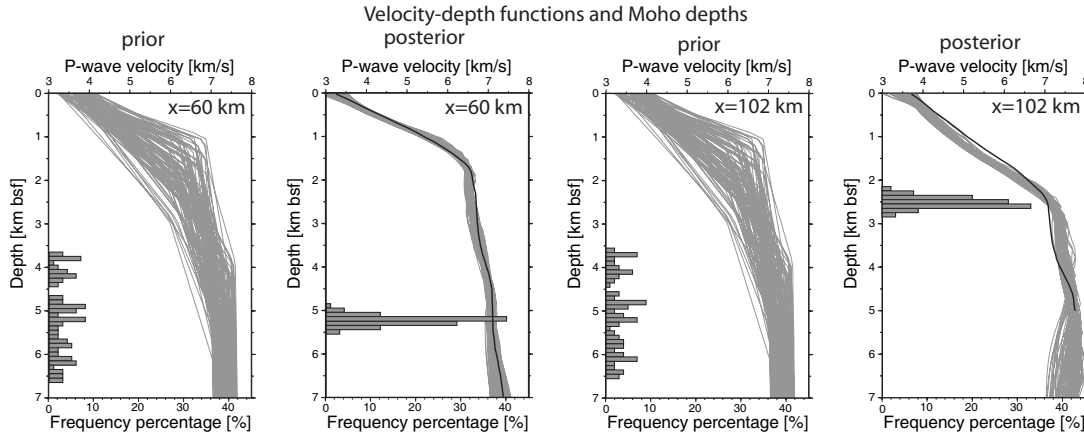


Figure 5.17: *Model profile distributions and histograms for Moho depths for two selected profile intersections sampled from the 100 Monte Carlo ensembles of Profile 09. Corresponding values are shown for prior and posterior models, respectively. Velocity (in km/s) is plotted as a function of depth (in km) below seafloor. Moho depths are binned at 0.1 km intervals. (Left): Profile intersection taken on northern segment crust (at 60 km). (Right): Profile intersection taken on inside corner crust of the southern segment (at 102 km). The black lines in the posterior distributions indicate corresponding results of the first-arrival tomography.*

parameter is resolved, thereby including a possible tradeoff between velocity and reflector nodes. Selected results in figure 5.16 reveal significant differences in correlation shapes and sizes suggesting a spatially varying and complex pattern of parameter resolution. The meaning of correlation in the applied approach is probably most easily demonstrated by the two end-members in figure 5.16 (b). The model parameters in the upper part of the figure are independently resolved. Calculated correlation shapes reveal length scales comparable to the correlation lengths applied in the smoothing constraints. There is virtually no blurring or leakage into other parts of the velocity model or the reflector. In the lower part of the figure, two model parameters placed at the model edges reveal a strong correlation with neighboring parameters but also with areas that lie near the opposite model edge. This interconnection over a wide distance is, of course, due to the 1D definition of the initial models and reflectors and provides direct evidence for a remaining bias towards the starting model. Furthermore, the emergence of anti-correlating areas indicates the need to compensate this bias.

Figure 5.17 shows the velocity-depth profiles from the prior and posterior model distributions as well as histograms for the corresponding Moho depths calculated at two different locations from the previous correlation plots. The geographic locations selected are well constrained by the data, which can be inferred from small standard deviations and correlation lengths shown in the previous figures. From the two profiles considered, the first lies on northern segment crust (at 60 km) whereas the second is situated at inside corner crust of the southern segment (at 102 km). The first feature noticeable is that the range of models and Moho depths in the posterior distributions has decreased significantly, and that the two final distributions are quite different. For the applied tomographic

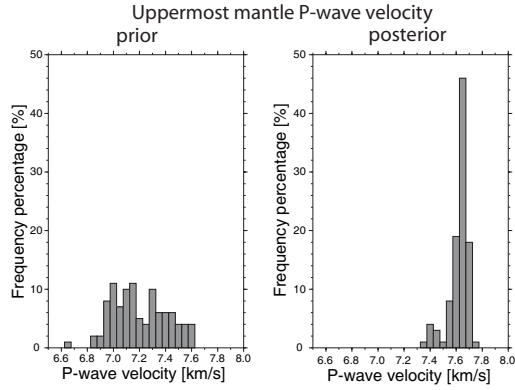


Figure 5.18: *Histograms for uppermost mantle P-wave velocities for prior (left) and posterior (right) models. Velocity values are **averaged** between 100km and 110km profile distance and 7.0-8.0km depth below sea level for each model and are finally binned in 0.05km/s intervals for all 100 Monte Carlo ensembles. Results compare favourable to **maximum** values of 7.7-7.8km/s obtained for the same area from the first-arrival tomography.*

scheme this implies that, in the presence of data, the model and reflector moves away from the prior distribution if the prior distribution does not adequately predict the observed data. The resulting distributions look Gaussian (at least in case of the Moho depths) and in cases have moved far outside the range of the prior distribution, which indicates that convergence has been reached and parameters have “forgotten” their starting value. At both locations, the reflector is rather associated with a change in the vertical velocity gradient than with a velocity jump. In case of the profile at kilometer 60, this is simply due to the lack of mantle turning rays resulting in a dominating influence of the smoothing constraints beneath the Moho. For the inside corner profile, mantle turning rays constrain the data down to ~ 5 km depth. In this case, the lower vertical velocity gradient goes conform with the observation of a rather weak P_n phase and a gradual increase in the apparent phase velocities in the observed data (cf. figure 5.19). A comparison with the corresponding velocity solutions of the first-arrival tomography (shown as thick black lines in the posterior distributions of figure 5.17) reveals a perfect match in case of the “regular” crust at 60 km. At 102 km, the slightly higher trend of the first-arrival solution in the upper part of the profiles is based on a ~ 3 km wide local velocity perturbation (cf. figure 4.9) which was introduced into the starting model during the top-to-bottom approach and which is barely resolvable with a simple 1D starting model. The apparent misfit in the lower portion is probably due to the sparse ray coverage in these depths, also indicated by very low DWS values and higher velocity uncertainties (cf. figure 5.14), resulting in a dominating influence of the smoothness constraints, and hence in less vertical structure for the joint tomography.

Figure 5.18 shows histograms of the prior and posterior distribution of velocities which have been averaged over a horizontal distance of 10 km and depths between 7.0 km and 8.0 km below sea level at profile kilometer 105 in each Monte Carlo model. Thus, the area sampled is constrained to lie well below the Moho-bulge in the uppermost mantle of Profile 09. Again, results have moved away from the prior distribution and reveal a strong cluster around average velocities of 7.6-7.7 km/s, which compares favourable to the results of the first-arrival tomography with maximum values of 7.7-7.8 km/s for the appropriate model region.

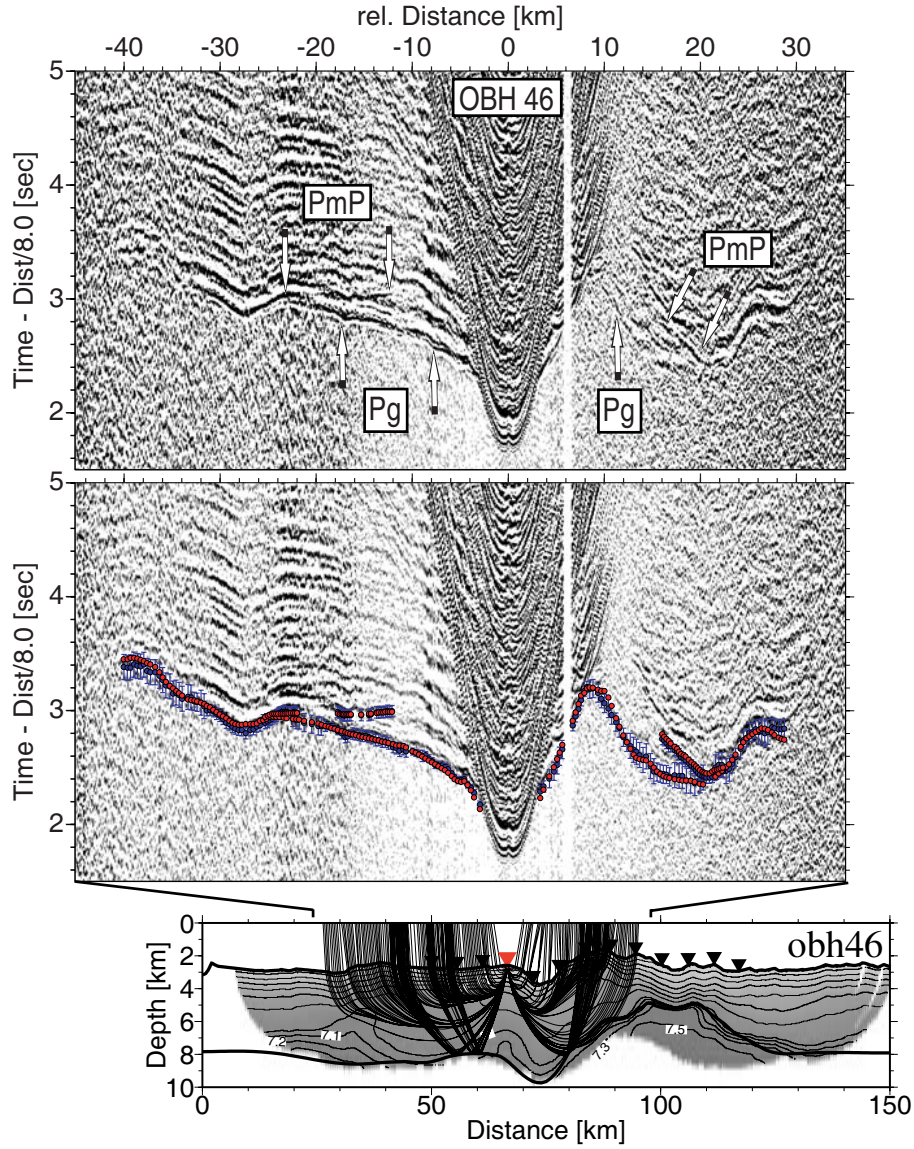


Figure 5.19: *Seismic record sections of Profile 09 (reduced to 8km/s). (Top): Interpreted seismic phases. (Center): Computed traveltimes (red) and associated picks with assigned pick-uncertainties (blue). Interpreted seismic arrivals are labeled: Pg (turning rays within the crust), PmP (reflections in the Moho), and Pn (turning rays in the upper mantle). (Bottom): Corresponding ray paths through the Monte Carlo derived model for Profile 09. Velocity contours are annotated in km/s. Only every third ray and traveltimes are shown.*

From the foregoing results it is clear that the Monte Carlo uncertainty analysis provides concrete error-bounds and plausibly visualizes the interconnection between different *posterior* model parameters on the basis of a wide range of realistic input parameters. In the manner described it takes into account the regularization terms, different starting models and errors in traveltimes data. Unlike the analytical approach to evaluate uncertainty, which involves the calculation and inversion of the Hessian matrix (e.g. *Hobro et al.*, 2003),

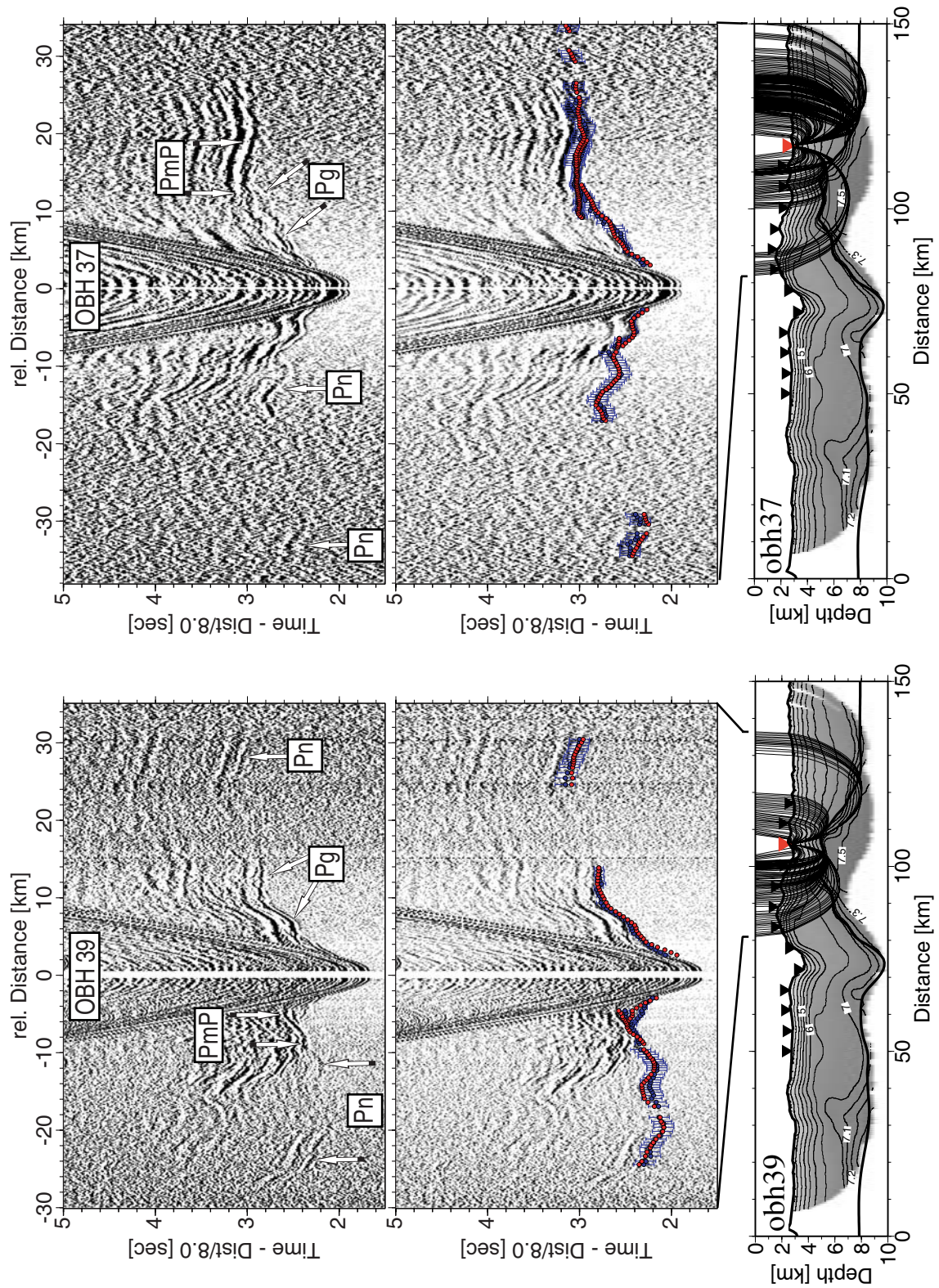


Figure 5.19: (continued)

it is not restricted to linear theory, since the computation of Monte Carlo solutions is a nonlinear iterative approach. Furthermore, the results are not based on Gaussian statistics for the pick-uncertainties, and prior model errors are additionally taken into account (in form of starting model randomization). There are, however, some principal difficulties, because (i) the model and data randomization usually does not allow for all possibilities, (ii) the method does not explicitly account for the final data fit (it is assumed that all solutions are equally valid, which is obviously not the case), and probably most important (iii) it is not clear whether the derived results are useful indicators of the “true” uncertainties in the solution model. It should be clear that model resolution will not solely depend on the starting model and data errors, but in fact to a much larger extent on factors like the number and distribution of available data, the model parameterization, the velocity-depth ambiguity and last but not least on the “true model” (i.e. on the velocity anomalies) itself. Therefore it is highly recommended not to mix resolution with uncertainty. However, in order to evaluate the results derived above, the Monte Carlo uncertainty analysis is tested on a synthetic model structure.

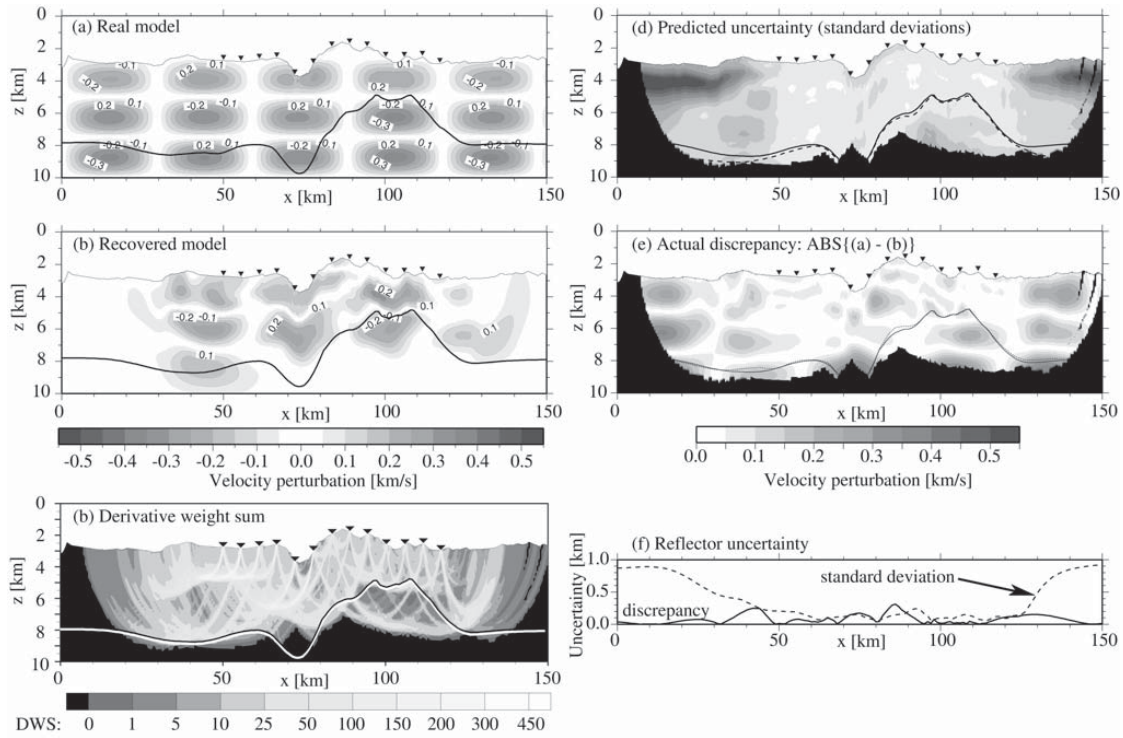


Figure 5.20: *Performance of the Monte Carlo uncertainty analysis in a test with synthetic anomalies. (a): Real model ($\pm 5\%$ checkerboard anomaly pattern plus the final model for Profile 09) (b): Recovered model (averaged over all solutions) using the same data errors and starting models of the previous 100 MC ensembles. (c): Derivative weight sum for the recovered model. (d): Standard deviations for the recovered model and reflector (dashed line). (e): Real model - recovered model (absolute values). (f): Estimated uncertainty and actual discrepancy for the reflector.*

An alternating checkerboard anomaly pattern is superimposed on the Monte Carlo derived solution shown in figure 5.14. Velocity perturbations reach up to $\pm 5\%$ with respect to the background model and have length scales of $\sim 20 \times 2.0$ km (cf. figure 5.20 a). Synthetic traveltimes data are computed for this model and complemented with the traveltimes errors used in the previous data randomization. The inversion scheme is initiated starting from the 100 randomly generated input models. The resulting final model (averaged over all solutions) is presented together with plots of uncertainties, estimated using the method described above, and plots of actual discrepancies between the final model and the real model. Discrepancies in this case are simply the absolute values of the differences in the corresponding model parameters (real model - final model).

The plot of uncertainties indicates, as expected, that the model edges and some deeper areas beneath the Moho bulge are only poorly constrained. A comparison with the model discrepancies reveals for the latter that the location has in fact been indicated correctly but the actual amplitude has been under-determined. At the very model edges, both the discrepancies and the uncertainties pretty much resemble their original patterns, because the tomography fails to resolve the anomalies here and, due to the regularization constraints, produces solutions close to the individual starting models. However, in the central portion of the model and at the transition to the less resolvable outer rim, the uncertainties seem to indicate the peaks of greater discrepancy correctly. But again, they usually underestimate the true amplitudes as well as the spatial extent, sometimes heavily (e.g. beneath the transform) but sometimes only slightly (e.g. near kilometer 40). Interestingly, a similar conclusion can be drawn from the reflector uncertainty, where trends seem to be indicated correctly but actual amplitudes locally exceed the predicted values. Therefore, Monte Carlo derived uncertainty limits based on starting model variations and realistic data errors do not predict correctly the actual discrepancies here, but they can serve at least as an indicator of the relative uncertainties to locate the “critical” (i.e. less resolvable) areas within the model space. Irrespective of this, the Monte Carlo derived velocity model correctly reproduces the first-arrival tomographic results, thereby even increasing slightly the final data fit. As a consequence, the Monte Carlo derived model is considered as the final solution of the joint refraction and reflection tomography.

Chapter 6

Results

6.1 Results for Profile 10

Profile 10 is the NS trending profile which runs east of the median valley through the crestral mountains of the northern segment and extends a few kilometers into the southern segment. Figure 6.1 shows the results of the joint refraction and reflection tomography for this line derived analogue to the above described scheme. On average 10 iterations are applied for each of the 100 Monte Carlo ensembles to reduce normalized χ^2 to <1 . The final model, which is taken as an average over all ensemble solutions, reveals a *RMS* data misfit of 41 ms (41 ms for 7350 refracted and 35 ms for 670 reflected rays), which is smaller than the misfit of 46 ms obtained by the first-arrival seismic tomography (FAST). As a result, the recovered velocity model, although in general very similar to the first-arrival results, exhibits slightly more features (cf. figure 4.9).

For the northern segment, calculated standard deviations for velocity nodes are mostly <0.1 km/s and in cases drop below 0.05 km/s. The uncertainties increase towards the model edges, and are also higher in areas which are barely sampled by available rays, for example in the lower crust between 25 km and 50 km. Beneath the transform fault and further south, velocity uncertainties rarely drop below 0.1 km/s. This is probably due to the greater structural complexity of the subsurface, which usually results in higher pick-uncertainties, but also to the sparser ray coverage, both indicated in figure 6.1 by on average lower DWS values.

Resolved seafloor velocities of 2.6-3.2 km/s in the northern segment are slightly smaller than corresponding values of the FAST model (3-3.4 km/s). However, in both cases, crustal velocities rapidly increase to ~ 5.5 km/s at 1-1.5 km depth below seafloor and then more gradual to ~ 6.5 km/s at 3-3.5 km depth. In case of the joint tomography, the pass of the 6.5 km/s velocity isoline is associated with a change of the velocity gradient to $\sim 0.15 \text{ s}^{-1}$ (cf. the solid line profile in figure 6.2). This change is also visible on Profile 11 at the line intersection with Profile 10, whereas the FAST models suggest a more gradual transition here (cf. figure 4.11). A significant portion of velocities 6.5-7.2 km/s and velocity gradients indicative of seismic layer 3 are present in the lower crust of the segment center, but are less common near the segment ends and largely absent beneath the southern flank of the transform (cf. figure 6.2).

As already predicted by the FAST results, the velocity structure of the transform fault

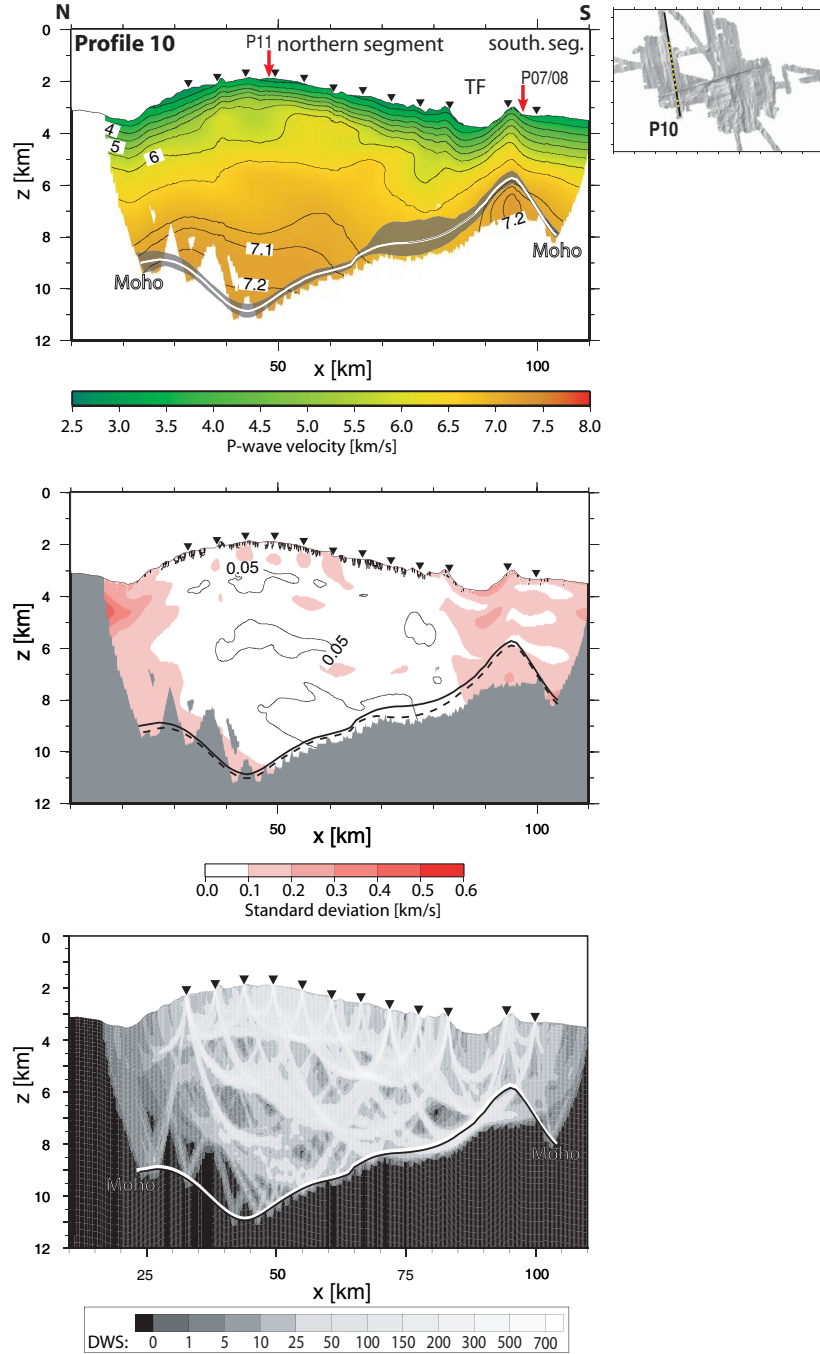


Figure 6.1: (Top): Final velocity model and Moho for Profile 10 derived from averaging all Monte Carlo solutions ($RMS=41$ ms). Black shaded areas are 90% confidence intervals for Moho-depths within the applied uncertainty analysis. White Moho is directly controlled by reflection coverage. (Center): Corresponding standard deviation for velocity and reflector nodes (dashed line, standard deviation is added to the corresponding reflector depth). Velocity contours are drawn at 0.05 km/s. (Bottom): Derivative weight sum for the final velocity model. Models are plotted at $5\times$ vertical exaggeration.

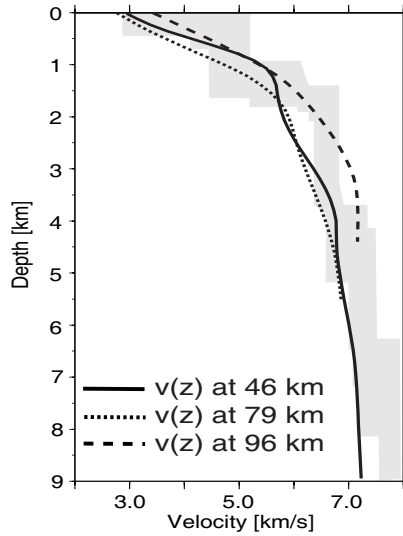


Figure 6.2: *Velocity-depth profiles (laterally averaged over 5 km) through different geologic regions and extracted from the final model for Profile 10: northern segment center crust (46 km, solid line), northern segment end crust (79 km, short dashed line) and southern segment end crust (96 km, long dashed line). Shaded backgrounds show, for reference purposes, the compilation of profiles in 1-7 Ma Atlantic crust of White et al. (1992). Depth is labeled below seafloor.*

is more complex than that of the segment center. The transition to the northern segment is characterised by lower velocities, especially in the upper portion of the crust, and there is a distinct change in gradient associated with the 5.5 km/s velocity iso-line (cf. the short dashed line in figure 6.2). Lower crustal velocities do not reach up to 7 km/s throughout the resolvable depth range. In contrast, the transition to the southern segment reveals higher seafloor velocities, and the velocity increases almost linearly with depth (cf. the long dashed line in figure 6.2). Velocities of 7 km/s are observed at 3 km depth below seafloor and hence at even shallower levels as suggested by the first-arrival tomography. In general, the magnitude and lateral variation of velocity structure is more pronounced in case of the joint tomography and probably allows for the fact that the FAST results consistently failed to fit the small traveltime undulations associated with the narrow high-velocity anomaly beneath the transform (cf. section 4.4.3).

The standard deviation of the crust-mantle interface is highest (~ 0.4 km) between 70 km and 85 km, associated with a local gap in reflection coverage, but usually takes lower values than 0.25 km for both the thinner and thicker portions of the crust (cf. figure 6.1). The crustal thickness of Profile 10 ranges from ~ 2.8 km near the transform fault to ~ 9 km at the line intersection with Profile 11. Since the thickness of the upper high-gradient portion of the crust remains relatively constant, most of these variations are accommodated by the lower crust (velocities > 6.5 km/s). The *PmP* modeling confirms (cf. figure 6.3) that the crust forms a pronounced root near the center of the segment and systematically thins out along-axis to ~ 6 km in 20-23 km distance from the center and finally reaches its minimum thickness slightly south of the transform fault. Further south crustal thickness increases again, perhaps to values > 4.5 km, although the exact extent is less certain here due to the dearth of ray coverage.

Near the transform fault, mantle turning rays penetrate through the uppermost 1-1.5 km beneath the Moho. A closer examination of sub-Moho velocities in all Monte Carlo solutions reveals a cluster around average values of 7.2-7.3 km/s (cf. figure 6.4). Calculated point correlations in this particular region confirm that the reflector depth is indeed independently resolved (note the small reflector correlation lengths in figure 6.5 right). Although placed relatively close to the model edge, there is no evidence for a remaining

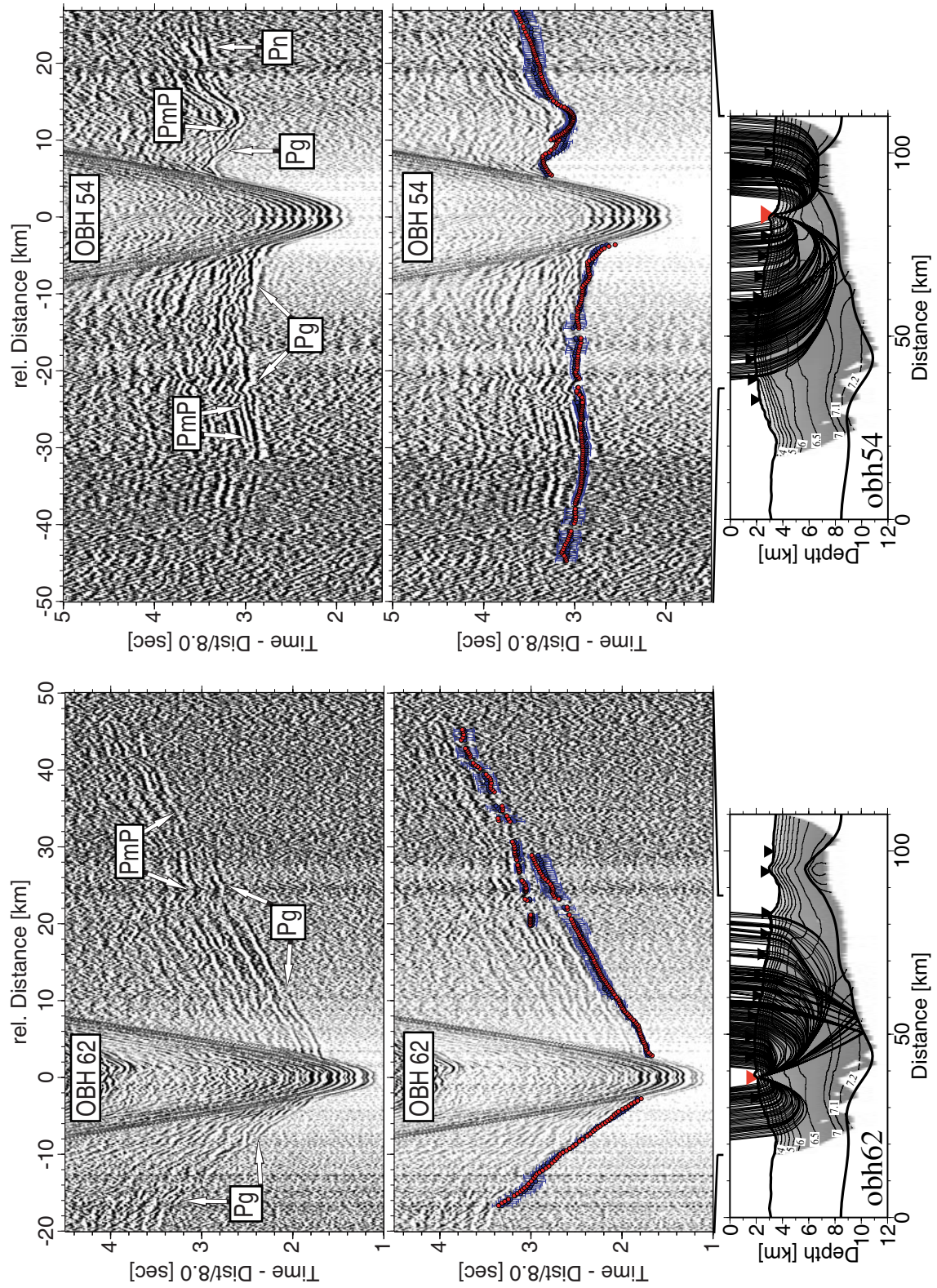


Figure 6.3: *Seismic sections of Profile 10 recorded by OBH54 and OBH62.*

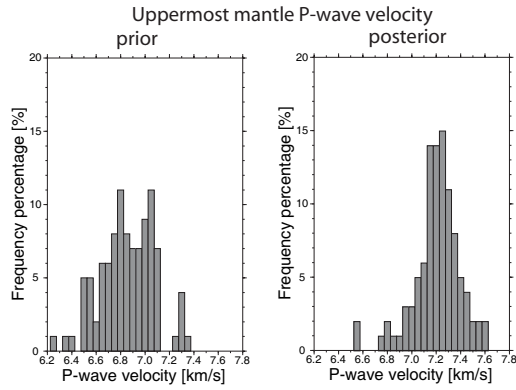


Figure 6.4: *Histograms for uppermost mantle P-wave velocities for prior (left) and posterior (right) models. Velocity values are averaged between 93km and 97km profile distance and 1-1.5km depth below the reflector for each model and are finally binned in 0.05km/s intervals for all 100 Monte Carlo ensembles. Posterior results reveal a cluster around average values of 7.2-7.3km/s.*

influence of the starting model, which would e.g. become apparent in a significant correlation with reflector nodes at the very model edges. In fact, this is also true for a velocity node placed at ~ 0.8 km depth beneath the Moho reflector (cf. figure 6.5 left). However, in case of the latter, there is evidence for a stronger correlation with neighboring velocity nodes over a significant model range (even across the Moho reflector). For the previous evaluation of upper mantle velocities, this suggests that obtained results may still suffer from noticeable lateral averaging with lower crustal velocities and hence, although slightly higher than the corresponding velocities of the first-arrival tomography, may still fail to predict correctly the maximum extent of the observed velocity perturbation.

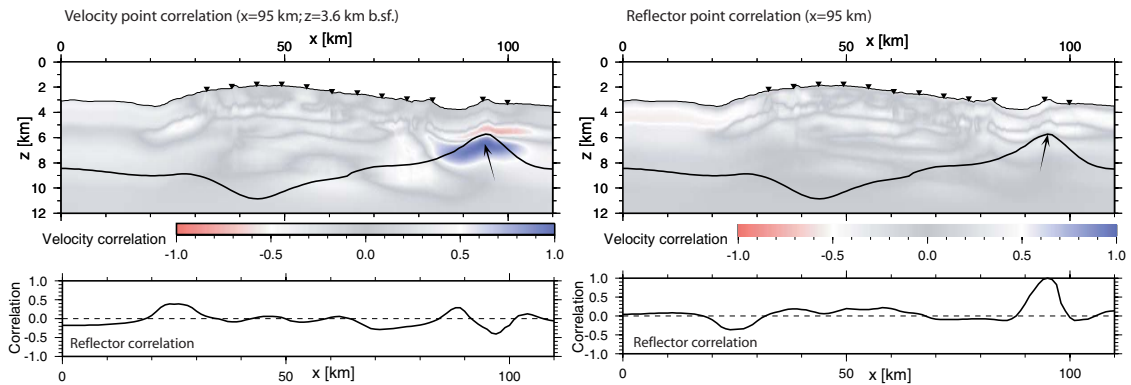


Figure 6.5: *(Left): Point correlation calculated for a velocity node placed at 95km profile distance and ~ 0.8 km depth beneath the Moho reflector. Results suggest a stronger correlation with neighboring velocity nodes (even across the Moho reflector). Hence, sub-Moho velocities may still suffer from interference with lower crustal velocities. (Right): Point correlation calculated for a reflector node at 95km profile distance. Results show no evidence for a remaining influence of the starting model.*

6.2 Results for Profile 11

Profile 11 crosses the median valley of the northern segment directly at the pronounced seafloor bulge. The Monte Carlo derived velocity model for this line is presented in figure 6.6. The final *RMS* data misfit is 57 ms (56 ms for 6800 refracted and 59 ms for 1020 reflected rays) which is in the same range as the 57 ms obtained from the first-arrival model. On average 13 iterations are used for each of the 100 Monte Carlo ensembles to reduce normalized χ^2 to <1 . Calculated standard deviations for velocity and depth nodes indicate low uncertainties (<0.1 km/s) in the central part of the model. Uncertainties increase to values >0.1 km/s in some parts of the lower crust and the uppermost crust and towards the model periphery. An inspection of the DWS reveals that large portions of the lower crust are only poorly sampled by rays and almost exclusively constrained by reflections, which results in higher velocity and reflector uncertainties for these areas. Interestingly, very low standard deviations (<0.05 km/s) are observed in the lower crust of the central part of the model, although corresponding DWS values barely differ from those found e.g. a few kilometers further west. Since the central part of the model is characterised by anomalously low seismic velocities, the lower uncertainties could be simply related to the fact that pick-uncertainties for lower velocities should result in lower velocity-uncertainties.

A comparison with the velocity model derived from the first-arrival tomography (cf. figure 4.15) reveals very similar structures for the upper portions of the crust, but also a more detailed image of the deeper portions of the crust due to the use of reflected phases. In the area of anomalous velocity structure beneath the median valley, obtained velocities are on average 0.1-0.2 km/s higher than those observed in the FAST model. However, compared to the average seismic structure of the profile, lower velocities are still present in the mid crust (within a ~ 10 -15 km wide band centered beneath the median valley) and in the lower crust (within a broader portion extending slightly more to the east). The area of negative vertical velocity gradients (LVZ) which is consistently found in the FAST results is less pronounced here (e.g. it is not visible with the applied contour spacing in figure 6.6), perhaps due to the higher weighting of vertical smoothness in the applied tomographic approach.

Figure 6.7 a shows the results of the reconstruction of a synthetic velocity anomaly in this particular model region. A starting model is obtained by horizontally averaging the Monte Carlo derived velocities in the area of available stations coverage (20-100 km), thereby excluding the region of anomalous velocity structure beneath the median valley (40-60 km). This model contains the 1D “background” (i.e. without the low-velocity anomaly) velocity structure of the well resolved portions of Profile 11. A synthetic velocity anomaly similar to the observed one is superimposed on the background velocities. Traveltimes are obtained from this model and from the Monte Carlo derived Moho, and are supplemented with Gaussian noise (standard deviation equal to the pick-uncertainty). Inversion is started from the background model and a flat Moho to invert for the known model structure.

Derived results are presented in the bottom part of figure 6.7 a, and corresponding velocity depth profiles through the original and recovered velocity perturbations are shown together with the actual observed anomaly in figure 6.11. Within the shallowmost 1.5 km

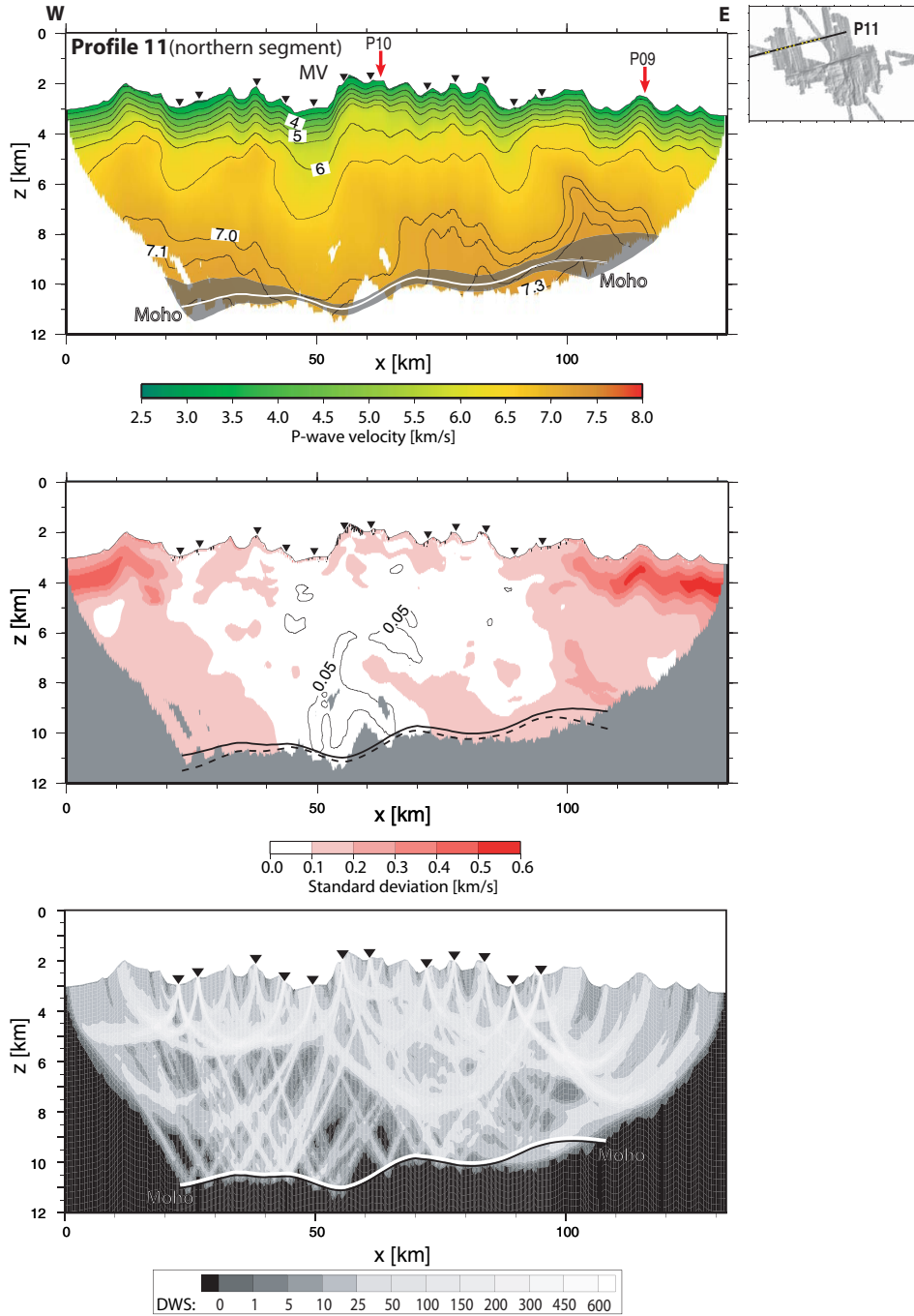


Figure 6.6: (Top): Final velocity model and Moho for Profile 11 derived from averaging all Monte Carlo solutions ($RMS=57ms$). Black shaded areas are 90% confidence intervals for Moho-depths within the applied uncertainty analysis. White Moho is directly controlled by reflection coverage. (Center): Corresponding standard deviation for velocity and reflector nodes (dashed line, standard deviation is added to the corresponding reflector depth). Velocity contours are drawn at 0.05 km/s. (Bottom): Derivative weight sum for the final velocity model. Models are plotted at $5\times$ vertical exaggeration.

below seafloor, recovery is best revealing very similar perturbational shapes and amplitudes (cf. figure 6.11). In depths of the highest original perturbation (2-3 km bsf), between 65% and 70% of the amplitudes are regained. At greater depths, the recovered velocity structure shows enhanced blurring, but observed amplitudes rise again and reach up to respectable 80% of the original values. Recapitulating the fact that the first ~ 25 km of the Moho are not sampled by reflections (and hence are entirely governed by the smoothing constraints), there is no major leakage of velocity into reflector structure discernable in the resolvable model portions.

Figure 6.7b shows the point correlation for two velocity nodes placed at different crustal depth levels beneath the median valley. Results indicate that velocity nodes at 2 km depth below seafloor indeed do not suffer from greater lateral leakage. The more widespread correlation for the velocity node placed at 5.5 km depth is probably due to the lesser amount of rays in the deeper crustal levels. However, although independently resolved, the relative amount of amplitude recovery is less for the shallower velocity node than for the deeper velocity node (cf. figure 6.11). Hence, a greater lateral model corre-

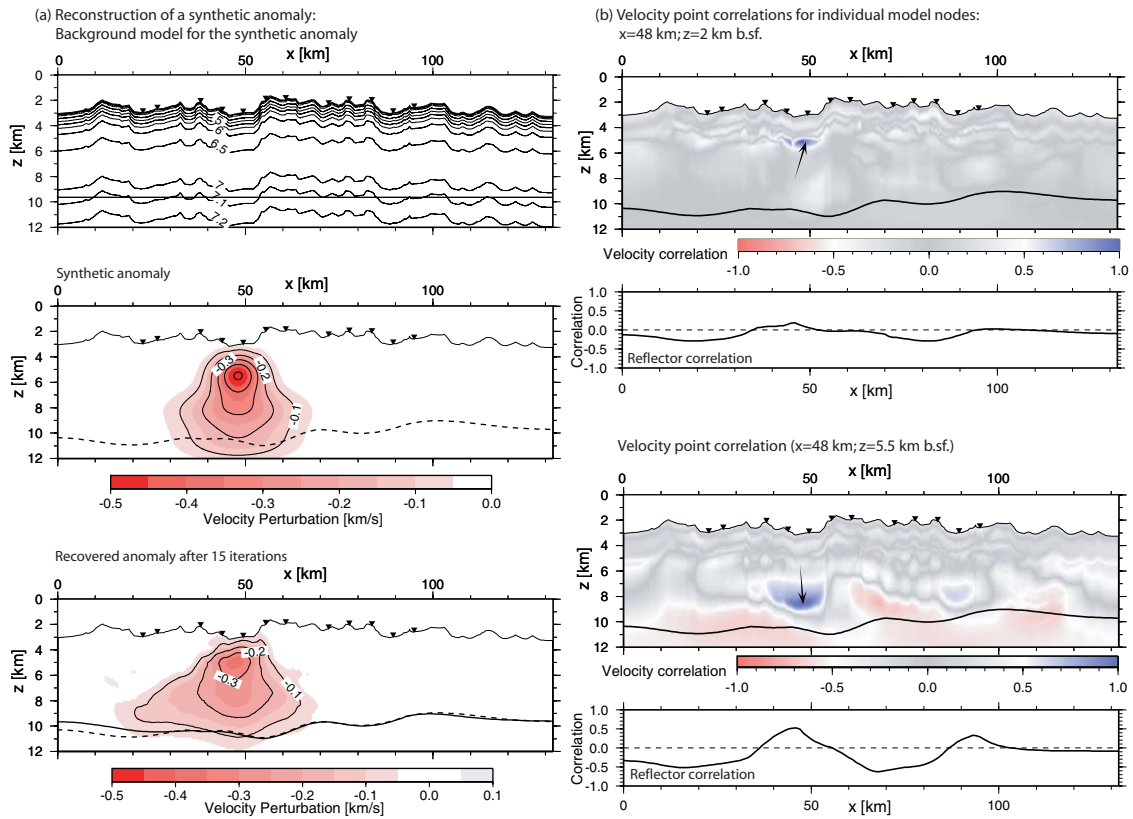


Figure 6.7: (a): *Reconstruction of a synthetic anomaly. The average velocity model of Profile 11 without the low velocity in the median valley (top) is taken as the reference model for the synthetic anomaly (center). Inversion is started from the reference model (top). The recovered anomaly pattern after 15 iterations is shown at the bottom.* (b): *Point correlation calculated for velocity nodes at 48 km profile distance in 2 km and 5.5 km depth below seafloor, respectively. For a discussion, see text.*

lation does not necessarily hamper the actual ability to regain a model perturbation, at least if the perturbation has comparable lateral dimensions.

In summary, a negative anomaly with a similar shape and amplitude, as observed beneath the median valley, is resolvable throughout the whole depth section, and the relative amount of amplitude recovery is depth-dependent and ranges from $\sim 65\%$ to more than 95%.

Aside from the median valley, the overall structure in the upper portions of the crust is very similar to the FAST results. However, the observed velocity contours tend to follow the seafloor relief due to a remaining influence of the hanging-mesh parameterization of the starting model. This means that the resolved velocity structures have greater wavelengths than the pronounced short-wavelength topography of the seafloor.

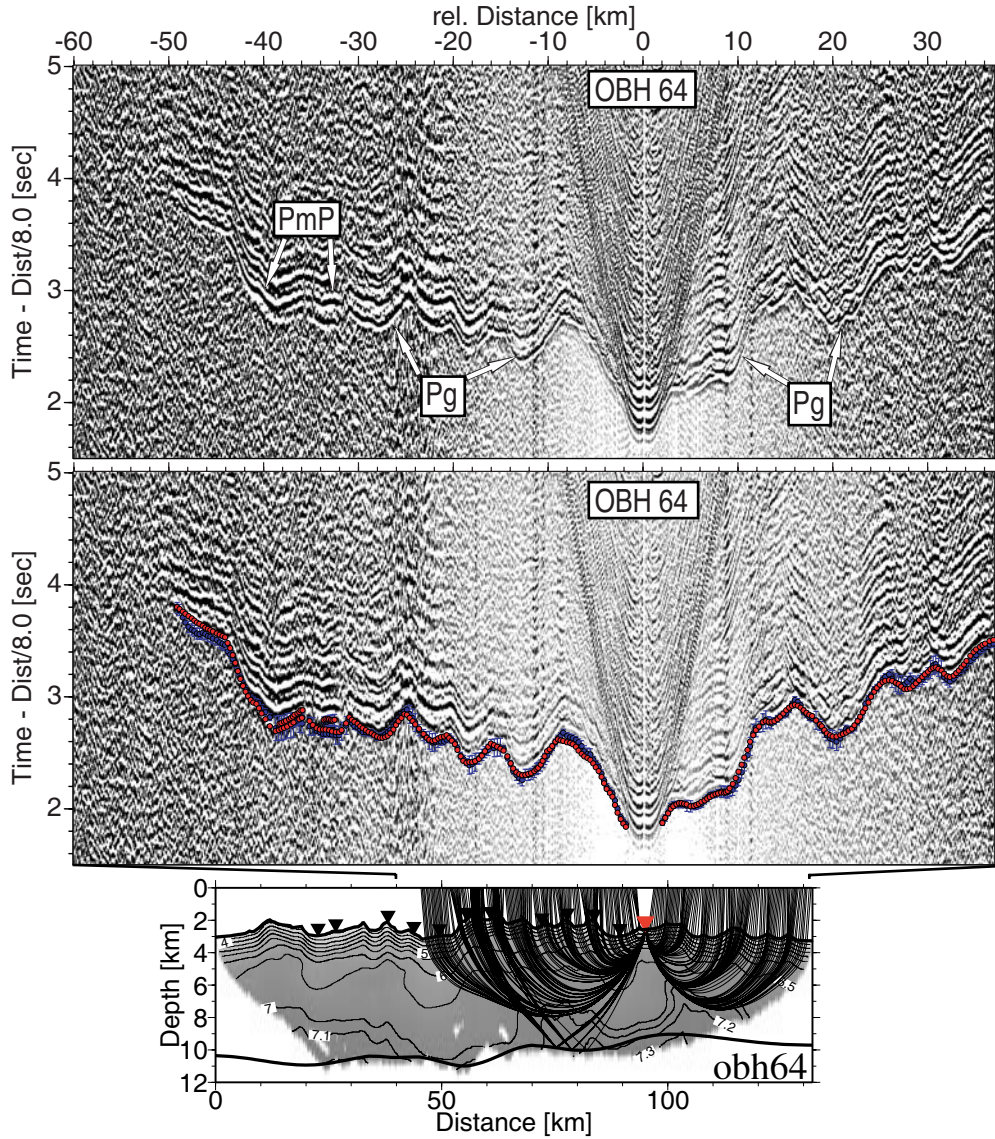


Figure 6.8: *Seismic section of Profile 11 recorded by OBH64.*

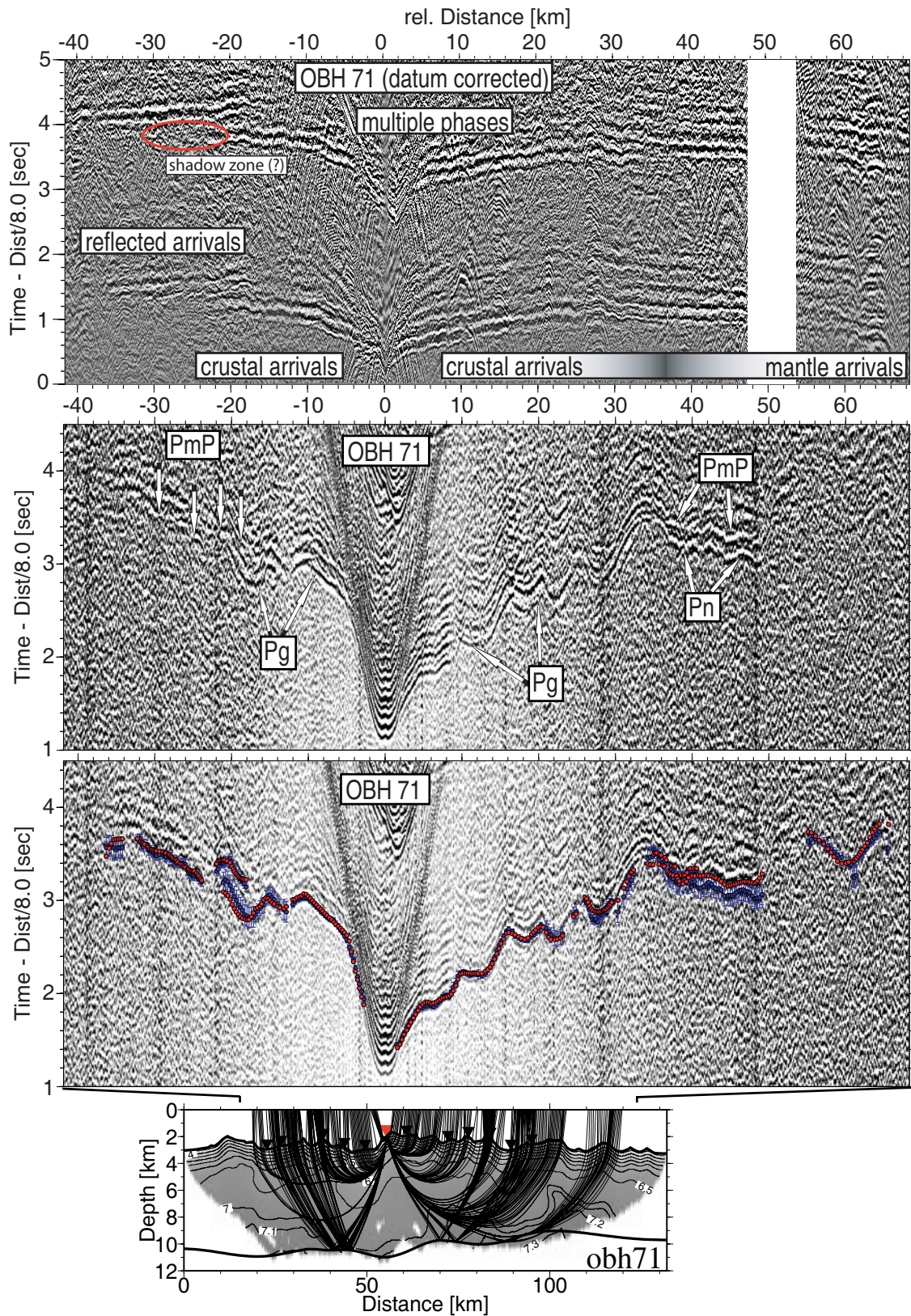


Figure 6.9: Seismic section of Profile 11 recorded by OBH71. The strong impact of the pronounced short-wavelength seafloor topography upon the seismic arrivals is markedly suppressed in the water-path corrected section (top). For a discussion, see text.

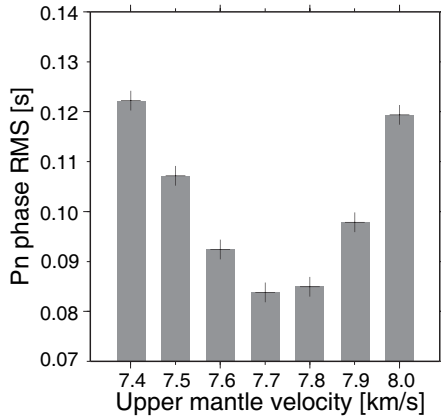


Figure 6.10: *RMS data misfits for 400 Pn arrivals (recorded by obh68, obh70, obh71) obtained by assuming different upper mantle velocities. For the forward calculations, the Monte Carlo derived velocities and reflector depths are used to define the crustal portion of the model. The smallest RMS values are obtained by assuming upper mantle velocities of 7.7-7.8 km/s.*

The off-axis lower crust is characterised by velocities (6.5-7.2 km/s) indicative of a normal seismic layer 3 (White *et al.*, 1992). However, near 22 km and 90 km, the observed velocities exhibit significant lateral variations suggesting in places a nonuniform structure. The transition to the 0.2-0.5 km/s lower velocities beneath the median valley occurs rather abrupt at shallower depths (over a distance of at most a few kilometers), but appears to be more gradual at greater depths (perhaps extending over a distance of 20 km). Observed seismic phases on this profile are strongly dominated by the short-wavelength topography of the seafloor, which often hampers the reliable identification of *PmP* reflections (cf. figures 6.9 and 6.8). However, Profile 11 reveals the highest measure of *PmP* reflections in this study.

The average crustal thickness constrained by *PmP* reflections is 7.8 ± 0.6 km. The crust is thickest (9.2 km) near 57 km profile distances and thins out to 6.6 km at the eastern model edge. Obtained standard deviations for reflector depths are < 0.15 km beneath the median valley and increase to ~ 0.6 km towards the edges of the resolved reflector portions.

Due to the thick crust of Profile 11, fewer than 6% of the first-arrivals in the seismic record sections are *Pn* phases. The area imaged by these arrivals is restricted to the uppermost 0.5-1 km beneath the Moho between 85 km and 100 km profile distance. A systematic under-prediction of arrival times for these phases (resulting partly in lower crustal ray paths - cf. figure 6.9) suggests that the observed gradual velocity increase at the Moho probably occurs more abrupt, and that obtained upper mantle velocities in the tomographic solution are too small. The impact of different mantle velocities on the traveltimes misfit of the *Pn* arrivals is shown in figure 6.10. Forward calculations using a number of different mantle velocities together with the Monte Carlo derived velocities and reflector depths for the crust indicate that the smallest RMS values are obtained for mantle velocities of 7.7-7.8 km/s. The same range of velocities is consistently found in the resolved deepest mantle portions of Profiles 07/08 and Profile 09 in both the first-arrival and the joint refraction and reflection tomographic results.

6.2.1 Evidence for elevated temperatures in the mid crust

The observed low velocities beneath the median valley are clearly anomalous. Compared to the crust beneath the rifted flanks 10 km further east, the velocity contrast exceeds

0.7 km/s (0.8 km/s in case of the FAST model) in depths of ~ 2.5 km below seafloor. Figure 6.11 shows the velocity perturbation with depth at 48 km profile distance beneath the median valley. The velocity perturbation is plotted with respect to the background model of Profile 11 (see above) and to well constrained northern segment crust of Profile 09 (extracted at 60 km profile distance). The original and recovered perturbational velocities of the synthetic test are presented for comparison.

Velocity depth profiles show a deviation of -0.4 km/s at a depth of 2.5 km below seafloor compared to “background” velocities of Profile 11. The velocity contrast with respect to velocities of Profile 09 exceeds -0.5 km/s at comparable depths. Velocity depth profiles at both profile locations reveal a clear change in the velocity gradient close to 1.5 km depth below seafloor, probably related to the layer 2/layer 3 boundary (cf. figure 5.17). This suggests no major difference in upper crustal thickness and means that the observed velocity contrast of 0.4-0.5 km/s at ~ 2.5 km depth is placed well beneath the upper crust. Since the seismic structure off-axis at similar levels is that of a relatively normal layer 3, it seems unlikely that petrological differences account for the observed anomalies. Possible causes include a gabbroic lower crust with reduced velocities due to cracks, elevated temperatures and/or small portions of partial melt.

The abundance of cracks and pores in the gabbro section is significantly reduced compared to the overlying highly fractured basaltic material because lithostatic pressure and ductile flow are likely to close pores and small cracks at greater depths. Although hydrothermal veins are not uncommon in the gabbro section (Karson, 1998) the very consistent seismic velocity structure of layer 3 suggests a restricted possible amount of hydrothermal alteration. A preferential orientation of cracks and fractures in an axis-parallel direction, as indicated by the large-scale morphology of the northern segment, could result in velocity anisotropy (i.e. greater axis-parallel velocities) for the brittle portions of the crust. Unfortunately, higher standard deviations for velocities at the line intersection with Profile 09 indicate that sampled depth portions on both profiles are not reliably constrained. Upper and mid crustal velocities of Profile 10, sampled at the line intersection with Profile 11, are rather lower or reveal an almost perfect match (in case of the FAST

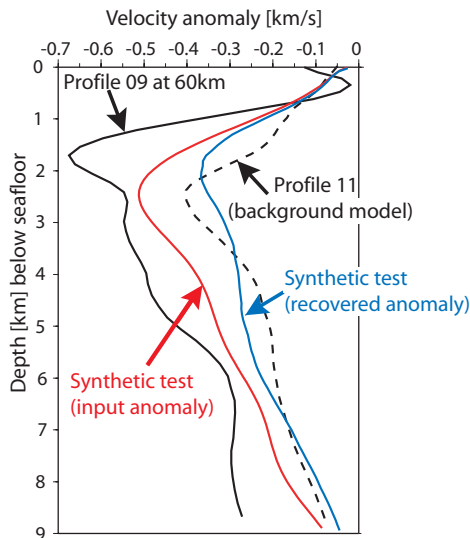


Figure 6.11: Velocity perturbation with depth in the median valley of Profile 11 (at 48 km profile distance) compared to “background” velocities of Profile 11 (see text, black dashed line) and to well constraint northern segment velocities extracted on ~ 4.1 Ma old crust of Profile 09 (black solid line). The results of the previous synthetic test (red and blue lines) are shown for comparison. The maximum perturbation is -0.4 km/s compared to average velocities of Profile 11. For a discussion, see text.

results). However, the portion of remaining cracks in these depths is a matter of speculation.

Several observations favour the role of elevated temperatures for the presence of the anomalous velocity structure beneath the median valley. An hour-glass shaped rise of the seafloor in the segment center and a continuous seamount chain off-axis suggest that the segment's melt supply is anomalously high. The high temperature Red Lion and Turtle Pits hydrothermal sites indicate elevated temperatures and heat sources at shallow or mid crustal levels, and the abundance of fresh glassy sheet flows in the area denotes a strong volcanic activity in recent years (*Haase et al.*, subm.). Hence, the velocity reduction may result from a temperature anomaly due to a recent intrusion of melt.

Assuming that the velocity contrast of 0.4-0.5 km/s is caused by cooling, this suggests that the axial upper portion of the lower crust is 700-900 K hotter (for $\delta V/\delta T = -0.57 \cdot 10^{-3} \text{ km s}^{-1} \text{ K}^{-1}$ *Christensen*, 1979). The solidus temperature of basalts, i.e. the onset of partial melting, depends on the MgO content in the form $T_s(^{\circ}\text{C}) = 18.3 \text{ MgO (wt \%)} + 907$ (*Sinton and Detrick*, 1993). Possible MgO values can provoke a wide range of temperatures, but for typical MgO MORB contents of 9 wt % (*Schilling et al.*, 1983) would result in $T_s \sim 1070^{\circ}\text{C}$. Thermal models including hydrothermal circulation predict off-axis temperatures of 200-300 $^{\circ}\text{C}$ in depths of 2-2.5 km below seafloor (*Henstock et al.*, 1993). Hence, the highest temperature likely reaches up to the solidus temperature. Since the tomographic method generally underestimates the amplitude of an anomaly, at least small portions of the mid crust on-axis may be partially molten. This is also confirmed by a sudden collapse of the seismic amplitudes in many seismic record sections of Profile 11 (cf. appendix D), which one might interpret as evidence for increased attenuation for rays passing through the anomalous model area. The median valley often marks the limit of available seismic offsets, or rays simply “pass around” the affected model portions (cf. the “shadow zone” in the datum corrected section in figure 6.9).

6.3 Results for Profile 07/08

Profile 07/08 runs in a spreading-parallel direction slightly south of the [5° S] fracture zone and covers the inside/outside corner pair. Figure 6.12 shows the Monte Carlo derived ensemble average together with a plot of associated uncertainties and weighted ray path lengths (DWS) for this line. On average 11 iterations are applied for each of the 100 ensembles to reduce normalized χ^2 to <1 . The final model reveals a *RMS* data misfit of 40 ms (38 ms for 6050 refracted and 56 ms for 650 reflected rays).

In the upper model portions, the close similarity to the FAST results is impressive (cf. figure 4.15). This is particular valid for the regions of highly heterogeneous velocity structure beneath the inside/outside corner pair and the median valley. The inside corner is characterised by anomalously high seafloor velocities of 5.2 km/s, which in case of the western flank abruptly increase to >6 km/s in the uppermost few hundred meters. Comparable velocity gradients result in velocities of 6 km/s in depths >1 km below seafloor beneath the transform facing slope. The velocities at the outside corner are slightly smaller, starting with seafloor velocities of 3-3.7 km/s and reaching up to 6 km/s within the upper-

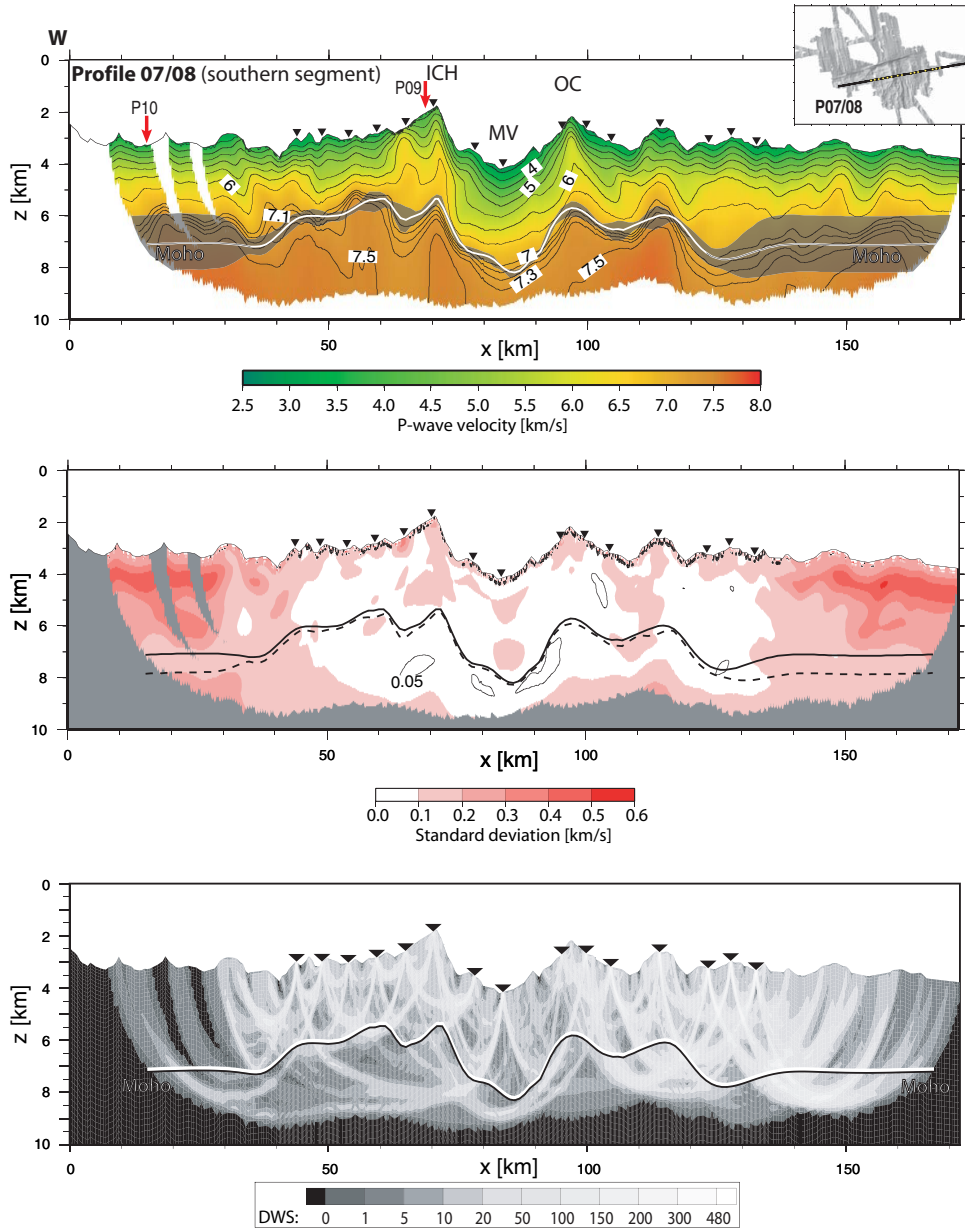


Figure 6.12: (Top): Final velocity model and Moho for Profile 07/08 derived from averaging all Monte Carlo solutions ($RMS=40ms$). Black shaded areas are 90% confidence intervals for Moho-depths within the applied uncertainty analysis. White Moho is directly controlled by reflection coverage. (Center): Corresponding standard deviation for velocity and reflector nodes (dashed line, standard deviation is added to the corresponding reflector depth). Velocity contours are drawn at $0.05km/s$. (Bottom): Derivative weight sum for the final velocity model. Models are plotted at $5\times$ vertical exaggeration.

most 1.5-2.5 km.

In the median valley a similar linear rise of velocities is observed as in the first-arrival model. Velocities increase from $\sim 2.7 km/s$ at the seafloor to $>7 km/s$ at 4 km depth. Obtained standard deviations for velocity nodes are on average somewhat higher than usually

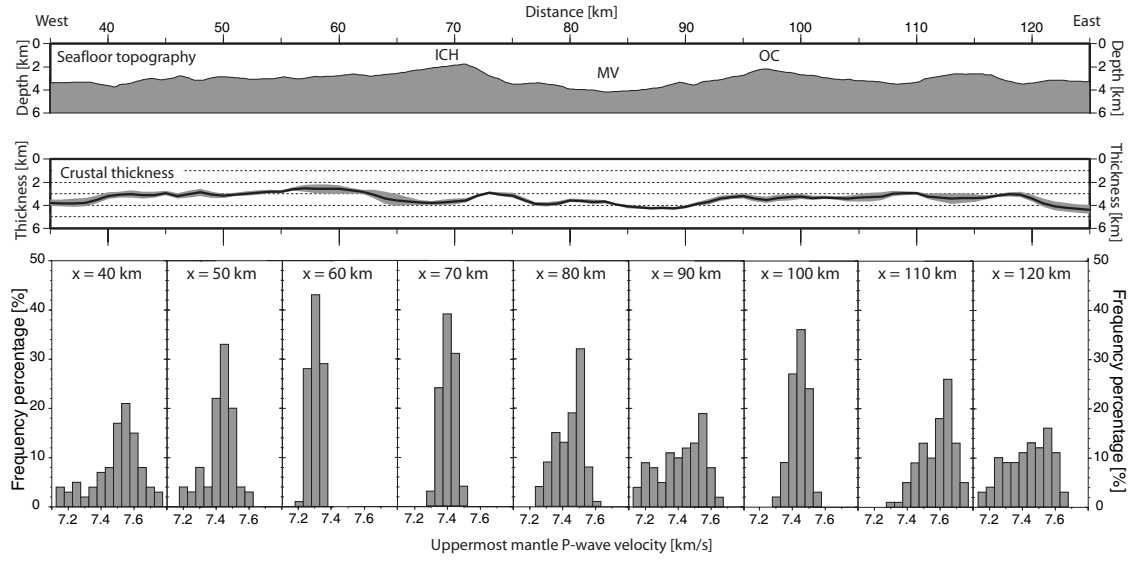


Figure 6.13: *Selected model features of Profile 07/08. (Top): Seafloor topography between 35km and 135km profile distance with no vertical exaggeration. (Center): Crustal thickness (black line) with corresponding 90% confidence bounds (black shaded areas) with no vertical exaggeration. (Bottom): Histograms of upper mantle velocities (binned in 0.05km/s intervals). Values are averaged over a horizontal distance of 10km between 1km and 2km depth beneath the Moho reflector in all Monte Carlo solutions and corresponding results are displayed every 10km.*

observed in this study. This might be related to the heterogeneous velocity structure and associated high velocity gradients.

Probably due to different assumptions concerning the weighting of horizontal vs. vertical smoothness in the joint tomography, the recovered velocities exhibit more horizontal structure at greater depths. This results in slightly lower velocities for the deeper model portions beneath the median valley and in slightly higher velocities beneath the adjacent rift flanks and beneath the outside corner massif. As already predicted by the FAST results, typical layer 3 velocities (6.5-7.2 km/s) are restricted to a ~ 1 km thick band, which often exhibits significant vertical velocity gradients. The major portion of the deeper model areas is characterised by velocities of 7.3-7.6 km/s. Since these velocities are intermediate between crust and mantle, the associated model region is referred to as *Moho transition zone*. Maximum observed velocities of 7.8 km/s (near 25 km and 110 km profile distance at ~ 5 km and ~ 4.6 km depth below seafloor, respectively) are virtually congruent to the FAST results.

In the models for Profile 07/08 the seismic Moho corresponds to the top of the transition zone. Derived Moho depths are well constrained by reflection coverage between 35 km and 125 km profile distance where obtained standard deviations are usually smaller than 0.25 km. The average crustal thickness along these reflector portions is 3.4 ± 0.4 km with slightly smaller values at the inside corner portions of the profile (3.2 ± 0.4 km) than at the outside corner portions (3.6 ± 0.4 km). Compared to the average crustal thickness of Profile 11 (7.8 ± 0.6 km) this would imply a reduction of more than 56% within an axial

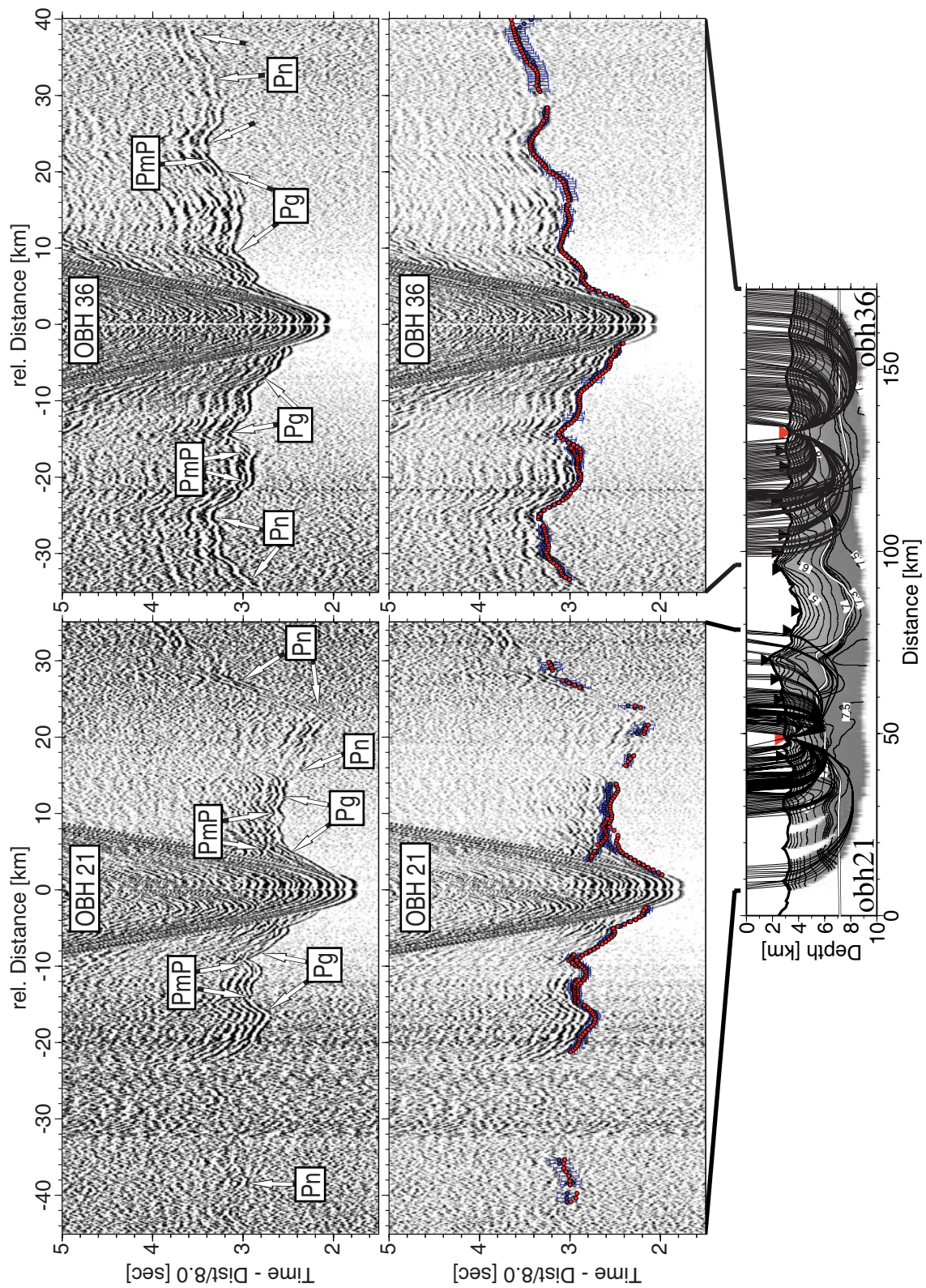


Figure 6.14: *Seismic Record sections of Profile 07/08 recorded by OBH21 and OBH36.*

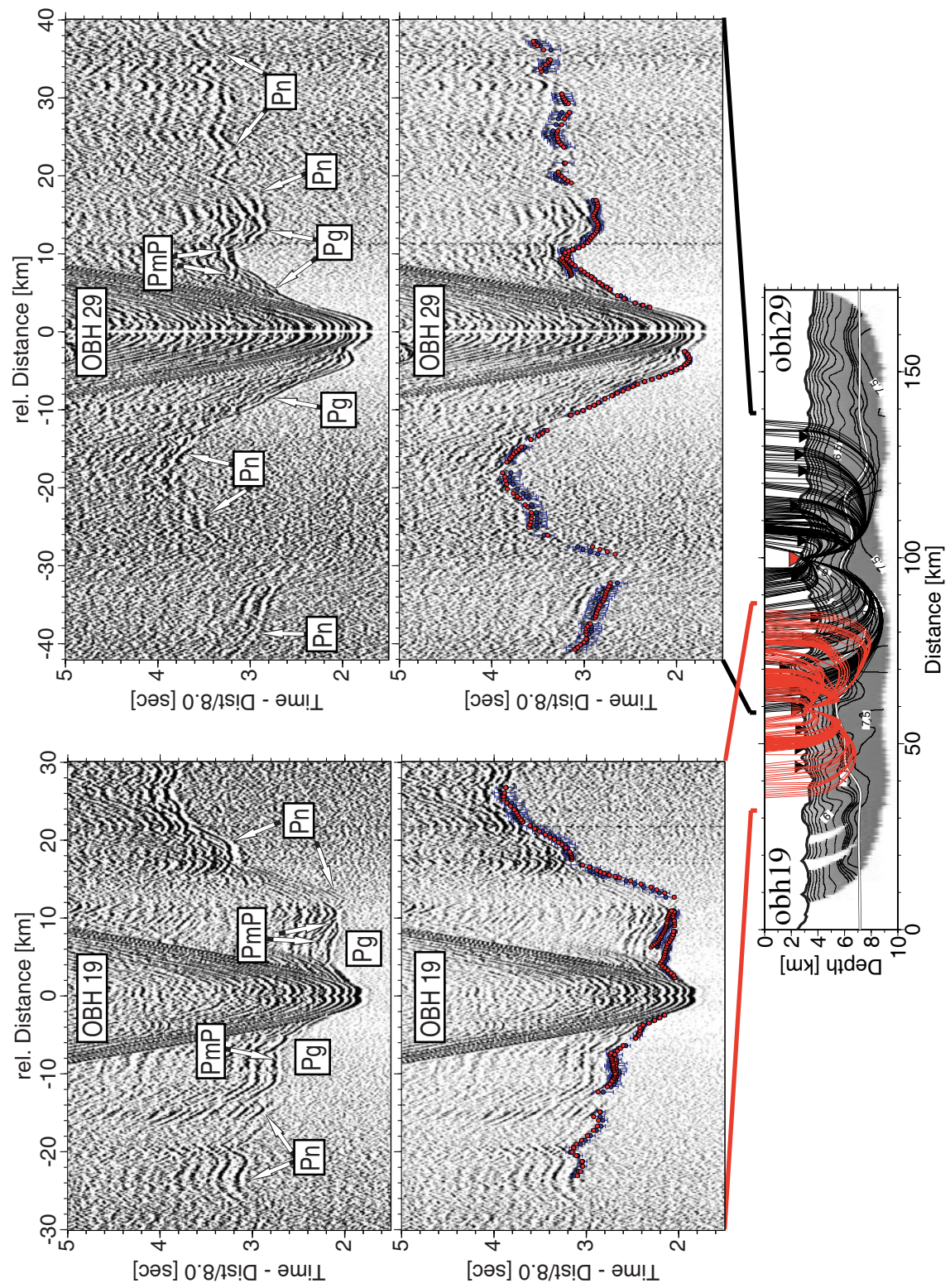


Figure 6.14: (continued) *Seismic record sections of Profile 07/08 recorded by OBH19 and OBH29.*

distance of only 50-60 km.

Figure 6.13 shows the seafloor topography and the variations in crustal thickness for the well constrained portions of Profile 07/08 with no vertical exaggeration. The lower part of the figure presents histograms of upper mantle velocities calculated for selected model sections spaced 10 km apart. The corresponding velocity values are extracted from all Monte Carlo solutions between 1 km and 2 km depth beneath the Moho reflector, averaged over a horizontal distance of 10 km and binned in 0.05 km/s intervals. Minimum values for crustal thickness (~ 2.5 km) are found at the western slope of the core complex, and spatially correlate with very low upper mantle velocities of ~ 7.3 km/s. Slightly thicker crustal portions (> 4 km) are observed in the median valley and at the model edges, and correlate with uppermost mantle velocities of 7.5-7.6 km/s. The highest velocities in this configuration can be found in the histograms obtained for 110 km profile distance, where velocities reach up to 7.6-7.7 km/s.

6.3.1 Density structure

Gravity ship data was acquired for the central portion of Profile 07/08 on RV METEOR cruise M62/4 as a part of the ASTERICS project (*Reston et al.*, in press). This data covers the seismic line between 20 km and 120 km profile distance, and hence the most interesting portions with the inside/outside corner pair and the median valley.

Different velocity density relationships are used to convert the Monte Carlo derived seismic velocities (cf. figure 6.12) into densities. The density model is divided into polygons, and the gravity response is calculated using a two-dimensional Talwani-type algorithm implemented in the forward modelling program MacRay (*Luetgert*, 1992). Edge effects are accommodated by laterally expanding the outermost structure to an arbitrarily large distance.

The empirically derived velocity density relation of *Carlson and Raskin* (1984) (hereinafter referred as CR84_lab), which was derived from laboratory experiments of rocks sampled at the seafloor and ophiolites, is used to convert the Monte Carlo derived velocity model into densities for the crust. A uniform density of $3.2 \cdot 10^3 \text{ Kg/m}^3$ is assumed for the upper mantle. The computation of the free air gravity anomaly (FAA) reveals similar features as the observed one (cf. solid line FAA in figure 6.15 a), but it continuously underestimates the observed values at the inside corner and overestimates corresponding values at the outside corner, respectively (the term “inside corner” is used here for the area west of the median valley and “outside corner” for the area east of the median valley; note that in this study a major portion of the outside corner crust actually consists of crust originally formed at the inside corner prior to a ridge jump (*Reston et al.*, 2002)). All lines in figure 6.15 a are shifted to zero-mean and no regional gravity trend is applied.

One possible explanation for such a systematic asymmetry is that the densities at the inside corner are consistently higher than those at the outside corner. Hence, an asymmetric density model is used for the crust together with a more realistic density model for the mantle. For the inside corner crust (0-83 km profile distance), a velocity density relation of (*Carlson and Raskin*, 1984) (hereinafter referred as CR84_log) is used, which is derived from in situ downhole logs of largely young oceanic crust and which is intended

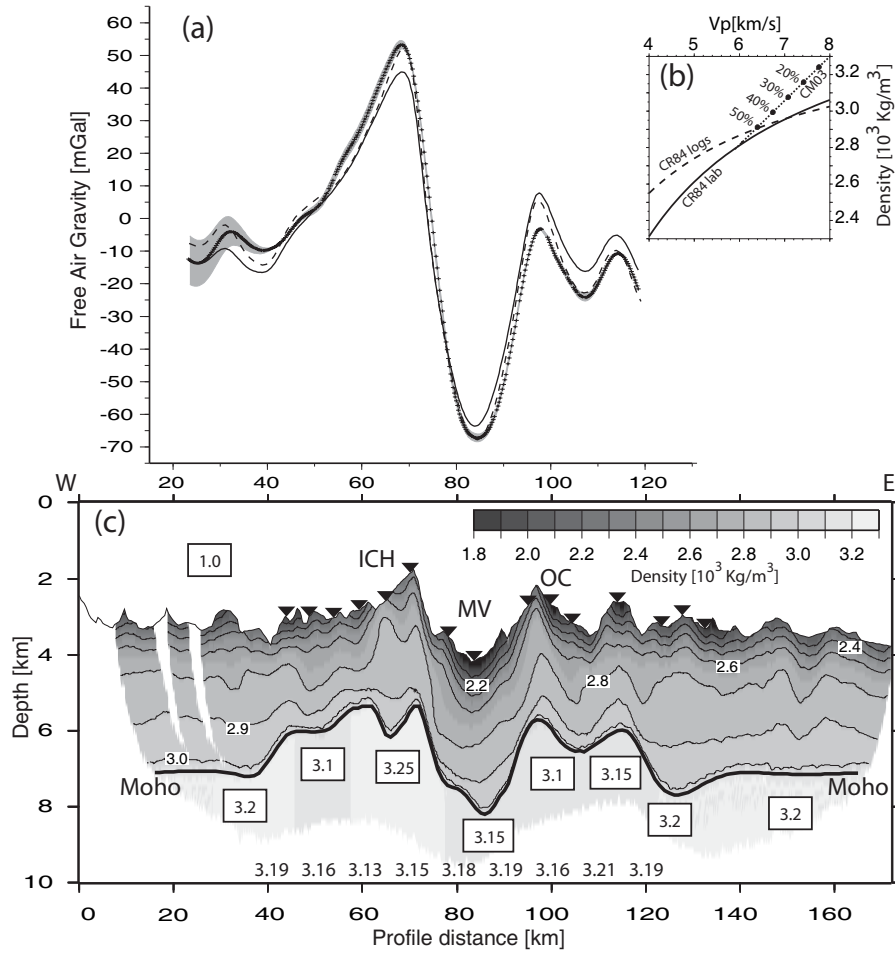


Figure 6.15: (a): Observed (crosses) and predicted (lines) free air gravity anomaly (FAA) for a variety of density models. The black solid FAA line is obtained from the CR84_lab velocity density relation (see figure b and text for details) for the crust and a constant mantle density of $3.2 \cdot 10^3 \text{ Kg/m}^3$. RMS is 6.6 mGal. The black dashed FAA line is obtained assuming an asymmetric velocity density relation for the crust (CR84_logs together with CM03 for inside corner crust and CR84_lab for outside corner crust) and the CM03 relationship for the entire mantle. RMS is 4.0 mGal. The lowest RMS (2.1 mGal) is obtained with the density model in c (see below). The grey shaded FAA derived from the model in c reflects the uncertainty bounds (± 1 standard deviation for crustal velocity nodes and reflector nodes) of the Monte Carlo analysis. All curves have zero mean. (b): Velocity density relationships. Dashed line corresponds to that of Carlson and Raskin (1984) obtained from in situ measurements at DSDP downhole logs. Solid line is the relationship of Carlson and Raskin (1984) for the lower crust obtained from laboratory experiments and the dotted line is derived from Carlson and Miller (2003) to account for serpentization in the mantle. Annotated dots show degree of serpentization. (c): Final density model. The CR84_lab velocity density relation is used for the entire crust (densities are colour coded and marked by iso lines). Mantle densities (black square annotations) are obtained by forward modelling. For comparison, the CM derived mantle densities for the velocities of figure 6.13 are displayed at the model bottom.

to account for the effects of large scale porosity in layer 2. However, crustal densities obtained from this relation are up to $0.3 \cdot 10^3 \text{ Kg/m}^3$ higher than those obtained from CR84.lab. The CM03 relation derived from *Carlson and Miller* (2003) is used for the Monte Carlo derived upper mantle velocities (cf. figure 6.13) to account for the dependence of V_p with the degree of serpentinization. For the same range of velocities CM03 predicts higher densities for peridotites less than 50% serpentinized than the relations of *Carlson and Raskin* (1984) for the gabbroic lower crust (cf. figure 6.15). Since serpentinized peridotites were dredged at the scarp of the inside corner (*Reston et al.*, 2002), it is likely that parts of the seismically defined “crust” actually consist of highly serpentinized peridotite (e.g. *Collins and Detrick*, 1997; *Schroeder et al.*, 2002). Hence, the CM03 relationship is also applied to lower crustal rocks ($V_p > 6.4 \text{ km/s}$) at the inside corner. The obtained density model improves the overall fit of the observed data (dashed line in figure 6.15) but still fails to explain the observed asymmetry at the inside/outside corner pair.

The observed trend of higher densities beneath the inside corner and lower densities beneath the outside corner, respectively, could also be related to asymmetries in mantle densities. The depth distribution of earthquakes in the median valley suggests that extension is accommodated along normal faults that penetrate into the upper mantle (*Tilman et al.*, 2004). The classical model of *Tucholke and Lin* (1994) for the formation of inside corner highs predicts tectonic extension along a major detachment fault which soles out near the brittle ductile transition. It is possible that single faults act as pathways for the penetration of fluids, leading to a spatially variable degree of alteration in the upper mantle. Hence, in assuming the CR84.lab relation for the entire crust, an alternative density model is obtained where mantle densities are derived by forward modelling.

The resulting density model is shown in figure 6.15 c. Adopting the Monte Carlo derived uncertainty limits for (crustal) velocity nodes and Moho depths (± 1 standard deviation) results in uncertainty bounds (grey shaded area) symmetrically distributed around the computed FAA. However, except for the western model edge where Moho depths are not well constrained, predicted uncertainties are rather negligible. This model improves the fit of the observed FAA by $\sim 2 \text{ mGal}$ when compared with the model where asymmetry is assumed for the crust.

Modification of mantle densities leads to discrepancies of $\sim \pm 0.1 \cdot 10^3 \text{ Kg/m}^3$ from those values obtained by adopting the CM relationship for the upper mantle velocities. This difference could be related to (1) incorrect velocities and Moho depths, especially beneath the inside and outside corner; (2) the fact that densities obtained from average uppermost mantle velocities do not correctly represent the mantle variations on a larger scale due to the limited depth penetration of P_n rays in this study, and (3) a nonuniform velocity density relationship for both the crust and the mantle.

A possible explanation for option 1 would be an underestimation of seismic velocities beneath the ICH. Higher velocities are sampled on Profile 02, which runs perpendicular to Profile 07/08 at the eastern slope of the ICH (cf. Profile 02 in section 6.4). These higher velocities could be due to seismic anisotropy, which is related to a preferred ridge-parallel orientation of cracks and fractures. However, the lack of comparable velocity deviations at the other profile intersections suggests a local phenomenon.

Since the density contrast between the lower crust and the upper mantle is rather moderate, unreasonably large uncertainties in Moho depths would be required to produce

the observed density variations. Option 2 cannot be ruled out since histograms of upper mantle velocities often reveal larger scattering even at shallower mantle depths (cf. the western outside corner slope in figure 6.13). However, the complicated and highly variable velocity structure of the profile as well as tectonic models for the evolution of inside and outside corners in general (c.f. *Tucholke and Lin, 1994*) and for this study area in particular (*Reston et al., 2002*) suggest that option 3 could also be a valid explanation.

6.4 Results for Profiles 02-05

Figure 6.16 shows the locations of Profiles 02, 04 and 05 with sections of Profile 07/08 and Profile 09 in the bathymetric framework of the ICH area. The shorter profiles run perpendicular to Profile 07/08 and cover the slopes of the core complex and the center of the median valley. For a more detailed view at the tomographic solutions, see figure 6.17.

Unlike for the longer profiles, no systematic assessment of starting model variations and traveltimes errors was done, i.e. the tomographic solutions for Profiles 02-05 are based on a single iterative approach. Inversion is started from a 1D velocity model and a flat lying Moho, both obtained from the final solution of Profile 07/08 sampled at the corresponding line intersection. This results typically in initial RMS data misfits of 140-200 ms.

Profile 05

Profile 05 covers 44 km of the median valley. The tomographic solution of figure 6.17 is based on the recordings of 3 stations, yielding a final RMS data misfit of 32 ms and 31 ms for a total of 570 refracted and 180 reflected arrivals, respectively.

The obtained velocity model suggests a relatively uniform structure for the entire crust. Velocities increase to 5.5-6 km/s within the uppermost 2 km and then rise somewhat more gentle to 6.5-7 km/s directly above the Moho, which can be found in 3.4-4 km depth beneath the seafloor. From the few available reflections and the often poorly constrained lower model portions it is difficult to assess the thickness variations of the crust. However, a thickness of 3.4 km near 12 km profile distance and a thickness of 4 km near 22 km profile distance suggest a crustal thinning towards the transform fault. The uppermost mantle is constrained for a small model portion between 20 km and 30 km profile distance. Here, the transition towards higher velocities occurs relatively abrupt and obtained values reach up to 7.5 km/s a few hundred meters beneath the Moho.

Profile 02

Profile 02 covers in its northern part (<20 km profile distance) the eastern ICH slope at roughly half of its total exhumed height and close to its steepest portion. The southern part of the profile (20-50 km) runs through a complex area of faulted blocks associated with the southward turn of the median valley and its adjacent bounding faults. With a total of 6 seismic stations and 1000 refracted and 250 reflected arrivals, Profile 02 provides the most densely sampled dataset of the three shorter profiles. The tomographic model in

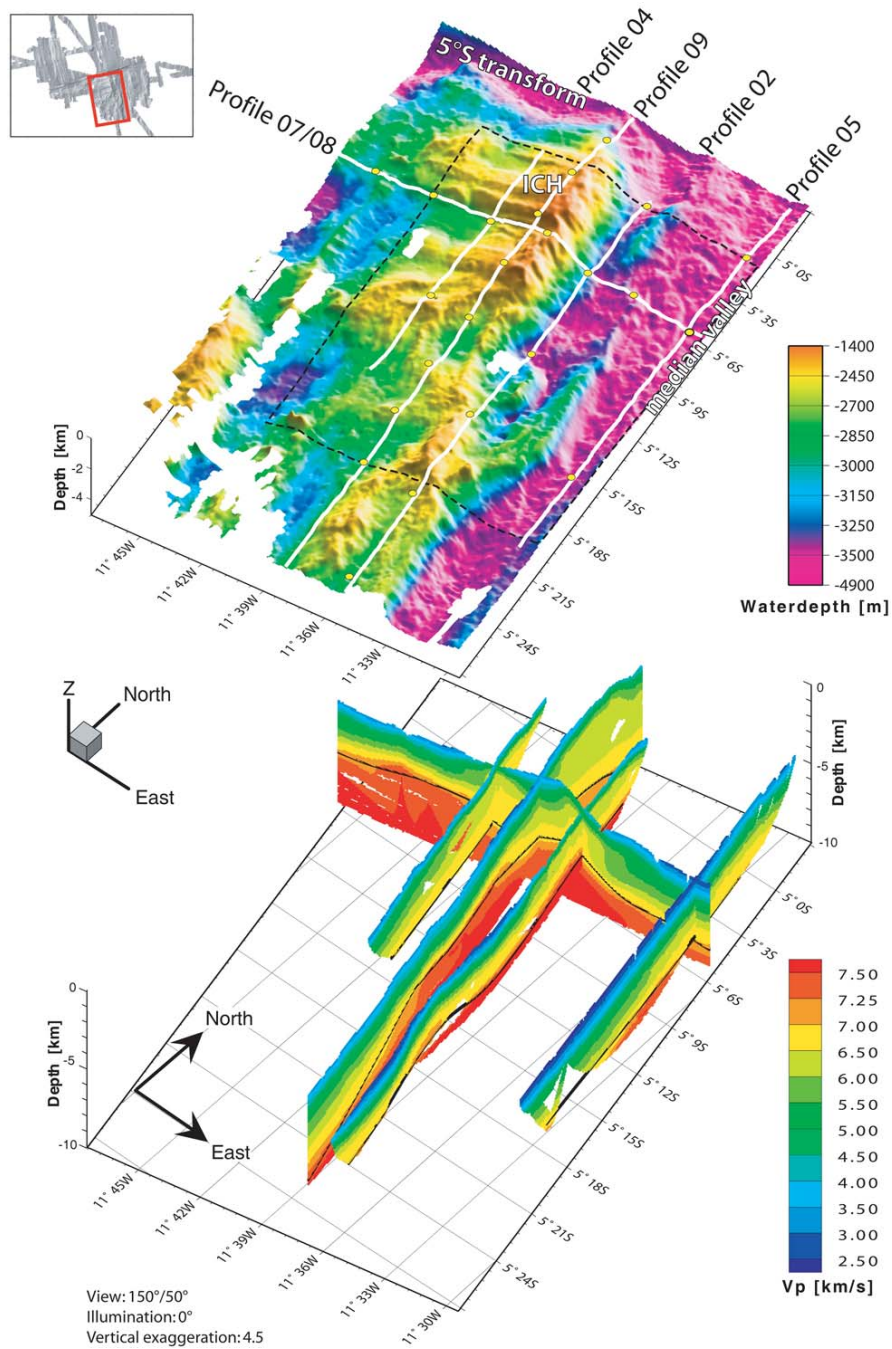


Figure 6.16: (Top): Perspective view of the ICH area with Profiles 02, 04 and 05 and sections of Profiles 07/08 and 09 in the bathymetric framework of the ICH area. Seismic profiles are projected on the seafloor (white lines). Yellow circles denote the locations of the seismic stations. The black-dashed square marks the area of the 3D crustal thickness interpolation of figure 7.3. (Bottom): Corresponding tomographic velocity models (colour coded) and Moho depths (black lines).

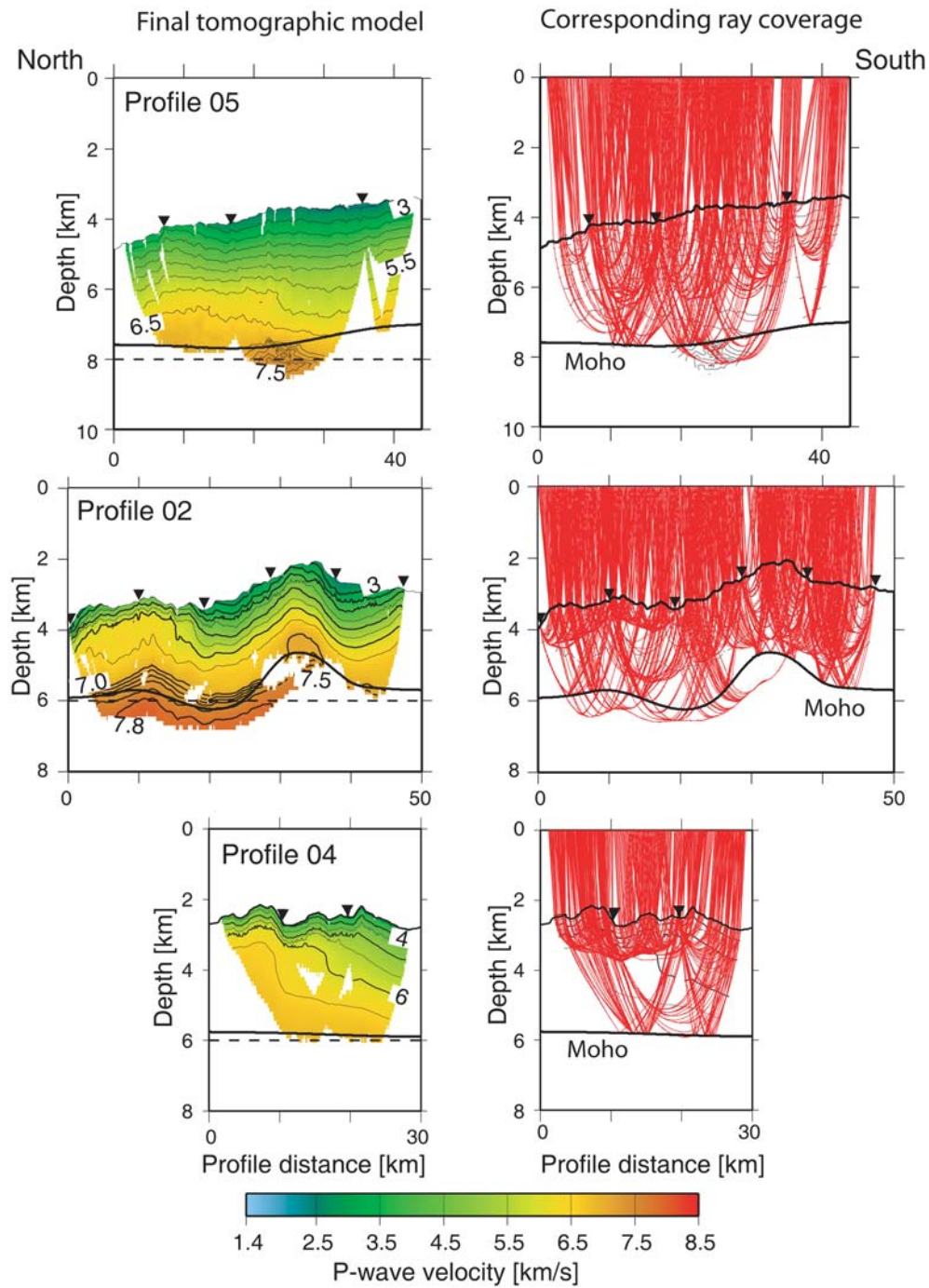


Figure 6.17: Tomographic models (left) and corresponding ray coverage (right) for the shorter profiles: Profile 05 (top), Profile 02 (center) and Profile 04 (bottom). View is from the West. Contour spacing and colour table are the same as for the longer profiles. Models are plotted at 5× vertical exaggeration. The black-dashed line indicates the initial reflector. RMS data misfits are (from top to bottom) 32ms, 39ms and 43ms, respectively.

figure 6.17 reveals a RMS data misfit of 33 ms for refracted and 54 ms for reflected arrivals.

The resolved velocity structure for the crust suggests strong lateral heterogeneities. In the area of the ICH slope, velocities increase to 6 km/s in the uppermost few hundred meters. Further south, seafloor velocities < 3 km/s are consistently found and an almost linear increase results in velocities of < 6 km/s for roughly the half depth range of the crustal portion. Obtained thicknesses for the crust vary between 2.4-2.7 km near the ICH slope and 2.7-3 km in the southern portion of the profile. Beneath the Moho, velocities rapidly increase to ~ 7.7 -7.9 km/s.

Compared to corresponding values of Profile 07/08 at the line intersection, the obtained velocities for Profile 02 are consistently higher (up to 1 km/s) and the resolved Moho depths are 0.3-0.4 km shallower. Although the available data quality is rather moderate, which is probably related to the profile's location within an extremely tectonized regime, a tomographic artefact due to poor traveltimes picks seems unlikely for the observed discrepancies. Possible causes include (1) topographic effects caused by the steep flank of the ICH, (2) the use of long (horizontal) correlation lengths in the tomographic approach of Profile 07/08, resulting in a suppression of locally higher velocities and (3) seismic velocity anisotropy. The first option is likely since slope angles of up to 24° (i.e. $\sim 45\%$ gradient) suggest significant deviations of the true ray paths from the assumed vertical plane. Adopting the seafloor bathymetry extracted 500 m uphill for the 2D tomographic modelling results in noticeable lower velocities for the upper model portions. However, it does not significantly affect the very high sub-Moho velocities.

The use of shorter correlation lengths for Profile 07/08 results in locally higher velocities beneath the eastern ICH slope, especially in the uppermost 1.5 km; it does not result in noticeable higher mantle velocities. Seismic velocity anisotropy, which is caused by a preferred orientation of cracks and fractures, could account for the observed discrepancies, where the faster orientation is given by the strike of the ICH scarps. However, there is no indication of significant anisotropy at the other profile intersections.

In conclusion, there is a major discrepancy in upper mantle velocities sampled at Profile 02 and Profile 07/08 which is too large to be explained by topographic effects and tomographic artefacts. Velocities of ~ 7.8 km/s in depths of 3 km disagree with corresponding values of ~ 7.5 km/s in depths of 4-5 km below seafloor. Thus, seismic velocity anisotropy appears to be the most likely explanation. As an alternative explanation, the possibility of strong lateral heterogeneity with dimensions beyond the resolution of (across-axis) seismic refraction data is discussed in section 7.3.2 for this particular region.

Profile 04

Profile 04 covers the more gentle dipping western slope of the ICH. Due to instrument problems, it consists of only 2 seismic stations. The tomographic solution in figure 6.17 is based on the inversion of 390 refracted and 120 reflected arrivals yielding a RMS data misfit of 42 ms and 48 ms, respectively. The resolved model structure indicates a decrease of crustal velocities to the south. Virtually no turning rays in the lower portions of the crust suggest that obtained Moho depths are only poorly constrained. However, the resolved crustal thickness ranges from 3-3.4 km.

Chapter 7

Interpretation and Discussion

Seismic measurements of crustal thickness at mid-ocean ridges provide a consistent view of the melt flux from the mantle to the crust and the partitioning of spreading into magmatism and faulting. The perhaps most important result from this study is that for the Mid-Atlantic Ridge at 5° S crustal thickness varies significantly both on an intrasegment scale and from one segment to the adjacent one.

7.1 Northern segment

7.1.1 Across-axis variations in crustal thickness

The seismic model of Profile 11 reveals an average across-axis crustal thickness of 7.8 ± 0.6 km for the northern segment. Although bathymetric coverage is not complete, the resolved morphology suggests that the profile covers the center of a 2nd order segment. Since along-segment variations are large, for comparison with global compilations it is necessary to assess the along-segment mean crustal thickness (see below).

A similar average crustal thickness of 7.5 km is found across a magmatically active axial volcanic ridge at 59° N, where seismic, electromagnetic and magnetotelluric soundings for the first time provided convincing evidence for a magma chamber beneath a slow spreading ridge (*Sinha et al.*, 1998; *Navin et al.*, 1998). But different to 5° S, the crustal thickness at the Reykjanes Ridge is relatively constant; the thickest portions are found beneath the spreading axis, and only minor thinning of ~ 0.75 km is observed over a distance of 50 km off-axis. In the segment north of the 5° S FZ, crust of 7.5 km thickness is found on-axis. There is no evidence for significant thinning by extensional faulting as the crust moves off-axis. In contrast, it thickens to 9.2 km in about 10 km distance east of the ridge-axis and then continuously thins to 6 km in 65 km distance at the line intersection of Profiles 9 and 11. Even if the increase in thickness might partly be an artefact of the short-scale morphology of the ridge flank, the trend to thicker crust east of the ridge-axis remains.

This irregular pattern may result from a temporal variability in the crustal emplacement process, which can either arise from a variable melt production or a variable melt delivery. This idea is confirmed by the observation that the continuous seamount chain in flow-line of the segment center shows gaps for distances greater than 60 km off-axis and finally seems to disappear at the edges of the bathymetric coverage. In the first

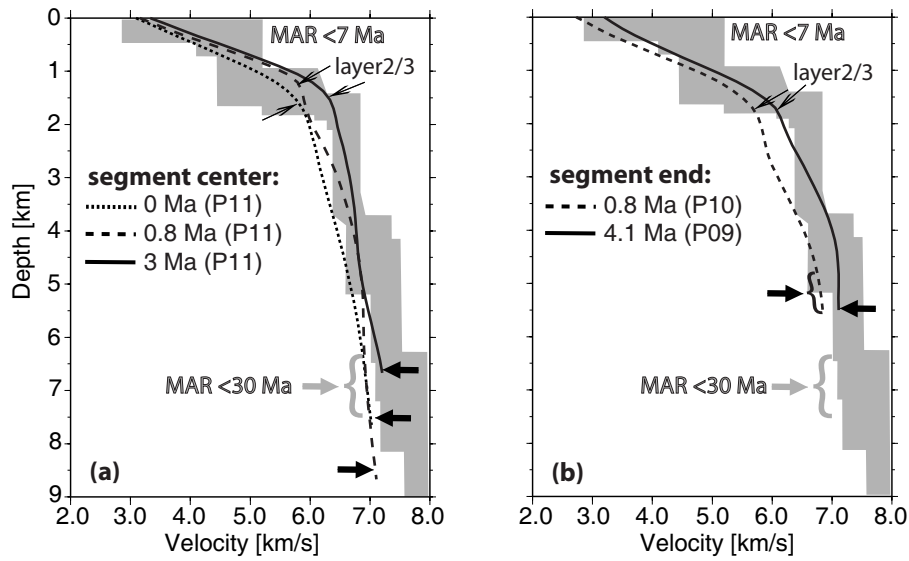


Figure 7.1: Velocity depth profiles (averaged over 5km profile distance) through northern segment crust, in comparison with an envelope of velocity depth profiles from the Mid-Atlantic Ridge for crust aged 0-7 Ma (White *et al.*, 1992). Across-axis variations: (a) Segment center crust on Profile 11: at 0 Ma (short-dashed line), at 0.8 Ma (Profile intersection with line 10; long-dashed line), and 3 Ma (solid line). (b): Segment end crust, extracted 10km north of the 5° S FZ: at Profile 10 (on crust aged 0.8 Ma; long-dashed line), and Profile 09 (on crust aged 4.1 Ma; solid line). Black arrows indicate Moho depth; grey arrows show Moho depths for Atlantic crust aged < 30 Ma from a compilation of White *et al.* (1992).

scenario, the thicker crust beneath the ridge mountains was formed during a period of mantle melting in which the average melt production was higher than before and perhaps also higher than today. Based on observations of cyclic variations of the residual mantle bouguer anomaly (MBA) over the run of segments at 25°-27° N, Tucholke *et al.* (1997) suggested that episodic crustal thickening and thinning occurs at intervals of 2-3 Ma. They attributed this pattern to the periodic formation of buoyant melt diapirs and/or mantle heterogeneities (Kuo and Forsyth, 1988; Lin *et al.*, 1990). Their results are compatible with seismic models, which reveal crustal thickness variations of 2-4 km across the ridge-axis within the predicted time scales (Hosford *et al.*, 2001). However, in case of the northern segment, the magmatic episode seems to persist at least over the last 3.7 Ma, reaching its maximum extent perhaps in the last 1 Ma.

In the second scenario, the relative amount of melt delivery could have changed due to small changes in plate geometry. Magde and Sparks (1997) showed that melt focussing and average crustal thickness might actually be controlled by the spreading rate and the degree of plate segmentation, as reflected in the segment length/offset ratio. Their results indicate that a higher ratio of segment length/offset should result in an increase of average crustal thickness. In this context it is noteworthy that the change of the active ridge axis in the southern segment ~0.75 Ma ago correlates with the period of greatest melt flux in the northern segment. However, how the ridge jump has changed the regional pattern of

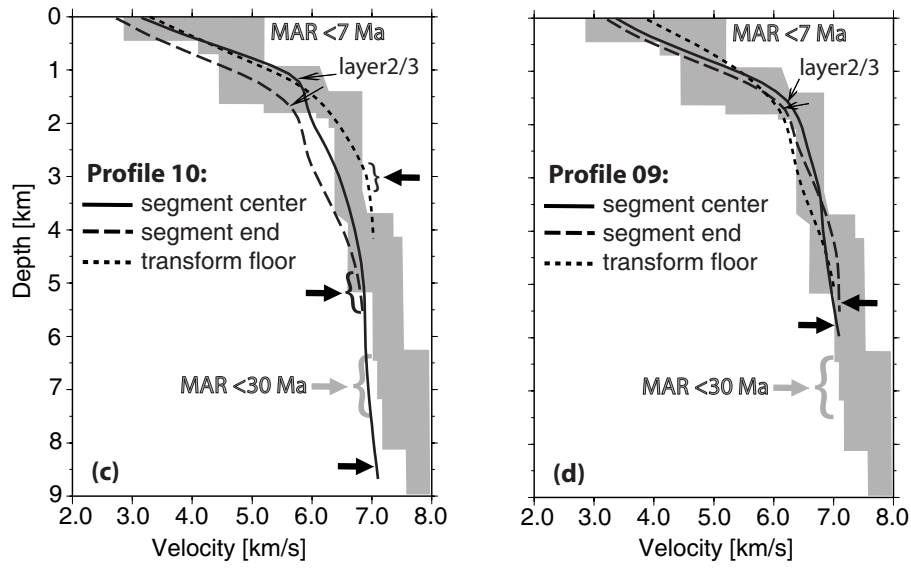


Figure 7.1: **(continued)** Along-axis variations: (c) Crust on Profile 10: at the segment center (solid line), at the segment end (long-dashed line), and at the transform floor (extracted at the deepest portion; short-dashed line). (d): Crust on Profile 09: at the segment center (extracted at 50km profile distance; solid line), at the segment end (long-dashed line), and at the transform floor (short-dashed line).

plate segmentation remains unclear, due to the lack of bathymetric coverage.

In an alternative scenario, the differences in crustal thickness may simply arise from an asymmetric partitioning after the crust formed, with preferential thinning on the western flank of the ridge axis. This asymmetry might be due to differences in the fault geometry of the flanks or to variations in crustal accretion; but it is rather unlikely that such a process can cause crustal thickness variations on the observed time-scale. Nonetheless, the lower topography west of the spreading axis suggests systematic asymmetries in the emplacement process or in the tectonic processes of rifting. However, the seismic model of Profile 11 cannot reveal such differences due to higher uncertainties for the western model portions.

7.1.2 Along-axis variations in crustal thickness

The seismic model of Profile 10 confirms that along slow-spreading ridges the melt supply is focussed at the segment center (e.g. Kuo and Forsyth, 1988; Lin *et al.*, 1990; Tolstoy *et al.*, 1993; Detrick *et al.*, 1995). There is a substantial decrease in crustal thickness from 9 km at the segment midpoint to 5 km in ~10 km distance from the transform offset and to only 3 km directly beneath the transform flank. If seismic layer 3 represents the gabbroic portion of the crust, its reduction in thickness to ~50% at the segment end and its vast absence beneath the transform suggests that the greatest volume of melt enters the crust at segment midpoints. However, the seismic model of Profile 09 suggests a temporal variable process. Although revealing a similar layer 3 thickness at the segment end, the variation in crustal thickness on Profile 09 is much smaller (6-5.2 km). The mean along-axis crustal

thickness of Profile 10 and Profile 09 is 6.8 ± 1.3 km and 5.6 ± 0.3 km, respectively. This confirms that the melt flux (volume of melt per unit time) has effectively increased in the last 4 Ma, and at present reaches “normal” values for Atlantic crust younger than 30 Ma (7 ± 0.6 km *White et al.*, 1992). The results also suggest that this increase in melt flux goes along with a more focussed supply to the segment center.

Seismic studies near 35° N show a similar variation in crustal thickness from 8-9 km at the segment center to 2.5-5 km directly at the Oceanographer fracture zone, resulting in an average crustal thickness of 5.1-5.7 km (*Hooft et al.*, 2000; *Canales et al.*, 2000b; *Hosford et al.*, 2001; *Dunn et al.*, 2005). Anomalous low velocity structures overlying the crustal root are interpreted as a magma plumbing system which redistributes the melts laterally and vertically through the overlying portions of the crust (*Magde et al.*, 2000). Magma which is focused before reaching the lower crust then travels vertically through the ductile region in pipe-like features, following the high-temperature and low-strength pathways left by previous upwelling events. Upon reaching the base of the lithosphere, the magma interacts with extensional tectonic stresses and propagates through the brittle layer both laterally and vertically as dikes (*Magde et al.*, 2000). This mechanism is proposed to generate the observed relatively uniform thickness of the upper crust (velocities < 6 km/s) for the area near 35° N. A similar uniform structure for the upper crustal portion is consistently found in the northern segment. In this context, the observed low-velocity anomaly on Profile 11, which is centered at a depth of 2-3 km beneath the median valley, might correspond to a combination of increased temperatures and retained melt left behind by magmatic intrusions in a crustal plumbing system. In the view of *Magde et al.* (2000), this system would primarily extend in an along-axis direction due to extensional tectonic stresses and might be fed from a central source region probably located beneath the segment center bulge.

7.1.3 Ridge morphology and crustal thickness

The results indicate that along-axis variations in crustal thickness influence axial seafloor depths (e.g. *Sempere et al.*, 1990; *Lin et al.*, 1990; *Tolstoy et al.*, 1993). The seismic model of Profile 10 shows that if crustal thickness increases the axial depth within a segment decreases. For example, the pronounced seafloor bulge on Profile 10 is underlain by anomalously thick crust. In contrast, the relatively uniform seafloor depths on Profile 09 reflect only small variations in crustal thickness. However, the asymmetric across-axis relief of the ridge-axis (cf. figure 2.3) suggests that morphology is not solely predicted by isostatic support but by a more complex interplay between lithospheric geometry, strength and isostasy, plate motion geometry and spreading rate asymmetry (e.g. *Pockalny et al.*, 1997; *Sloan and Patriat*, 2004; *Buck et al.*, 2005). For rift topography generated by tectonic stretching, wider and deeper grabens are predicted where the brittle layer is thicker and stronger (*Shaw and Lin*, 1993, 1996). Since oceanic crust is rheological weaker than oceanic mantle, the net effect of crustal thickening is to reduce the overall strength of the lithosphere. Hence, the presence of locally thickened crust in the segment center is associated with a weaker and thinner lithosphere with smaller fault heaves and spacings, and a narrow, shallow rift valley. This usually results in an overall decrease in across-

axis relief. However, this trend is not observed in the northern segment, where the total fault heave reaches up to 1.5 km in the segment center (cf. figure 2.3). Furthermore, the width of the median valley floor does not show systematic variations and is smallest at roughly halfway between the bulge and the transform. This suggests that it is not crustal thickness alone that governs the ridge morphology. Possible other factors include a thermal impact that is out of phase or unassociated with the measured crustal thickness, and in which the topography is not compensated due to the short elapsed time since the last magmatic event (*Hoofft et al.*, 2000). *Curewitz and Karson* (1998) showed that faulting on the walls of the rift valleys could be strongly influenced by magmatic processes such as subaxial dike intrusion. In particular, magmatically active segments may have muted axial relief as dike intrusion could have accommodated extension otherwise expressed as normal faulting. However, this mechanism could rather explain the smaller relief on the western bounding walls. Interestingly, results from a magmatically active segment of the intermediate spreading Juan de Fuca Ridge show that the maximum axial graben heights are found where the brittle layer is thinnest, not thickest (*Carbotte et al.*, 2006). This suggests that the rift topography associated with seafloor spreading is likely to be much more complex; though crustal thickness plays a major role, it is by far not the only controlling factor.

7.2 Velocity structure of the transform valley

Close to the transform in the northern segment, the velocity depth functions show consistently lower velocities compared to the segment midpoints, at least in the uppermost 3 km. This is commonly attributed to a dominant role of alteration and fracturing of the cooler and thinner crust and commonly observed in the proximity of fracture zones (for a compilation of the crustal structure of North-Atlantic fracture zones see *Detrick et al.*, 1993). However, the velocity structure of the transform valley seems to be different. The velocities in the upper layer are higher and the transition in the velocity gradient from layer 2 to layer 3 is less pronounced. In case of Profile 10, this results in an almost linear increase of velocities with depths. High velocity gradients and the absence of a normal layer 3 may be interpreted as a thin basaltic crust overlaying partially serpentinized mantle rock, as suggested by *Detrick et al.* (1993) for several Atlantic fracture zones. Velocities of 6-7 km/s on Profile 10 would indicate that 30-60% serpentinization will be required to reduce the compressional wave velocity of peridotite to these values (*Carlson and Miller*, 2003). Such a high percentage of serpentinization can only arise if the overlying rock is highly fractured to provide pathways for seawater into the upper mantle, which has to be cooler than the 400-500 °C limit for serpentinization (*Hacker et al.*, 2003). However, the relatively high velocities in the upper layer may also be related to the close proximity to tectonically modified crust of the southern segment. Seismic refraction velocities are average velocities over entire crustal blocks measuring up to tens of kilometers across. In the narrow transform valley of Profile 09, the southern flank of the transform passes directly into the northern flank of the core complex. Hence, the observed velocity structure on this line might be affected by the anomalously high velocities found at shallower levels at the inside corner flank. It is possible that the uplift of deeper crustal rocks at the adjacent slope during core complex formation (*Tucholke and Lin*, 1994; *Escartin and Can-*

nat, 1999) in combination with mass wasting processes at the steep flank resulted in the emplacement of these rocks at the transform valley. The upper layer might then consist largely of a mixture of extrusive products from the adjacent segment end. However, the presence of smaller portions of serpentinites at shallower depths, preferentially associated with fractures in the transform trough, seems likely.

On Profile 09, the Moho directly beneath the transform is unconstrained by the seismic data, which might suggest that velocities at deeper levels are mainly controlled by fracturing and the degree of alteration. The anomalously thin crust of 2.8-3.5 km on Profile 10 is consistent with previous studies at MAR fracture zones (e.g. *Detrick et al.*, 1993). Crust of 2-3 km (in cases <1 km) based on seismic observations is found for example at the Kane fracture zone (*Purdy and Detrick*, 1986), the Oceanographer fracture zone (*Sinha and Loudon*, 1983), the Charlie Gibbs fracture zone (cf. figure 7.2 *Whitmarsh and Calvert*, 1986), the Vema fracture zone (*Louden et al.*, 1986), and several smaller transform and non-transform offsets of the MAR (e.g. *White et al.*, 1992; *Detrick et al.*, 1993; *Hooft et al.*, 2000; *Canales et al.*, 2000b). However, more “normal” crustal thicknesses (4.5-5 km) are also present along many portions of these fracture zones (*Detrick et al.*, 1993). The compilation of fracture zone crust of *White et al.* (1992) obtains a mean crustal thickness of 4.0 ± 1.3 km with some outliers reaching up to values >6 km thickness. The region of thinnest crust is often related to a rise of the Moho over a relatively broad zone (15-30 km) centered beneath the deepest portion of the trough resulting in a gradual thinning of the crust towards the fracture zone (e.g. at Kane FZ). But similar to Profile 10, the area of thinnest crust can also be centered beneath the edges of the transform valley (e.g. at Vema FZ), and the transition to relatively normal thicknesses on either side can occur very abrupt (i.e. over a distance of at most a few kilometers). Away from the transform and non-transform offsets, anomalously thick crust (>8 km) is found in some of these segments (e.g. *Detrick et al.*, 1993; *Hooft et al.*, 2000; *Canales et al.*, 2000b).

In most of the above named cases, crustal thinning within the fracture zones is related to a very thin or absent seismic layer 3, resulting in relatively high velocity gradients ($1\text{-}2\text{ s}^{-1}$) throughout the entire crustal section. Unusually low compressional wave velocities are frequently observed beneath the trough, although the adjacent flanks can locally exhibit higher velocities (e.g. at Vema, Kane FZ) (*Detrick et al.*, 1993). Some studies have found material with seismic velocities in the range of 7.2-7.6 km/s at the base of the crust, which have been interpreted as a “crustal root” or “mantle”, respectively (*Detrick et al.*, 1993; *Canales et al.*, 2000b). In case of Profile 10, velocities of 7.2 km/s would imply 20-25% serpentinitization of mantle peridotite (*Carlson and Miller*, 2003). Alternatively, these velocities may correspond to a mixture of mafic and ultramafic rocks (e.g. *Spudich and Orcutt*, 1980).

7.3 Southern segment

The seismic models for the southern segment comprise a completely different tectonic setting. Obtained crustal thicknesses are very small (2.4-5.5 km) and the Moho topography usually “follows” the seafloor bathymetry. This suggests that topography is tectonically maintained (e.g. *Tucholke and Lin*, 1994). The rate of crustal thinning from the segment

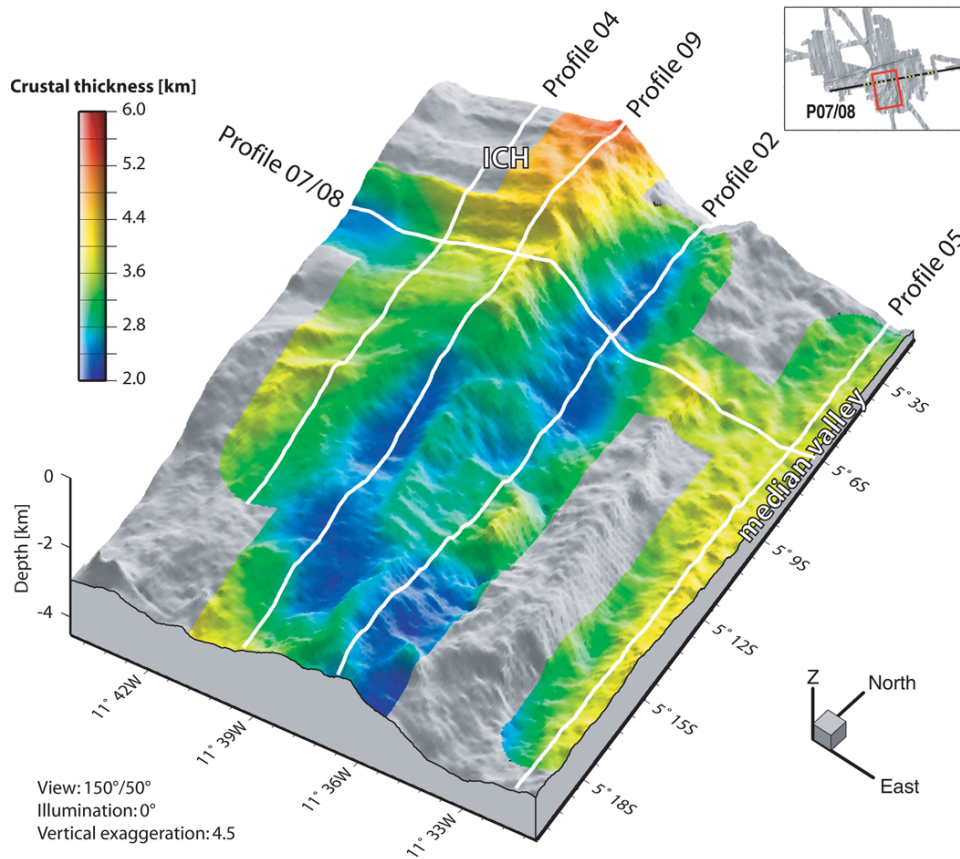


Figure 7.3: Crustal thickness (colour coded) for the ICH area and its southern and eastern flanking regions. The area shown is the black-dashed marked sector in figure 6.16. The 3D thickness interpolation is based on the Moho reflectors in figure 6.16 and the hydrosweep bathymetry. Available seismic profiles are indicated as white lines. The thinnest crust is associated with a series of sub-basins south of the ICH and the eastern ICH flank.

center to the segment end observed on Profile 09 is consistent with the idea that the crust at the inside corner is tectonically modified when rafted away from the ridge-axis during spreading (*Mutter and Karson, 1992; Tucholke and Lin, 1994*). However, the thinnest crust in the study area is clearly associated with the western and eastern flanks of the ICH and a series of sub-basins immediately south of the ICH, not with the area of highest elevation (cf. figure 7.3). There are no major differences in the depth of the seismic Moho between the inside corner and the adjacent outside corner massif, or between the inside corner and the model portions which are supposed to be the outside corner prior to the ridge jump (cf. figure 7.4).

Based on the proposed segment evolution by *Reston et al. (2002)*, the seismic models may be sampling two classes of events: an earlier phase of detachment faulting and a subsequent phase of normal faulting, which is associated with a change of the active spreading-axis and continues until present (*Reston et al., 2002; Tilmann et al., 2004*). By this view, the two massifs were formed at the inside corner of the now abandoned spreading-axis which is located east of the present outside corner (cf. figure 7.4). This is confirmed

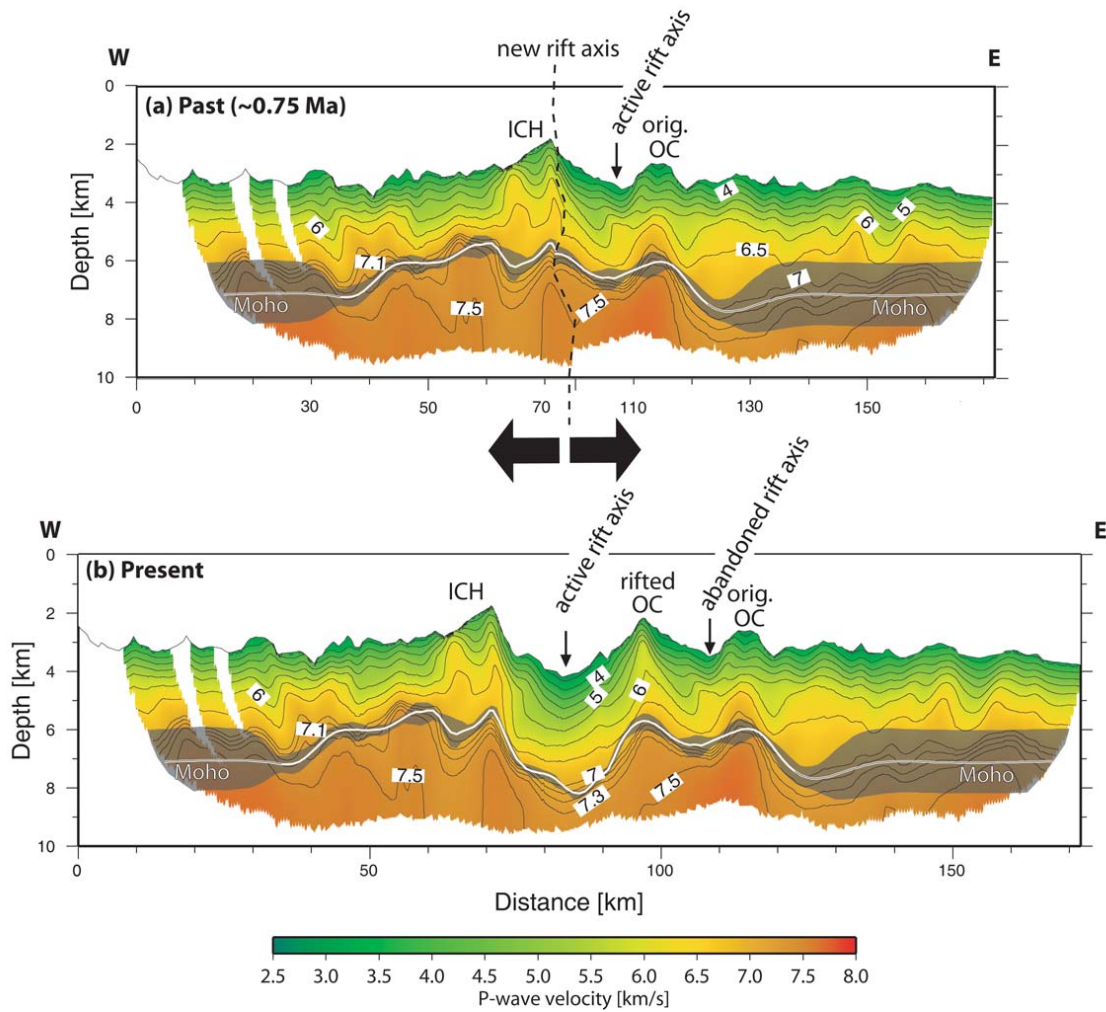


Figure 7.4: Velocity model for the development of the rifted ICH complex based on the tomographic model of Profile 07/08. The idea of a rifted core complex was originally proposed by Reston et al. (2002). (a): A rifting event ~ 0.75 Ma ago resulted in a change in the axis of active seafloor spreading and initiated a split of the ICH core complex (indicated with the dashed line). The smaller massif east of the active spreading axis is the “original” outside corner in the view of the classical model by Tucholke and Lin (1994). (b): Present day situation. The formerly conjoint core complex is split into two massifs. In the current plate geometry, the rifted portion of the inside corner (rifted OC) belongs to the outside corner. The velocity model used for the restoration is the Monte Carlo solution for Profile 07/08 of figure 6.12. Note the good match of the velocity isolines and Moho depths in (a).

by the similar shapes and heights of the massifs, the close match of the corrugations on top and by the velocity structure of both massifs. The segment reconstruction in figure 7.4a shows that the inside corner is characterised by higher velocities than the “original” outside corner. This is consistent with the hypothesis that the core complex was formed by large-scale detachment faulting, resulting in the emplacement of deeper

crustal and upper mantle portions at shallower levels (*Mutter and Karson, 1992; Tucholke and Lin, 1994; Cann et al., 1997; Tucholke et al., 1998; Blackman et al., 1998; MacLeod et al., 2002*). According to the model of *Tucholke and Lin (1994)*, the upper crust may be stripped from the the inside corner crust and largely restricted to the outside corner.

7.3.1 Nature of the crust in the IC and OC region

A wide range of lithologies might explain the observed velocity structure of the crust formed at the inside corner during the phase of detachment faulting, including gabbro and serpentinitized mantle peridotite. In the latter, a velocity of 5-6 km/s would correspond to 60-100% serpentine (*Carlson and Miller, 2003*); it is thereby presumed that ambient temperatures are lower than $\sim 500^\circ\text{C}$. Velocities below 5.0 km/s are rarely observed in laboratory samples of serpentine but might arise if the rock is highly fractured. However, several observations favour a different composition of the inner core. Two dredges, one at the base and one at the midway of the transform facing ICH scarp, recovered largely undeformed gabbros. Blocks of sheared serpentinites were found at the very top of the scarp in one dredge haul, adjacent to the corrugated surface. If these dredges are representative, they provide some important constraints on the formation and the composition of the core complex: (1) Since samples dredged at different levels of the scarp should indicate the internal sequence of the massif, the presence of gabbros suggests that they might form a significant portion of the inner core (*Reston et al., 2002*). (2) The fact that all recovered gabbros, in particular those which were dredged directly beneath the corrugated fault surface are undeformed would rule out a wide zone of ductile deformation associated with this detachment. As a consequence, these observations are not consistent with detachment models rooting at or near the brittle-ductile transition. (3) The presence of sheared serpentinites close to the exposed fault plane might confirm the idea that they contribute significantly to the weakening of the fault zone during the process of detachment faulting (*Cann et al., 1997; MacLeod et al., 2002; Reston et al., 2002; Escartin et al., 2003*). On the other hand, their complete absence in the deeper hauls might indicate that they do not form a major volume within the core complex.

A plausible interpretation of the data is that the upper, high-velocity layer beneath the inside corner represents an accumulation of gabbroic intrusions embedded into serpentinitized mantle rocks (cf. figure 7.5). The relative volume of gabbro with respect to the surrounding serpentinites may progressively decrease with depth. The *PmP* reflector would then correspond to the structural deepest level to which peridotite is intruded by gabbros (e.g. *Cannat, 1993*), and hence it would represent a petrological boundary and not an alteration front. The upper mantle might be primarily composed of serpentinitized peridotites. Alternatively, a greater volume of retained melts in the upper mantle could explain the observed velocities and would reduce the amount of serpentinitization. This scenario would implicate smaller mantle densities (cf. figure 6.15 b). Since the gravity of Profile 07/08 predicts rather higher densities for the inside corner, the latter seems to be less likely, but it cannot be ruled out on the basis of available seismic data.

The crust formed at the outside corner prior to the ridge jump is characterised by typical layer 2 velocities and associated velocity gradients, which suggests the presence of

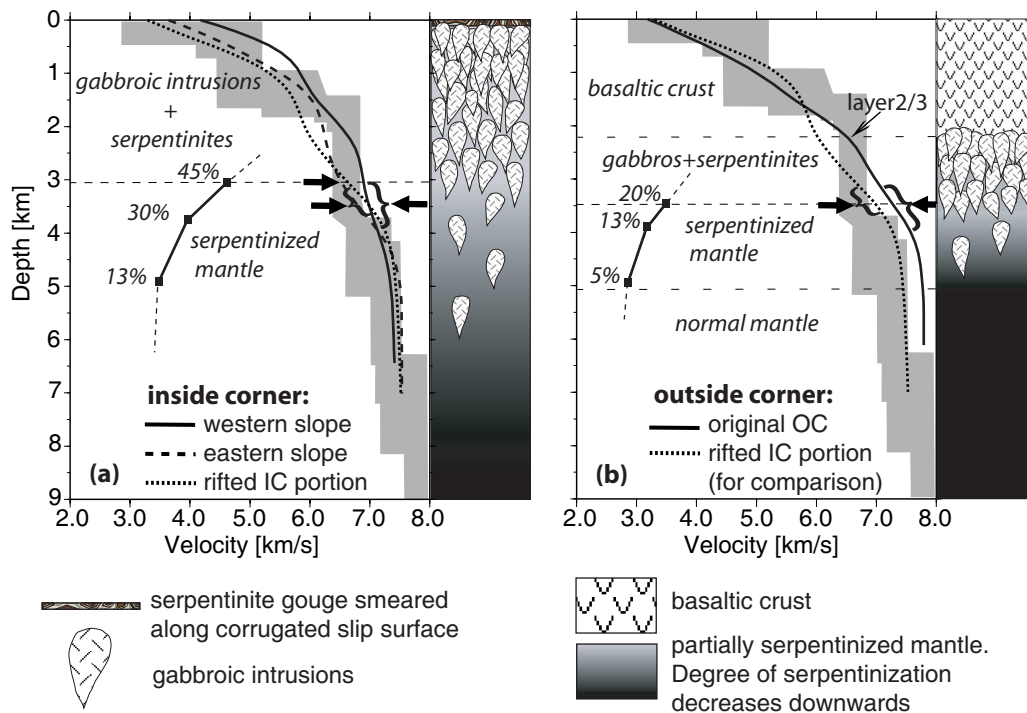


Figure 7.5: Velocity depth profiles (averaged over 4 km profile distance) through inside corner and outside corner crust on Profile 07/08. The grey-shaded envelope of velocity depth profiles from the Mid-Atlantic Ridge for crust aged 0-7 Ma (White et al., 1992) is shown for comparison. (a) Inside corner crust extracted at different locations: western slope (solid line), eastern slope (long-dashed line), rifted IC portion (labelled “rifted OC” in figure 7.4; short-dashed line). (b): Outside corner crust extracted at the “original” outside corner in figure 7.4 (solid line). The short-dashed line from (a) is shown for comparison. Black arrows indicate Moho depths with corresponding 90% uncertainties. Horizontal dashed lines indicate lithology changes in the structural interpretation. Numbers indicate percentage of serpentinization in the upper mantle (Carlson and Miller, 2003). Due to the possible tradeoff between the volume of gabbroic intrusions and the percentage of serpentinization in the mantle, the values rather represent maximum estimates.

a “normal” upper crust (cf. figure 7.5). A slightly lower velocity gradient beneath ~2 km depth is interpreted as the transition to a gabbro unit embedded into serpentinized mantle rocks. Similar to the inside corner, a petrological Moho may be present at the outside corner, although it is probably associated with a much thinner mantle transition zone. Relatively “normal” mantle velocities of 7.8 km/s are observed only 1.5 km beneath the Moho.

A larger degree of serpentinization, as predicted for the upper mantle beneath the inside corner, implicates some important caveats: The detachment fault system and/or vertical faults must have provided pathways for deep fluid circulation beneath the massif. Circulation may be facilitated by the subsequent rifting of the massif and by the transform fault in the north. It may also be aided by the large free surfaces created by the rift and transform facing walls and by unloading due to landslides (cf. figure 2.3), as proposed

for the Atlantis Massif by *Schroeder et al.* (2002). Hence, serpentinitisation is likely to be primarily the result of the subsequent rifting. Deep serpentinitization may also help to explain the anomalously high elevation of the northern part of the massif through volume expansion during serpentinitization.

A serpentine content of 10%-15% or less can significantly weaken the strength of the lithosphere resulting in an abrupt change in the rheological behaviour rather than a gradual decrease (*Escartin et al.*, 2001). This will pose major constraints for the abundance of mid-ocean ridge earthquakes for the inside corner area. *Tilman et al.* (2004) showed, that the seismic activity appears to be concentrated in the median valley at depths of 1-8 km below seafloor. Only a few scattered events occurred beneath the ICH at depths of 4-10 km below seafloor. If the observed seismicity pattern is related to the presumably weaker lithospheric rheology of the inside corner is unknown, but at least it is not in conflict with the obtained results.

A unique correlation between seismic velocities and lithologies for the observed range of velocities is impossible in the absence of drilling and more detailed sampling or direct observations. This is impressively documented by the results obtained from IODP drilling at Atlantis Massif (*Blackman et al.*, 2005). Hence, the structural models cannot be straightforwardly applied to draw specific conclusions for the mechanisms of rifting. However, the following section will discuss the implications of the obtained results for the existing models of detachment faulting.

7.3.2 Implications for the mechanisms of rifting

Different models have been proposed to explain the large detachment faults at the Mid-Atlantic Ridge and at the Southwest Indian Ridge and the involved mechanisms of rifting. Currently, there is a consensus that these faults are rooting in a rheological boundary beneath the spreading axis, but the nature of this boundary, the associated style of deformation and the type of lithology formed differ largely in the corresponding scenarios (cf. figure 7.6).

In the model proposed by *Tucholke and Lin* (1994) the detachment fault cuts through the whole lithosphere and soles out at its lower base at the brittle-plastic transition (cf. figure 7.6 b). In this model detachment faulting occurs in periods of amagmatic extension when the lithosphere is cold; faulting terminates when magmatism is reinitiated. An alternative detachment model proposes that the fault roots in a melt-rich zone in the shallow lithosphere, probably related to the gabbro/dike transition (cf. figure 7.6 c). This model is based on detailed observations (incl. ODP drilling, dredging, rock coring, ROV, and refraction seismic studies) at the Atlantis Bank, which is an uplifted block on an eastern transverse ridge of the Atlantis II Fracture Zone at the Southwest Indian Ridge (e.g. *Dick et al.*, 1991, 2000; *Muller et al.*, 2000). In this case, the observation of melt-assisted deformation in the uppermost 250 m beneath the detachment fault has been interpreted as evidence for a direct link between the fault and the axial magmatic system. In contrast, observations at an oceanic core complex at the Fifteen-Twenty Fracture Zone (*MacLeod et al.*, 2002; *Escartin et al.*, 2003) and recent results from IODP drilling at Atlantis Massif at 30° N (*Blackman et al.*, 2005) at the Mid-Atlantic Ridge indicate that deformation

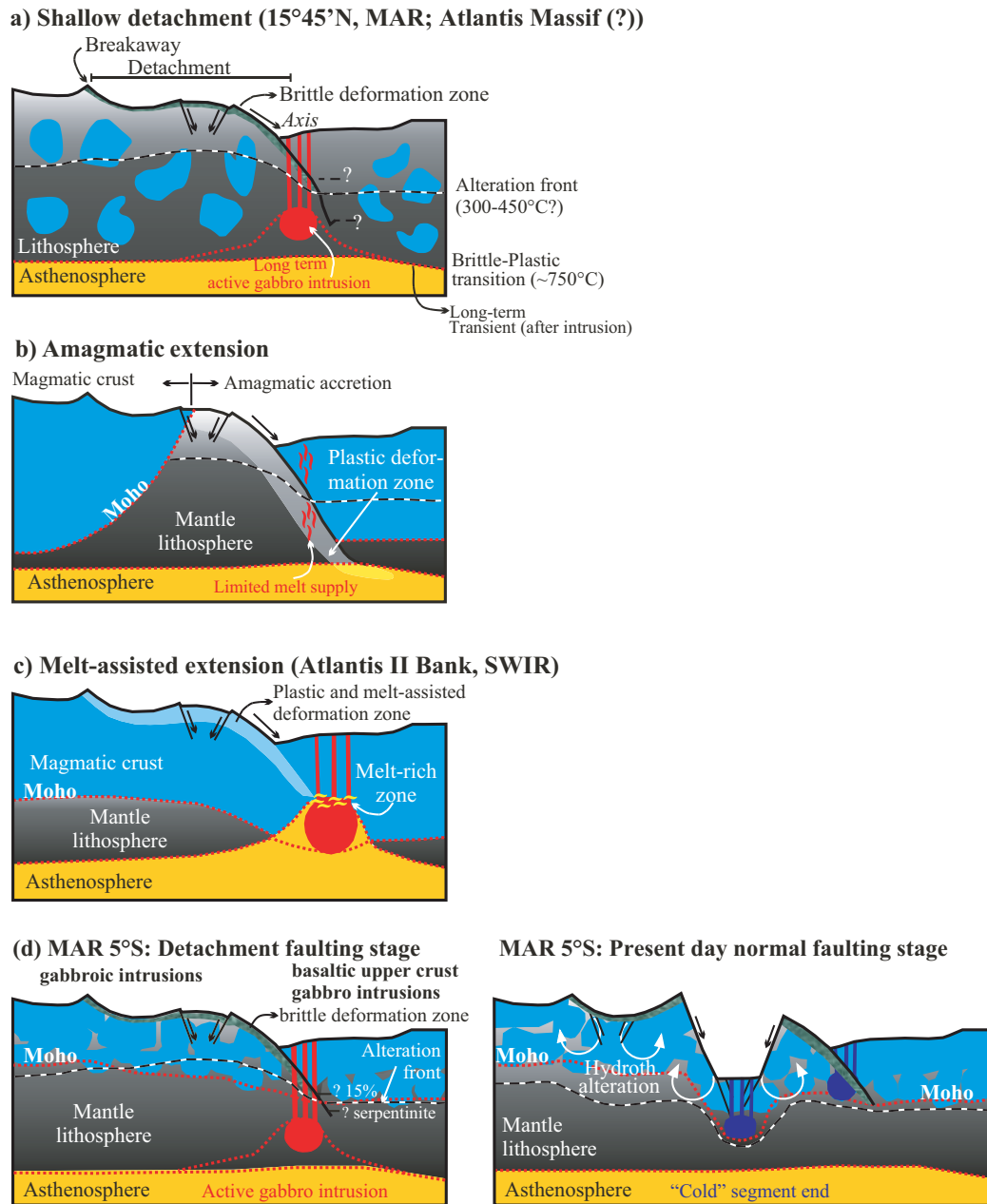


Figure 7.6: Models for the development of oceanic core complexes (modified from Escartin et al., 2003). (a) Shallow detachment model (Escartin et al., 2003) (b) Amagmatic extension model (Tucholke and Lin, 1994) (c) Melt-assisted extension (Dick et al., 1991). (d) Proposed model for the MAR at 5° S. Similar to the model in (a), the detachment fault is rooting in the shallow lithosphere. The alteration front may correspond to a rheological boundary between the altered (weak) and less-altered (strong) lithosphere. Magmatic intrusions may result in transient variations of the thermal structure, affecting the depth of the brittle-ductile transition. The detachment exposes mainly gabbroic intrusives at the inside corner. At the outside corner, a magmatic upper crust is underlain by a thin gabbro portion. The Moho is a petrological boundary. (Right): Present day stage of normal faulting.

occurred at low temperatures and was strongly localized at the fault plane, which is consistent with a low-temperature shallow rooting detachment model (cf. figure 7.6 a).

In case of the core complex at 5° S, the presence of relatively undeformed rocks at the dredge from immediately beneath the fault surface might indicate a similar mechanism as proposed for the shallow detachment at 15° N. In this scenario the detachment probably slipped at low angle, rather than steepening to a high angle, and soled out along an alteration front horizon at relatively shallow depth within the brittle lithosphere directly beneath the ridge-axis. Limited support for the shallow rooting has come from seismic reflection studies at a Cretaceous inside corner on North-Atlantic oceanic crust (*Ranero and Reston, 1999*), the study of dike intrusions at the massif at MAR 15° N (*MacLeod et al., 2002; Escartin et al., 2003*), and IODP drilling at Atlantis Massif, which revealed a lack of footwall rotation (*Blackman et al., 2005*). Footwall rotation is expected to occur in case of fault steepening towards the ridge-axis (e.g. *Buck et al., 2005*). The abrupt decrease of strength at small degrees of serpentinization (<15%; *Escartin et al., 2001*) may provide a profound rheological contrast between a weaker, serpentinized upper lithosphere and a stronger, only slightly serpentinized or serpentine-free lower lithosphere (*MacLeod et al., 2002*). *Reston et al. (2002)* suggested that the volumes of involved serpentine may actually be very small because volume expansion is likely to result in the preferential injection into the dilatant fault. The weakness of serpentinites may concentrate movement along these faults which may then remain active as “detachment faults”.

Several lines of evidence indicate that the core of the massif at 5° S is formed at least partially of gabbros. These include the recovery of gabbros in dredges from the rifted scarps and the fact that typical mantle velocities are not observed within resolved depths of 7 km below seafloor. The only exception is the rifted scarp of the inside corner west of the current spreading axis where velocities of 7.7-7.9 km/s are observed along-axis at depths of ~3 km below seafloor. However, the obtained velocities disagree with corresponding values observed on the across-axis profile (cf. section 6.4). These discrepancies may in fact reflect the limitations in spatial resolution of seismic refraction studies in case of a highly heterogeneous velocity structure. Interestingly, geophysical studies at the Atlantis Massif might support this view: IODP drilling recovered ~1.4 km of gabbroic rocks at the exposed footwall structure. Analysis of seismic refraction data, centered ~2 km north of the hole, indicates that rocks with a seismic velocity greater than 7.5 km/s are present at about 0.8 km depth below seafloor, and an apparently significant volume of peridotite which hosts the Lost City vent field crops out only 5 km south of the hole. These observations suggest a complex lateral and vertical heterogeneity in lithography, alteration and structure as the most likely explanation (*Blackman et al., 2005*).

The composition of the inner core of the massif raises questions about the nature of the observed Moho reflector. In this study, also due to the applied tomographic approach, the seismic Moho corresponds to a gradual increase of velocities or to a change in the velocity gradient. The lateral variations of the Moho in the velocity models as well as the weak amplitudes corresponding to this reflection in the seismic data suggest a heterogeneous boundary, defined by individual intrusive bodies with lateral dimensions only partly resolvable by seismic refraction data, rather than a sharp and uniform boundary. In an alternative scenario, the seismic Moho could be a serpentinization front (e.g. *Hess, 1962; Dilek et al., 1998; Muller et al., 2000; Canales et al., 2000b*). In case of the ICH this

would imply the transition from serpentized mantle to unaltered mantle at depths of 3-3.5 km below seafloor. Observed sub-Moho velocities of ~ 7.5 km/s would then be due to the presence of a significant gabbroic mantle component (up to 50%). However, a gradual decrease of the mantle melt component is probably more difficult to explain. Moreover, the affected mantle portions are restricted to a relatively small area beneath the inside corner. Higher mantle velocities suggest a different type of mantle further west and east of the ICH. Although this cannot be ruled out, it seems unlikely given the relatively small dimensions of this feature. Even more, it would disagree with the rather higher densities predicted for the inside corner by the gravity modeling. Lastly, a thermal impact on the observed low mantle velocities can be ruled out since the observed pattern indicates a velocity decrease with distance from the ridge-axis.

The occurrence of a well-developed axial volcanic ridge prior to the rifting (cf. figure 7.4) implies that the formation of the core complex need not be amagmatic (*Reston et al.*, 2002). Long-lived detachment faulting and coeval magmatism has been reported from a corrugated massif north of the Fifteen-Twenty Fracture Zone (cf. figure 7.6 a; *MacLeod et al.*, 2002; *Escartin et al.*, 2003). In this case, synkinematic emplacement of diabase dikes into the fault zone from an immediately subjacent gabbro pluton implies that the detachment must have been active at low angles at very shallow levels directly beneath the ridge-axis. However, it is obvious that sustained dike injections across the fault zone would have intersected its mechanical continuity and result in its termination.

In case of the core complex at 5° S it is unknown whether the formation of the axial volcanic ridge (i.e. increasing axial magmatism) or the shift of the rift-axis finally terminated the process of detachment faulting. *Canales et al.* (2004) proposes on the basis of seismically derived layer 2a thickness that the termination of faulting at the Atlantis Massif (MAR 30° N) was associated with a phase of normal magmatism. By this view, the pronounced layer 2 beneath the fossil ridge at 5° S may imply that detachment faulting already ceased prior to the ridge jump. On the other hand, seismic results indicate a very thin or even absent seismic layer 3 beneath the outside corner and beneath the active spreading axis at that time, with no indication of crustal thickening prior to the ridge jump (cf. figure 7.5 b). If the thickness of the lower crust reflects the melt supply of the ridge (*Tolstoy et al.*, 1993), this would suggest in fact a rather “cold” final phase of detachment faulting. For comparison, the present day axial thickness of 4 km exceeds that of the fossil ridge by roughly 1 km. However, this does not take into account the asymmetric dismembering of the lower crustal portions during the process of detachment faulting and, in the absence of magnetic data, a possible spreading asymmetry (e.g. *Allerton et al.*, 2000; *Fujiwara et al.*, 2003; *Okino et al.*, 2004).

7.3.3 Implications for rift propagation

Reston et al. (2002) proposed two possible mechanisms for the initiation of subsequent rifting of the core complex: Depending on the preceding plate geometry, rifting may have been tectonically controlled, i.e. related to the propagation of major faults from a 2nd order ridge-axis discontinuity (RAD), or may have been caused by the propagation of dikes from a magmatic center. As pointed out in section 2.4.1, the west-turn of the median valley

at the southern tip of the reconstructed core complex and the occurrence of a pronounced massif further south (cf. figure 2.4) implies the presence of a 2nd order RAD in the plate geometry prior to the rifting event, even if the continuation of the spreading-axis further south is less clear due to sparse bathymetric coverage. Profile 02, which roughly covers the proposed course of the new rift-axis at the time of the ridge jump, reveals the thinnest crust observed in this study (2.4-3 km thickness; cf. figure 6.16). Furthermore, there is no evidence for increased melt supply for the area directly south of the reconstructed ICH (cf. figure 7.3). Thin crust beneath the series of sub-basins instead indicates that the RAD was a region of extremely low melt supply.

Allerton et al. (2000) demonstrated that the state of stress of the upper crustal plate is an important controlling factor on the locus of accretion (dike intrusion and fissure eruptions). For a large detachment fault it is likely that stresses are at least partially controlled by flexure associated with the fault. The locus of dike intrusions or fissuring is then likely to be placed, where the bending results in local extension. In case of the core complex, fracturing could start at the thinnest crustal portion which is presumably exposed to large bending stresses. Once started, fracturing would lead to increased serpentinization. The low frictional strength of serpentinites might then result in the localization of the rift where serpentinites form first. A similar mechanism is proposed for the evolution of nonvolcanic rifted margins, where serpentinites are believed to contribute significantly to the weakening of the upper lithosphere (*Peréz-Gussinyé and Reston*, 2001).

Kleinrock et al. (1997) inferred from the study of fast propagators (i.e. smaller migrating ridge offsets) that they appear to have formed as a result of tectonic extension. The course of these features seems to correlate with changes from lower to higher residual gravity anomalies. This implies some combination of crustal thinning and/or mantle cooling occurred coevally with the initiation and migration of the fast propagators and might reflect a causal relationship. Based on the above considerations, a tectonic control on the initiation of rifting might be feasible. However, the rifting of the thicker lithosphere at the segment end, although probably weaker in the upper part, is presumably difficult.

Chapter 8

Conclusions and Outlook

The aim of this study was to provide seismic constraints on the structural variations of the oceanic crust across a 1st order ridge-offset and an inside corner high, where geological models of ridge segmentation and core complex formation predict significant deviations from the layered model.

Using the wide-angle seismic data acquired in the 2000 GERSHWIN experiment at the Mid-Atlantic Ridge at 5° S, the P-wave velocity structure along seven 30-170 km long intersecting seismic profiles is obtained applying different tomographic approaches such as first-arrival tomography and joint refraction and reflection tomography. For the latter, the accuracy of the hybrid forward algorithm is demonstrated. Strong lateral heterogeneity both in velocities and reflector depths is recovered, and the Monte Carlo uncertainty analysis shows that most of the model parameters are well constrained, with 0.05-0.1 km/s standard deviation for velocity and 0.1-0.25 km standard deviation for reflector depth nodes. A good resolution of the relevant model features as well as an acceptable trade-off between velocity and depth is demonstrated. Gravity modelling for one profile provides additional constraints for the obtained model features.

The main results presented in this thesis can be summarized as follows:

- The two spreading segments separated by the 5° S FZ are of markedly contrasting character. The northern segment is characterised by a pronounced seafloor bulge in the median valley, an associated seamount chain in flow-line of the segment center and a quite regular ridge-parallel tectonic fabric. The southern segment is characterised by irregular fault patterns and morphology including the inside corner high and several smaller massifs and basins.
- The maximum crustal thickness in the northern segment is 9 km at the segment center; this is the high end of crustal thickness measurements for the MAR. The crust thins to 5 km at the southern segment end and 6 km at the northern segment end. The reduction in crustal thickness is almost exclusively accommodated by the thinning of velocity portions typical for seismic layer 3. The along-axis average crustal thickness has increased from 5.6 ± 0.3 km to 6.8 ± 1.3 km in the last 4 Ma. The increase is accompanied by a more focused melt supply to the segment center. To a first order, crustal thickness seems to control axial depth of the rift valley; however, other thermal and dynamic factors may also play a role.

- At the median valley of the northern segment, anomalously low velocities (-0.4 to 0.5 km/s) at depths of ~ 2.5 km below seafloor may indicate the presence of elevated temperatures and perhaps small portions of partial melt. This suggests that the northern segment is currently in a magmatically active period.
- At the segment ends of the northern segment, lower velocities (-0.1 to 0.5 km/s) in the upper crustal portions may result from fracturing facilitated by the greater tectonic deformation.
- Anomalously thin crust of 2.8-3.5 km is found in the transform valley. Almost linearly increasing velocities suggest that the velocity structure is rather controlled by fracturing and alteration of a thin crust and underlying mantle.
- Most parts of the southern segment are underlain by anomalously thin crust. The thinnest crustal portions (2.4-3 km) are associated with the eastern and western flanks of the ICH and a series of sub-basins south of the ICH, which may correspond to a fossil 2nd order NTD prior to the ridge jump. The thickest crustal portions (>5 km) are found away from the segment end and at the transform facing flank of the ICH, close to the transition to northern segment crust. There are no major differences in average crustal thickness between the ICH, the rifted portion of the ICH and the outside corner (3-3.5 km).
- The very similar velocity structure and Moho depth beneath the ICH and the smaller massif, which is now located at the outside corner, confirm that the latter was split by a rifting event, as previously proposed by *Reston et al.* (2002).
- The crust of the core complex, formed at the inside corner prior to the ridge-jump, reveals throughoutly higher velocities than corresponding outside corner crust. This is consistent with models of asymmetric magmatic accretion along a detachment fault. Moreover, the inside corner is characterised by strong lateral velocity heterogeneities, resulting locally in anomalously high seafloor velocities (>5 km/s), which reach up to >6 km/s in the uppermost few hundred meters. Beneath the Moho, a pronounced mantle transition zone reveals velocities of 7.2-7.5 km/s. In contrast, the outside corner crust is characterised by “normal” layer 2 velocities and gradients in the upper crustal portion, a slightly lower velocity gradient below and a smaller mantle transition zone (rel. “normal” upper mantle velocities of 7.8 km/s are found 1.5 km beneath the Moho). The lower mantle velocities directly beneath the Moho at the ICH and its rifted portion may derive from post-emplacement modification (e.g. hydrothermal alteration) related to the subsequent rifting.
- The across-axis average crustal thickness of 3.2 ± 0.4 km suggests that relatively magma-poor spreading was the dominant mode of crustal accretion for the inside corner at least for the last ~ 3 Ma.
- The rifting of the core complex was initiated at its thinnest crustal portion with no indication of a pronounced magmatic center directly south of the ICH. These observations suggest that the rifting might have been tectonically controlled.

- The crust between the ICH and its rifted portion is relatively thin (~ 4 km) and does not exhibit a well-developed axial volcanic ridge, which indicates that it might be tectonically thinned. These observations are typical for a “cold” segment end. This is in general agreement with seismological studies (*Tilman et al.*, 2004).

Outlook

This study proposed elevated temperatures and perhaps small amounts of partial melt in depths of ~ 2.5 km beneath the northern segment seafloor bulge. These temperature anomalies may correspond to a crustal magma-plumbing system similar to the one observed at the MAR at 35° N by *Magde and Sparks* (1997). The detailed geometry and depth extent of these features would provide important constraints for models of three-dimensional melt flow within slow spreading oceanic lithosphere.

As previously suggested by *Reston et al.* (2002), the ridge-facing scarps of the rifted inside corner high expose deep lithologic sections of the footwall structure which are accessible to *in situ* observations and sampling. A study of the spatial variations of the bulk lithologies and the associated degree of alteration may further clarify the mechanisms of this detachment system and might also be of significant importance for future drilling campaigns (e.g. *Blackman et al.*, 2005).

Segmentation of mid-ocean ridges plays a vital role not only in geological but also in chemical and biological processes. The Mid-Atlantic Ridge at 5° South presents an excellent study area to explore segmentation from the tectonic, magmatic, hydrothermal and biological viewpoint (cf. figure 8.1) and to understand how these processes interrelate.

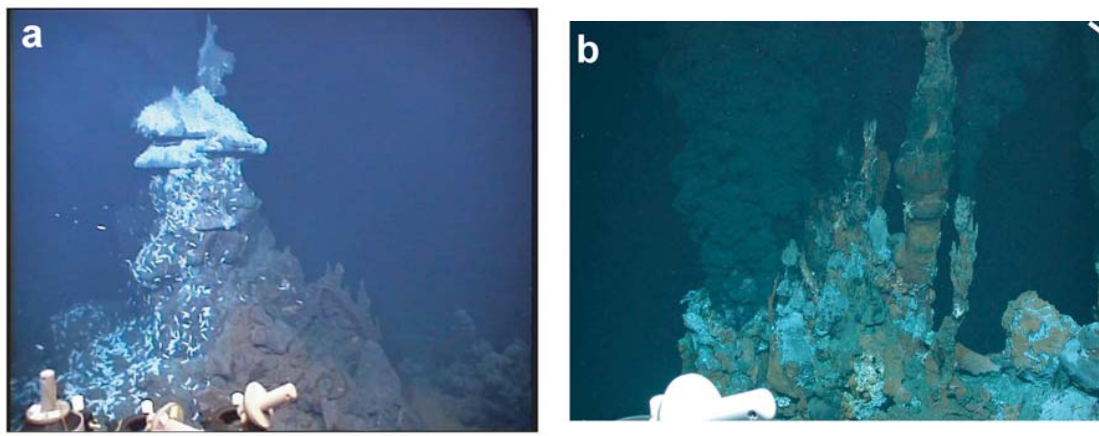


Figure 8.1: *Photographs of vents, located on top of the seafloor bulge in the median valley of the northern segment (from Haase et al., subm.; pictures were taken using the MARUM ROV (University of Bremen) during METEOR cruise M64; Haase and Lackschewitz, in press). (a): Sugar Head smoker in the Red Lion field showing abundant shrimp. (b): Black smoker in the Turtle Pits field showing gas bubbles, i.e. evidence for boiling at a water depth of 2990 m.*

Bibliography

- Abrams, L. J., R. S. Detrick, and P. J. Fox, Morphology and crustal structure of the Kane Fracture Zone transverse ridge, *J. Geophys. Res.*, *93*, 3195–3210, 1988.
- Allerton, S., J. Escartin, and R. S. Searle, Extremely asymmetric accretion of oceanic crust at the ends of slow-spreading ridge-segments, *Geology*, *28*, 179–182, 2000.
- Berryhill, J. R., Wave-equation datuming, *Geophysics*, *44*, 1329–1344, 1979.
- Bickel, S. H., Velocity-depth ambiguity of reflection traveltimes, *Geophysics*, *55*, 266–276, 1990.
- Bishop, T. N., K. P. Bube, R. T. Cutler, R. T. Langan, P. L. Love, J. R. Resnick, R. T. Shuey, D. A. Spindler, and H. W. Wyld, Tomographic determination of velocity and depth in laterally varying media, *Geophysics*, *50*, 903–923, 1985.
- Blackman, D. K., J. R. Cann, B. Janssen, and D. K. Smith, Origin of extensional core complexes: Evidence from the Mid-Atlantic Ridge at Atlantis Fracture Zone, *J. Geophys. Res.*, *103*, 21,315–21,315, 1998.
- Blackman, D. K., et al. (Eds.), *IODP Expedition 305, Preliminary Report: Ocean Core Complex Formation, Atlantis Massif*, 2005.
- Buck, W. R., L. L. Lavier, and A. N. B. Poliakov, Modes of faulting at mid-ocean ridges, *Nature*, *434*, 719–723, 2005.
- Canales, J. P., J. A. Collins, J. Escartin, and R. S. Detrick, Seismic structure across the rift valley of the Mid-Atlantic Ridge at 23°20' (MARK area): implications for crustal accretion processes at slow spreading ridges, *J. Geophys. Res.*, *105*, 28,411–28,425, 2000a.
- Canales, J. P., R. S. D. J. Lin, and J. A. Collins, Crustal and upper mantle seismic structure beneath the rift mountains and across a non-transform offset at the Mid-Atlantic Ridge (35°N), *J. Geophys. Res.*, *105*, 2699–2719, 2000b.
- Canales, J. P., B. E. Tucholke, and J. A. Collins, Seismic reflection imaging of an oceanic detachment fault: Atlantis megamullion (Mid-Atlantic Ridge, 30°10'N), *Earth Planet. Sci. Lett.*, *222*, 543–560, 2004.
- Cann, J. R., D. K. Blackman, D. K. Smith, E. McAllister, B. Janssen, S. Mello, E. Avgerinos, A. Pascoe, and J. Escartin, Corrugated slip surfaces formed at North Atlantic ridge-transform intersections., *Nature*, *385*, 329–332, 1997.

- Cannat, M., Emplacement of mantle rocks in the seafloor at mid-ocean ridges, *J. Geophys. Res.*, *98*, 4163–4172, 1993.
- Cannat, M., et al., Thin crust, ultramafic exposures, and rugged faulting patterns at the Mid-Atlantic Ridge (22°–24°N), *Geology*, *23*, 49–52, 1995.
- Carbotte, S. M., R. S. Detrick, A. Harding, J. P. Canales, et al., Rift topography linked to magmatism at the intermediate spreading Juan de Fuca Ridge, *Geology*, *34*, 209–212, 2006.
- Carlson, R. L., and D. J. Miller, Mantle wedge water contents estimated from seismic velocities in partially serpentinized peridotites, *Geophys. Res. Letters*, *30*, 1250–1254, 2003.
- Carlson, R. L., and G. S. Raskin, Density structure of the oceanic crust, *Nature*, *311*, 555–558, 1984.
- Chen, H. W., and C. W. Chang, Implicit Noise Reduction and Trace Interpolation in Wavefield Depth Extrapolation, *Geophys. Res. Letters*, *26*, 3705–3708, 1999.
- Christensen, N. I., Compressional wave velocities in rocks at high in temperatures and pressures, critical thermal gradients and crustal low-velocity zones, *J. Geophys. Res.*, *84*, 6849–6857, 1979.
- Collins, J. A., and R. S. Detrick, Seismic structure of the Atlantis Fracture Zone megamullion, a serpentinized ultramafic massif, *Eos (Transactions, American Geophysical Union)*, *79*, 800, 1997.
- Curewitz, D., and J. A. Karson, Geological consequences of dike intrusion at Mid-Ocean Ridge Spreading Centers, in *Faulting and Magmatism at Mid-Ocean Ridges*, edited by W. R. Buck, P. T. Delaney, J. A. Karson, and Y. Lagabriele, pp. 117–136, AGU, Geophysical Monograph 106, 1998.
- DeMets, C., R. Gordon, D. F. Argus, and S. Stein, Current plate motions, *Geophys. J. Int.*, *101*, 425–478, 1990.
- Detrick, R. S., P. Buhl, E. Vera, J. Mutter, J. Orcutt, J. Madsen, and T. Brocher, Multichannel seismic imaging of a crustal magma chamber along the East Pacific Rise, *Nature*, *326*, 35–41, 1987.
- Detrick, R. S., J. C. Mutter, P. Buhl, and I. I. Kim, No evidence from multichannel reflection data for a crustal magma chamber in the mark area on the mid-atlantic ridge, *Nature*, *347*, 61–64, 1990.
- Detrick, R. S., R. S. White, and G. M. Purdy, Crustal structure of North Atlantic fracture zones, *Reviews of Geophysics*, *31*, 439–458, 1993.
- Detrick, R. S., H. D. Needham, and V. Renard, Gravity anomalies and crustal thickness variations along the Mid-Atlantic Ridge between 33°N and 40°N, *J. Geophys. Res.*, *100*, 3767–3787, 1995.

- Dick, H. J. B., H. Schouten, P. S. Meyer, D. G. Gallo, H. Bergh, R. Tyce, P. Patriat, K. T. M. Johnson, J. Snow, and A. Fisher, Tectonic evolution of the Atlantis II Fracture Zone, in *Proc. ODP, Sci. Results, 118*, edited by R. Von Herzen, P. Robinson, et al., pp. 359–398, College Station, TX (Ocean Drilling Program), 1991.
- Dick, H. J. B., H. J. Natland, et al., A long in situ section of the lower oceanic crust: results of ODP leg 176 drilling at the Southwest Indian Ridge, *Earth Planet. Sci. Lett.*, *179*, 31–51, 2000.
- Dietz, R. S., Continent and ocean basin evolution by spreading of the seafloor, *Nature*, *190*, 1961.
- Dilek, Y., E. M. Moores, and H. Furnes, Structure of modern oceanic crust and ophiolites and implications for faulting and magmatism at oceanic spreading centers, in *Faulting and Magmatism at Mid-Ocean Ridges*, edited by W. R. Buck, P. T. Delaney, J. A. Karson, and Y. Lagabriele, pp. 219–265, AGU, Geophysical Monograph 106, 1998.
- Dunn, R. A., V. Lekic, R. S. Detrick, and D. R. Toomey, Three-dimensional seismic structure of the Mid-Atlantic Ridge 35°N: Evidence for focused melt supply and lower crustal dike injection, *J. Geophys. Res.*, *110*, 2005.
- Escartin, J., and M. Cannat, Ultramafic exposures and the gravity signature of the lithosphere near the Fifteen-Twenty Fracture Zones (Mid-Atlantic Ridge, 14°–16°N), *Earth Planet. Sci. Lett.*, *171*, 411–429, 1999.
- Escartin, J., G. Hirth, and B. Evans, Strength of slightly serpentinized peridotites: Implications for the tectonics of oceanic lithosphere, *Geology*, *29*, 1023–1026, 2001.
- Escartin, J., C. Mevel, C. J. MacLeod, and A. M. McCaig, Constrains on deformation conditions and the origin of of oceanic detachments: the Mid-Atlantic Ridge core complex at 15°45'N, *Geochem. Geophys. Geosyst.*, *4*, 1067, 2003.
- Fischer, R., and J. M. Lees, Shortest path ray tracing with sparse graphs, *Geophysics*, *58*, 987–996, 1993.
- Flueh, E. R., and J. Bialas, A digital, high data capacity ocean bottom recorder for seismic investigations, *Int. Underwater Systems Design*, *18*, 18–20, 1996.
- Flueh, E. R., V. Spiess, and F. Schott (Eds.), *Trans Atlantic 2000, Cruise No. 47, 16. March-03. July 2000*, 172p. ISSN 0936-8957, METEOR-Berichte, Universität Hamburg, 2000.
- Flueh, E. R., D. Klaeschen, and J. Bialas, Options for multi-component seismic data acquisition in deep water, *First Break*, *20*, 764–769, 2002.
- Fontignie, D., and J. G. Schilling, Mantle heterogeneities beneath the South Atlantic: a Nd-Sr-Pb isotope study along the Mid-Atlantic Ridge (3°S–46°S), *Earth Planet. Sci. Lett.*, *142*, 209–221, 1996.

- Fujiwara, T., J. Lin, T. Matsumoto, et al., Crustal evolution of the Mid-Atlantic Ridge near the Fifteen-Twenty Fracture Zone in the last 5 Ma, *Geochem. Geophys. Geosyst.*, *4*, 2003.
- Grevemeyer, I., W. Weigel, and C. Jennrich, Structure and ageing of oceanic crust at 14°N on the East Pacific Rise, *J. Geophys. Res.*, *135*, 573–584, 1998.
- Haase, K., and K. Lackschewitz (Eds.), *Cruise No. 64, 02. April-06. Juni 2005*, METEOR-Berichte, Universität Hamburg, in press.
- Haase, K. M., C. German, S. Petersen, A. Koschinsky, R. Seifert, et al., Exceptionally high-temperature venting associated with extensive fresh volcanism on the slow-spreading Mid-Atlantic Ridge near 5° S, *Geology*, subm.
- Hacker, B. R., G. A. Abers, and S. M. Peacock, Subduction factory I. theoretical mineralogy, densities, seismic wave speeds, and water contents, *J. Geophys. Res.*, 2003.
- Hanan, B. B., R. H. Kingsley, and J. G. Schilling, Pb isotope evidence in the South Atlantic for migrating ridge-hotspot interaction, *Nature*, *322*, 137–144, 1986.
- Harding, A. J., J. A. Orcutt, M. E. Kappus, et al., Structure of young oceanic crust at 13°N on the East Pacific Rise from expanding spread profiles, *J. Geophys. Res.*, *94*, 12,163–12,196, 1989.
- Heezen, B. C., The rift in the ocean floor, *Scientific American*, *203*, 99–106, 1960.
- Henstock, T. J., A. W. Woods, and R. S. White, Accretion of oceanic crust by episodic sill intrusions, *J. Geophys. Res.*, *98*, 4143–4161, 1993.
- Hess, H. H., A history of ocean basins, in *Petrological Studies: A Volume in Honor of A.F. Buddington*, edited by A. E. J. Engel, H. L. James, and B. F. Leonard, pp. 599–620, Boulder, CO, Geological Society of America, 1962.
- Hobro, J. W. D., S. C. Singh, and T. A. Minshull, Three-dimensional tomographic inversion of combined reflection and refraction traveltime data, *Geophys. J. Int.*, *152*, 79–93, 2003.
- Hole, J. A., and B. C. Zelt, 3-d finite-difference reflection traveltimes, *Geophys. J. Int.*, *121*, 427–434, 1995.
- Hooft, E. E. E., R. S. Detrick, D. R. Toomey, J. A. Collins, and J. Lin, Crustal thickness and structure along three contrasting spreading segments of the Mid-Atlantic Ridge 33.5°–35°N., *J. Geophys. Res.*, *105*, 8205–8226, 2000.
- Hosford, A., J. Lin, and R. S. Detrick, Crustal evolution over the last 2 m.y. at the Mid-Atlantic Ridge OH-1 segment, 35°N., *J. Geophys. Res.*, *106*, 13,269–13,286, 2001.
- Huang, P. Y., and S. C. Solomon, Centroid depths of mid-ocean ridge earthquakes: Dependence on spreading rate., *J. Geophys. Res.*, *93*, 13,445–13,477, 1988.

- Karson, J. A., Internal structure of oceanic lithosphere: A perspective from tectonic windows, in *Faulting and magmatism at mid-ocean ridges*, edited by W. R. B. et others, pp. 177–218, AGU, Geophysical monograph 106, 1998.
- Karson, J. A., and H. J. B. Dick, Tectonics of ridge-transform intersections at the Kane fracture zone, *Mar. Geophys. Res.*, *6*, 51–98, 1983.
- Kleinrock, M. C., B. E. Tucholke, J. Lin, and M. A. Tivey, Fast rift propagation at a slow spreading ridge, *Geology*, *25*, 639–642, 1997.
- Klingelhöfer, F., L. Geli, L. Matias, N. Steinsland, and J. Mohr, Crustal structure of a super-slow spreading center: a seismic refraction study of Mohns Ridge, 72° N, *Geophys. J. Int.*, *141*, 509–526, 2000.
- Korenaga, J., TOMO2D - A C++ package for 2-D joint refraction and reflection travel-time tomography, <http://earth.geology.yale.edu/jk525/software/tomo2d.html>, pp. 1–11, 2000.
- Korenaga, J., W. S. Holbrook, G. M. Kent, P. B. Kelemen, R. S. Detrick, H.-C. Larsen, J. R. Hopper, and T. Dahl-Jensen, Crustal structure of the southeast Greenland margin from joint refraction and reflection seismic tomography., *J. Geophys. Res.*, *105*, 21,591–21,614, 2000.
- Kuo, B. Y., and D. W. Forsyth, Gravity anomalies of the ridge-transform system in the South Atlantic between 31 and 34.5°S: Upwelling centers and variations in crustal thickness, *Marine Geophysical Researches*, *10*, 205–232, 1988.
- Lagabriele, Y., D. Bideau, M. Cannat, J. A. Karson, and C. Mevel, Ultramafic-mafic plutonic rocks suites exposed along the Mid-Atlantic Ridge (10°N-30°N). Symmetrical-asymmetrical distribution and implications for seafloor spreading processes, in *Faulting and Magmatism at Mid-Ocean Ridges*, edited by W. R. Buck, P. T. Delaney, J. A. Karson, and Y. Lagabriele, pp. 153–176, AGU, Geophysical Monograph 106, 1998.
- Lawson, K., R. C. Searle, J. A. Pearce, P. Browning, and P. Kempton, Detailed volcanic geology of the MARNOK area, Mid-Atlantic Ridge north of Kane transform, in *Tectonic, Magmatic, Hydrothermal, and Biological Segmentation of Mid-Ocean Ridges*, edited by C. J. MacLeod, C. J. Tyler, and C. L. Walker, pp. 29–48, Geol. Soc. Lond., Spec. Publ. 118, 1996.
- Lin, J., and J. Phipps Morgan, The spreading rate dependence of three-dimensional mid-ocean ridge gravity structure, *Geophys. Res. Letters*, *19*, 13–16, 1992.
- Lin, J., G. M. Purdy, H. Schouten, and J. C. Sempere, Evidence from gravity data for focused magmatic accretion along the Mid-Atlantic Ridge., *Nature*, *344*, 627–632, 1990.
- Louden, K. E., R. S. White, C. G. Potts, and D. W. Forsyth, Structure and seismotectonics of the Vema Fracture Zone, Atlantic ocean, *J. Geol. Soc. Lond.*, *143*, 795–805, 1986.
- Luetgert, J. H., MacRay - Interactive Two-Dimensional Seismic Raytracing for the Macintosh, *U.S. Geological Survey, Open-File Report 92-356*, p. 44, 1992.

- Macdonald, K. C., Linkages between faulting, volcanism, hydrothermal activity and segmentation on fast spreading centers, in *Faulting and Magmatism at Mid-Ocean Ridges*, edited by W. R. Buck, P. T. Delaney, J. A. Karson, and Y. Lagabriele, pp. 27–58, AGU, Geophysical Monograph 106, 1998.
- Macdonald, K. C., D. S. Scheirer, and S. M. Carbotte, Mid-Ocean Ridges: Discontinuities, Segments and Giant Cracks., *Science*, *253*, 986–994, 1991.
- MacLeod, C. J., J. Escartin, D. Banerji, G. J. Banks, M. Gleeson, D. H. B. Irving, R. M. Lilly, A. M. McCaig, Y. Niu, and D. K. Smith, Direct evidence for oceanic detachment faulting at the Mid-Atlantic Ridge, 15°45'N., *Geology*, *30*, 879–882, 2002.
- Magde, L. S., and D. W. Sparks, Three-dimensional mantle upwelling, melt generation and melt migration beneath segmented slow spreading ridges, *J. Geophys. Res.*, *102*, 20,571–10,583, 1997.
- Magde, L. S., A. H. Barclay, D. R. Toomey, R. S. Detrick, and J. A. Collins, Crustal magma plumbing within a segment of the Mid-Atlantic Ridge , 35° N, *Earth Planet. Sci. Lett.*, *175*, 55–67, 2000.
- Menard, H. W., The East Pacific Rise, *Science*, *132*, 1737–1742, 1960.
- Menke, W., *Geophysical Data Analysis: Discrete Inverse Theory*, International Geophysics Series, Volume 45, 285p., 1989.
- Mével, C., M. Cannat, P. Gente, E. Marion, J. M. Auzende, and J. A. Karson, Emplacement of deep crustal and mantle rocks on the west median valley wall of the MARK area (MAR, 23°N, *Tectonophysics*, *190*, 31–53, 1991.
- Minshull, T. A., Along-axis variations in oceanic crustal density and their contribution to gravity anomalies at slow spreading ridges, *Geophys. Res. Letters*, *23*, 849–852, 1996.
- Mitchell, N. J., J. Escartin, and S. Allerton, Detachment faults at mid-ocean ridges garner interest., *Eos Trans. AGU*, *79*, 127–127, 1998.
- Morgan, J. P., and D. W. Forsyth, Three-dimensional flow and temperature perturbations due to a transform offset: Effects on oceanic crustal and upper mantle structure, *J. Geophys. Res.*, *93*, 2955–2966, 1988.
- Moser, T. J., Shortest path calculation of seismic rays, *Geophysics*, *56*, 59–67, 1991.
- Moser, T. J., G. Nolet, and R. Snieder, Ray bending revisited, *Bull. Seismol. Soc. Am.*, *82*, 259–288, 1992a.
- Moser, T. J., T. Van Eck, and G. Nolet, Hypocenter determination in Strongly Heterogeneous Earth Models Using the Shortest Path Method, *J. Geophys. Res.*, *97*, 6563–6572, 1992b.
- Muller, M. R., T. A. Minshull, and R. S. White, Segmentation and melt supply at the Southwest Indian Ridge, *Geology*, *27*, 867–870, 1999.

- Muller, M. R., T. A. Minshull, and R. S. White, Crustal structure of the Southwest Indian Ridge at the Atlantis II Fracture Zone, *J. Geophys. Res.*, *105*, 25,809–25,828, 2000.
- Mutter, J. C., and J. A. Karson, Structural processes at slow-spreading ridges, *Science*, *257*, 627–634, 1992.
- Nakanishi, I., and K. Yamaguchi, A numerical experiment on nonlinear image reconstruction from first-arrival times for two-dimensional island arc structure, *J. Phys. Earth*, *34*, 195–201, 1986.
- Navin, D. A., C. Pierce, and M. C. Sinha, The RAMESSES experiment-II. Evidence for accumulated melt beneath a slow spreading ridge from wide-angle refraction and multichannel reflection seismic profiles, *Geophys. J. Int.*, *135*, 746–772, 1998.
- Nolet, G., *Seismic wave propagation and seismic tomography*, in *Seismic Tomography*, D. Reidel, Norwell, Mass., 1987.
- Okino, K., K. Matsuda, D. M. Christie, Y. Nogi, and K. Koizumi, Development of oceanic detachment and asymmetric spreading in the Australian-Antarctic Discordance., *Geochem. Geophys. Geosyst.*, *5*, Q12,012, 2004.
- Paige, C. C., and M. A. Saunders, LSQR: An algorithm for sparse linear equations and sparse least squares, *Trans. Math. Software*, *8*, 43–71, 1982.
- Papazachos, C., and G. Nolet, P and S deep velocity structure of the hellenic area obtained by robust non-linear inversion of traveltimes., *J. Geophys. Res.*, *102*, 8349–8367, 1997.
- Peréz-Gussinyé, M., and T. J. Reston, Rheological evolution during extension at nonvolcanic rifted margins: Onset of serpentinization and development of detachments leading to continental breakup, *J. Geophys. Res.*, *106*, 3961–3975, 2001.
- Perfit, M. R., and W. W. Chadwick, Magmatism at Mid-Ocean Ridges: Constraints from Volcanological and Geochemical Investigations, in *Faulting and Magmatism at Mid-Ocean Ridges*, edited by W. R. Buck, P. T. Delaney, J. A. Karson, and Y. Lagabriele, pp. 59–115, AGU, Geophysical Monograph 106, 1998.
- Phillips, W. S., and M. C. Fehler, Traveltime tomography: A comparison of popular methods, *Geophysics*, *56*, 1639–1649, 1991.
- Phipps Morgan, J., and Y. J. Chen, Dependence of ridge-axis morphology on magma supply and spreading rate, *Nature*, *364*, 706–708, 1993.
- Pockalny, R. A., P. J. Fox, D. J. Fornari, K. C. Macdonald, and M. R. Perfit, Tectonic reconstruction of the Clipperton and Siqueiros Fracture Zones: Evidence and consequences of plate motion change for the last 3 myr, *J. Geophys. Res.*, *102*, 3167–3181, 1997.
- Poliakov, A. N. B., and W. R. Buck, Mechanics of stretching elastic-plastic-viscous layers: Applications to slow-spreading mid-ocean ridges, in *Faulting and Magmatism at Mid-Ocean Ridges*, edited by W. R. Buck, P. T. Delaney, J. A. Karson, and Y. Lagabriele, pp. 305–323, AGU, Geophysical Monograph 106, 1998.

- Purdy, G. M., and R. S. Detrick, The crustal structure of the mid-atlantic ridge at 23°N from seismic refraction studies, *J. Geophys. Res.*, *91*, 3139–3762, 1986.
- Ranero, C. R., and T. J. Reston, Detachment faulting at oceanic core complexes, *Geology*, *27*, 983–986, 1999.
- Rathor, B. S., Velocity-depth ambiguity in the dipping reflector case, *Geophysics*, *62*, 1583–1585, 1997.
- Reston, T. J., W. Weinrebe, I. Grevemeyer, E. R. Flueh, N. C. Mitchell, L. Kirstein, C. Kopp, H. Kopp, and participants of METEOR 47/2, A rifted inside corner massif on the Mid-Atlantic Ridge at 5°S., *Earth Planet. Sci. Lett.*, *200*, 155–269, 2002.
- Reston, T. J., C. Devey, P. Brandt, , M. Rhein, and I. Grevemeyer (Eds.), *Cruise No. 62, 24. June-30. December 2004*, METEOR-Berichte, Universität Hamburg, in press.
- Ross, W. S., The velocity-depth ambiguity in seismic traveltime data, *Geophysics*, *59*, 830–843, 1994.
- Sandwell, D. T., and W. H. F. Smith, Marine gravity anomaly from Geosat and ERS 1 satellite altimetry, *J. Geophys. Res.*, *102*, 10,039–10,054, 1997.
- Scales, J. A., and R. Snieder, To Bayes or not to Bayes, *Geophysics*, *62*, 1045–1046, 1997.
- Schilling, J. G., M. Zajac, R. Evans, T. Johnston, W. White, J. Devine, and R. Kingsley, Petrologic and geochemical variations along the Mid-Atlantic Ridge from 27°N to 73°N, *American Journal of Science*, *283*, 510–586, 1983.
- Schouten, H., H. J. B. Dick, and K. D. Klitgord, Migration of mid-ocean ridge volcanic segments, *Nature*, *326*, 835–839, 1987.
- Schroeder, T., and B. E. John, Strain localization on an oceanic detachment fault system, Atlantis Massiv, 30° N, Mid-Atlantic Ridge , *Geochem. Geophys. Geosyst.*, *5*, 1–30, 2004.
- Schroeder, T., B. John, and B. R. Frost, Geologic implications of seawater circulation through peridotite exposed at slow-spreading mid-ocean ridges, *Geology*, *30*, 367–370, 2002.
- Searle, R. C., M. Cannat, K. Fujioka, C. Mevel, H. Fujimoto, A. Bralee, and L. Parson, FUJI DOME: A large detachment fault near 64°E on the very slow-spreading southwest Indian Ridge, *Geochem. Geophys. Geosyst.*, *4*, 9105, 2003.
- Sempere, J. C., G. M. Purdy, and H. A. Schouten, Segmentation of the Mid-Atlantic Ridge between 24°N and 30°40'N., *Nature*, *334*, 427–431, 1990.
- Shaw, P. R., and J. Lin, Causes and consequences of variations in faulting style at the Mid-Atlantic Ridge , *J. Geophys. Res.*, *98*, 21,839–21,851, 1993.
- Shaw, P. R., and J. Lin, Models of ocean ridge lithospheric deformation: Dependence on crustal thickness, spreading rate and segmentation, *J. Geophys. Res.*, *101*, 17,977–17,993, 1996.

- Shaw, P. R., and J. A. Orcutt, Waveform inversion of seismic refraction data and applications to young Pacific crust, *Geophys. J. R. Astron. Soc.*, *82*, 375–414, 1985.
- Shtivelman, V., and A. Canning, Datum correction by wave-equation extrapolation, *Geophysics*, *53*, 1311–1322, 1988.
- Sinha, M., and K. E. Louden, The Oceanographer fracture zone: Crustal structure from seismic refraction studies, *Geophys. J. R. Astron. Soc.*, *75*, 713–736, 1983.
- Sinha, M., S. C. Constable, C. Pierce, A. White, G. Heinson, L. M. MacGregor, and D. A. Navin, Magmatic processes at slow spreading ridges: implications of the RAMESSES experiment at 57°45'N on the Mid-Atlantic Ridge, *Geophys. J. Int.*, *135*, 731–745, 1998.
- Sinton, J. M., and R. S. Detrick, Mid-ocean ridge magma chambers, *J. Geophys. Res.*, *97*, 197–216, 1993.
- Sloan, H., and P. Patriat, Reconstruction of the flanks of the Mid-Atlantic Ridge, 28°N to 29°N: Implications for evolution of young oceanic lithosphere at slow spreading centers, *Geochem. Geophys. Geosyst.*, *5*, 2004.
- Small, C., Global systematics of Mid-Ocean Ridge Morphology, in *Faulting and Magmatism at Mid-Ocean Ridges*, edited by W. R. Buck, P. T. Delaney, J. A. Karson, and Y. Lagabriele, pp. 1–25, AGU, Geophysical Monograph 106, 1998.
- Smith, D. K., and J. R. Cann, Hundreds of small volcanoes on the median valley floor of the Mid-Atlantic Ridge at 24–25°N, *Nature*, *348*, 152–155, 1990.
- Smith, D. K., and J. R. Cann, The role of Seamount Volcanism in Crustal Construction at the Mid-Atlantic Ridge (24°–30°N), *J. Geophys. Res.*, *97*, 1645–1658, 1992.
- Smith, D. K., and J. R. Cann, Building the crust at the mid-atlantic ridge, *Nature*, *365*, 707–715, 1993.
- Smith, W. H. F., and D. T. Sandwell, Global seafloor topography from satellite altimetry and ship depth soundings, *Science*, *277*, 1957–1962, 1997.
- Spudich, P., and J. Orcutt, A new look at the oceanic crust, *Rev. Geophys. Space Phys.*, *18*, 627–645, 1980.
- Tarantola, A., *Inverse Problem Theory*, Elsevier, 1987.
- Tieman, H. J., Investigating the velocity-depth ambiguity of reflection traveltimes, *Geophysics*, *59*, 1763–1773, 1994.
- Tilman, F., E. R. Flueh, L. Planert, T. J. Reston, and W. Weinrebe, Microearthquake seismicity of Mid-Atlantic Ridge at 5°S: A view of tectonic extension, *J. Geophys. Res.*, *109*, doi:10.1029/2003JB002,827, 2004.
- Tolstoy, M., A. J. Harding, and J. A. Orcutt, Crustal thickness on the Mid-Atlantic Ridge: Bull's eye gravity anomalies and focussed accretion, *Science*, *262*, 726–729, 1993.

- Tolstoy, M., D. R. Bohnenstiehl, M. Edwards, and G. J. Kurras, Seismic character of volcanic activity at the ultraslow spreading Gakkel Ridge, *Geology*, *29*, 1139–1142, 2001.
- Toomey, D. R., S. C. Solomon, and G. M. Purdy, Tomographic imaging of the shallow crustal structure of the East Pacific Rise at 9°30'N, *J. Geophys. Res.*, *99*, 24,135–24,157, 1994.
- Tucholke, B. E., and J. Lin, A geological model for the structure of ridge segments in slow spreading ocean crust., *J. Geophys. Res.*, *99*, 11,937–11,958, 1994.
- Tucholke, B. E., J. L. M. C. Kleinrock, et al., Segmentation and crustal structure of the western Mid-Atlantic Ridge flank, 25°25'–27°10' N and 0–29 m.y., *J. Geophys. Res.*, *102*, 10,203–10,223, 1997.
- Tucholke, B. E., J. Lin, and M. C. Kleinrock, Megamullions and mullion structure defining oceanic metamorphic core complexes on the Mid-Atlantic Ridge., *J. Geophys. Res.*, *103*, 9857–9866, 1998.
- Tucholke, B. E., K. Fujioka, T. Ishihara, G. Hirt, and M. Kinoshita, Submersible study of an oceanic megamullion in the North Atlantic., *J. Geophys. Res.*, *106*, 16,145–16,162, 2001.
- Van Avendonk, H. J. A., An investigation of the crustal structure of the Clipperton transform fault using 3D seismic tomography, Ph.d. thesis, Univ. of California, 1998, San Diego.
- Van Avendonk, H. J. A., A. J. Harding, J. A. Orcutt, and J. S. McCain, A two-dimensional tomographic study of the Clipperton transform fault, *J. Geophys. Res.*, *103*, 17,885–17,899, 1998b.
- Van Avendonk, H. J. A., A. J. Harding, J. A. Orcutt, and W. S. Holbrook, Hybrid shortest path and ray bending method for traveltime and raypath calculations., *Geophysics*, *66*, 648–653, 2001.
- Vera, E. E., J. C. Mutter, P. Buhl, et al., The structure of 0- to 0.2-m.y.-old oceanic crust at 9°N on the East Pacific Rise from expanded spread profiles, *J. Geophys. Res.*, *95*, 15,529–15,556, 1990.
- Vidale, J. E., Finite-difference calculation of travel times, *Bull. Seismol. Soc. Am.*, *78*, 24,135–24,157, 1988.
- White, R. S., D. McKenzie, and R. K. O'Nions, Oceanic Crustal Thickness From Seismic Measurements and Rare Earth Element Inversion, *J. Geophys. Res.*, *97*, 19,683–19,715, 1992.
- Whitmarsh, R. B., and A. J. Calvert, Crustal structure of Atlantic fracture zones, I, The Charlie Gibbs fracture zone, *Geophys. J. R. Astron. Soc.*, *85*, 107–138, 1986.
- Wiener, N., *Extrapolation, interpolation, and smoothing of stationary time series*, New York, John Wiley and Sons, Inc., 1949.

- Wilson, D. S., Fastest known spreading on the Miocene Cocos-Pacific plate boundary, *Geophys. Res. Letters*, *23*, 3003–3006, 1996.
- Wolfe, C. J., G. M. Purdy, D. R. Toomey, and S. C. Solomon, Microearthquake characteristics and crustal velocity structure at 29°N on the Mid-Atlantic Ridge, *J. Geophys. Res.*, *100*, 24,449–24,472, 1995.
- Zelt, C. A., FAST - Programme package for First Arrival Seismic Tomography, <http://www.geophysics.rice.edu/departement/faculty/zelt/fast.html>, pp. 1–17, 1998.
- Zelt, C. A., and P. J. Barton, 3D seismic refraction tomography: A comparison of two methods applied to data from the Faeroe Basin, *J. Geophys. Res.*, *103*, 7187–7210, 1998.
- Zhang, J., and M. N. Toksöz, Nonlinear refraction travelttime tomography, *Geophysics*, *63*, 1726–1737, 1998.

Appendix A

Selected seismic record sections of Profile 07/08

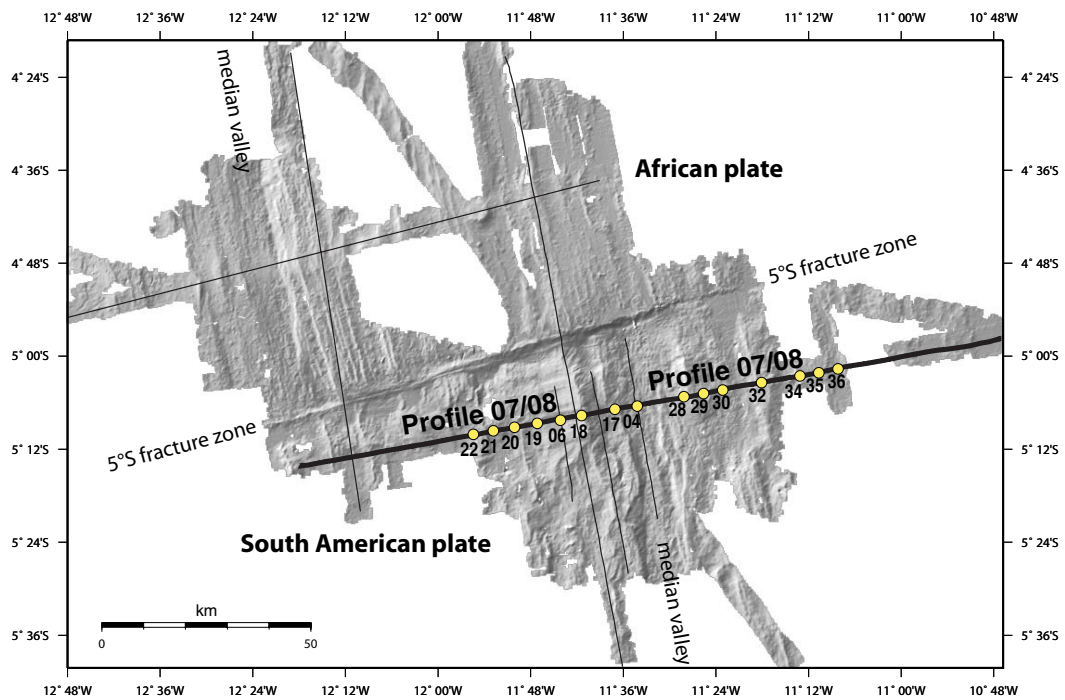


Figure A.1: *Profile geometry and station distribution of Profile 07/08.*

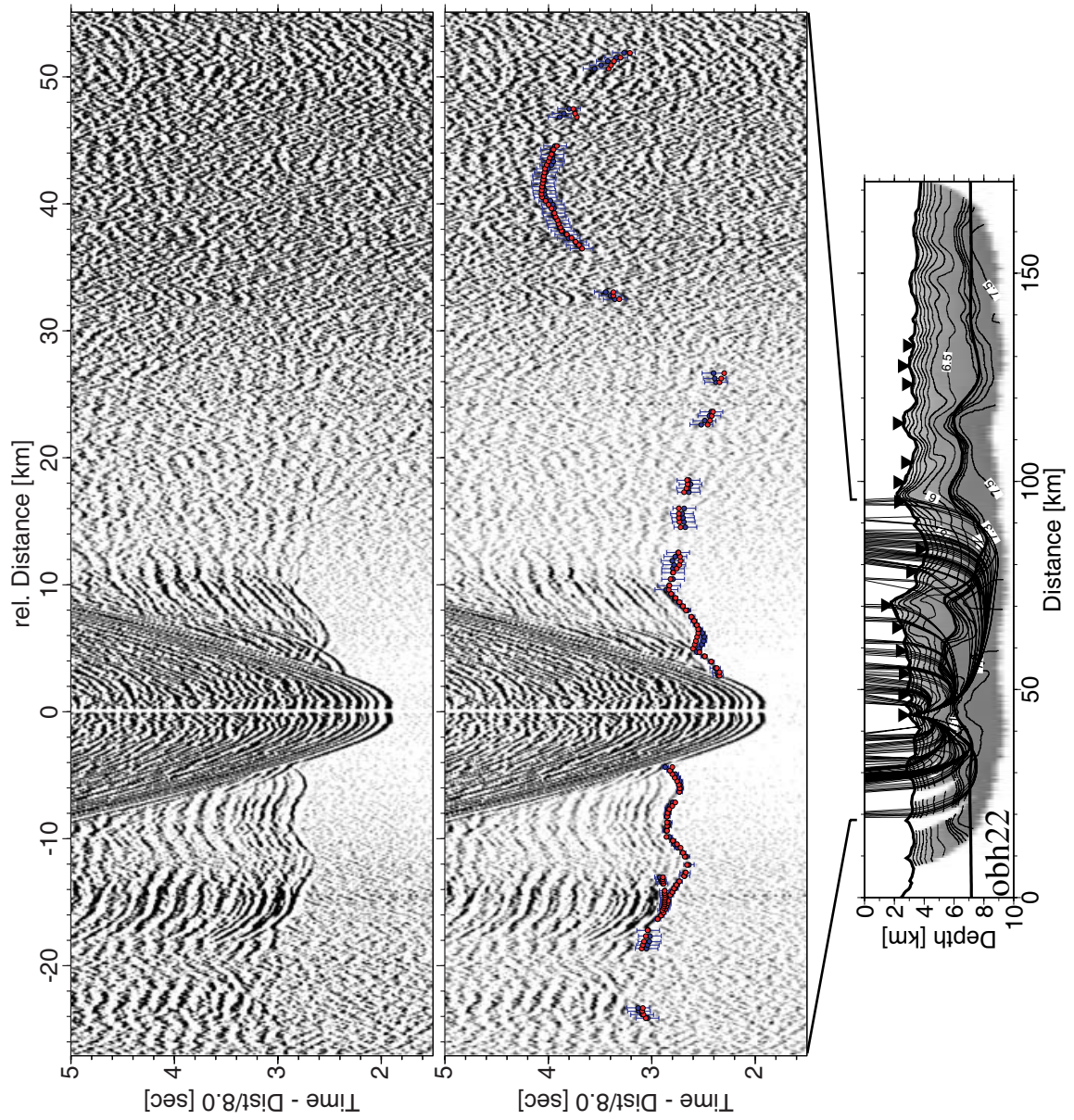


Figure A.2: Profile 07/08, OBH 22.

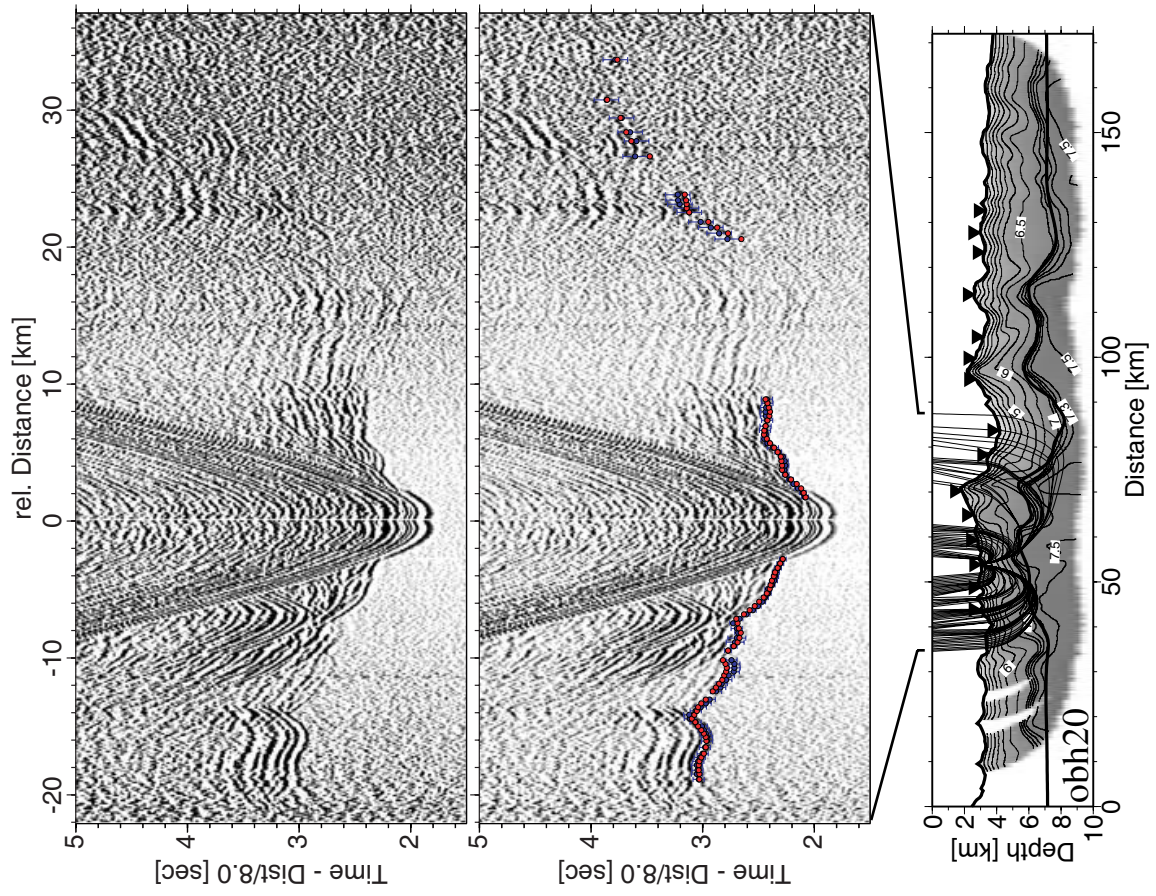


Figure A.3: *Profile 07/08, OBH 20.*

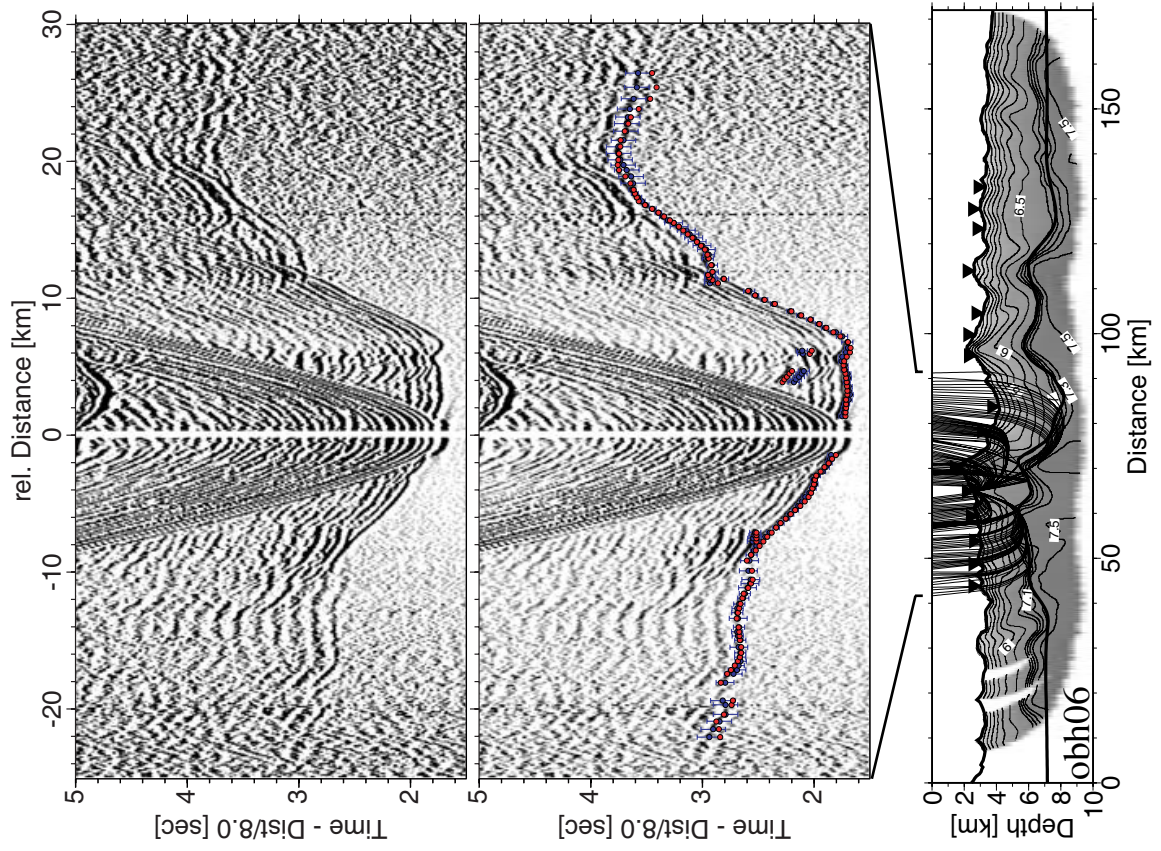


Figure A.4: Profile 07/08, OBH 06.

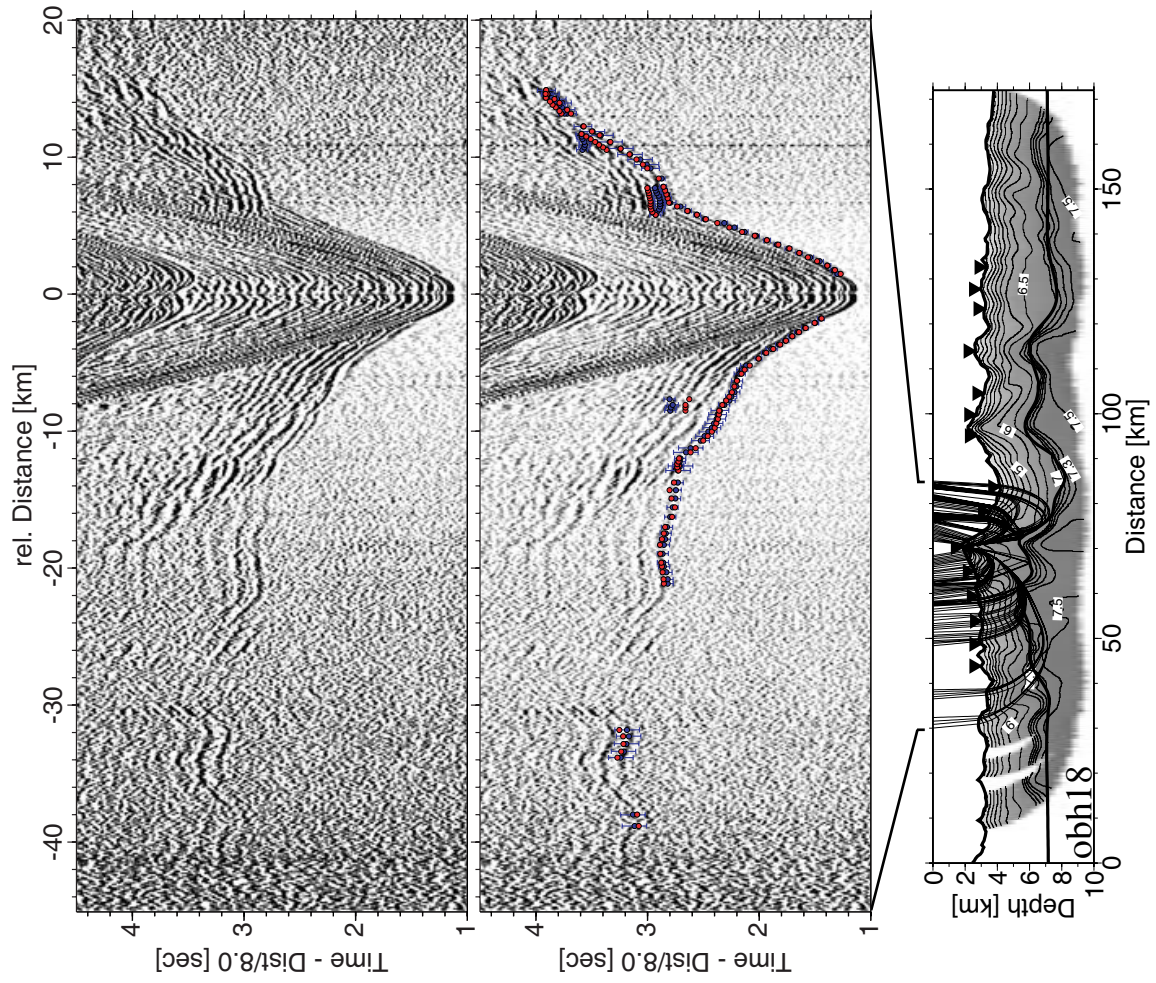


Figure A.5: *Profile 07/08, OBH 18.*

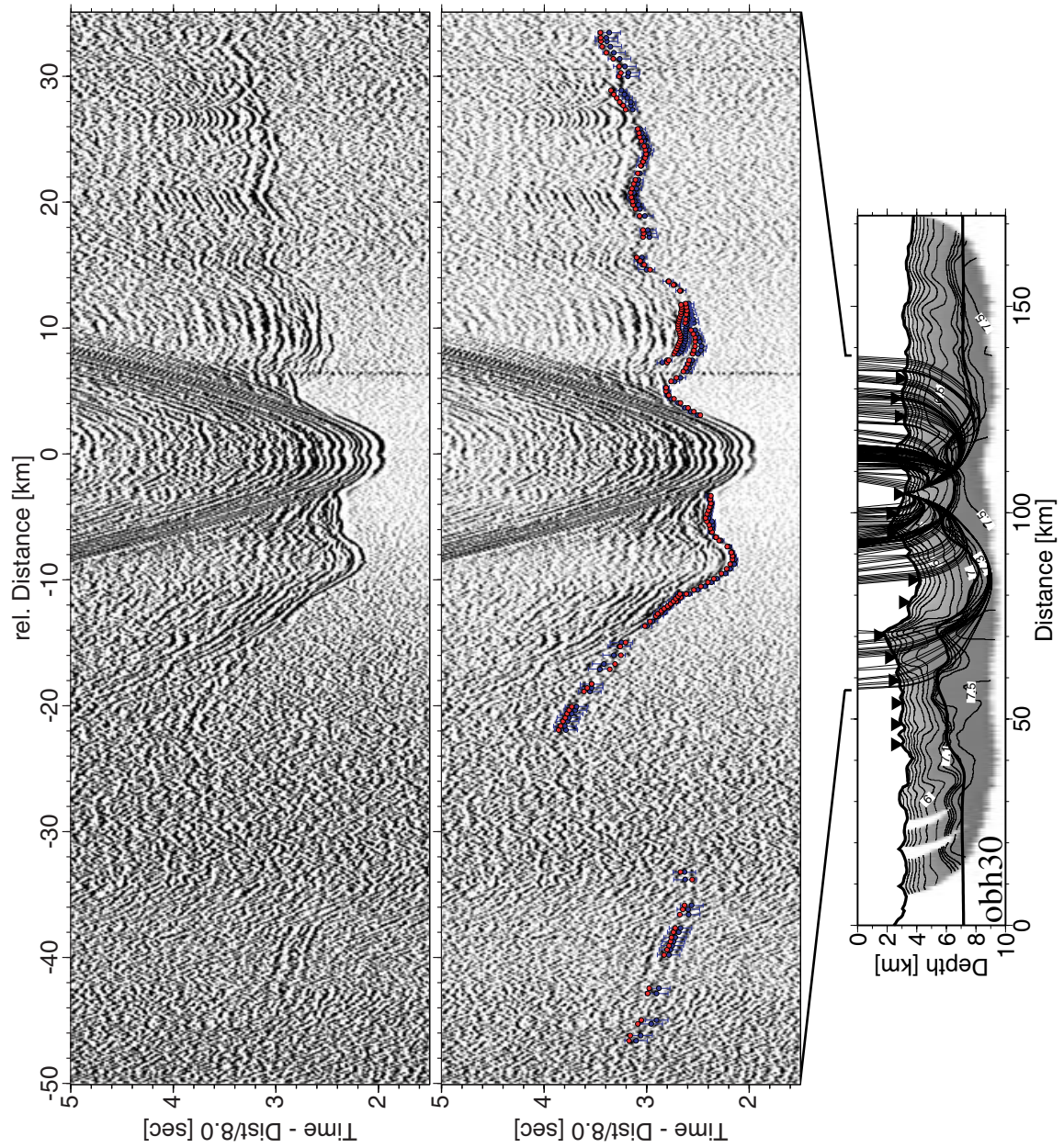


Figure A.6: Profile 07/08, OBH 30.

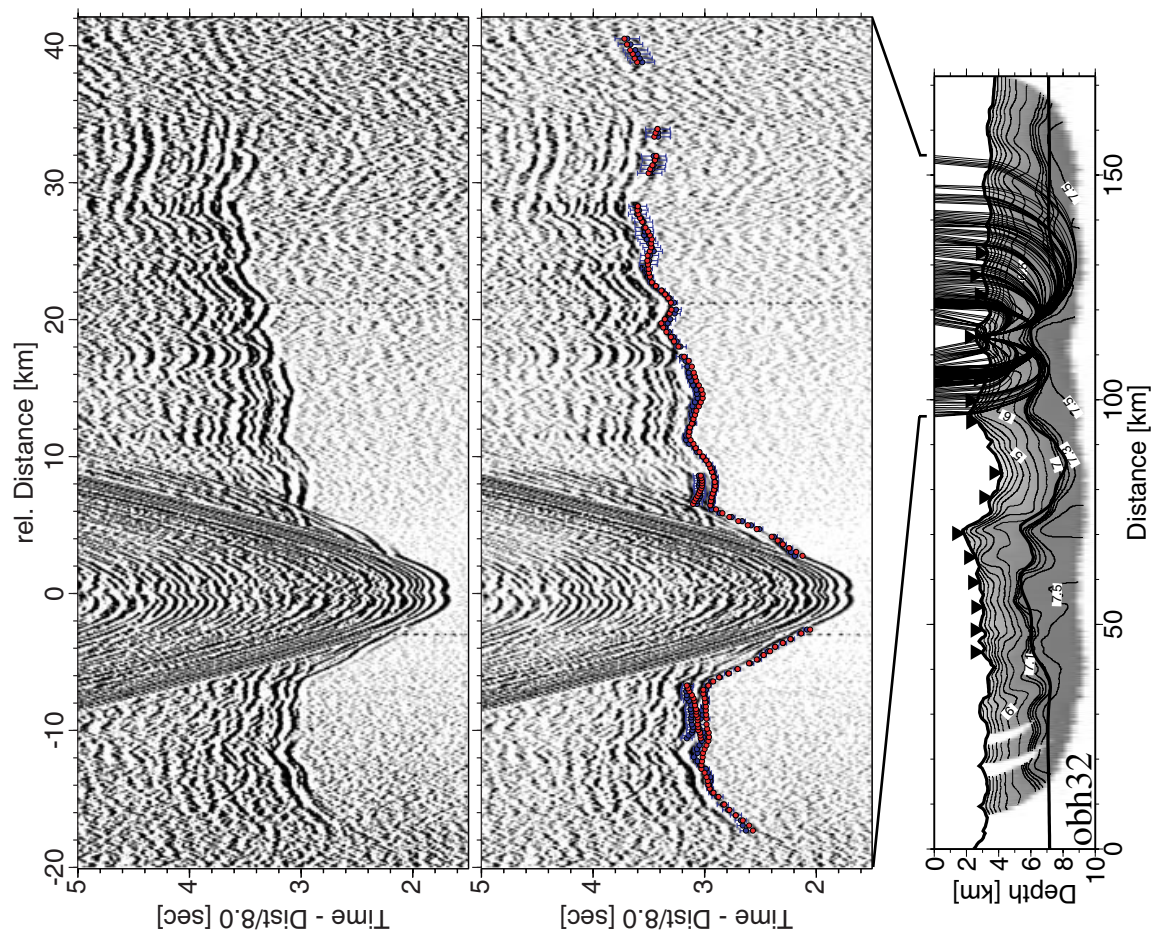


Figure A.7: Profile 07/08, OBH 32.

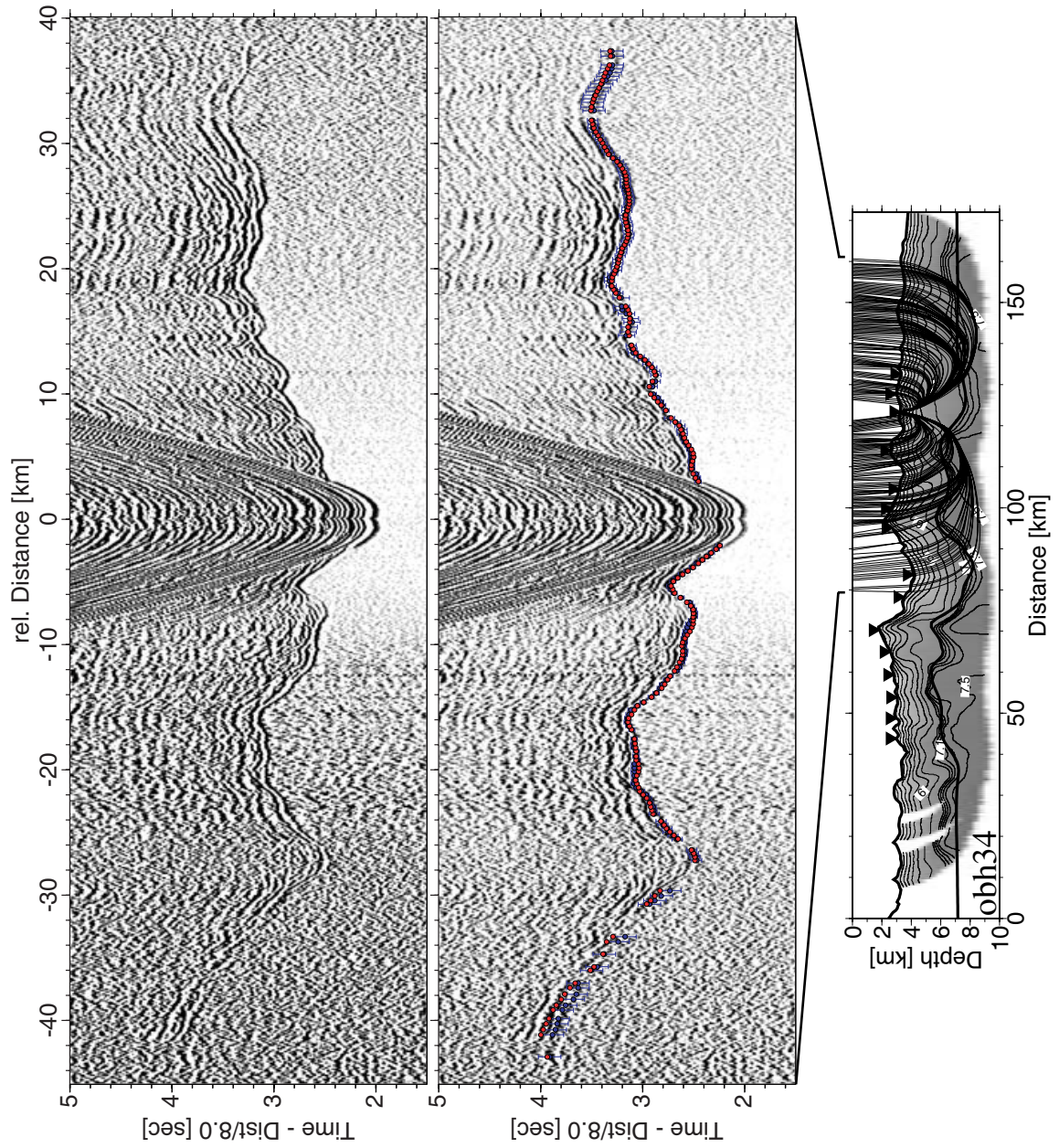


Figure A.8: Profile 07/08, OBH 34.

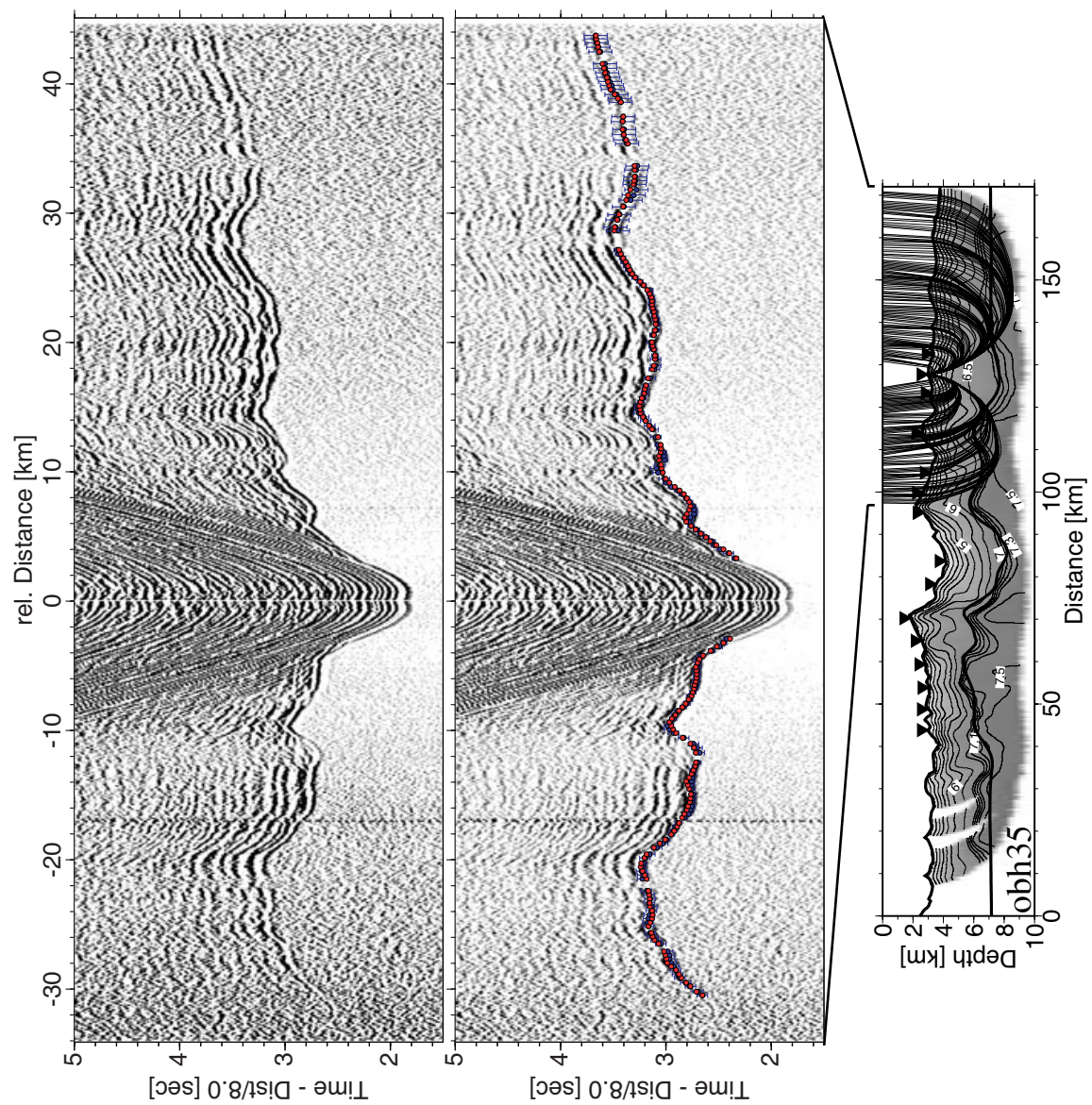


Figure A.9: *Profile 07/08, OBH 35.*

Appendix B

Selected seismic record sections of Profile 09

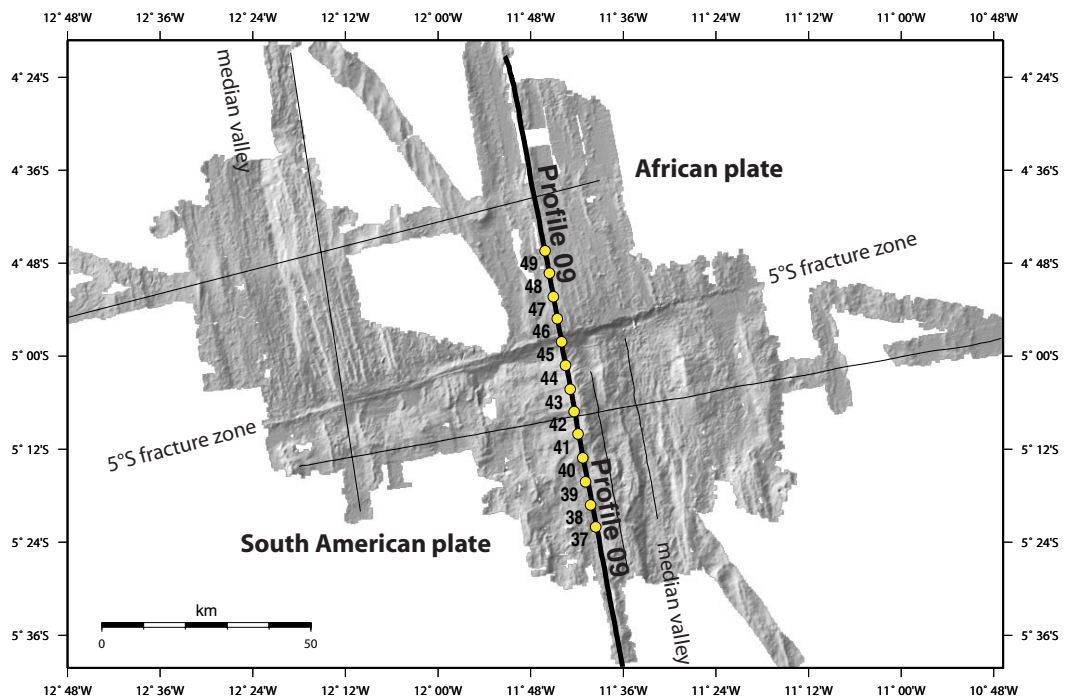


Figure B.1: *Profile geometry and station distribution of Profile 09.*

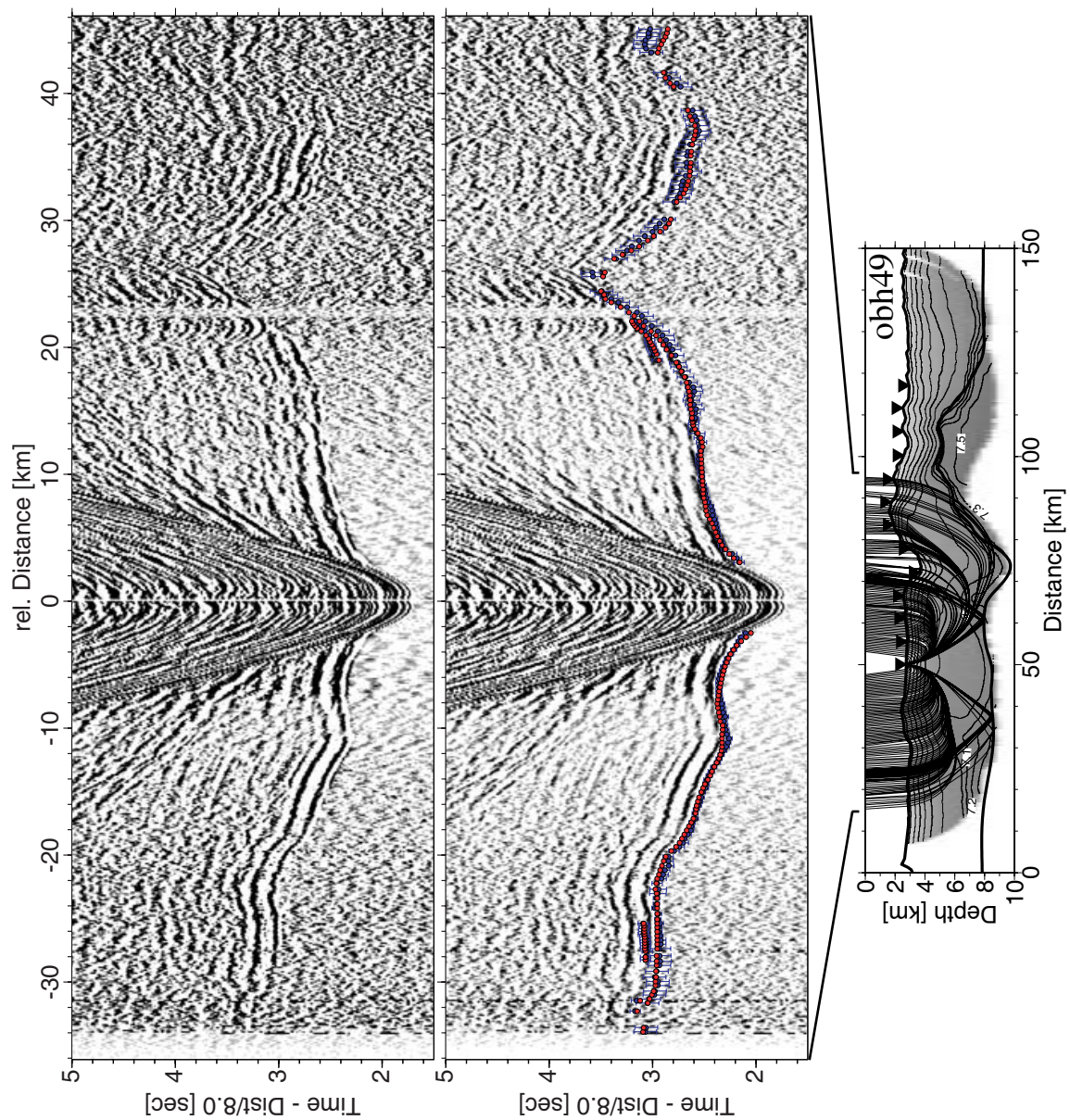


Figure B.2: Profile 09, OBH 49.

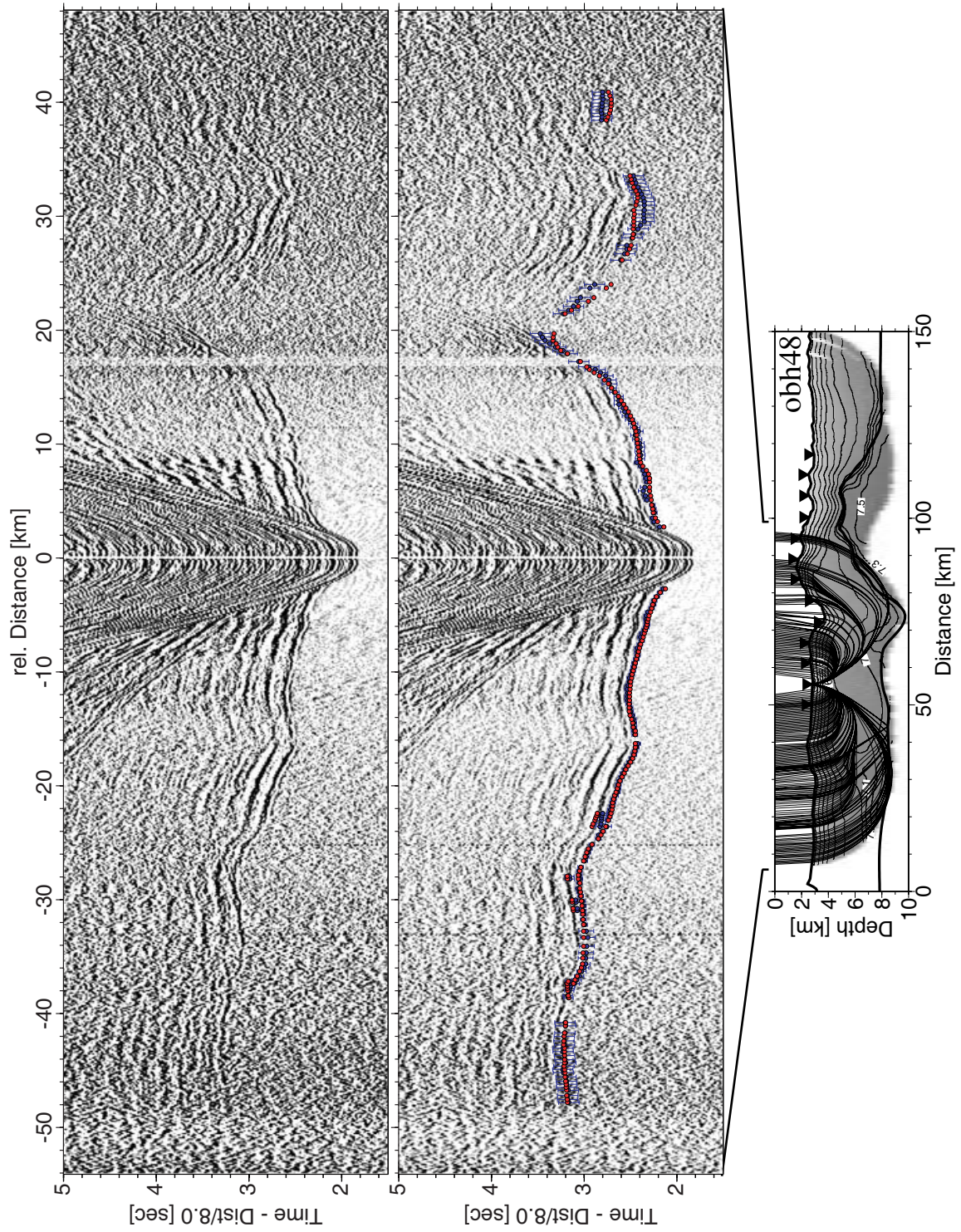


Figure B.3: *Profile 09, OBH 48.*

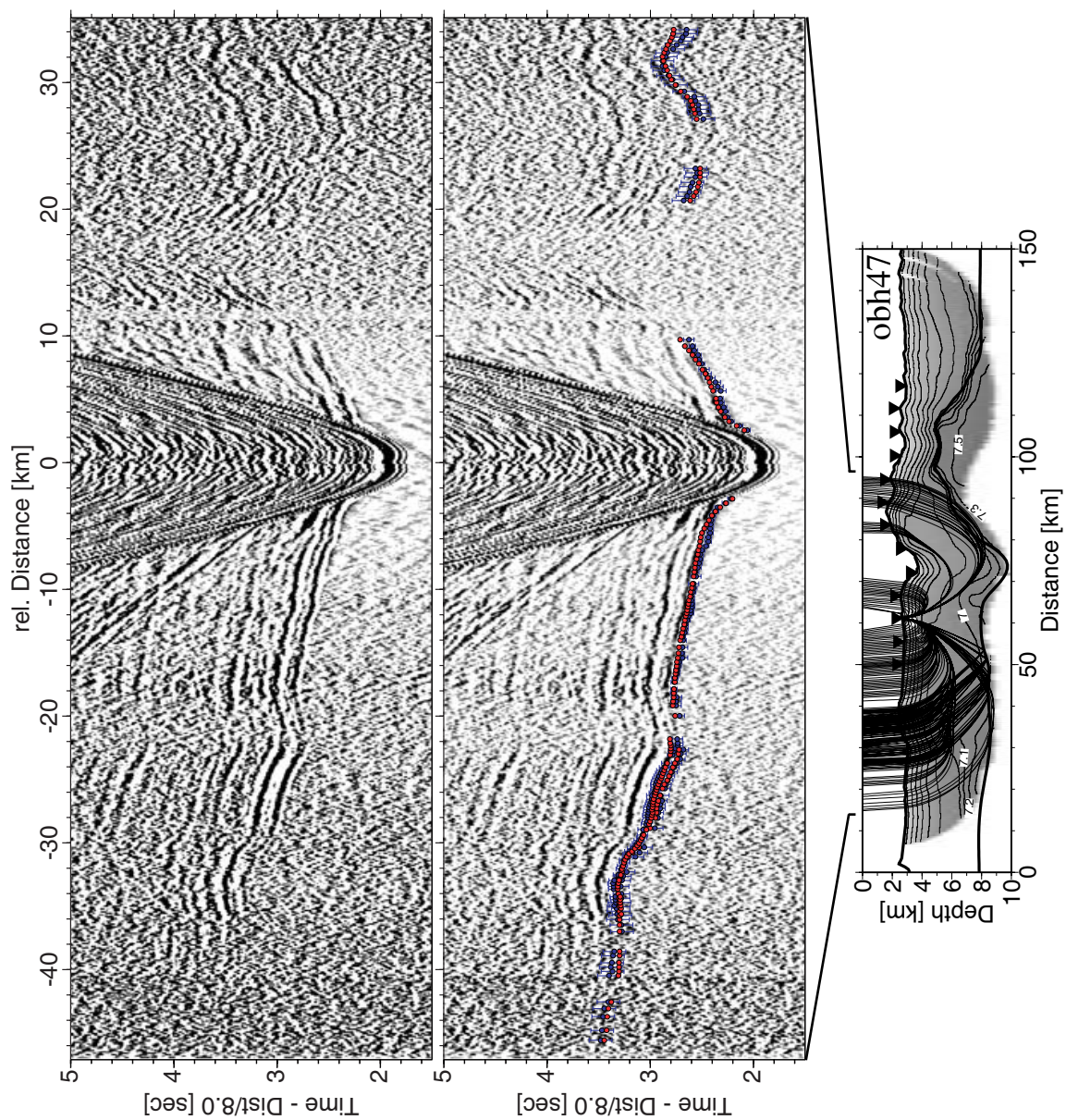


Figure B.4: Profile 09, OBH 47.

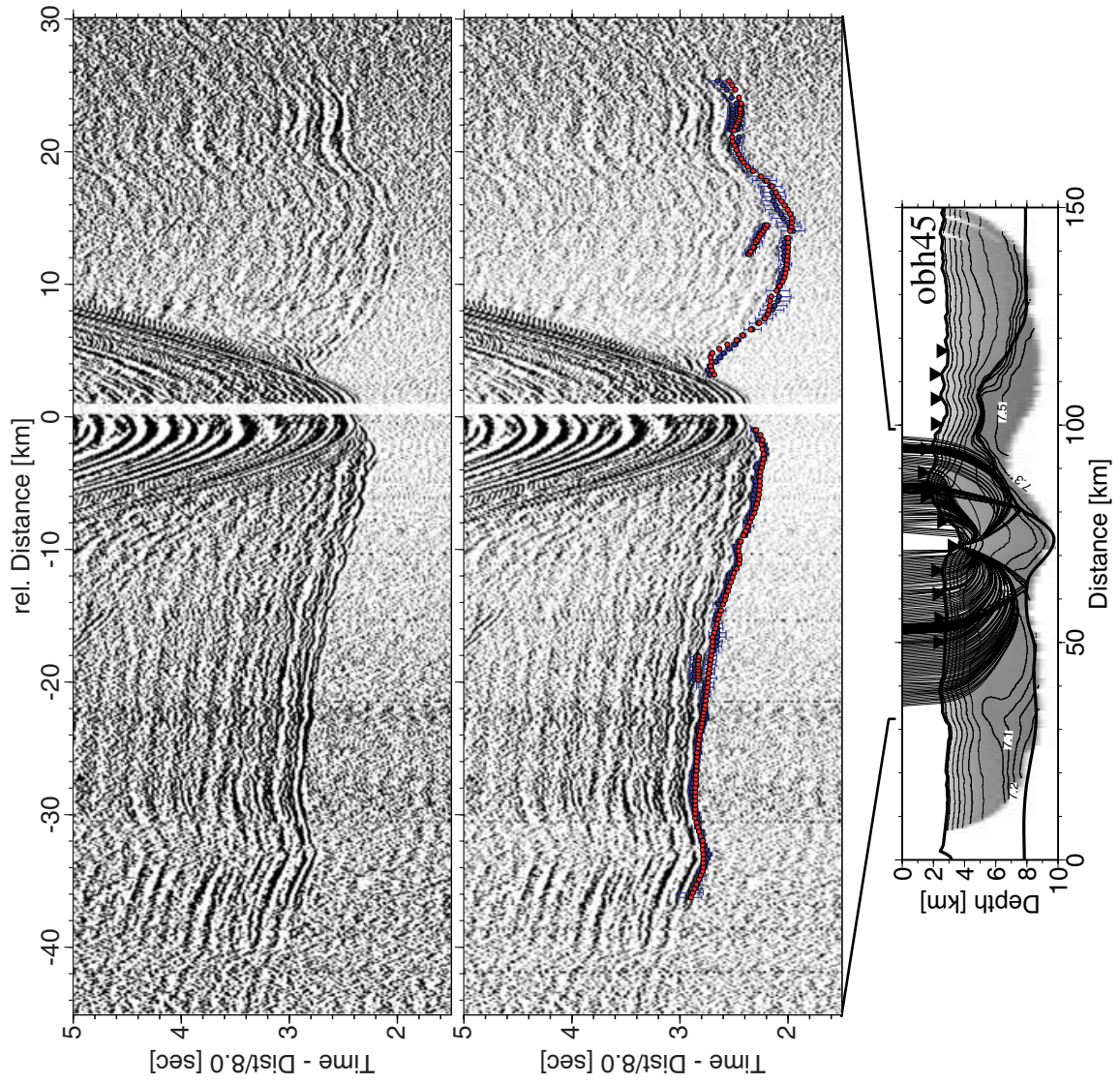


Figure B.5: *Profile 09, OBH 45.*

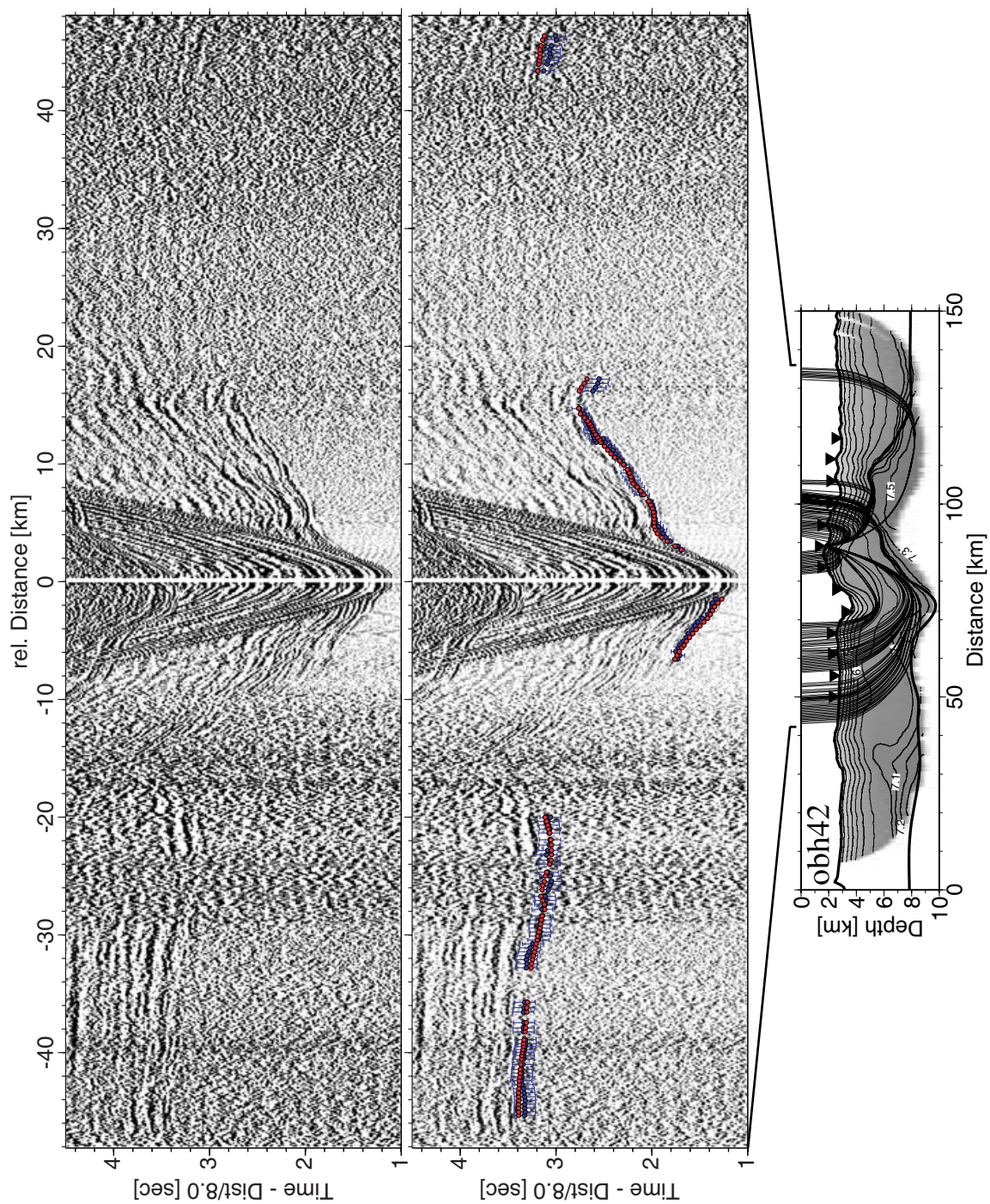


Figure B.6: Profile 09, OBH 42.

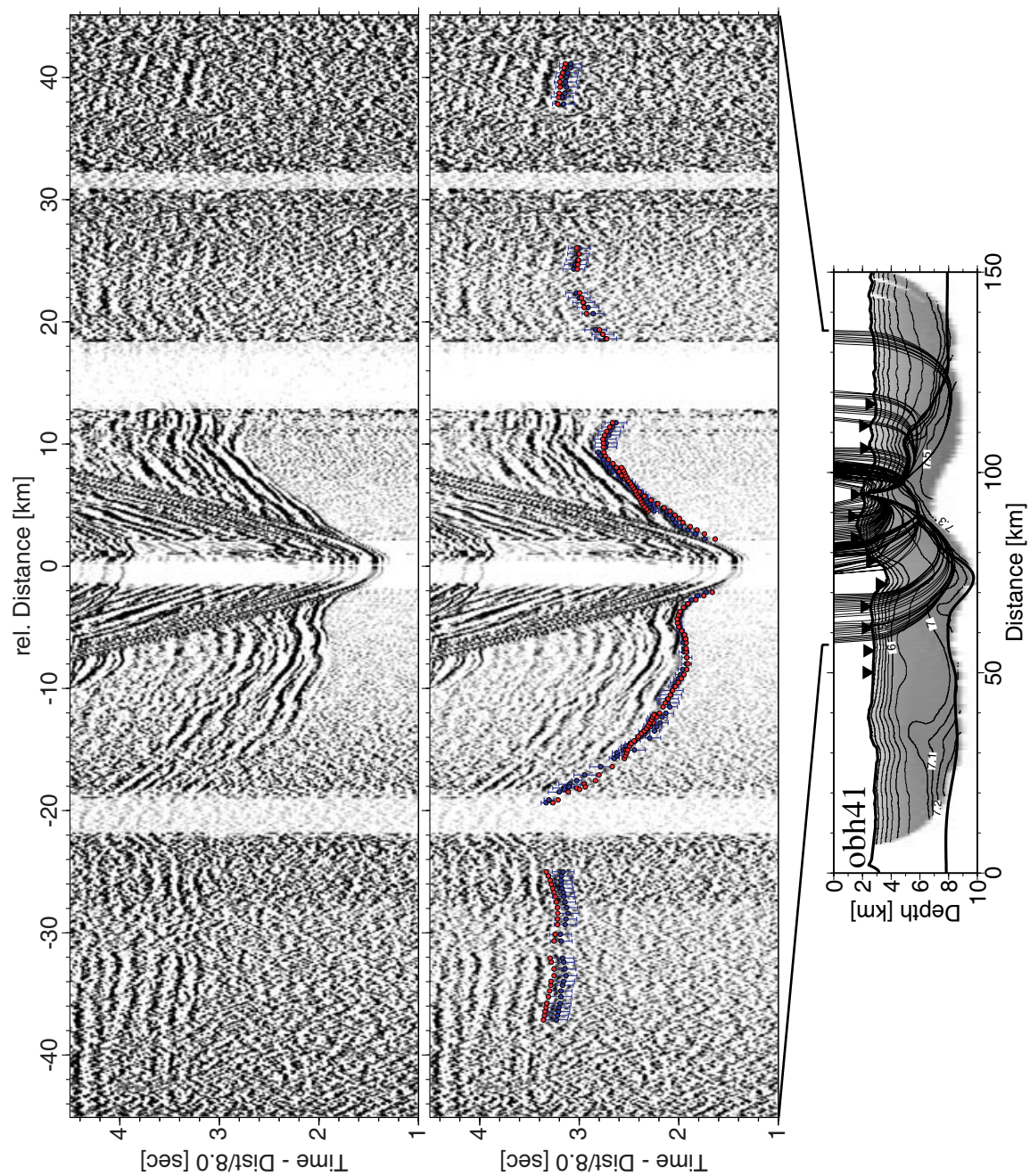


Figure B.7: *Profile 09, OBH 41.*



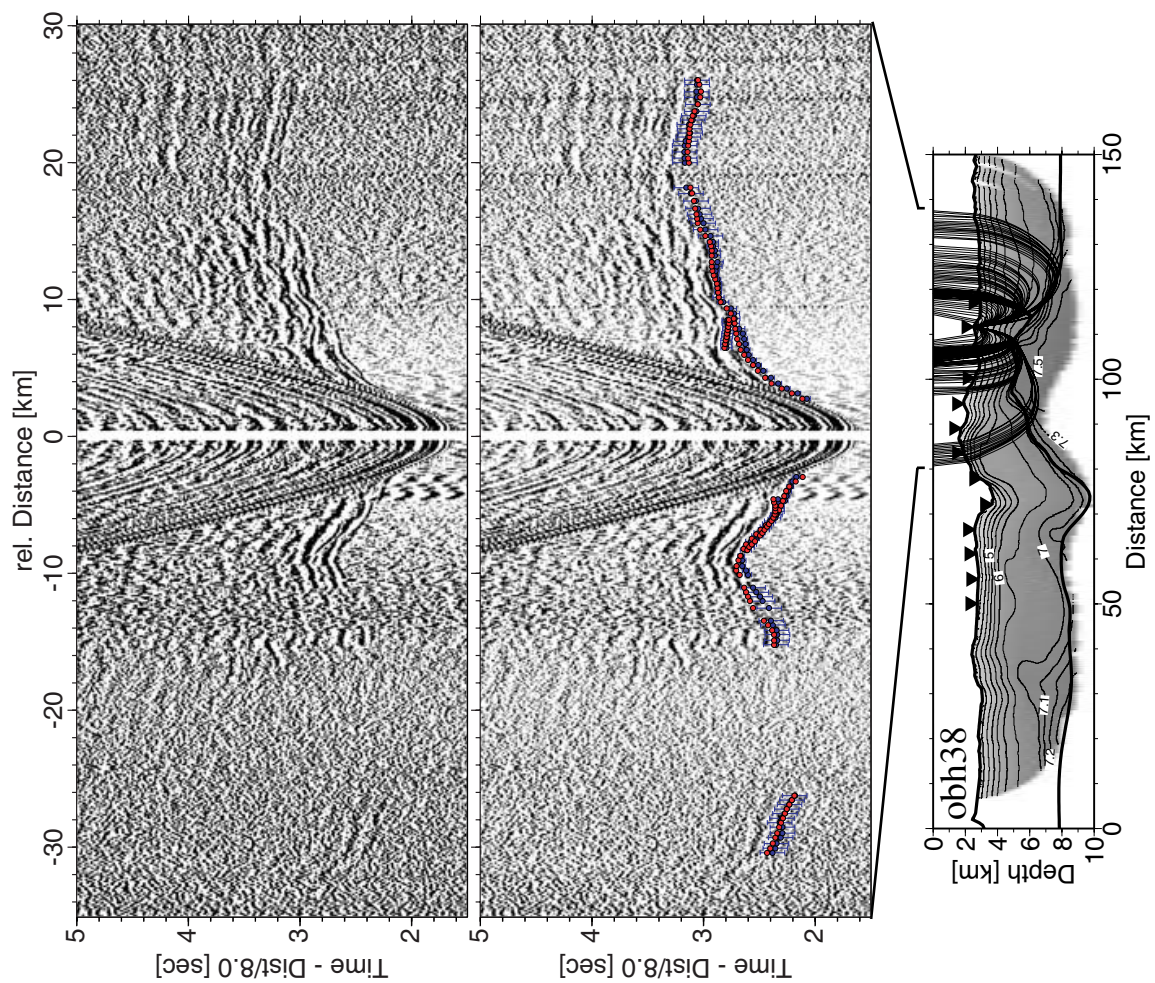


Figure B.9: Profile 09, OBH 38.

Appendix C

Selected seismic record sections of Profile 10

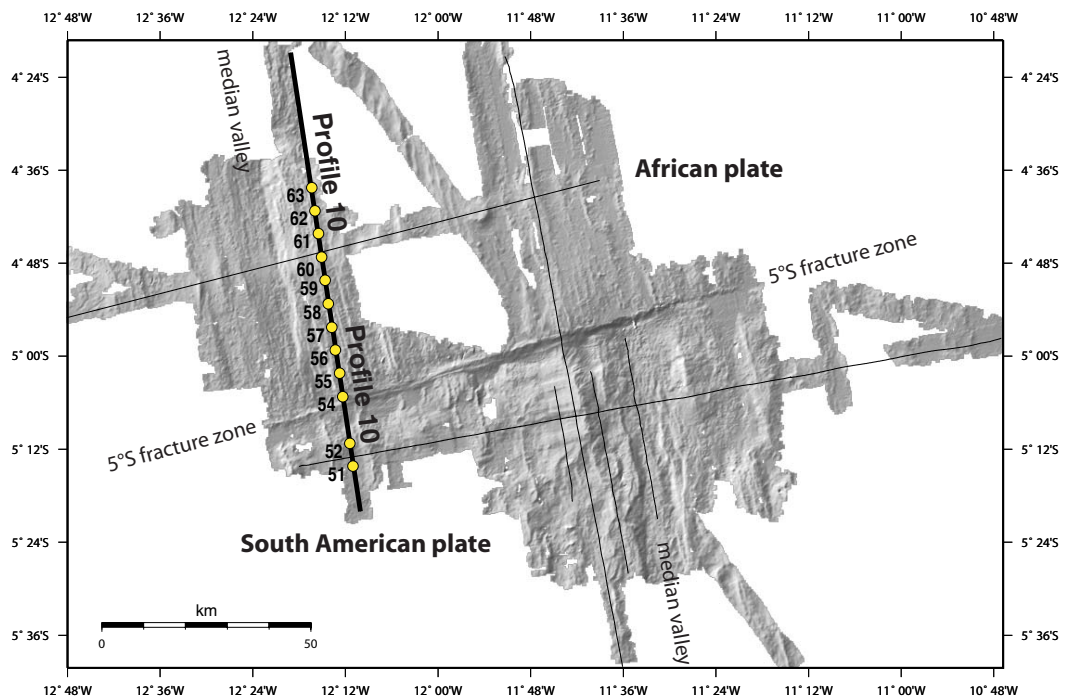
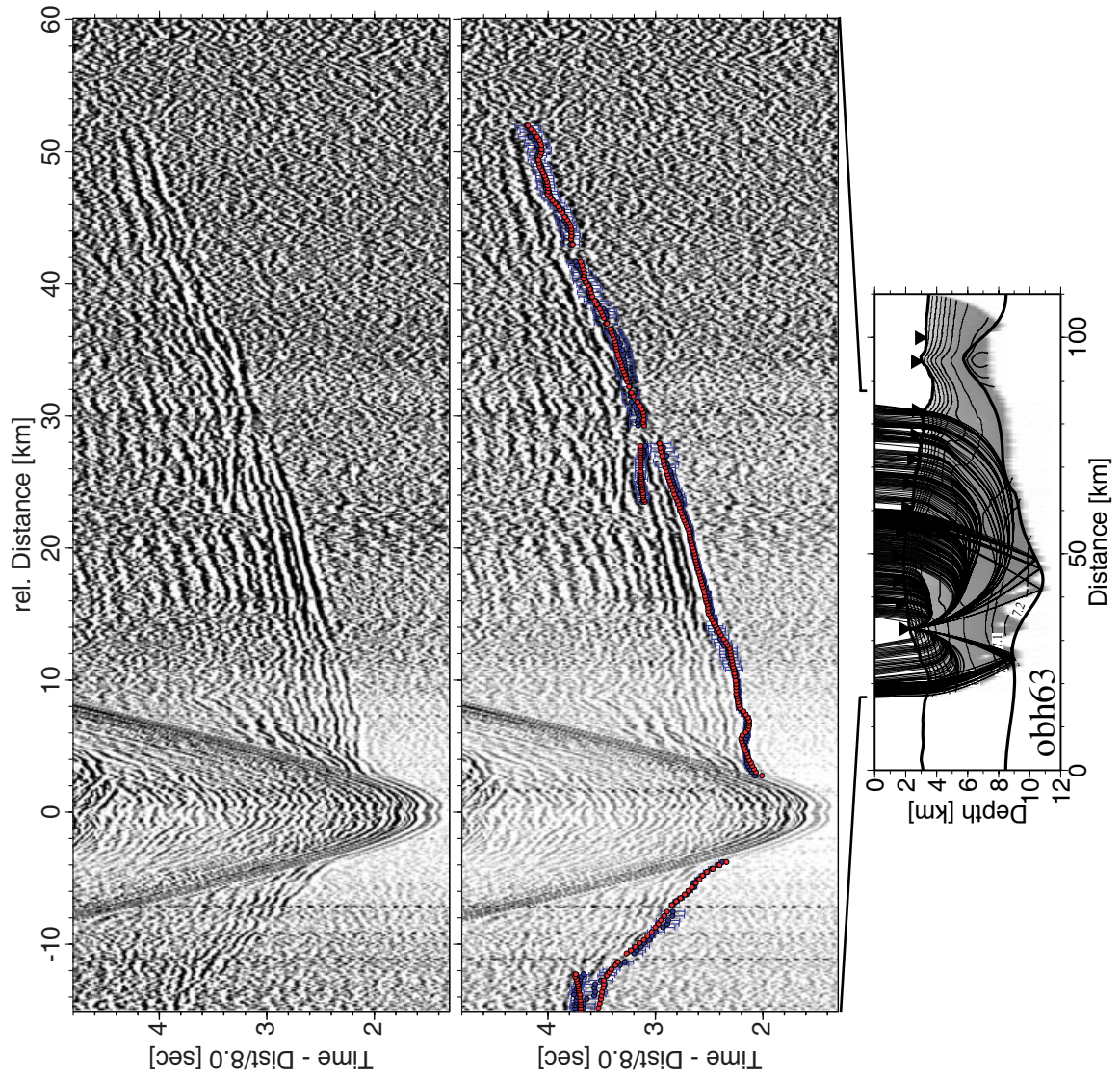


Figure C.1: *Profile geometry and station distribution of Profile 10.*

Figure C.2: *Profile 10, OBH 63.*

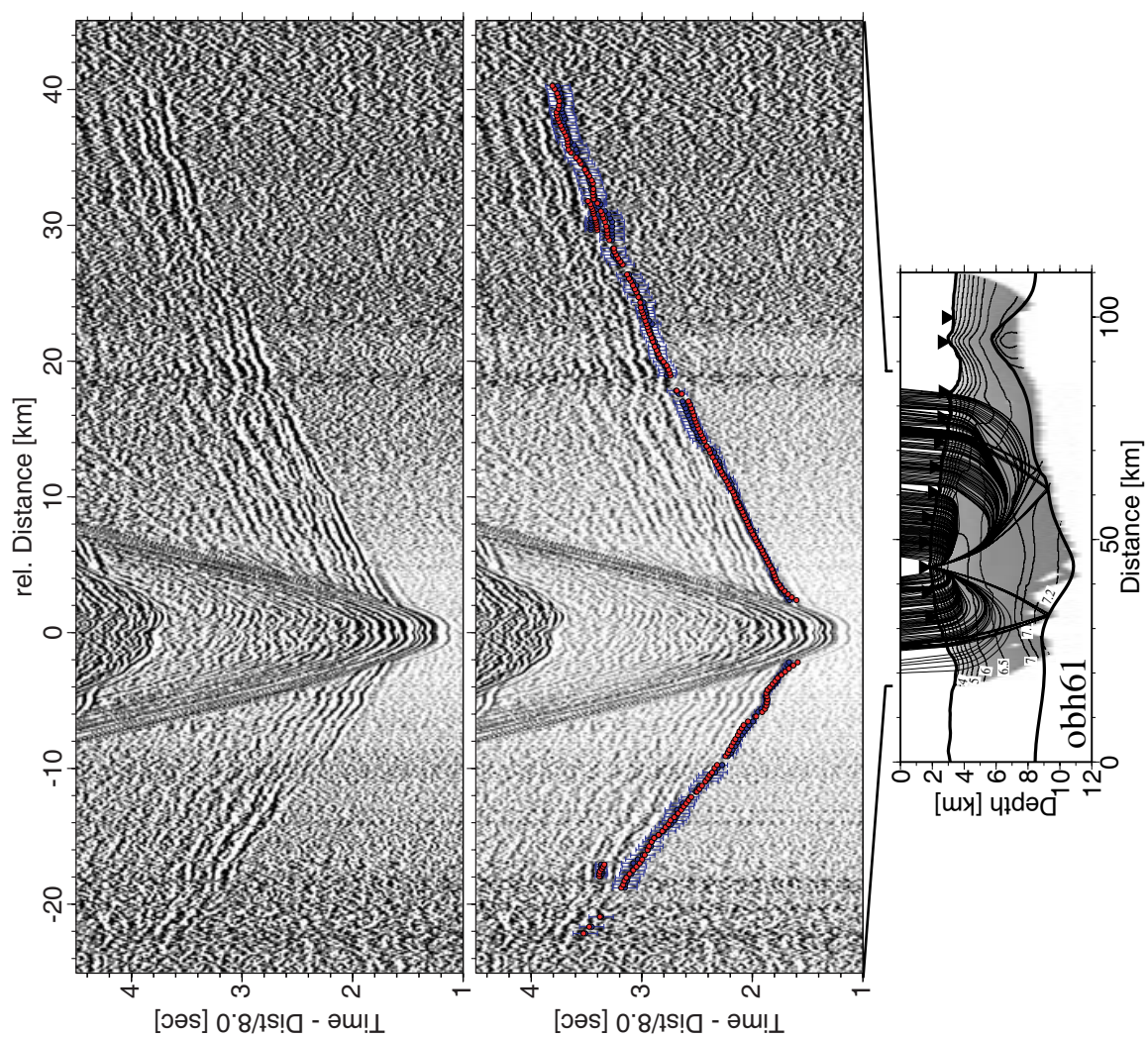
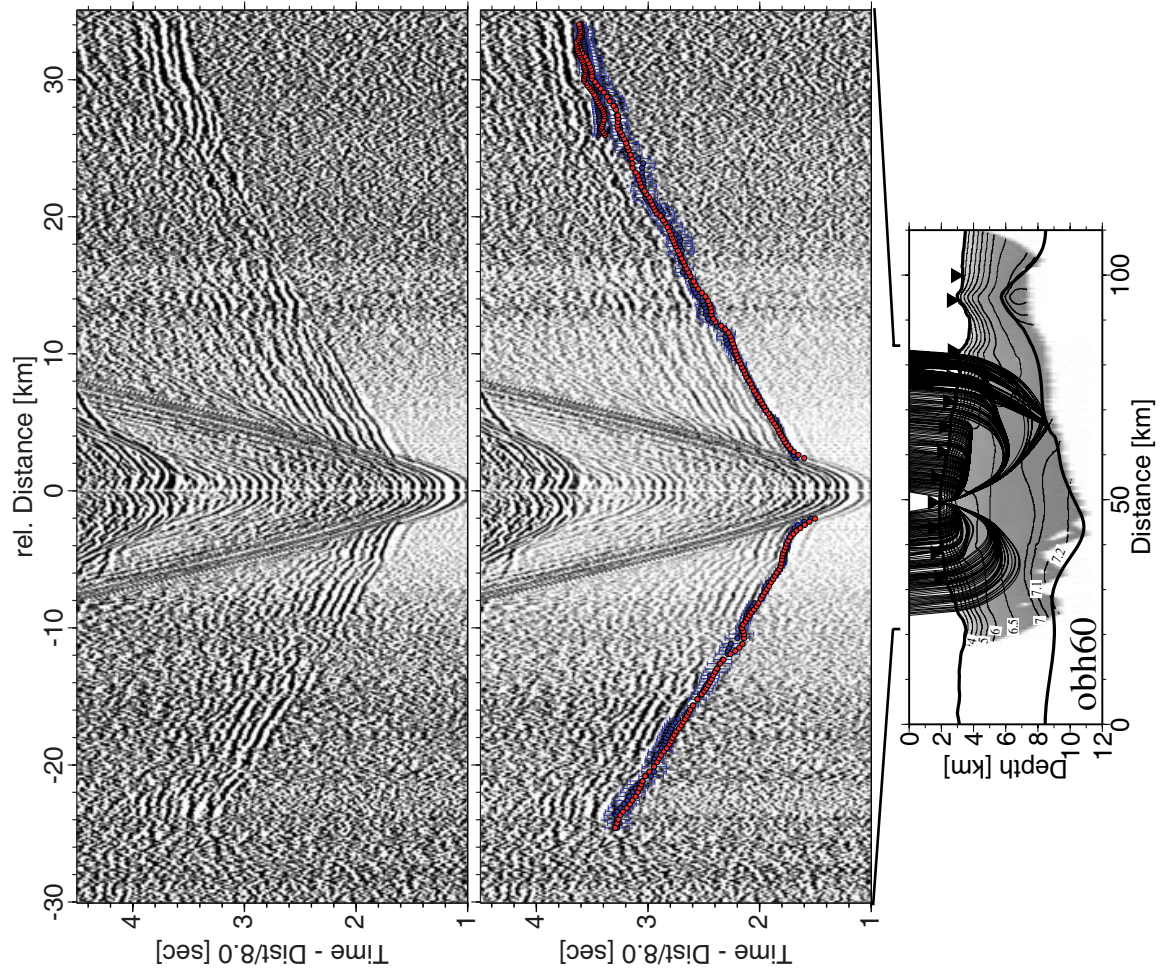


Figure C.3: *Profile 10, OBH 61.*

Figure C.4: *Profile 10, OBH 60.*

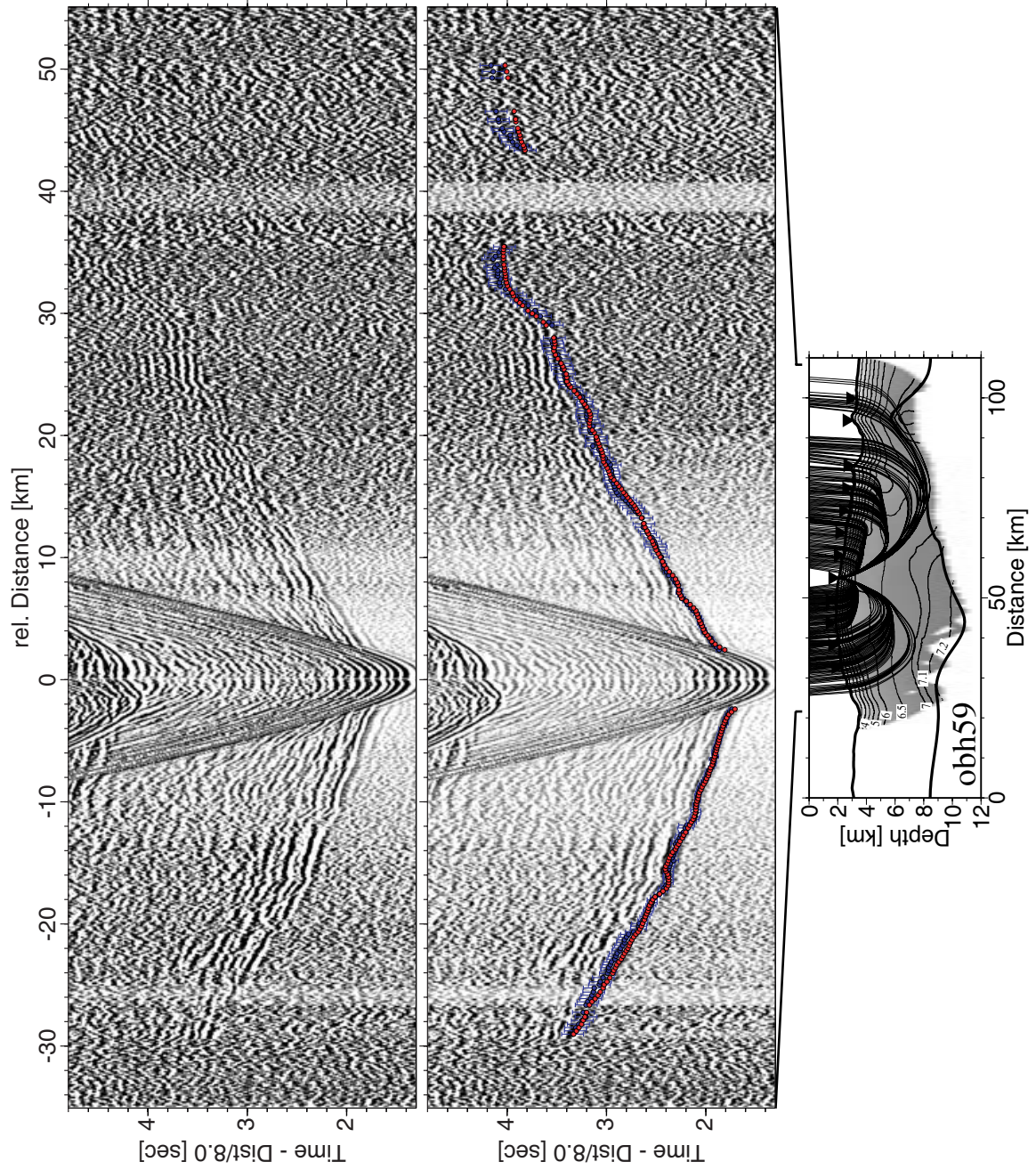


Figure C.5: *Profile 10, OBH 59.*

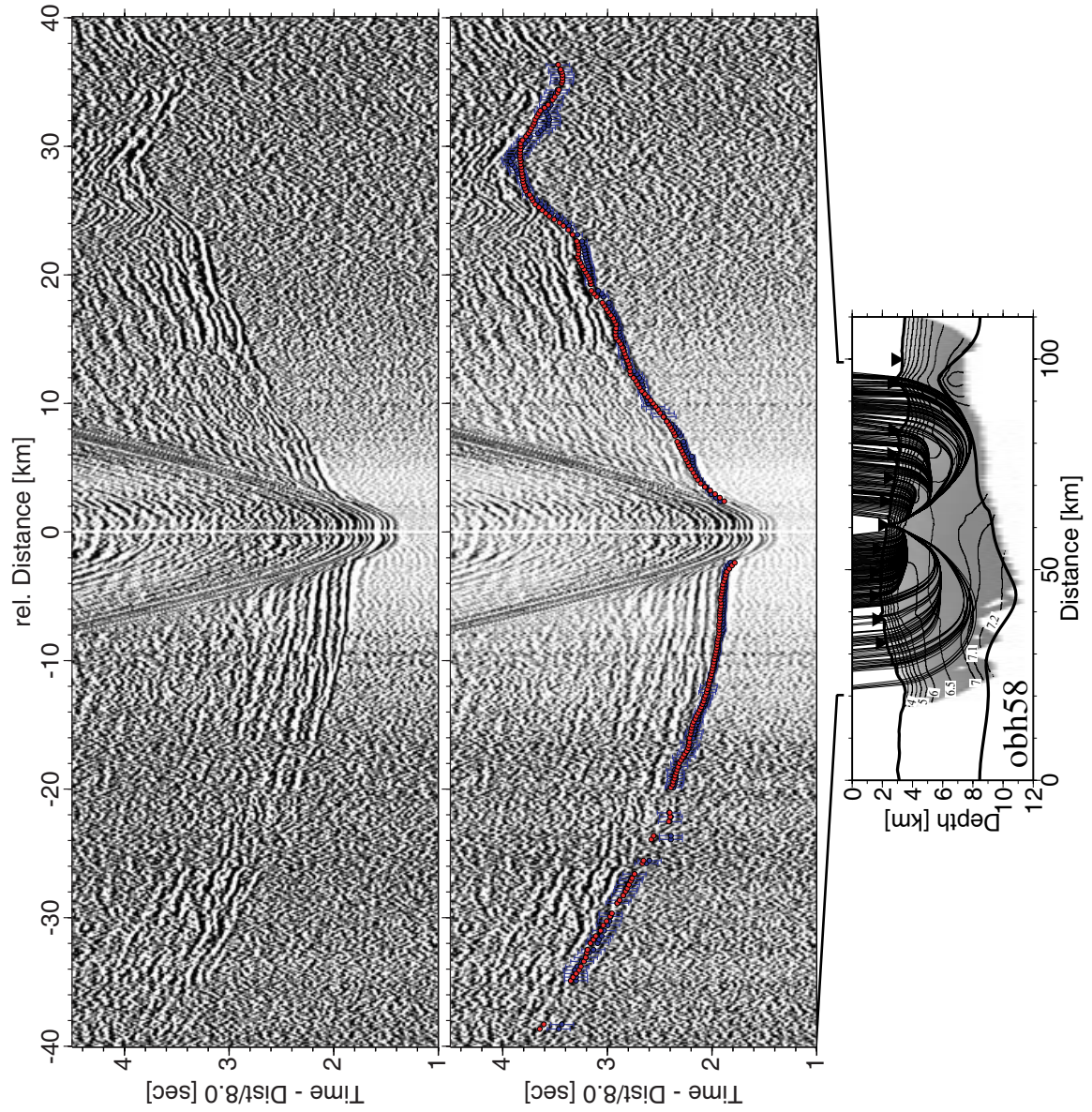
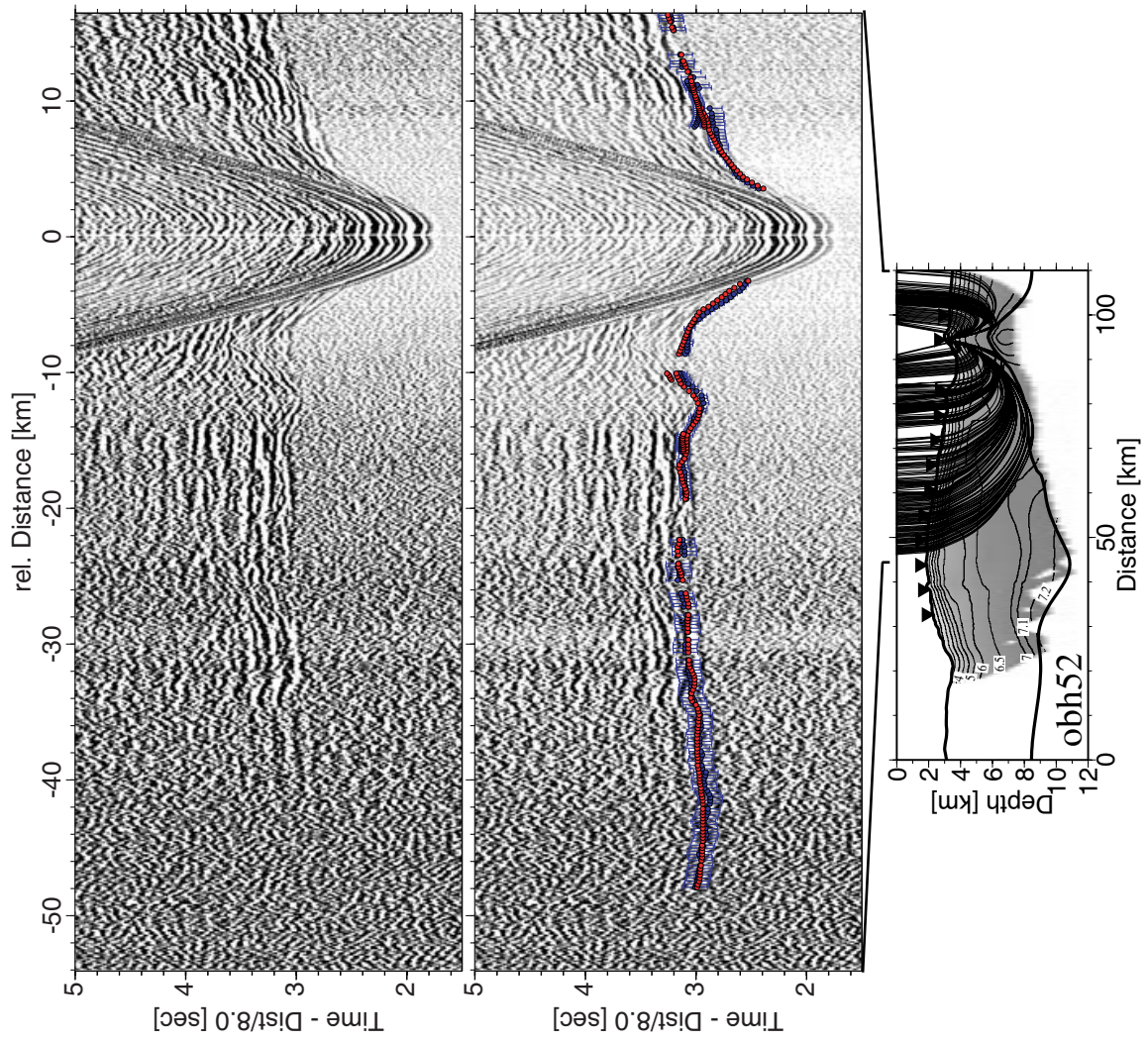


Figure C.6: *Profile 10, OBH 58.*

Figure C.7: *Profile 10, OBH 52.*

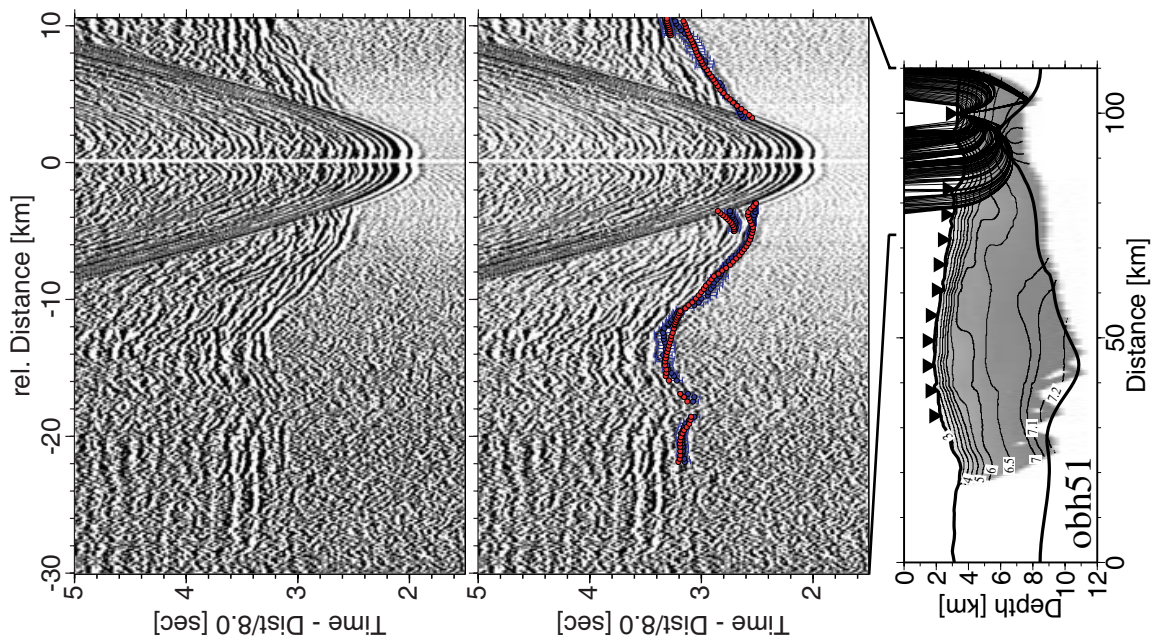


Figure C.8: Profile 10, OBH 51.

Appendix D

Selected seismic record sections of Profile 11

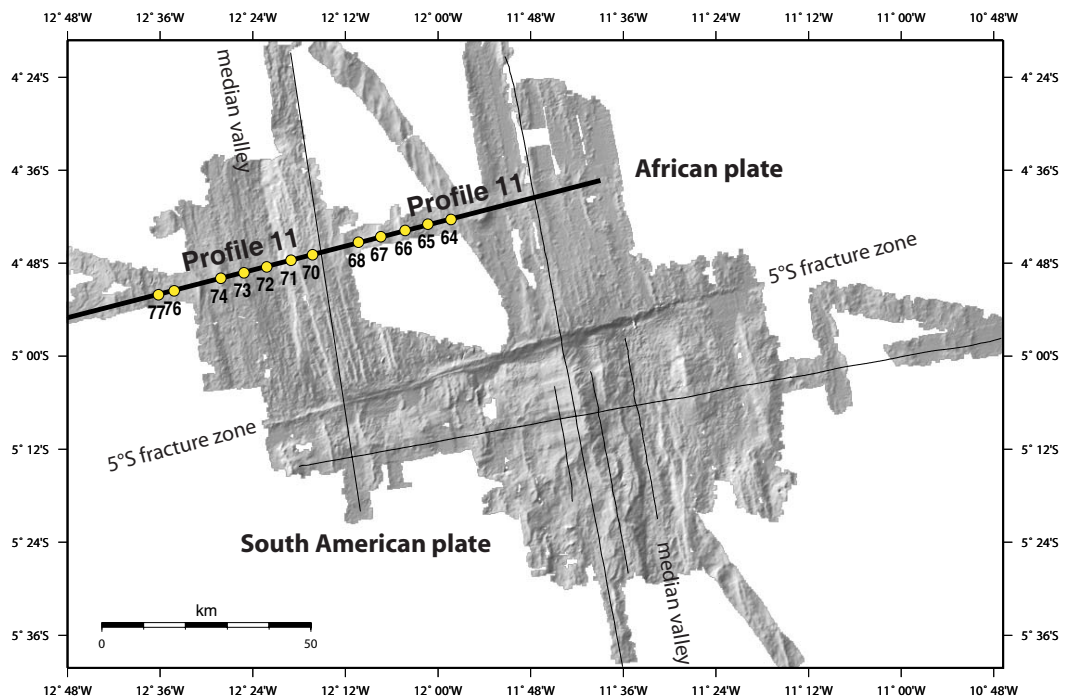


Figure D.1: *Profile geometry and station distribution of Profile 11.*

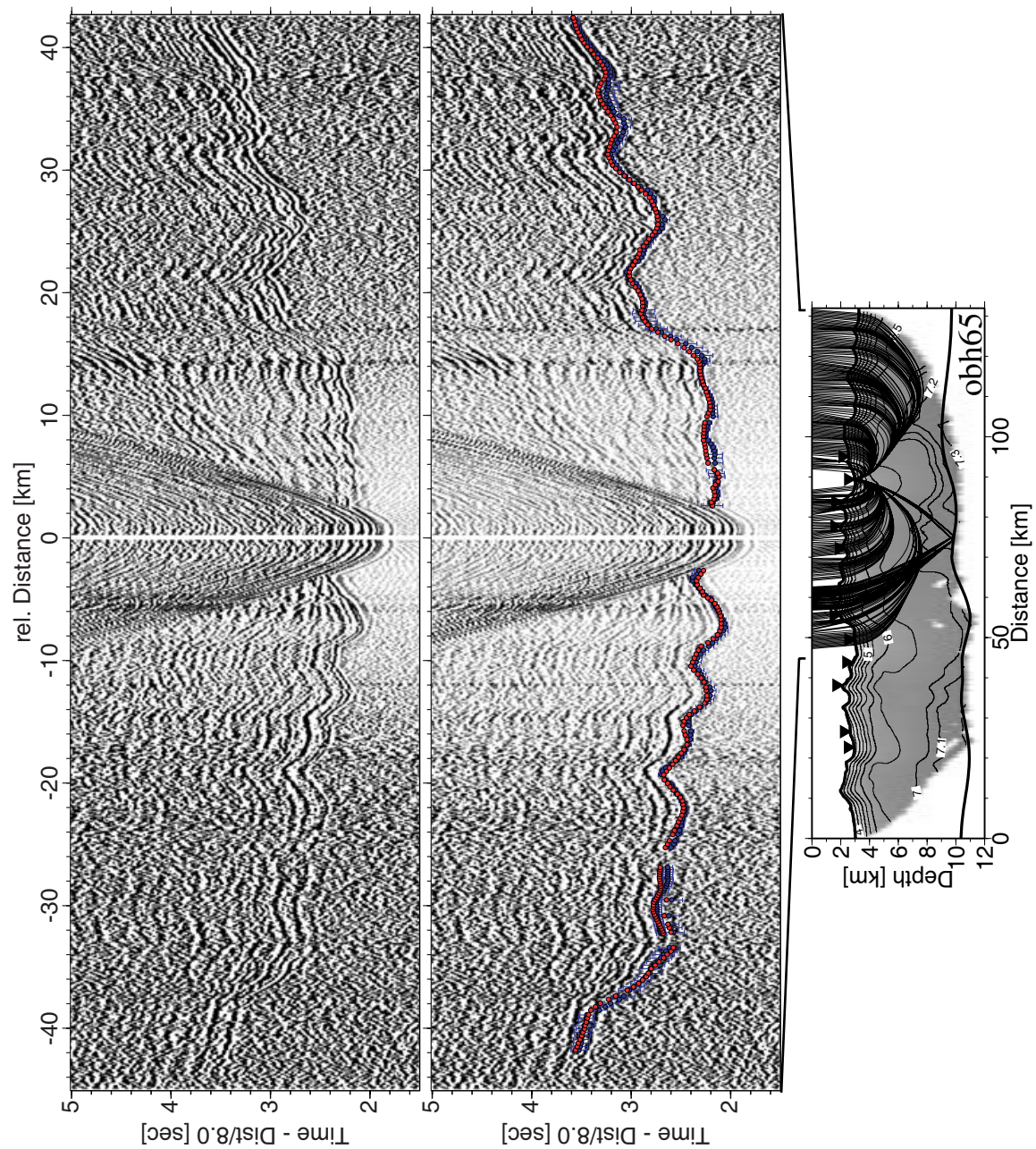


Figure D.2: Profile 11, OBH 65.

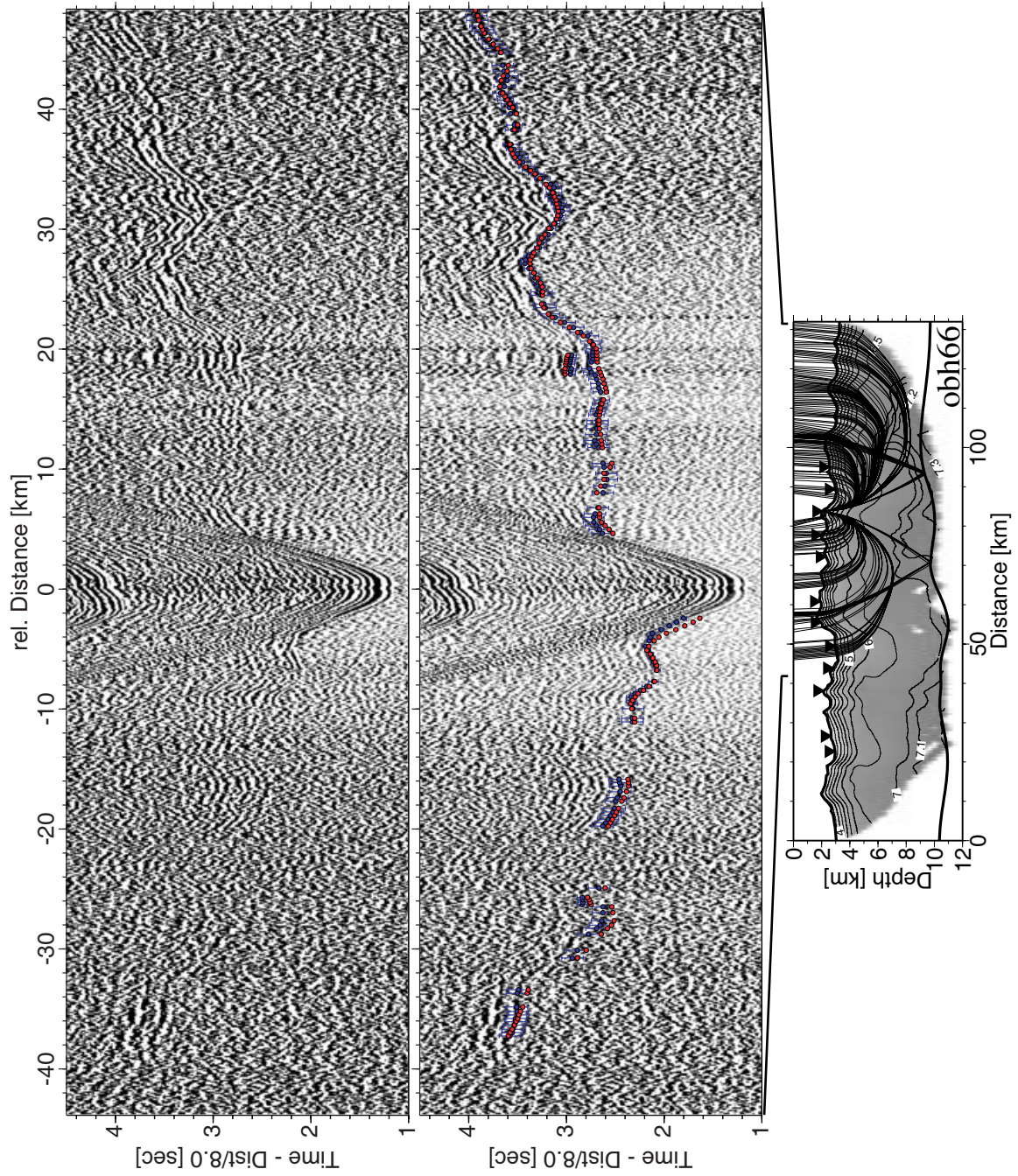
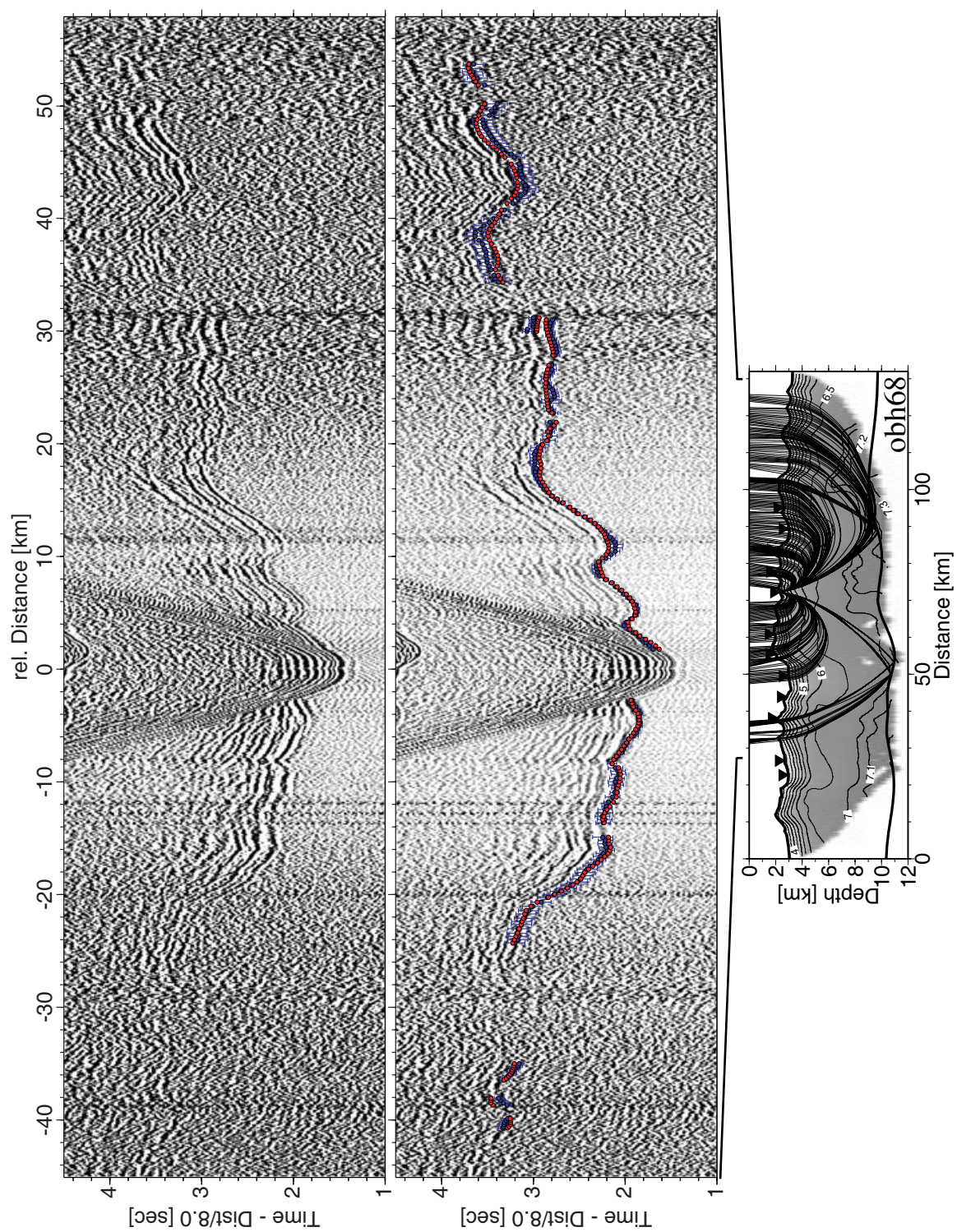
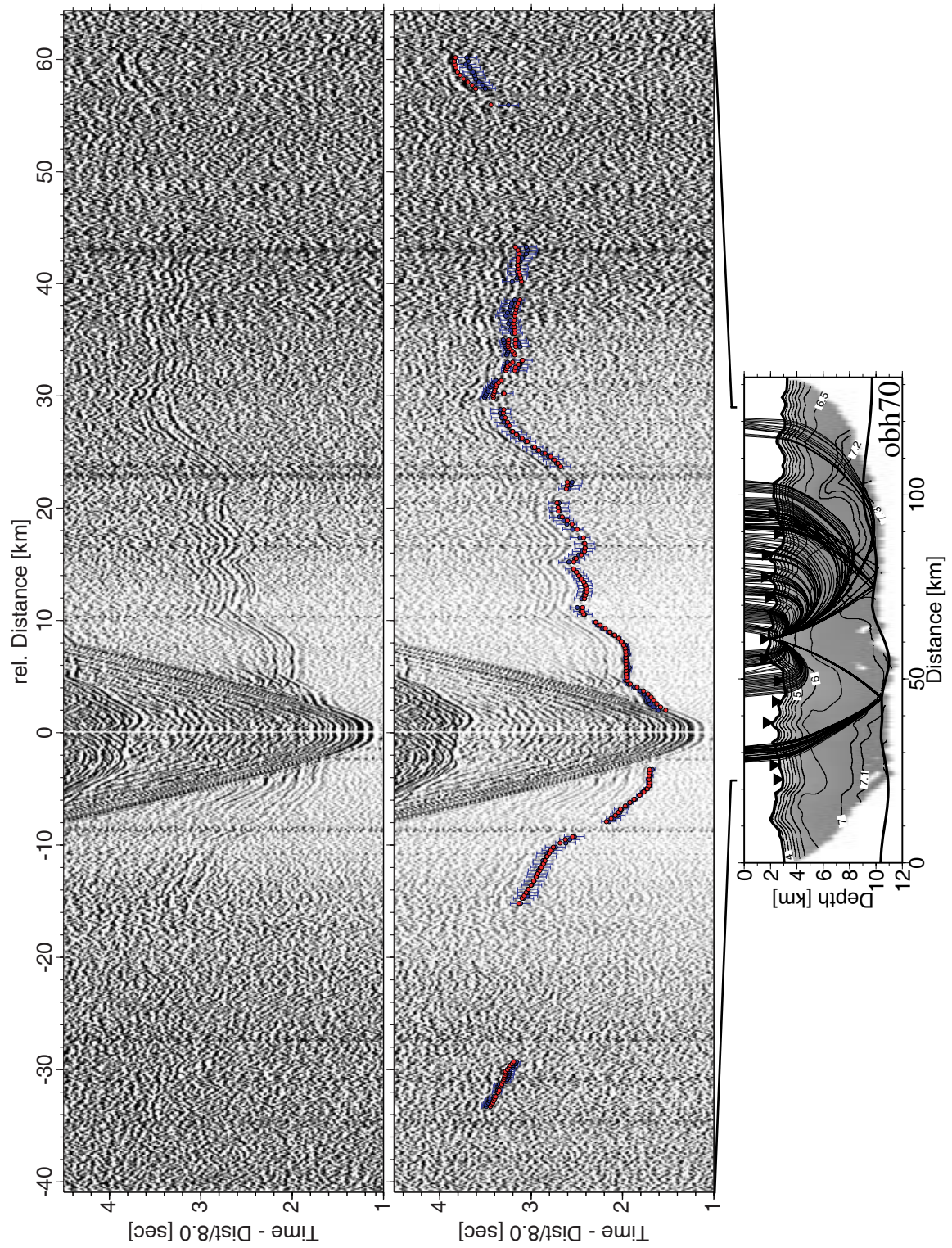
Figure D.3: *Profile 11, OBH 66.*



Figure D.4: *Profile 11, OBH 67.*

Figure D.5: *Profile 11, OBH 68.*

Figure D.6: *Profile 11, OBH 70.*

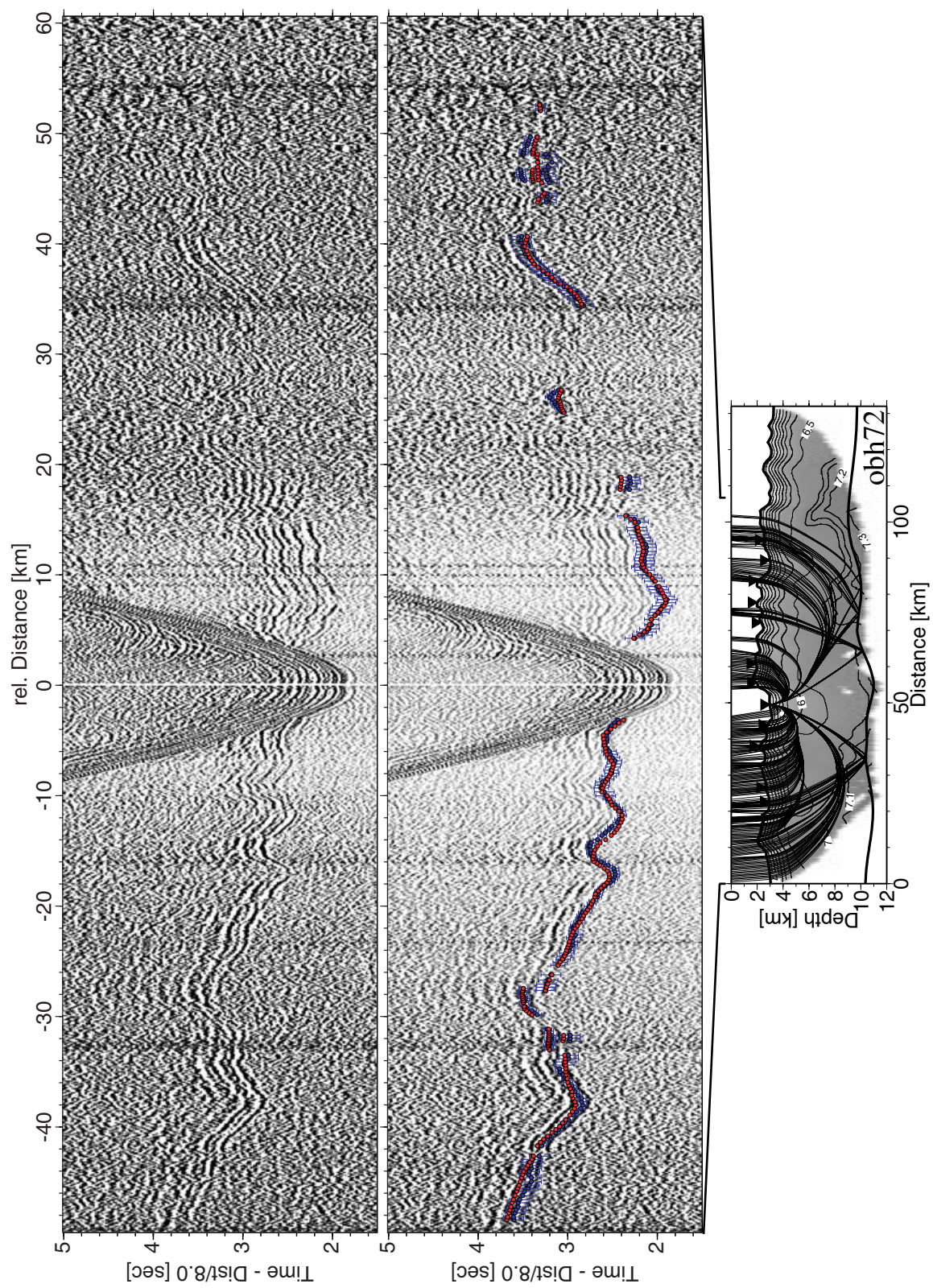


Figure D.7: Profile 11, OBH 72.

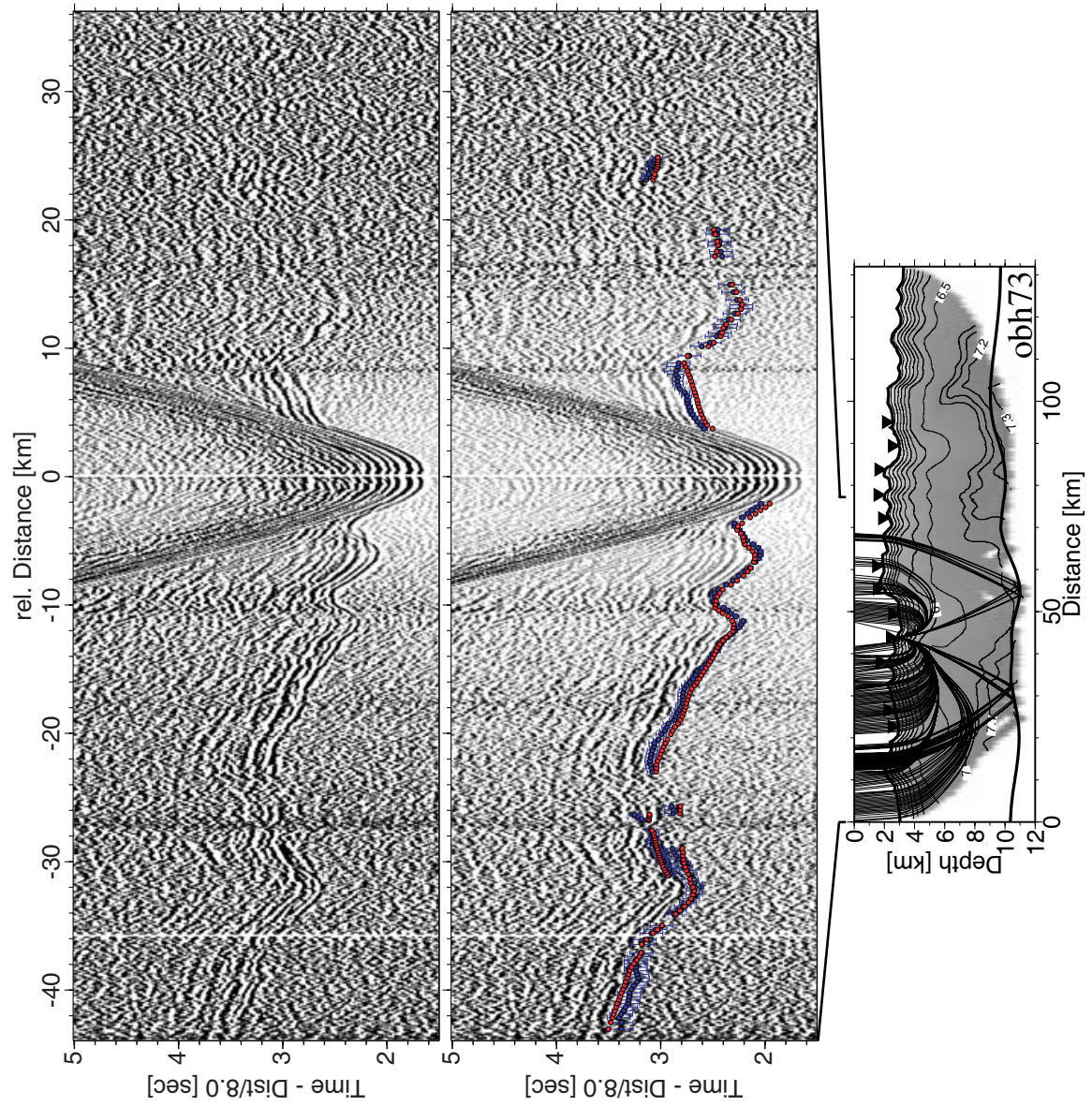


Figure D.8: Profile 11, OBH 73.

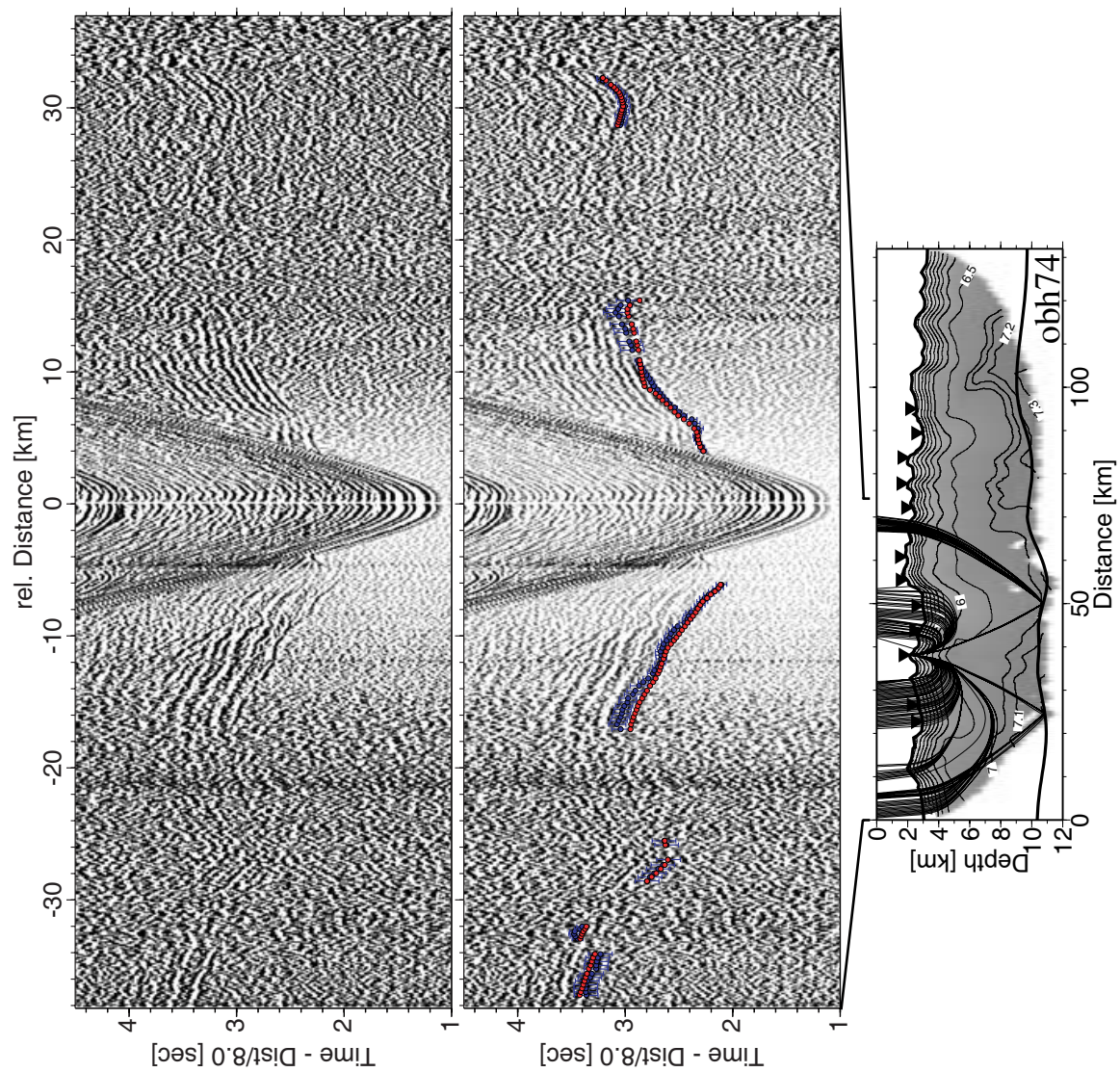


Figure D.9: *Profile 11, OBH 74.*

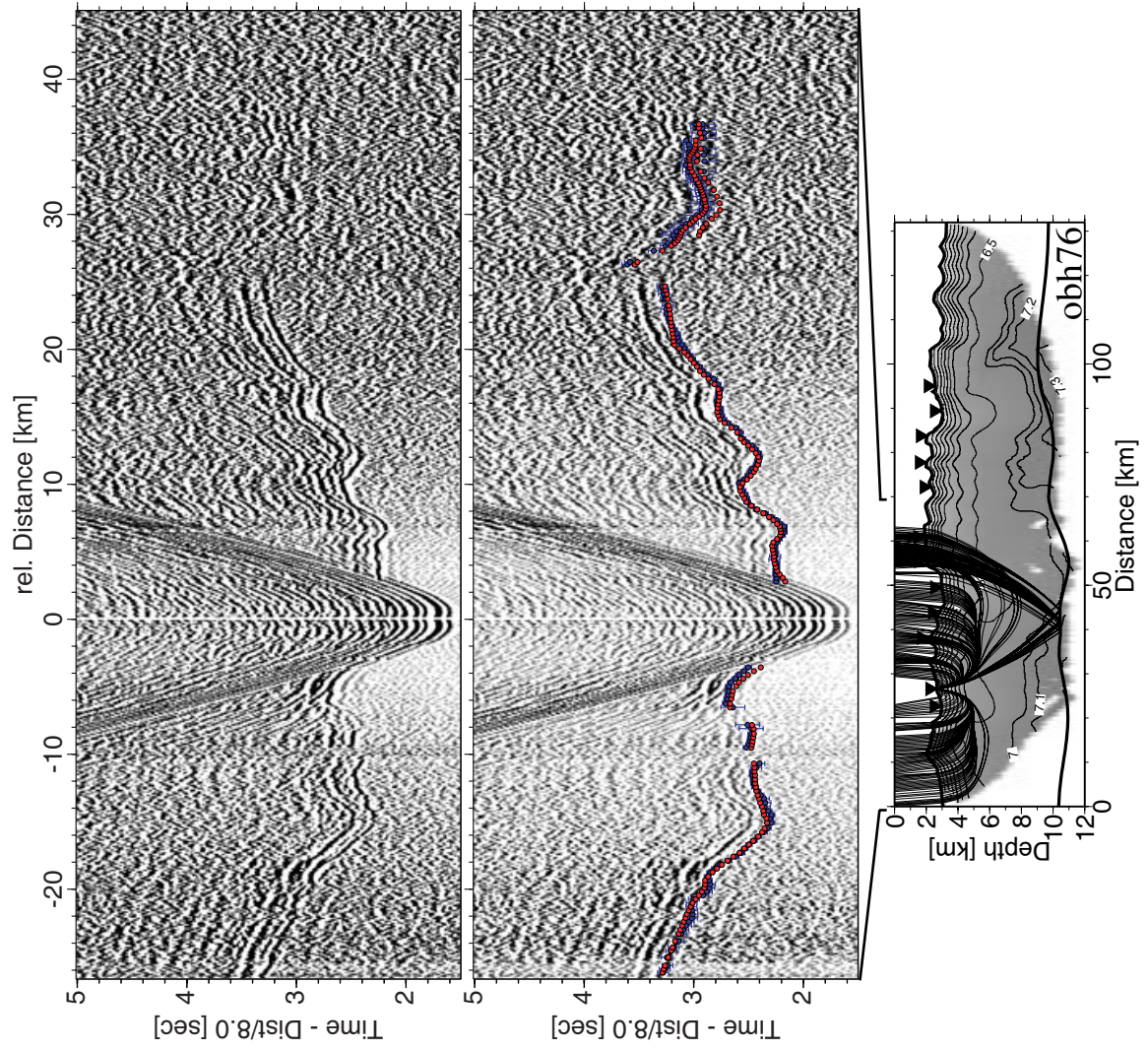


Figure D.10: Profile 11, OBH 76.

Acknowledgments

I am grateful to the Deutsche Forschungsgemeinschaft, which provided funding for most of my time at IFM-GEOMAR under the grant FL147/16.

I would like to thank Ernst Flüh for his continuous support and his friendly advice over the past years. He offered me generous freedom to cope with my work and provided new ideas in helpful discussions which often clarified important aspects of seismic modeling.

I am afraid Tim Reston still knows more about the MAR at 5°S than me. However, I would like to thank him for many “Aha!” moments and extended financial support.

Heidrun Kopp introduced me to the “world of tomography” in the early days of my time here. This was very much appreciated.

I spend many nice days on several research cruises. I would like to thank all the *Fahrt-leiter* for chartering me - especially Jörg Bialas - and “thanks!” to the *Junkers* compressors for not bursting completely during my stay in the container!

Many thanks to Matthias Zillmer and Ingo Grevemeyer for the numerous suggestions to improve the manuscript. Unfortunately, there was no time left to allow for them all.

Thanks to all the members of the Marine Geodynamics Department for their assistance and the nice working atmosphere in recent years. Special thanks belong to the “Mensa group”. The enjoyable debates at lunch time always gave new motivation for the second (and much longer) half of the day and sometimes even solutions to actual problems. In particular I wish to thank my colleagues in 8B that made life in this solitary part of the building less lonely and much easier. Thanks to Anne Krabbenhöft, Cord Papenberg, Jörchi Petersen, Ivonne Aden, Frank Lohmann, Arnim Berhorst and Thomas Leythäuser!

Last but not least, I would like to thank my family for their patient support and most important Wendy Pérez for her encouragement and active assistance especially in the turbulent phase of the last weeks (or months) - and even more for all the things beyond work!

Curriculum Vitae

Name:	Lars Planert
Date and Place of birth:	22 July 1973 in Stadthagen
Citizenship:	German
1980-1984:	Grundschule Bad Nenndorf
1984-1986:	Orientierungsstufe Bad Nenndorf
1986-1993:	Gymnasium Bad Nenndorf
May 1993:	Abitur
1993-1994:	Civil service, Barsinghausen
1994-1995:	Study of Meteorology at the University of Hanover
1995-2001:	Study of Geophysics at the University of Hamburg
Sept. 2001:	Diploma (M. Sc.) in Geophysics
since 2002:	Research Assistant at IFM-GEOMAR, Kiel

Eidesstattliche Erklärung

Hiermit versichere ich an Eides Statt, daß ich diese Arbeit ausschließlich unter Anleitung meiner wissenschaftlichen Lehrer und unter Verwendung der angegebenen Hilfsmittel angefertigt habe.

Kiel,